in part

Dc

Depar

NUMERICAL MODELING OF FLAME DEVELOPMENT OVER POLYMERIC MATERIALS

Volume I

By

Guanyu Zheng

A DISSERTATION

Submitted to
Michigan State University
in partial fulfillment of the requirements
for the degree of

DOCTOR OF PHYLOSOPHY

Department of Mechanical Engineering

2000

lecent flame development
ame transition and steady st
pplicable to fire safety issues
ic thermal mechanisms inclu
ow, reaction-induced ther
ndensed phase, melting, pyr
e interface, radiation heat
developed to describe such tra
the complex condensed beha
he models utilized are in the
mbustion model, in the cond
ensity global pyrolysis reac
ame model includes a mac
ensity using volume averagi
e flame development proces
ed anisotropic solid polym
ar variations. (2) flame

ABSTRACT

NUMERICAL MODELING OF FLAME DEVELOPMENT OVER POLYMERIC MATERIALS

By

Guanyu Zheng

Transient flame development over plastic polymeric materials comprises of preheating, ignition, transition and steady state flame spread and is of both fundamental and practical importance to fire safety issues. The flame behavior is determined by various physical and chemical mechanisms including (1) in the gas phase, combustion reaction, channel cross flow, reaction-induced thermal expansion, and interface injection flow; (2) in the condensed phase, melting, pyrolysis reaction, bubble nucleation, growth, and movement; (3) at interface, radiation heat loss and fuel and oxidizer transport. A numerical model is established to describe such transient flame spread process over a polymer with emphasis on the complex condensed behavior including melting, pyrolysis, and bubble generation. The models utilized are in the gas phase, a Navier-Stokes laminar flow model and combustion model; in the condensed phase, an enthalpy-based phase change model, a one-step global pyrolysis reaction model and a volume averaged bubble model. The bubble model includes a macro-scale transport model and a micro-scale bubble transport model by using volume averaging method. The investigation is carried out by modeling the flame development process with increasing complexities. It includes: (1) flame spread over an anisotropic solid polymers by using assumed flow pattern in the gas phase (Oseen approximation); (2) flame spread over melting polymers by using the Oseen

approximation; (3) flame spread over melting polymers with realistic flow pattern by solving the Navier Stokes equations; (4) ignition analysis for melting polymers with both flow patterns by using energy balance principle; (5) revisit of flame spread over an anisotropic melting polymer with realistic flow pattern by solving the Navier Stokes equations; (6) the mathematical model that describes the bubble forming, melting, and pyrolysis by using volume averaging approaches. Various parameters are obtained for flame structure, ignition delay, interface phenomena, and flame spread rate. These numerical results are favorably compared to experimental and analytical formulas. Furthermore, energy balance approaches are applied to ignition and flame spread. A simple ignition theory is derived for ignition delay; flame spread mechanism is interpreted in terms of weights of heat transfer mechanisms.

To my father Shenfu Zheng

To my father Shenfu Zheng, my mother Shifang Tang and my grandfather Yin Zheng.

I would like to express m
Patrick S. Wichman, wh
many I am grateful to Dr
would like to thank Dr. C
I am indebted to my pare
Jing and my sister Sh ng
really grateful to my w
many" but also shares the
I would also like to than
in Pathology for their fina

ACKNOWLEDGEMENTS

I would like to express my deep gratitude to my co-advisors, Dr. Andre Benard and Dr. Indrek S. Wichman, whose guidance and encouragement are invaluable throughout this study. I am grateful to Dr. Tom I-P. Shih for his advice on numerical algorithms. I would also like to thank Dr. Charles B. Owen during the final stage of this work.

I am indebted to my parents, Shenfu Zheng and Shifang Tang, my brother Guanhong Zheng and my sister Sujing Zheng for their constant support during my studies. I am especially grateful to my wife Junhua Gu, who not only supports me during the long "journey" but also shares the pain and joy with me.

I would also like to thank the State of Michigan and National Institute of Standard and Technology for their financial supports of this research.

TABLE OF CONTENTS

LIST OF TABLES

LIST OF FIGURES

A_c	pre-exponent
A_g	pre-exponent
c	gas phase co
C_p	specific heat
$\overline{C}_p$	non-dimens
D	diffusion co
E_c	activation en
E_g	activation en
g	gravitationa
h	reference le
h_v	enthalpy of
J	bubble nucl
k	thermal con
K	ratio of liq
k_B	Boltzman c
k_n	constant flo
$\bar{k}$	volume ave
$\overline{k}_r$	non-dimen
K_p	permeabili
l_x	streamwise
l_y	transverse
l_z	thickness
l_{z_0}	transverse
Le	Lewis nu

NOMENCLATURE

A_c	pre-exponential factor of pyrolysis reaction in condensed material, s^{-1}
A_g	pre-exponential factor of combustion reaction in gas phase, $m^3/(kg \cdot s)$
c	gas phase concentration in liquid, --
C_P	specific heat, J/(kg·K)
$\overline{C}_{Pl}$	non-dimensional liquid thermal capacity, C_{Pl} / C_{Ps}
D	diffusion coefficient, m^2/s
E_c	activation energy of pyrolysis reaction in solid phase, J/mol
E_g	activation energy of combustion reaction in gas phase, J/mol
g	gravitational acceleration, m/s^2
$\hbar$	reference length for non-dimensionalization, m
h_c	enthalpy of condensed material, J/kg
J	bubble nucleation rate, (number of bubble/m^3.s)
k	thermal conductivity, W/(m·K)
κ	ratio of liquid and gas viscosity $\kappa = \mu_g / \mu_l$, --
k_B	Boltzman constant, $5.67*10^8$ $W/m^2 \cdot K^4$
k_h	constant for Henry's law
$\overline{k}$	volume averaged thermal conductivity, W/(m·K)
$\overline{k}_l$	non-dimension liquid conductivity, k_l / k_s
K_e	permeability factor of pyrolysis products, --
ℓ_x	streamwise length of computational domain, m
ℓ_{sy}	transverse length of condensed material in computational domain (the thickness of the polymer), m
ℓ_{gy}	transverse length of gas phase in computational domain, m
Le	Lewis number, α_g / D

$\vec{j}$ unit vector n

L_f latent heat of

m fuel mass fl

m_{liquid} mass of liqu

M species mole

M the number

n number den

$\vec{n}$ unit vector n

P pressure of

P_∞ pressure in

q_c heat of com

q_{rad} external rad

$\bar{q}_{rad}$ average net

q_c heat of pyr

Q_{cg} Longitudin

Q_{cm} heat of com

Q_{cl} longitudina

Q_{conv} heat conve

Q_{lat} latent enth

Q_{pyr} Pyrolysis h

Q_{sen} sensible en

condensed

Q_T total heat r

Q_{tg} transverse

$\hat{l}$	unit vector normal to the boundary of the condensed material,--
L_s	latent heat of melting, J/kg
$\dot{m}$	fuel mass flow rate through gas-condensed interface, kg/(m^2·s)
m_{liquid}	mass of liquid in the condensed material, kg
M	species molecular weight, g/mol
M	the number of molecules per unit volume, 1/m^3
n	number density of the bubble, --
n^*	unit vector normal to moving solid-liquid interface in condensed phase, --
p	pressure of the gas phase, Pa
p_f	pressure in polymer liquid, N/m^2
q_g	heat of combustion reaction in gas phase, J/kg
$\dot{q}_{ig}$	external radiant heat flux for ignition, W/(m^2)
$\overline{q}_{ig}$	average net heat flux into the condensed material before ignition, J/s
q_c	heat of pyrolysis reaction in condensed material, J/kg
$\dot{Q}_{cg}$	Longitudinal heat conduction in the gas phase, W
$\dot{Q}_{com}$	heat of combustion reaction in the gas phase, W
$\dot{Q}_{cs}$	longitudinal heat conduction in the condensed phase, W
$\dot{Q}_{cvg}$	heat convection in the gas phase, W
Q_{lat}	latent enthalpy increase (associated with phase change) of condensed phase, J
$\dot{Q}_{py}$	pyrolysis heat in the condensed phase, W
Q_{sen}	sensible enthalpy increase (associated with temperature increase) of the condensed material at ignition, J
$\dot{Q}_T$	total heat in the condensed control volume, W
$\dot{Q}_{wg}$	transverse gas heat conduction at interface, W

$Q_{s,t}$ transverse s

R bubble radi

$Q_{s,n}$ total heat tra

R_u universal ga

Sr Stefan numb

t time, s

T temperature

T_f flame temp

T_g glass-transi

T_l temperature

T_m melting tem

u velocity in

u_d diffusion ve

u_f flame sprea

u_∞ velocity of

v velocity in

V_b bubble vel

$\bar{V}$ volume ave

V_f velocity of

V_g mass avera

w velocity of

w energy sou

w velocity of

w_g mass conv

w_p mass prod

x streamwise

$\dot{Q}_{ws}$ transverse condensed heat conduction at interface, W

R bubble radius, m

Q_{tot} total heat input to the condensed phase, J

R_u universal gas constant, 8314 J/(mol·K)

St Stefan number, $C_{Ps}(T_m - T_\infty)/L_s$

t time, s

T temperature, K

T_f flame temperature, K

T_G glass-transition temperature of polymer, K

T_i temperature of the gas-condensed interface, K

T_m melting temperature of condensed phase, K

u velocity in the longitudinal direction, m/s

u_i diffusion velocity of species i in the liquid phase, m/s, $i = m, p$

u_s flame spread rate, m/s

u_∞ velocity of uniform longitudinal inlet flow, m/s

v velocity in transverse direction, m/s

v_b bubble velocity, m/s

$\bar{v}$ volume averaged gas velocity in polymer liquid, m/s

v_i velocity of species i in the liquid phase, m/s, $i = m, p$

v_β mass averaged velocity in the liquid phase, m/s

w velocity of moving phase interface, m/s (in Appendix IV)

w energy source term from decomposition, J/(kg.s)

v_{n^*} velocity of moving solid-liquid interface, m/s

w_g mass consumption rate of fuel in combustion reaction of gas phase, kg/(m^3·s)

w_s mass production rate of monomer in pyrolysis reaction of polymer, kg/(m^3·s)

x streamwise distance downstream from origin, m

)	transverse d
	condensed m
Y	mass fracti
Greek	
α	thermal diff
ε	volume frac
ε_s	surface emis
μ	dynamic vis
ρ	density, kg
σ	surface ten
:	reference t
γ	temperature
ig	ignition de
Σ	solid-liquid
Ω	coefficient
Ξ	stoichiome
Subscript	
b	bubble
c	condensed
f	fuel in gas
g	gas phase
ig	ignition
l	liquid in c
m	monomer
p	polymer or
o	oxidizer in

y	transverse distance normal to the interface between the gas phase and the condensed material, m
Y	mass fraction of species in gas phase, --

Greek

α	thermal diffusivity $\alpha = k/\rho C_P$, m^2/s
ε	volume fraction (porosity), --
ε_e	surface emissivity, --
μ	dynamic viscosity, kg/(m·s)
ρ	density, kg/m^3
σ	surface tension, N/m
τ	reference time for non-dimensionalization, s
γ	temperature coefficient of surface tension
τ_{ig}	ignition delay time, s
Σ	solid-liquid interface in condensed material
Ω	coefficient for non-dimensionalization $\Omega = \alpha_s / \alpha_g$, --
Ξ	stoichiometric coefficient, $\Xi_i = \mathrm{M}_i \nu_i / \mathrm{M}_f \nu_f, \quad i = f, o$

Subscript

b	bubble
c	condensed material
f	fuel in gas phase
g	gas phase
ig	ignition
l	liquid in condensed material
m	monomer
p	polymer or product
o	oxidizer in gas phase

s	solid in condensed material
σ	solid (in Appendix IV)
β	liquid (in Appendix IV)
∞	initial condition

Flame spread over

...sitions in a ...

...ustion science ...

...nsport and chemica...

...portance of flame ...

...search since the tra...

...mmies than the ga...

...kground informati...

...ntial phenomen...

...The motivation a...

...ching physics rat...

...ady cover the flame...

... Polymers and Fir...

... Brief Descriptio...

Polymeric materi...

...mpounds such as ...

...macromolecules is th...

... When macrom...

...Higher Polymers are...

...bjects that are of t...

CHAPTER 1

INTRODUCTION

Flame spread over polymeric materials is of importance because for fire-safety considerations in a living environment and for fundamental questions arising in combustion science. Flame spread basically results from the complex interaction of transport and chemical processes that occur in both gas and condensed phases. The dependence of flame behavior on polymer properties is of particular interest in this research since the transport phenomena inside polymers receive comparatively less attentions than the gas phenomena. The layout of this chapter is composed of: (1) Background information on the polymers and their related fire hazard; (2) Description of fundamental phenomena during flame spread; (3) A review of previous modeling efforts; (4) The motivation and scope of the research. The introduction is oriented toward describing physics rather than listing research facts because some excellent reviews [1-7] already cover the flame spread problem from a wide range of perspectives.

1. Polymers and Fire Hazards

1.1. Brief Description of Polymeric Materials

Polymeric materials are composed mainly of macromolecules and other types of compounds such as mineral fillers or dyes. The essential characteristic of the macromolecules is that they consist of a relatively large number of repeating structural units. When macromolecular weights are greater than 1500 g/mol, the material is called a polymer. Polymers are normally solids and are bounded by a surface. Some thermoplastic polymers that are of interest to fire research are listed below [6].

- Polyethylene (PE) is
and low softening
construction indus
- PMMA (methylme
windows. Other ap
jewelry.
- Polypropylene is hig
and moldings, whic

From the viewpoint
materials can be class
be carbonaceous char
generally cellulosic fu
which produces almos
materials. It is gener
polymers show differ
emulations of flame
material, and PMMA
like non-charring m
during heating and de

C. Production and U

The production
production of plastics
the decades. Total p

- Polyethylene (PE) is the most important synthetic polymer and has low crystallinity and low softening and melting points. PE is used primarily in the packaging and construction industries.
- PMMA (methylmethacrylate) is used as "organic glass", for example in airplane windows. Other applications include contact lenses in medical systems and costume jewelry.
- Polyprolefin is highly crystalline and has a low density. It is used widely in fiber, film and moldings, which require high tensile strength.

From the viewpoint of condensed phase decomposition and combustion, polymeric materials can be classified as charring and non-charring materials. For charring materials, the carbonaceous char residue is produced during thermal degradation. Wood, or more generally cellulosic fuels, is the most representative of the charring materials. PMMA, which produces almost no char during combustion, is representative of the non-charring materials. It is generally understood and accepted that charring and non-charring polymers show different fire performance. Most of the experiments and numerical simulations of flame spread over solid fuels have been carried out with paper, a charring material, and PMMA, a non-charring material. PMMA has been chosen as perhaps the main non-charring material for fire research because of its relatively simple behavior during heating and decomposition and more literature results.

1.2. Production and Use of Polymeric Materials

The production and use of synthetic polymers is continuously growing. The production of plastics has increased much more than the production in general over the past decades. Total polymer production in the USA in 1992 was roughly 26 million tons.

A healthier global ec

ermal plastic resins

lymeric materials ha

3 Fire Hazards of P

It is of particular

ossibility of exposure

mospheric oxygen le

for certain applicatio

However, for a large m

based in many indus

pplastic polymeric m

egulatory standards h

erms of burning T

society. The combine

mage [6]. Since fire

assify the behavior

afety requirements F

ermal. Thermal haz

re caused by the

velopment can be c

ming or steady

ensive, and odor

ntamination and ca

A healthier global economy and end-use market will help boost world demand for thermal plastic resins to 122 million metric tons by the year 2000. [8] In addition, polymeric materials have become increasingly versatile and widely accepted.

1.3. Fire Hazards of Polymers

It is of particular concern that many of these polymeric materials involve the possibility of exposure to fire. Upon exposure to a sufficient heat source and sufficient atmospheric oxygen level, it is very possible that these materials may catch fire and burn. For certain applications, the ability to undergo combustion is a desirable requirement. However, for a large majority of purposes, polymer combustion is a serious disadvantage. Indeed, in many industries such as the automotive and construction industries, the use of synthetic polymeric materials has raised concerns about the flammability issues. Certain regulatory standards have been published in order to enforce public safety of the material in terms of burning. The financial cost of fire induced by polymers is enormous to human society. The combined cost of loss adds up to several times higher than the physical damage [6]. Since fire is an important practical problem, it is important to understand and quantify the behavior of polymeric materials in a fire environment to meet certain fire safety requirements. Fire hazards are defined in terms of two categories, thermal and non-thermal. Thermal hazards are caused by heat released from the fire. Non-thermal hazards are caused by the production of toxic gases and smoke [7]. Qualitatively, flame development can be described as: (1) ignition; (2) transition; (3) flame spread; (4) peak burning or steady state combustion; (5) generation of heat and undesirable toxic, corrosive, and odorous chemical compounds including those which obscure light transmission and cause electric damage. Flame development can be defined in terms of:

flammability measu

mical compounds.

asurements, which

asurements. (3) flam

ssible a fire is dete

2. Fundamental Phen

Flame develop

nsport processes in

nsport phenomena

nsport as well as

will be described be

mplified. A schema

2. Overall Descrip

Fundamentally,

rocesses one is the

e gas phase. Both p

ase reaction is co

ch as inert gases,

Figure 2 is compose

is assumed inside

(1) flammability measurements for ignition, generation rate of heat and generation rate of chemical compounds, generally under the steady state conditions, (2) flame spread measurements, which include pyrolysis, flame heights, and flame spread rate measurements, (3) flame extinction measurements where the effectiveness of an agent to extinguish a fire is determined [9].

2. Fundamental Phenomena of Polymer Combustion[1]

Flame development over solid polymers is complicated because it encompasses the transport processes in the gas phase (momentum, mass, heat, combustion reaction), transport phenomena in the condensed phase (melting, pyrolysis, bubble generation and transport) as well as coupling between gas and condensed phases. The overall phenomena will be described below, and then detailed aspects of the fundamental phenomena will be explained. A schematic description of the physical phenomena is given in Figures 1 and 2.

2.1. Overall Description

Fundamentally, the cyclic scheme as shown in Figure 1 represents two distinct processes: one is the fuel generation in the condensed phase; the other is the combustion in gas phase. Both processes are regulated by volatile and thermal feedback. The gas-phase reaction is controlled by the relative amount of three types of pyrolysis products, such as inert gases, combustible gases and carbonaceous char. The volatile shown in Figure 2 is composed of the former two gas products. Generally an amount of energy Q_1 is consumed inside the solid phase, and Q_2 is the heat generation during combustion in

[1] Combustion of polymers can be divided into three types: flaming combustion, smoldering and glowing combustion. Here mainly flaming combustion is considered.

e gas phase. The q...

ation. Inert gases d...

ygen and the comb...

ating environment...

ssible protecting th...

ve alternative pathw...

flaming combustion ...

ctable provides the h...

he temperature or the ...

sustaining combustio...

process is not possible...

ause, in general, to g...

1. Fuel and oxidizer...

mixture with suitable...

sufficiently high to m...

heated zone must be...

temperature rise can ...

and hot wires. In m...

absorption of radiati...

The next stage is fla...

with the burning reg...

flame up determines ...

the process mechanis...

the gas phase. The quantity $(Q_2 - Q_1)$ establishes the exothermic character of the reaction. Inert gases dilute the combustible gases, providing an inert gas layer between oxygen and the combustible zone. Furthermore, for charring materials exposed to an oxidizing environment, the char underlying the polymer acts as a thermally stable insulator protecting the underlying polymer from heat [10]. Combustion may proceed by two alternative pathways. These are flaming combustion and smoldering combustion. Flaming combustion is achieved when the heat released by gas phase combustion of volatile provides the heat flux needed for both solid degradation and flame spread. When the temperature or the heat flux is below a certain level, oxidization of char may produce smoldering combustion [4]. It is obvious that for non-charring polymers, the smoldering process is not possible because of the absence of a matrix or porous structure in the solid phase. In general, to get flaming ignition, there are three conditions that must be met [11]: (1) Fuel and oxidizer must be available at a proper level of concentration to yield a mixture with suitable flammability limits; (2) the gas temperature must attain values sufficiently high to initiate and accelerate the combustion reaction; (3) the extent of the heated zone must be sufficiently large to overcome heat losses. Before ignition, the temperature rise can be caused by external heating sources such as a pilot flame, sparks and hot wires. In most cases, the external source is thermal radiation, therefore the heat absorption of radiation in both gas phase and solid surface are important mechanisms. The next stage is flame spread. To allow the flame to propagate, the energy feedback from the burning region (gas phase plus solid phases) to the unburned solid ahead of the flame tip determines the flame spread rate. It is often difficult to determine which one of the process mechanisms is the controlling factor. An understanding of the dominant mode

flame spread. Many

three principal mo

the flame, (2)

radiation through the

relative importance of

temperature distribution

spread rate. The relat

mpairing its magnit

ombustible. In [5,

increasing importance

the different fire p

cluded that for sm

ed radiation from

However, for thin ma

heat transfer mechan

echanisms that acc

chanisms that con

ical picture of the co

2. Solid Phase Phe

For melting solid

ayer of the fuel samp

ed gases are transp

of heat transfer would facilitate the development of a simplified and accurate description of flame spread. Many analyses have been devoted to analyzing such energy feedback. In [5] three principal mechanisms besides external sources were proposed: (1) radiation from the flame; (2) conduction or convection through the gas from the flame; (3) conduction through the solid. Experimental approaches that were followed to define the relative importance of the different modes of heat transfer had been used to measure the temperature distribution in the solid and gas phases as well the gas velocity and flame spread rate. The relative importance of each mode of heat transfer was deduced by comparing its magnitude with the total enthalpy flow needed to pyrolyze the solid combustible. In [5, 12] it was inferred that radiation from the flame becomes of increasing importance as the scale of the fire increases. It is observed that thick materials have different fire performance from thin materials. For thick materials [5], it is concluded that for small-scale fires, heat conduction through the thick solid is dominant and radiation from the flame contributes significantly to the heat transfer process. However, for thin materials [4], it is stated that gas phase heat conduction is the major heat transfer mechanism for flames spreading over very thin fuel beds. There are other mechanisms that account for overall flame spread over solid polymers. The possible mechanisms that contribute to flame development are listed in Table 1, which provide a total picture of the complexity of flame spread.

2.2. Solid Phase Phenomena

For melting solid polymers such as PMMA, the decomposition is confined to a thin layer of the fuel sample near the gas/solid interface. In the melt layer, bubbles are formed and gases are transported to the surface. Thermal degradation behaves differently in inert

ng environ

ed by the la

1.1 Decomposition

When a polymer

bonds start to rupture

ated literatu

which means therm

oxidation participatio

has been emphasized

the thermal degradati

[5]

1) The change o

extent of de

2) The qualitat

products of de

3) The rate and a

With regard to the

degradation very lit

the polymers The

usually very rapidly

Degradation only re

photodegradation

thermodegradation a

photo-oxidation a

degradation

reactions

and oxidizing environments. In the latter case, the oxygen may diffuse through the melt layer, favored by the large holes produced by bursting bubbles.

2.2.1. Decomposition

When a polymer is heated it eventually reaches a temperature at which the weakest bonds start to rupture. Three definitions, degradation[2], decomposition[3], and pyrolysis[4] are used in related literature. It is generally accepted that pyrolysis takes place on the surface, which means thermal degradation without oxidation. However, the importance of oxidation participation on the surface of the burning polymers and in-depth degradation has been emphasized in [13]. For a better understanding of the mechanism involved in the thermal degradation of polymers, it is necessary to know three fundamental things [14],

1) The change of molecular weight of the polymer as a function of temperature and extent of degradation.
2) The qualitative and quantitative composition of the volatile and non-volatile products of degradation.
3) The rate and activation energy of the degradation process.

With regard to the change of molecular weight with temperature and extent of degradation, very little is found in the literature on this subject, except in the case of a few polymers. The information available indicates that the molecular weight drops initially very rapidly during the first few percent loss of weight. Afterwards the drop is

---

[2] Degradation: only relatively few bonds break and result in only minor changes in structure and properties, e.g. discoloration.
[3] Decomposition: at high temperature the polymer structure undergoes more extensive breakdown and results in disassociation of a significant proportion of the total number of constituent chemical bonds.
[4] Pyrolysis: irreversible chemical decomposition of materials due to an increased temperature *without oxidization*.

gen. As for the nat

parative analyses h

ene polymers, for ex

pyrolysis in a vacuum

ible in the case of p

fragmentation fragment

between these two ex

radical fragments

polyvinyl fluoride),

ated in structure to

ch are parts of the

ible products for

Most of the experim

temperature to about 4

higher temperature

greater fragmentation.

degradation of a giv

where E is the activa

T is the temperature,

the time rate of the

first-order reaction.

first temperature a

slow. As for the nature of the products of degradation, systematic qualitative and quantitative analyses have been done. The data that have accumulated so far indicate that some polymers, for example, polytetrafluoroethylene and poly-α-methylstyrene, yield on pyrolysis in a vacuum at temperatures up to about 500-600 °C almost 100% monomer, while in the case of polyethylene pyrolysis under similar conditions yields a spectrum of hydrocarbon fragments varying in molecular weight from 16 (CH_4) to 1000. Intermediate between these two extremes are polymers that yield on pyrolysis a mixture of monomers and chain fragments of varying sizes. There are also polymers like poly (vinyl chloride), poly(vinyl fluoride), and polymethylacrylate, which yield on pyrolysis fragments not related in structure to the polymer chains from which they derive, along with fragments that are parts of the chains. In pyrolysis at temperatures above 500 °C, the nature of the volatile products for any given polymer depends to a large extent on the temperature. Most of the experimental work on pyrolysis reported in the literature relates to the temperate to about 400-500 °C. However, some experiments have been carried out at far higher temperature than these. The results indicate that higher temperatures produce greater fragmentation of the degradation products. The reactions involved in the thermal degradation of a given polymer can be calculated by means of the Arrhenius equation:

$$K = Ae^{-E/R_u T} \tag{1}$$

where E is the activation energy, K is the rate constant, A is the pre-exponential constant, T is the temperature, and R_u is the universal gas constant. The reaction rate is defined as the time rate of the weight loss with respect to the percent of the original samples. In a zero-order reaction, which happens very seldom, the reaction rates are constant for any given temperature and can be used as values for the rate constants in the Arrhenius

ignition. Frequently th

ckup-out in a first or

ition C is the concen

rmal degradation p

ncentively. Then

ne and is based on

It is worth noting that

ondensed phase may

ase oxygen is tra

Kanwagi concluded

important for ignition

ncluding oxygen

ning or steady stat

*** Phase Change

The melting o

morphous or cryst

ystalline. The deg

ffect on the soften

morphous plastics

Molecules are the sa

Properly termed a p

equation. Frequently the degradation is composed of several reactions and the order is not clearly-cut, in a first order reaction, the rate is proportional to the reacting substance:

$$-\frac{dC}{dt} = KC, \tag{2}$$

where C is the concentration of the reacting species and T is the time. In some polymers, thermal degradation proceeds by two or more reactions, which run either concurrently or consecutively. Then the activation energy in a single step representation is a composite value and is based on the overall rate of degradation.

It is worth noting that, not only pyrolysis reactions but also oxidative degradations in the condensed phase may significantly affect the gasification rate of a polymer if enough gas phase oxygen is transported to the solid phase during combustion of the polymer. Kashiwagi concluded [13] that the contribution of oxidative degradation could be important for ignition processes at low incident flux. Brauman [15] concluded that the surrounding oxygen does not affect the polymer degradation process in steady state burning or steady state radioactive gasification of PMMA and PE.

2.2.2. Phase Change (Melting)

The melting characteristic of thermoplastic polymers depends on the types: amorphous or crystalline. Most polymers are neither entirely amorphous nor entirely crystalline. The degree of crystallinity and the strength of binding forces have a profound effect on the softening range or melting point of a polymer. The melting point of amorphous plastics is not as clearly defined as that of monomer solids where all the molecules are the same size. The melting point T_m of amorphous thermoplastics is more properly termed a melting range, since a single specimen consists of more than one

molecular weight and more than one crystal size. Examples of this type are PMMA and PVC. These gradually softening plastics become softer and softer as the temperature is raised and the actual melting point is obscure, being only a change in slope in a plot whose one axis is temperature [16]. In contrast to amorphous are crystalline polymers, examples of which are nylon and polypropylene. These polymers tend to maintain its structure. When the melting point is reached, the crystalline portions quickly melt and the whole plastic becomes fluid over a narrow range of temperature. Above the melting point of these polymers, the difference between the amorphous and crystalline polymers disappear, although the branching and regularity of the chain structures still influence their flow properties. Decreasing molecular weight, or adding a solvent to a polymer, or decreasing the crystal size lowers T_m [17]. The glass-transition temperature T_G is called a second order transition, since the change in volume is not discontinuous as it is with T_m. Below T_G the polymer segments do not have sufficient energy to move past one another. For partially crystalline materials, T_m is always greater than T_G and that the difference is a maximum for homo-polymers. An examination of these parameters for many homo-polymers leads to the generalization that,

$$1.4<(T_m/T_G)<2.0$$

Almost all thermoplastics soften above their glass transition temperature; some will exhibit flow motions in the polymer melt. For some thermoplastic polymers with high initial molecular weight[5], flame spread is relatively steady and clean because they form

[5] Since melt viscosity of molten polymers depends strongly on their molecular weight [13], the initial molecular weight was taken as an important parameter for evaluation of flame spreading.

igible molten po
ight form both m
pyrizing surface a
lame spread phenom
eights is shown in
urface regressed, a s
forward movement
his opposing slow
slowdown of flame
flame started to climb
nd the front portion
igher molecular we
eight PS sample [
ample did not show
ne high molecular
ntinual flame spre
flame over the low
forward flame spr
rning polymer m
ertain experimental
f their flammability
ently ignored by
section, some new

negligible molten polymer near the flame front. Polymers with low initial molecular weight form both molten polymer and opposed slow fluid motion along the inclined vaporizing surface against the traveling flame. A schematic illustration of horizontal flame spread phenomena for two PS (polystyrene) samples with high and low molecular weights is shown in Figure 4 in [18]. Since the flame spread slowly while the sample surface regressed, a steep wall of molten polymer appeared in front of the flame. A slow downward movement of the molten polymer toward the bottom of the wall was observed. This opposing slow fluid movement against the flame spreading direction caused the slowdown of flame spread and consequently the formation of the steep wall. Then the flame started to climb the steep wall. The flame continued to climb to the top of the wall until the front portion of the sample burned out. It was observed that flame spread rate of higher molecular weight PS sample was about 25% larger than that for the low molecular weight PS sample [18]. Downward flame spread over high molecular weight PMMA sample did not show any dripping, and the flame spread steadily. However, flame spread over high molecular weight PS yielded a much-enhanced rate compared with the rate for horizontal flame spread. This resulted from streaking of small molten polymer balls. The flame over the low molecular weight PS and PMMA samples self-extinguished during downward flame spread because of heat loss from the downward streaking of small burning polymer molten balls to the cold sample surface. The results indicate that, in certain experimental configurations, the melting of thermoplastics has a large influence on their flammability properties and subsequent spread. However, such effects have been largely ignored by previous researchers who have employed non-melting samples. In addition, some new inorganic polymers, whose backbone elements are not carbon, exhibit

ugh different fire b

rmulation of silica

2.3. Bubble Formati

A proper unders

ssential to the mat

oiling temperatures

olymer degradation

ubble and form b

egradation products

3. Visual observat

°C and 4.0 W, in wh

itrogen environme

ble as shown in Fig

as large as 1 mm d

ese surface bubbles fo

ilm surface of the s

rface appears is st

ses directly through

mall neck-like holes

his process is viole

as phase, it can als

the ambient gas, th

be substantially low

totally different fire behavior. For example, the burning of PDMS samples will result in accumulation of silica at or near the surface [13].

2.2.3. Bubble Formation

A proper understanding of the rate of polymer gasification in a fire environment is essential to the mathematical prediction of fire growth on such materials. Since the boiling temperatures of some of the degradation products are much lower than the polymer degradation temperatures, these products are superheated as they form. They nucleate and form bubbles. Then these bubbles grow with the supply of more small degradation products to the bubbles by diffusion from the surrounding molten polymer [19]. Visual observation of PMMA gasification was reported in [20] at radiant fluxes of 1.7 and 4.0 W, in which the effects of gas phase oxygen on the mass flux were studied. In a nitrogen environment, rough surfaced, snowball-like bubbles develop and grow with time as shown in Figure 2 (a) in [20]. By the end of exposure, these bubbles' size can be as large as 1 mm diameter, formed up to 2-3 mm below the sample surface. When subsurface bubbles form, they grow toward the direction offering least resistance, i.e., the front surface of the sample. Because the viscosity of the molten polymer layer near the surface appears is still high, only bubbles within 1mm or so of the surface are able to burst directly through the front surface. Bubbles further below the surface burst through small neck-like holes into near surface bubbles, then vent through to the gas phase. The burst process is violent and can cause a vapor jet that extends a few centimeters into the gas phase; it can also throw molten polymer into the gas phase. When oxygen is present in the ambient gas, the viscosity of the near surface layer of degrading PMMA appears to be substantially lower. The bubbles start earlier, the bubble frequency is higher, and the

heating process is is

interior in the fron

interior volume. At hi

and oxidizing atmosp

[5] is for the case of

smaller because of th

uses the surface ten

ten in the case of p

ion but it is not cle

degradation products

2.3 Gas Phase Phen

Once the solid c

the solid surface an

oxidizer. The flame

fraction of the prop

flow field, pressure

Compared to the c

developed in more de

2.3.1. Combustion P

Exothermic rea

sufficiently high tem

complicated. One c

isolated from degra

bursting process is less violent. The burst bubbles leave larger holes (up to ~1 mm diameter) in the front surface of the sample. These holes admit oxygen to the sample interior volume. At higher fluxes, the differences in the near surface behavior due to inert and oxidizing atmosphere are less pronounced but still present. Figure 2(c) and 2(d) in [20] is for the case of higher flux 4 W/cm^2. In both cases, the snowball-like bubbles are smaller because of the thinner thermal layer and shorter exposure time. The higher flux raises the surface temperature and apparently decreases the degrading polymer viscosity even in the case of pure nitrogen. The subsurface degradation is important for gasification too, but it is not clear what is the main transport mechanism to the surface for small degradation products. [13]

2.3. Gas Phase Phenomena

Once the solid combustible pyrolyzes, the fuel vapors convect and diffuse away from the solid surface and produce the spreading flame by reacting with ambient gaseous oxidizer. The flame leading edge stays very close to the fuel surface, travels in the direction of the propagation and acts as an "anchor" to the trailing diffusion flame. The flow field, pressure field, and combustion reaction influence the flame behavior. Compared to the condensed phase phenomena, the gas phase phenomena have been developed in more detail.

2.3.1. Combustion Reaction

Exothermic reaction occurs when fuel vapor and oxidizer coexist in a region of sufficiently high temperature. There are several factors that make the combustion reaction complicated. One complexity comes from the very high number of chemical species evolved from degrading solid both for cellulosic materials and thermoplastic polymers.

for example, in flame

tention complexity re

olecules and formal

lame has to account

ely large even for

ecules nearly 300

ropane, octane), the

n approximate

ith the size of the

olecules actually

ethane flame two (

he C2Hb mechani

agments form cycli

3.2 Flow Field

In the gas phase

the solid fuels ca

onditions: (1) flow

eaction as the oxid

preads against the

low pushes the fla

one of reacting

flame because the

the vapors genera

For example, in flame above the PMMA surface, the species are of at least fifteen types. Another complexity results from the long sequences of steps in which breakdown of fuel molecules and formation of combustion product proceeds. A fully detailed model of a flame has to account for all such elementary reactions. The number of reactions needed is very large even for small hydrocarbons. For example, combustion of methane (CH_4) requires nearly 300 elementary reactions. For more complicated fuels (such as ethane, propane, octane), the number of elementary reactions can easily exceed 300 or even 500. In an approximate sense, the number of elementary reactions increases geometrically with the size of the fuel molecule. Complications occur when lower-order hydrocarbon molecules actually combine to form higher order hydrocarbon molecules, e.g., in the methane flame two CH_3's combine to form C_2H_6: then the CH_4 mechanism includes also the C2H6 mechanism. An even greater complication arises when the hydrocarbon fragments form cyclical compounds that combine to form "soot".

2.3.2. Flow Field

In the gas phase, an external laminar flow is parallel to the interface. Flame spread over solid fuels can be classified into two main categories according to the flow conditions: (1) flow assisted flame spread, occurs when flame spread is in the same direction as the oxidizing flow; (2) Opposed flow flame spread, occurs when the flame spreads against the oxidizing gas flow. In the flow-assisted flame spread, the concurrent flow pushes the flame ahead of the vaporizing fuel surface. The heat transfer from the mixture of reacting gases and the combustion products favors the propagation of the flame, because the diffusion flame is driven ahead of the pyrolysis front. In addition, the fuel vapors generated upstream of the pyrolysis front that are not consumed by the

gream diffusion f

iffusion flame dow

ppears to be controll

the unburned fuel

nd this more hazar

he flame spread rat

ased to its pyrolys

When the size of th

ppears to be the d

pread the transfer

difficult because the

ermal effects incl

pread. It is domina

nd high oxygen co

xygen concentration

A Review. Model

The formulation

quires the conser

ondensed phase co

This would further

imensional, elliptic

hase combustion

ation of the fu

upstream diffusion flame are driven ahead of the pyrolysis front, thus extending the diffusion flame downstream from the pyrolysis region. For this reason, the flame spread appears to be controlled primarily by the rate of heat transfer from the downstream flame to the unburned fuel. Thus as a result, the flame spread process is generally more rapid and thus more hazardous than the spread in opposed flow configuration [5]. The rate of the flame spread rate will depend on how fast the surface temperature of the solids is raised to its pyrolysis temperature. The flow remains laminar only in the initial stage. When the size of the flame increases, the flow becomes turbulent and flame radiation appears to be the dominant mode of heat transfer. In the case of opposed-flow flame spread, the transfer of heat from the flame to the upstream region is rendered more difficult because the gas flows against the propagating flame. It is concluded that various external effects including oxygen level and flow rate among others influence flame spread. It is dominated by (1) heat transfer mechanisms at low opposed-flow velocities and high oxygen concentrations; (2) chemical kinetics at high flow velocities or low oxygen concentrations.

3. A Review: Modeling of Flame Spread over Non-Charring Polymers

The formulation of a rigorous mathematical model of the flame spread process requires the conservation equations for the gas phase coupled at the interface to the condensed phase conservation equations through the appropriate boundary conditions. This would further require the solution of a system of coupled, transient, two-dimensional, elliptic, nonlinear partial differential equations that includes appropriate gas phase combustion reactions and condensed phase pyrolysis reaction mechanisms. The solution of the full problem is formidable, not only because of the limitations of

mputational power

ause the models to

mple model is lim

ctions at the ga

uid phase, but ass

me of the first theore

veral important as

pproximation (a sp

mperature. The fir

ns consumed and h

he flow field. The

henomena inside th

he thin material ar

as fuel, and flame

nder fast reaction

een raised [1]. Th

elocity is contra

Fernandez-Pello [

nfection limit. The

by pointing out that

e used *a priori*. In

milar form but

ignition temper

computational power, but also because of the lack of available experimental data. For this reason the models to date have treated the problem at different levels of complexity. The simpler model is limited to the condensed phase energy analysis with *a priori* specified conditions at the gas-condensed interface. More refined models include both gas and solid phase, but assume an infinite rate gas phase reaction. The De Ris model [21] was one of the first theoretical models to successfully attack the flame spread problem. It used several important assumptions: (1) Infinite reaction rate in the gas phase; (2) Oseen approximation (a specified uniform gas phase flow field); (3) constant solid vaporizing temperature. The first assumption reduces the flame to a sheet where fuel and oxidizer are consumed and heat is generated. The second assumption avoids the complication of the flow field. The third assumption avoids the complication of the complex transport phenomena inside the condensed phase. de Ris derived two flame spread formulas for a fuel-thin material and a fuel-thick material, each being an arithmetic correlation including gas, fuel, and flame properties. The predictions of two formulas are found to be good under fast reaction conditions although concerns over the various approximations have been raised [1]. The independence of the flame-spread rate from the opposed flow velocity is contrary to existing experimental observations near extinction limit (Fernandez-Pello [22]). The flame sheet assumption eliminates consideration of extinction limit. The constant vaporizing temperature was questioned by Sirignano [23] by pointing out that this temperature is a function of the flame properties and should not be used *a priori*. In order to remedy this, he proposed a flame model [24], which has a similar form but has coupling at the solid-gas interface. Although the a priori vaporization temperature was removed, this flame model is only applicable to the surface

raining case. Fernan

pproximation They

ner region and (2)

hemical kinetics Th

keen approximation

mportant near the fl

merical solution

umber They kept t

onservation aspect

upling of the c

ernández-Pello at

ombustion and fl

echanism far from

Wichman and Will

rmulated a surface

ey include the sol

he equations and b

he streamwise heat

Wall energy balan

ass and the proces

erived a formula f

hich redistributes

ave could be rea

reacting case. Fernandez-Pello and Williams [25] were not satisfied with the Oseen approximation. They devided the gas phase into two regions: (1) An upstream boundary layer region and (2) A downstream diffusion region. In addition, they used finite rate chemical kinetics. The introduction of the boundary layer, in some sense, "remedied" the Oseen approximation, but it removed the upstream diffusion that was later proved to be important near the flame leading edge. The work of Frey and Tien [26] was the first numerical solution by obtaining a flame structure and its dependence on Damkohler number. They kept the Oseen approximations and only emphasize the species and energy conservation aspects of their work. These assumptions remove the interaction of the coupling of the combustion and aerodynamics such as the gas expansion effect. Fernandez-Pello at al. [22] experimentally investigated the influence of oxidizer concentration and flow velocity on the flame spread rate. They found that the controlling mechanism far from the extinction limit is thermal (de Ris) and otherwise is chemical. Wichman and Williams [27] proposed the global energy balance approach, which formulated a surface flame sheet in a flame-fixed coordinates. The resulting equations only include the solid and gas phase energy equations, which, however, is consistent with the equations and boundary conditions for the de Ris model. Physically they assumed that the streamwise heat conduction in both gas and condensed phase does not influence the overall energy balance. This is correct as long as the reaction in the gas phase is infinitely fast and *the process is steady*. Atreya [28] applied the global energy balance principle and derived a formula for charring fuel. A parabolic-type char-wood interface was postulated, which redistributes the heat from the gas phase. The flame spread formula for charring wood could be readily applied to the melting polymer since both participate the similar

processes.

We consider now
were first incorpora
raction of the ac
gas injection from in
premixed flame
ky and Glassman
Navier-Stokes equa
low-off phenomen
Zeldovich number
under micro-gravity
which is not impor
creases the flame
Glass [33] formulate
chemical predictor
ption transition.
has increased with
ction is shifting tow
In summary, th
implify the proble
Kovas [1, 23, 3
mperature of the
nd a boundary la

processes.

We consider now the pure numerical solutions. The full Navier-Stokes equations were first incorporated into steady flame spread modeling by Mao et al. [29]. The interaction of the aerodynamics and combustion, especially the thermal expansion and gas injection from interface were explored in detail. The flame structure was confirmed to be a premixed flame upstream and diffusion flame downstream that was first proposed by Ray and Glassman [30]. Chen [31] modeled the flame spread process by using the Navier-Stokes equations for thin fuel flame spread problem, and investigated the flame blow-off phenomenon with respect to the dependence of the flame spread rate on the Damköhler number. Bhattacharjee [32] investigated the thin-fuel flame spread problem under micro-gravity conditions by using similar approaches. He found that radiation, which is not important under normal gravity condition, becomes so significant that it decreases the flame spread rate to a factor of 2-3 times smaller than in normal cases. Di Blasi [33] formulated the first transient flame spread model, which makes possible the numerical prediction of the transient flame development. This model yields results for ignition, transition, and steady flame spread. The complexity of the flame spread model has increased with time. With the rapid expansion of computational power, the modeling effort is shifting toward tasks that had previously been deemed too difficult.

In summary, the early studies of flame spread employed numerous assumptions to simplify the problem. Simplified models based on these assumptions are available in reviews [1, 23, 34, 35]. The most commonly used approximations are constant temperature of the solid during thermal degradation, a flame sheet (infinite chemistry) and a boundary layer. More comprehensive mathematical models include the partial

ifferential equations

plied to describe sp

lame spread, and ex

ot amenable to ana

present the gas phas

rocesses, reflecting

ose in the condens

iscussed.

1 Solid Phase Tra

Most of the m

ased on a simple en

urface, and have be

he molten layer o

olymers, were hard

PMMA under a spe

ansport in thick po

ne heated polyme

ccording to a ze

ecomer. In such a

hich depends on t

onductivity and de

olymers assume th

onfiguration. In ch

differential equations for conservation of mass, momentum, energy, and chemical species applied to describe specific aspects of combustion of synthetic polymers, such as ignition, flame spread, and extinction, see review articles [4, 36]. These more complete models are not amenable to analytical solutions and it is necessary to use numerical techniques. At present the gas phase models are more advanced and include many important physical processes, reflecting a greater understanding of the gas phase phenomena compared with those in the condensed phase [13]. In the following, the modeling of the solid phase is discussed.

3.1. Solid Phase Transport Modeling

Most of the models for thermoplastic polymer flame spread, available to date, are based on a simple energy balance equation for the solid with localized degradation at the surface, and have been coupled to the gas phase equations. The effects of bubbles inside the molten layer on the transport of volatile, during degradation of thermoplastic polymers, were hardly considered except for some work on steady sate gasification of PMMA under a specified external energy flux [37]. However, two-dimensional bubble transport in thick polymers is not taken into account. Thermally thick fuel models assume that heated polymeric materials remain solid until finally gasifying at the surface according to a zero-order Arrhenius pyrolysis reaction giving the corresponding monomer. In such a way, the phase-change effect and in depth degradation were ignored, which depends on fuel properties and environmental parameters. Heat capacity, thermal conductivity and density are assumed to be constant. The models for thermally thin polymers assume that variables across the solid thickness are uniform in their spatial distribution. In char-forming polymers, char formation in numerical modeling was

scribed in a very

egradation, it occ

mination, propag

lits into two categ

rrhenius rate react

idely used in com

nsport processes

for chain initializati

ven proposed. Suc

rocesses. Some of

2 Gas Phase Mod

For the gas p

nentum, energy

rincipally for lamin

verall, second or

ompressible work

quations and the

quations are inclu

tate pressure vari

inear pressure is r

omentum equatio

nd the determinati

Read models hav

described in a very simple fashion and only for thin fuels [26]. In terms of PMMA degradation, it occurs according to the following main stages: depolymerization initialization, propagation of reaction chain and termination. Kinetic modeling of PMMA falls into two categories: (1) One step global models which employ a one-step, global, Arrhenius rate reaction to account for all chemical processes. Such an approximation is widely used in computer models, which couple the gas and solid phase chemical and transport processes. (2) Detailed degradation models using kinetic schemes that account for chain initialization reactions, depropagation reactions and termination reactions, have been proposed. Such models have never been coupled to the description of physical processes. Some of research that belongs to this group is available in [26-40].

3.2. Gas Phase Modeling

For the gas phase model, most advanced models published to date include momentum, energy and chemical species mass balance equations. Analyses are principally for laminar flow, and finite rate combustion kinetics are described through an overall, second order reaction such as $F + \nu_o O \rightarrow \nu_p P$. Viscous dissipation and compressible work are neglected. Furthermore, the coupling between the momentum equations and the state equation due to pressure terms, when momentum balance equations are included in the mathematical formulation of the problem, is neglected. Since pressure variations in space are very small and, in general the system is open, the mean pressure is reduced to the specified ambient pressure. The decoupling of the momentum equations from the state equations cuts off considerations of acoustic waves, and the determination of the pressure field becomes an elliptic problem. To date, flame-spread models have numerically solved and treated the velocity field differently. The

mplest models con-

gas density and pre-

been approximatio-

herefore been wide-

ns depend strongly

lso shown a great

elocity profiles are

1 Motivations and

Combustion of

many chemical and

dvanced than solid

quations. On the

formulation of heat

he surface or in-d

nfluence to the flam

n fact, there are no

henomena, even in

Therefore the object

with some complex

ubble nucleation, g

ate of theoretical

n Chapter 2, the c

pecified flow field

simplest models consider the solution of species and energy equations assuming that the gas density and pressure are constant and the velocity field is known (similar to the Oseen approximation). The computational cost is very low, and this approach has therefore been widely used. It is found that predicted values of the opposed flow spread rate depend strongly on the velocity profile used in the computations. Recent work has also shown a great sensitivity of spread rate to solid properties. Normally two types of velocity profiles are chosen: (1) Oseen profile; (2) Hagen-Poiseuille profile [4].

4. Motivations and Scope

Combustion of solid polymeric materials arises from a complex interaction among many chemical and physical processes. Comparatively gas phase models are much more advanced than solid models, and normally include mass, momentum, species, and energy equations. On the contrary, the solid models are always simplified by a simple formulation of heat conduction as well as a one-step global degradation reaction, either at the surface or in-depth. The phenomena of melting and bubble transport and their influence to the flame spread behavior have largely been ignored by previous researchers. In fact, there are no published flame spread models that consider the above-mentioned phenomena, even in a sense of emphasizing one single aspect such as the melting. Therefore the objective of the current research is to investigate the flame spread problem with some complex solid/liquid phase physics such as anisotropic characteristic, melting, bubble nucleation, growth and movement. The layout of the chapters follows the logical route of theoretical exploration, with increasing complexities of the physical phenomena. In Chapter 2, the flame spread is investigated for an anisotropic polymer with *a priori* specified flow field (Oseen Approximation). The transient flame spread rate is analyzed

according to a set of variable traverse conductivity and longitudinal conductivity. Chapter 3, still retaining the Oseen approximation, investigates the influence of melting on the flame spread behavior. Flame spread rate as a function of non-dimensional parameters from material properties is obtained and compared to theoretical formulas. Transient behaviors such as ignition, flame development stages, and so on are defined. In addition, flame structures and heat transfer mechanisms are examined. In Chapter 4, the Oseen approximation is removed from the formulation; instead the complete Navier-Stokes equations are incorporated into the flame spread model for melting polymers. Rich physics of the gas phase effects such as the thermal expansion and gas injection at the interface on the flame spread behavior are explored in detail and compared to previous theoretical and experimental findings. In Chapter 5, the influence of anisotropic solid properties is revisited under the situation of the realistic flow condition and melting solid. In Chapter 6, the ignition is investigated by using energy balance analysis for both a realistic flow pattern and an assumed flow pattern. An ignition theory is constructed to predict the ignition delay time by using observations from the numerical results. In Chapter 7, the comprehensive transport phenomena in the condensed phase such as melting, bubble nucleation, growth, and movement are modeled using a two-scale model, that is, a macro-scale transport model and a micro-scale transport model. The former provides the temperature and liquid fraction and the latter accounts for single bubbles' nucleation, growth and movement. The influences of bubbles on the material properties are further investigated by a representative case, where the evaporation effect, the bubble induced fluid flow, and the temperature field are investigated. In Chapter 8, conclusions are provided and further modeling developments are suggested. In addition, appendixes

re also given to su
ching sub-model
sues (Chapter 3).
(Chapter 3). (4) Th
efinition of the int
The derivation of th

are also given to supplement each chapter. They are: (1) Numerical verification of the melting sub-model (Chapter 3); (2) Numerical techniques for combustion and general issues (Chapter 3); (3) A derivation of the flame spread formula for melting polymers (Chapter 3); (4) The numerical methods for flow field calculation (Chapter 4); (5) The definition of the integral heat transfer mechanisms for ignition analysis (Chapter 6); (6) The derivation of the volume averaged equations for bubble transport (Chapter 7).

Figure 1

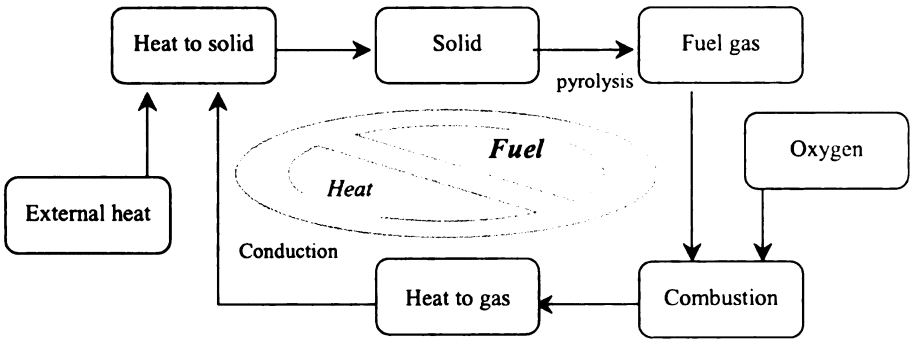

Figure 1 Schematic diagram of combustion of non-charring polymers.

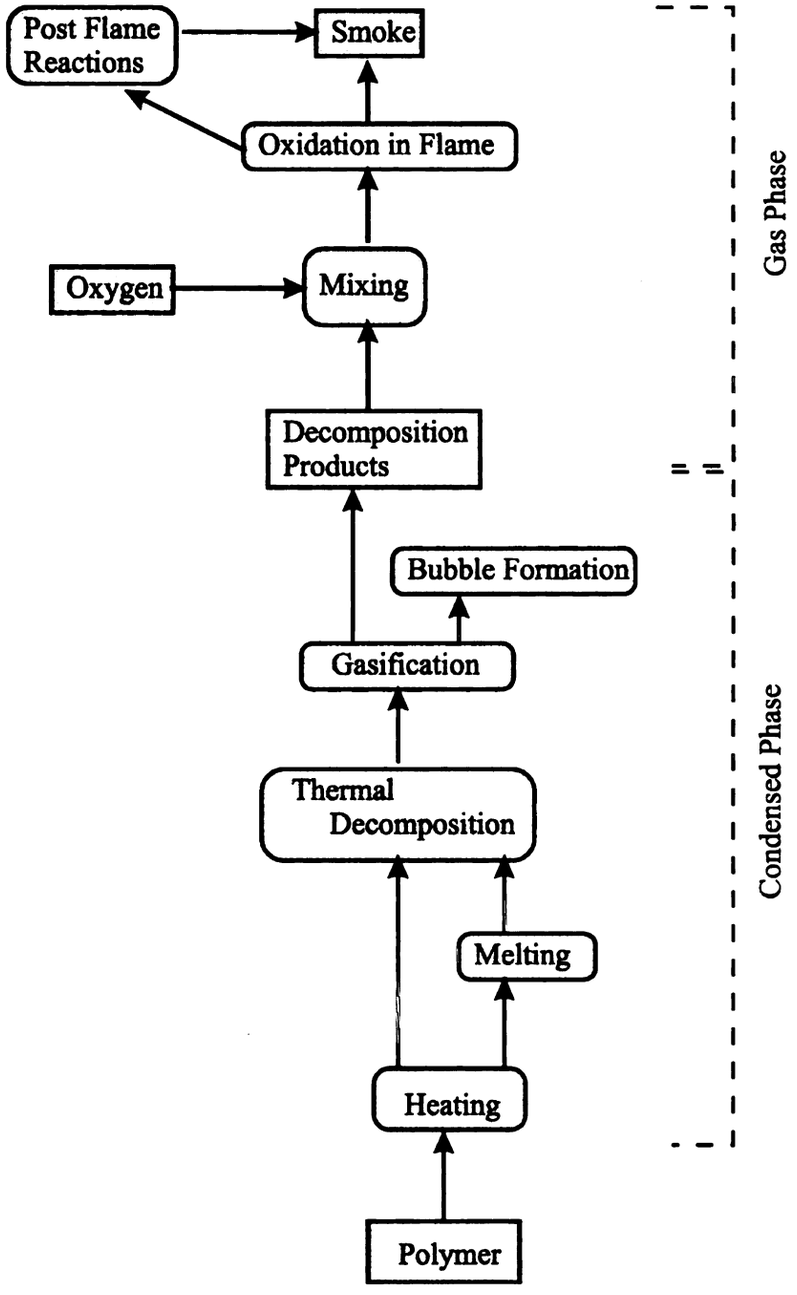

Figure 2 Schematic of the flaming combustion of a polymer.

Table 1. The me

Gas ph
Ambient oxygen c
Flow vel
Gas phase react
Radiation and
Gas phase heat
Boundary lay
Opposed or cons

Table 1. The mechanisms that contribute to the flame development over polymers.

Gas phase	Solid phase	Other
Ambient oxygen concentration	Conductivity	Initial temperature
Flow velocity	Thickness	External radiation
Gas phase reaction kinetics	Thermal degradation kinetics	Gravity
Radiation and absorption	Melt viscosity	Scale of fire
Gas phase heat conduction	Charring or non-charring	Ambient pressure
Boundary layer effect	Phase change	Interface radiation
Opposed or concurrent flow	Bubble formation	

MODELING OF I

Introduction

The present st
phase, and mainly
investigate ignition
transient two-dime
and gas phase. W
concentrations in th
These quantities p
interaction. The th
leading ignition a
ne and ignition
umerical cases. I
solid phase influe
concerning oppose
thermally thick an

Mathematica

The mathema
model [41] for
undergoing chem

CHAPTER 2

MODELING OF IGNITION, TRANSITION AND STEADY FLAME SPREAD OVER ANISOTROPIC SOLID POLYMERS

1. Introduction

The present study is a first step toward the complex phenomena in the condensed phase, and mainly concentrates on the anisotropic influence of the solid conductivity. To investigate ignition, transition and steady flame spread over anisotropic solid polymers, a transient two-dimensional combustion model is constructed considering both the solid and gas phase. With a given uniform velocity flow field, the temperature and species concentrations in the gas phase and temperature in the solid phase are numerically solved. These quantities provide information on the details of the flame structure and gas-solid interaction. The three stages of flame development over the solid phase include pre-heating, ignition and steady flame spread. Moreover, the trends of steady flame spread rate and ignition time with respect to k_{sx}/k_{sy} are obtained from eight different numerical cases. Information about the mechanism of flame spread, flame structure and solid phase influence of the solid anisotropy is also presented. Brief numerical studies concerning opposed flow, ignition, transition and steady flame spread over a horizontal thermally thick anisotropic slab will be provided.

2. Mathematical Model

The mathematical model in the present study is formulated by considering Di Blasi's model [41] for two-dimensional transient heat transfer over a polymer material undergoing chemical decomposition. The solid phase is anisotropic and the flame

spreads over the s

direction of flame p

1. The gas phase re

2. The solid phase

3. The buoyancy t

4. The radiation fl

5. The thermal an

With the above as

phase, the transient

Gas phase:

Solid phase:

Interface:

The other boundar

spreads over the surface of the solid phase in an oxidizing gas flow opposing the direction of flame propagation. The following basic assumptions are made:

1. The gas phase reaction is based on a one-step second-order Arrhenius rate.
2. The solid phase is non-reactive except *at the interface*.
3. The buoyancy in the flow field is ignored in the forced flow field.
4. The radiation from the surface and flame is ignored.
5. The thermal and flow properties are constant.

With the above assumptions the governing equations include the transient reactive gas phase, the transient inert solid phase and the decomposing interface as follows:

Gas phase:

$$\frac{\partial Y_i}{\partial t} + u_\infty \frac{\partial Y_i}{\partial x} = \mu_i w_g + D\nabla^2 Y_i, \; i=o, f, p \tag{1}$$

$$C_{Pg}\rho_g[\frac{\partial T_g}{\partial t} + u_\infty \frac{\partial T_g}{\partial x}] = q_g w_g + k_g \nabla^2 T_g \tag{2}$$

Solid phase:

$$\rho_s C_{Ps} \frac{\partial T_s}{\partial t} = k_{sx} \frac{\partial^2 T_s}{\partial x^2} + k_{sy} \frac{\partial^2 T_s}{\partial y^2} + 2k_{sxy} \frac{\partial^2 T_s}{\partial x \partial y}, \tag{3}$$

Interface:

$$\begin{cases} \rho_g D \dfrac{\partial Y_f}{\partial y} = \dot{m}(Y_f - 1), \quad \rho_g D \dfrac{\partial Y_i}{\partial y} = \dot{m} Y_i \\ T_s = T_g \qquad\qquad\qquad\qquad\qquad\qquad , i=o, f, p \\ -k_g \dfrac{\partial T_g}{\partial y} = -(K_{sxy} \dfrac{\partial T_s}{\partial x} + K_{sy} \dfrac{\partial T_s}{\partial y}) + \dot{m} L_s \end{cases} \tag{4}$$

The other boundary conditions are:

$$\text{Inflow} \begin{cases} T_g = \\ Y_F = Y_F \\ Y_O = Y \end{cases}$$

The initial conditio

which $\dot{m} = A$

$\Xi = M_F Y_F \quad M_F Y$

Numerical Tre

A two-dimens

coordinate system

The convective ter

main non-linear s

was solved by sw

the heat flux betw

decision. Grid line

The computationa

directions, respect

by giving a fixed

concentration. Th

conditions are sim

gas properties are

$$\text{Inflow} \begin{cases} T_g = T_0 \\ Y_f = Y_p = 0 \\ Y_o = Y_{o0} \end{cases}; \text{ outflow} \begin{cases} \dfrac{\partial T_g}{\partial x} = 0 \\ \dfrac{\partial Y_i}{\partial x} = 0 \end{cases}^{i=o,f,p}; \text{ upper wall} \begin{cases} \dfrac{\partial Y_i}{\partial y} = 0 \\ \dfrac{\partial T_g}{\partial y} = 0 \end{cases}. \quad (5)$$

The initial conditions are:

$$t = 0,\ T_g = T_s = T_0,\ Y_f = Y_p = 0 \text{ and } Y_o = Y_{o0}, \quad (6)$$

in which $\dot{m} = A_s \rho_s EXP(-E_s / RT_s)$, $w_g = -A_g \rho_g EXP(-E_g / RT_g) Y_o Y_f$ and $\Xi_i = M_i \nu_i / M_f \nu_f$, i=o, f, p. Note that in Equation (3), we have $k_{sxy} = k_{syx}$.

3. Numerical Treatment

A two-dimensional semi-implicit finite difference scheme was applied in a Cartesian coordinate system. The time-splitting ADI method was used in both gas and solid phases. The convective term was treated by the upstream method. Since the chemical term is the main non-linear source in this model, it was treated implicitly. The interface interaction was solved by switching back and forth between the solid phase and the gas phase, and the heat flux between both phases was evaluated as a judgment for a further marching decision. Grid lines were clustered near the flame region with a minimum of 0.025 mm. The computational domain of 10mm × 12 mm in the horizontal (x) and transverse (y) directions, respectively, is represented by a 30 × 50 mesh system. Modeling is performed by giving a fixed uniform flow velocity u_∞ at the inlet boundary with 30% oxidizer concentration. The preheating horizontal length is 1.8 mm. The configuration and flow conditions are similar to those used in [41]. Some of the solid properties of PMMA and gas properties are given in table 1.

4 Results and D:

The flame dev

pre-heating process

case with k_{gx} =

constant radiant fl

ignition the extern

s therms before ig

around the heated

phase conduction

oxidizer concentra

surface temperatu

reaches the pyroly

face. While in th

concentration and

contributes partly

is large enough to

the solid phase. A

16s. The flame le

As explained by

reaction priority is

Figure 3 at time 1

16s also shows

temperature isoth

4. Results and Discussions

The flame development with time can be classified into three categories as (1) the pre-heating process, (2) the ignition process and (3) the steady flame spread process. One case with $k_{sx}=0.065$ and $k_{sy}=0.015$ is studied. At the beginning and prior to ignition a constant radiant flux of 50 kW/m^2 was applied on a limited length of surface. After ignition the external radiation is removed. Figure 1 at time 1.4 s shows the calculated isotherms before ignition, which indicate that the temperature is almost evenly distributed around the heated region. During this period the gas phase is heated dominantly by gas phase conduction and the temperature is not high enough to initiate a fire. The fuel and oxidizer concentrations are extremely low, which is the consequence of a low solid surface temperature by pyrolysis. As the heating process proceeds, the solid surface reaches the pyrolysis point and hence a tremendous increase in the vaporization takes place. While in the gas phase, the reaction rate is dependent on both the gas mixture concentration and the temperature. Therefore the increase in reactant concentration only contributes partly to the reaction rate. This process continues until the gas phase reaction is large enough to maintain a strong heat source and hence a flame can be sustained near the solid phase. At this time ignition begins, which can be seen from Figure 1 at time 1.6s. The flame leading edge is almost formed upstream in front of the preheating region. As explained by [42], due to the greater supply of oxidizer to the flame front, the reaction priority is upstream of the approach flow. Further affirmation can be made by Figure 3 at time 1.6s that almost no oxidizer exists in the downstream region. Figure 2 at 1.6s also shows that the larger fuel concentration corresponds well with the larger temperature isotherms in solid phase near the location of the leading edge. After ignition,

he flame will stabilize
nd mass flux between
oted also that the dow
ompletely [42]. A s
omparison of Figures
ransition period due t
42]

The period between 2
regime. By applying t
there exist two regions
region of heat-up, gas
chemical reaction take
there are three region
diffusion flame, in the
hel nch region. It is
Figure 1.

In view of heat
ver thick solid polyr
ter (10) times as larg
the free convection e
for thermally thick s
valid in this case.

For thick PMM

the flame will stabilize until a steady state flame spread exists. During this period the heat and mass flux between both solid phase and gas phase attains a quasi-steady state. It is noted also that the downstream oxidizer under the combustion plume will be consumed completely [42]. A stabilized flame is not attained until 2.0s, which is shown by comparison of Figures 1, 2 and 3. The transient flame spread rate is larger during this transition period due to the preheating of the sample by the initial external incident flux [42].

The period between 2.0s and 4.8s is characterized as the steady state flame spread regime. By applying flame structure theory by Sirignano [23], it can be observed that there exist two regions for the flame structure horizontally. The flame front region is the region of heat-up, gasification and mixing ahead of the flame leading edge. The region of chemical reaction takes up the highest temperature region of the gas phase. Transversely there are three regions inside the flame, that is, in the middle is the fully established diffusion flame, in the upper region is the fuel lean region and in the lower region is the fuel rich region. It is easy to qualitatively identify the regions defined by the above from Figure 1.

In view of heat transfer, there are many controlling mechanisms for flame spread over thick solid polymer [1]. In this case the scale of the external flow rate is found to be ten (10) times as large as the flame spread rate, which provides a valid basis for ignoring the free convection effect. It is also reported that flame radiation is relatively unimportant for thermally thick solid materials [41], therefore non-treatment of the radiation seems valid in this case.

For thick PMMA materials experiments show that for particular [23] but not typical

]] cases of small-sc

echanism. Therefo

onductivity on flame

k_g and k_{sy} but kee

erved. Figure 4 sh

me is defined as th

evious that the large

ring initial heating

ho determines the

hows the trend of st

from a different view

5 Conclusions

A two dimension

nergy equations a

ualitatively evaluate

Based on the num

re described. Relev

analyzed.

For anisotropic th

flame spread rate w

onduction in the so

results

[1] cases of small-scale fires, the heat conduction in the solid phase is the dominant mechanism. Therefore it is meaningful to investigate the effect of the anisotropic conductivity on flame development. First keep k_{sxy} as a constant, change the values of k_{sx} and k_{sy} but keep the $(k_{sx}+k_{sy})$ as a constant, then two flame characteristics are derived. Figure 4 shows the trend of ignition time vs. k_{sx}/k_{sy}, in which the ignition time is defined as the critical point when the heat flux is equal to 60 kW/m^2 [9]. It is obvious that the larger the ratio of the k_{sx}/k_{sy}, the more heat is transferred streamwise during initial heating and hence the smaller is the ignition time. Therefore the k_{sx}/k_{sy} ratio determines the temperature distribution in the initially heated solid phase. Figure 5 shows the trend of steady flame spread rate vs. k_{sx}/k_{sy}, which affirms the above theory from a different viewpoint.

5. Conclusions

1. A two dimensional transient mathematical model incorporating the gas species and energy equations and solid heat conduction equation are solved numerically to qualitatively evaluate the flame development over anisotropic solid polymers.

2. Based on the numerical results, ignition, transition and steady flame spread processes are described. Relevant physical mechanisms and certain theories of flame structure are analyzed.

3. For anisotropic thick solid polymer materials, the relationship of the ignition time and flame spread rate with k_{sx}/k_{sy} is obtained for a particular case. The importance of heat conduction in the solid phase for initial flame development is evident from the numerical results.

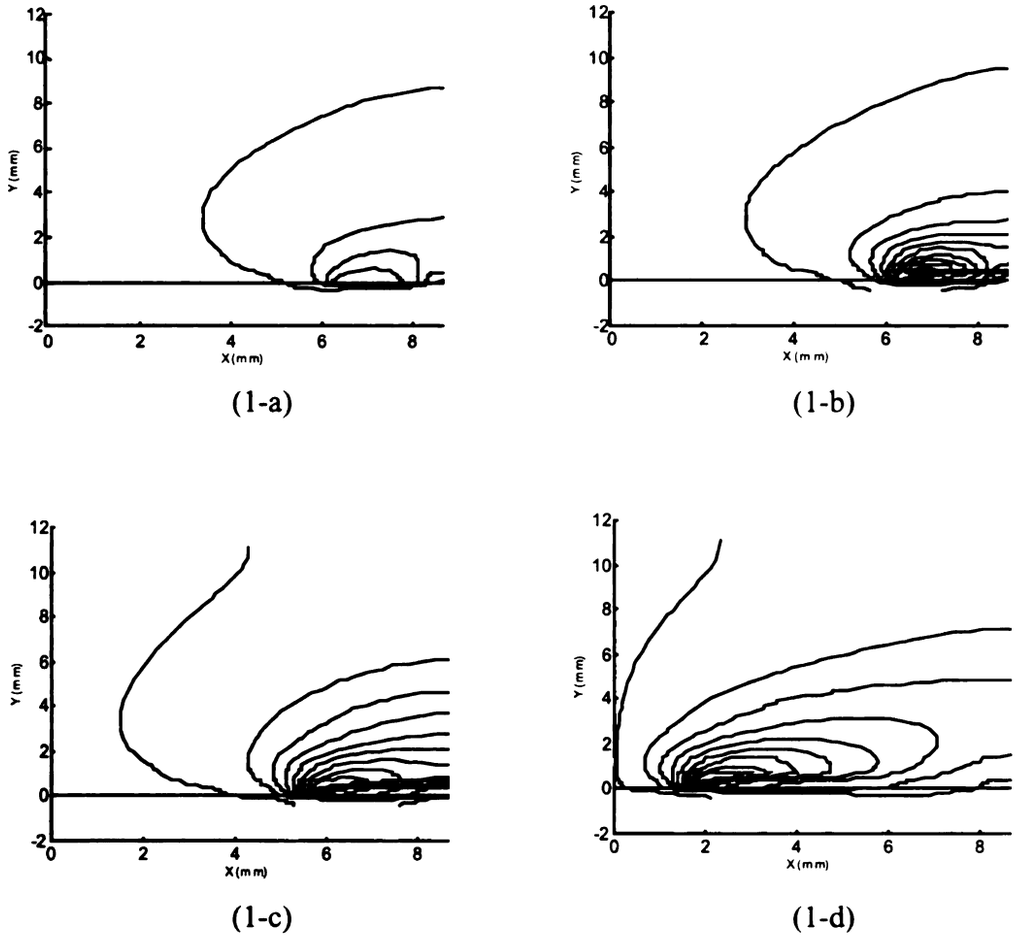

Figure 1 Constant temperature contours at four different times (The outermost contour is 300K, increment 100K between two adjoin constant levels. (a) t=1.4s; (b) t=1.6s; (c) t=2.0s; d: t=4.8s.

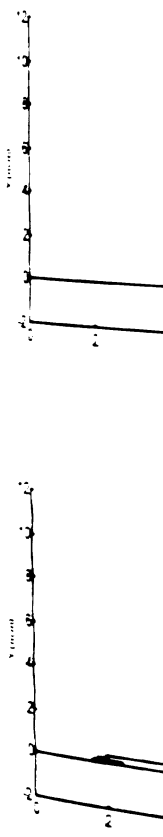

Figure 2 Constant
level is 0.1, incre
Ess.

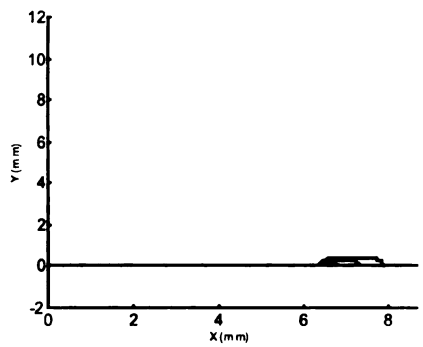

(2-a)

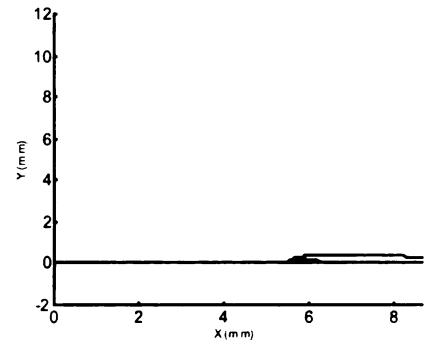

(2-b)

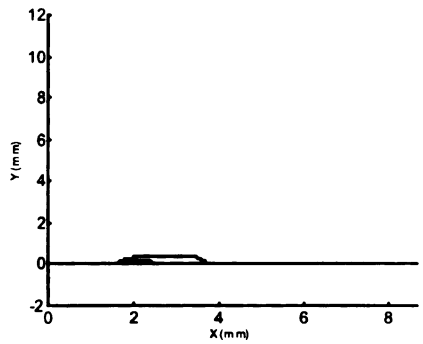

(2-c)

Figure 2 Constant fuel concentration contours at different time (The outermost constant level is 0.1, increment 0.1 between two adjoin contours). (a) t=1.6s; (b) t=2.0s; (c) t=4.8s.

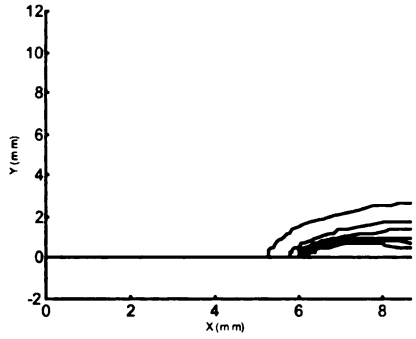

(3-a)

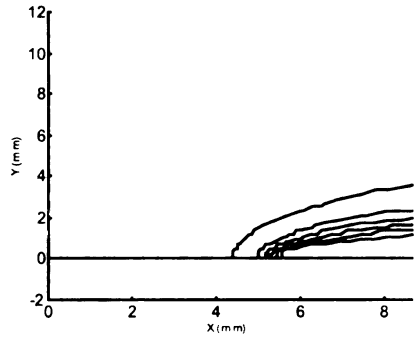

(3-b)

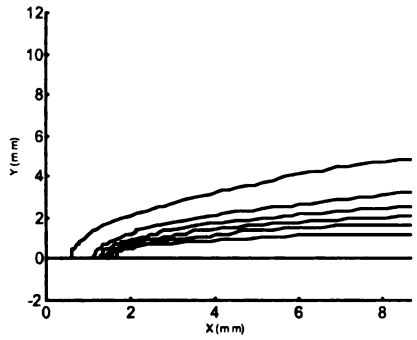

(3-c)

Figure 3 Constant oxidizer concentration contours at different time (The outermost constant level is 0.3, decrement 0.05 between two adjoin contours). (a) t=1.6s; (b) t=2.0s; (c): t=4.8s.

Table 1 Th

A_s	A_g
[illegible]	1 6E-
[illegible]	5 m.

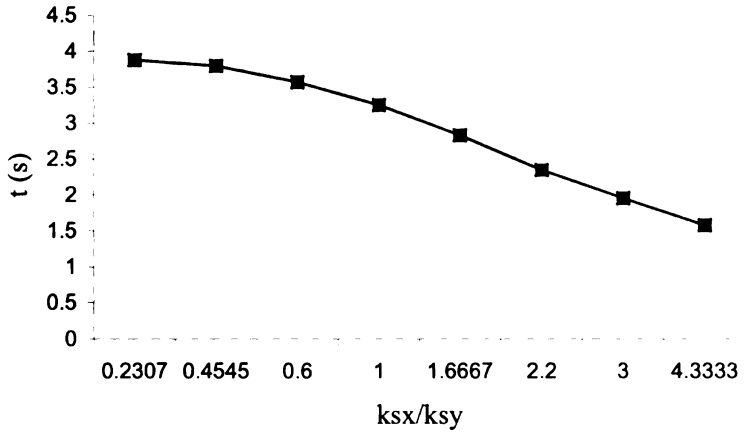

Figure 4 Ignition time vs. k_{sx} / k_{sy}.

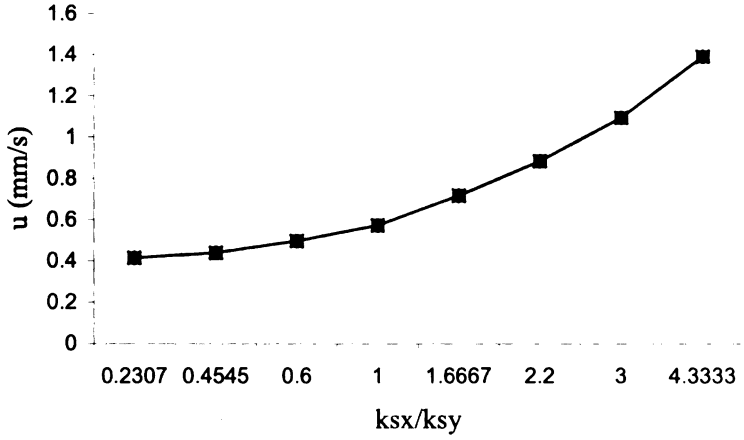

Figure 5 Flame spread rate vs. k_{sx} / k_{sy}.

Table 1 The thermal properties and chemical kinetics used in the modeling.

A_s	A_g	E_s	E_g	L_s	q_g	k_g	k_{xy}	u_∞
1.0E+06 m/s	1.6E+15 m/s	145520 J/mol	135730 J/mol	1355.6 kJ/kg	12945 kJ/kg	0.04 J/m.s	0.035 J/m.s	0.1 m/s

OPPOSED-FLO

1. Introduction

Transient flame

theoretical and pedi

ediation. The latte

mutual influences, an

When a polymeri

heat flux, it can be ig

Because surface ignit

will be concerned in

flow of oxidizer.

An extensive res

reviews of Refs. 1-

addresses flame spre

surface driven flo

complications are

precedes the flame

convection may be

develop in the gas a

occur between flam

CHAPTER 3

OPPOSED-FLOW FLAME SPREAD OVER POLYMERIC MATERIALS – INFLUENCE OF PHASE CHANGE

1. Introduction

Transient flame growth over polymeric materials is important in fire safety, and has theoretical and pedagogical importance in basic combustion science research and education. The latter stems from a large number of complicated phenomena, their mutual influences, and the challenge of describing them in an orderly, logical manner.

When a polymeric material is subjected at a portion of its exposed surface to a high heat flux, it can be ignited. The ignition of flame may lead to subsequent flame spread. Because surface ignition at a point is associated with induced inflow of air (oxidizer), we will be concerned in the model with flame spread against an induced or forced opposing flow of oxidizer.

An extensive research literature exists for this class of flame spread problem, see the reviews of Refs. 1-3. Most of the literature addresses solid fuels. The review of [2] addresses flame spread over liquid fuels, which possess additional complications such as surface driven flow, enhanced buoyancy and liquid vaporization, etc. These complications are potentially important when the liquid phase melt layer actually precedes the flame leading edge. Heat transfer ahead of the flame by liquid phase convection may be important under same conditions. In addition, recirculating cells may develop in the gas and pulsating spread may be possible. Then, a significant overlap may occur between flame over initially solid fuels (which liquefy) and flame spread over

liquid fuels.

Many formulati
ppeared in the res
ystematic examinat
multi-dimensional t
subsequently examin
balance perspective
importance of the g
o derive flame spre
was derived. The g
streamwise conduc
problems, relatively
balance streamwise

By utilizing th
materials was derive
more suitable for a
process than solid py
isotherm. It is well
at a specific isother
melted polymer agr
flame spread formu
other model or theo
in terms of local ph

liquid fuels.

Many formulations of the theoretical opposed-flow flame spread problem have appeared in the research literature. The study of deRis [21] stands out as the first systematic examination including simplified gas-phase chemistry, solid decomposition, multi-dimensional transport and convective/buoyant flow. Many other models were subsequently examined (see [1]) but only one studied flame spread from a global energy balance perspective, thus adding insight into the flame spread process [43]. The importance of the global balance principle arises from the ease with which it can be used to derive flame spread formulas under conditions more general than those for which it was derived. The global balance principle is easy to apply because of the neglect of streamwise conduction. Instead of solving complicated elliptic boundary value problems, relatively simple parabolic conservation equations can be formulated, which balance streamwise convection and cross-stream conduction.

By utilizing the global balance principle a flame spread formula for charring materials was derived ([28], see the discussion of [28] in [1]). This formula is perhaps more suitable for a solid that liquefies upon heating since liquefaction is a simpler process than solid pyrolysis and degradation, and usually occurs along or near a specific isotherm. It is well known however that solid degradation and pyrolysis does not occur at a specific isotherm. We shall demonstrate that our model for flame spread over a melted polymer agrees, under many conditions, extremely well with predictions of the flame spread formula where considerations of dripping and running are not included in either model or theory. The flame spread formula therefore can be interpreted physically in terms of local physics near the point of flame attachment. Recent work on transient

solid-phase ignition

colleagues on micro

model of the gas

developed and then

It is known that

gas-phase combustio

conduction, phase

ming and conden

complexities, the co

[25] Studies of flam

some experimental

The purpose o

condensed) phase c

flame spread resear

Finite-rate gas chem

(solid→liquid in-d

properties (conduct

Our numerical

to flame ignition t

Comparisons are m

of our research is

flame spread with p

2. Numerical Mod

solid-phase ignition and flame spread has been undertaken by Kashiwagi, Baum and colleagues on microgravity flame initiation on cellulosic materials [13]. A detailed model of the gas flow and its thermal expansion during ignition and spread was developed and then solved numerically.

It is known that many complicated, simultaneous processes occur in the solid with gas-phase combustion above it. These include detailed degradation chemistry, anistropic conduction, phase change, bubble formation and transport, charring of the surface, pitting and condensed-matter expulsion at the surface. Because of these and other complexities, the condensed phase has been studied considerably less than the gas phase [25]. Studies of flame spread over melting polymers have rarely been reported except for some experimental observations [25].

The purpose of this chapter is to examine a flame spread model whose solid (or condensed) phase contains some solid phase complexities not described previously in flame spread research [1-5]. The gas will be described by a standard Oseen-flow model. Finite-rate gas chemistry is retained. In the condensed material, we retain phase change (solid $\rightarrow$ liquid in-depth; liquid $\rightarrow$ gas at surface). Upon phase change, thermophysical properties (conductivity, and specific heat) may change.

Our numerical model will be transient, enabling computation from incipient heating to flame ignition to eventual steady spread. Melting and phase change alter ignition. Comparisons are made with predictions of theory in the steady state. The eventual goal of our research is to include bubble formation in the liquid melt layer. The study of flame spread with phase change of the fuel from solid to pure liquid is a first step.

2. Numerical Model

2.1 Problem Formul

A schematic

simplifications are

describe unsteady fl

approximation of

momentum equation

thermal and chemic

condition if the o

considered to occur

the vertical config

unaware of any

work in a highly

flame and radian

radiant absorption

data (pre-expone

regression or d

polymer melt ne

relevant to the

removable in p

complications

restrictions (ne

extensively stu

those for the t

2.1 Problem Formulation

A schematic formulation of the problem is provided in Figure 1. Some simplifications are made to reduce the complexity of the governing equations that describe unsteady flame initiation and spread over polymeric materials. First, the Oseen approximation of uniform velocity profile is used, thereby: (1) eliminating the momentum equations from the solution; (2) uncoupling the velocity field from the thermal and chemical fields; (3) reducing the N-S equations to the constant pressure condition if the opposed flow Mach number is negligibly small. Flame spread is considered to occur in the horizontal plane, thereby eliminating required consideration in the vertical configuration of melt flow from the melting surface. The authors are unaware of any theoretical or numerical work on this subject outside of preliminary work in a highly idealized configuration [44, 45]. Second, radiation absorption by the flame and radiant emission from the flame are ignored, as are surface and in-depth radiant absorption by the condensed material. Third, the thermal properties and kinetic data (pre-exponential factor and activation energy) are assumed constant. Fourth, the regression or deformation of the gas-condensed interface and Marangoni flow of polymer melt near the interface are assumed negligible. The other assumptions that are relevant to the specific equations will be introduced hereafter. All restrictions are removable in principle, but when initial studies are conducted in a simple manner, the complications that are later introduced are more clearly understood. Some of our restrictions (negligible interface regression, no surface Marangoni flow) have not been extensively studied in the context of flame spread. The governing equations include those for the transient reactive gas phase, the transient reactive condensed phase, the

non-reactive gas-c

coordinates is fixed

phase, while the sub

The transport

convection, and che

given by

$$\rho_g[\frac{\partial Y_i}{\partial t} + u_\infty \frac{\partial}{\partial}$$

$$\rho_g C_{P_g}[$$

It is assumed that

irreversible sec

$$\dot{w}_g = -\rho_g^2 Y_O Y_f A_g$$

$$\Xi_i = M_i V_i \quad M_f V$$

material include th

conservation equa

where subscript "

"I" or "s" in indiv

order Arrhenius r

with reaction rate

take the form of

non-reactive gas-condensed interface, and boundary conditions. The origin of coordinates is fixed at the interface, therefore the subscript "$y > 0$" denotes the gas phase, while the subscript "$y < 0$" denotes the condensed phase.

The transport mechanisms in the gas phase include diffusion, streamwise convection, and chemical reaction. The species and energy conservation equations are given by

$$\rho_g[\frac{\partial Y_i}{\partial t} + u_\infty \frac{\partial Y_i}{\partial x}] = \rho_g D \nabla^2 Y_i + \Xi_i w_g, \quad i = f, o, \quad y > 0, \tag{1}$$

$$\rho_g C_{Pg}[\frac{\partial T}{\partial t} + u_\infty \frac{\partial T}{\partial x}] = k_g \nabla^2 T + q_g w_g, \quad y > 0. \tag{2}$$

It is assumed that the combustion reaction $F + \nu_o O \rightarrow P$ is an overall single-step, irreversible second-order Arrhenius reaction, with reaction rate $w_g = -\rho_g^2 Y_o Y_f A_g e^{-E_g / RT}$ and stoichiometric ratio $\Xi_i = M_i \nu_i / M_f \nu_f, \quad i = f, o$. The heat transfer mechanisms in the condensed material include thermal diffusion, phase change, and pyrolysis reaction. The energy conservation equation in enthalpy form is

$$\rho_c \frac{\partial h_c}{\partial t} = k_c \nabla^2 T + q_c w_c, \quad y < 0, \tag{3-a}$$

where subscript "c" denotes the condensed material in general, and will be denoted by "l" or "s" in individual liquid and solid phases, respectively. An overall single-step first-order Arrhenius reaction of *polymer* $\rightarrow$ *monomer* is assumed for the pyrolysis process, with reaction rate $w_c = -\rho_c A_c \exp(-E_c / RT)$. The condensed-phase density ρ_c may take the form of ρ_l or ρ_s in the condensed material. The kinetic data for E_c and A_c

are constants for bo

Figure 2 is provid

enthalpy and tempe

a fixed melting temp

and liquid are ass

mplies the existe

nterface The ener

form includes three

moving phase front

$$\begin{cases} -(k\frac{\partial T}{\partial n} \\ T_\Sigma = T_m \end{cases}$$

Equations (3-b i,

respectively. Equa

the unit vector nor

phase front velocity

At the gas con

The melting point of
the literature, and no

are constants for both solid and liquid phases. The enthalpy-temperature relationship in Figure 2 is provided along with equation (3-a), thereby reducing two unknowns (enthalpy and temperature) to one. In Figure 2, phase change is assumed to take place at a fixed melting temperature T_m[6], and the thermal properties ρ, C_P and k in the solid and liquid are assumed constant in each phase, but not necessarily the same. This implies the existence of discontinuous thermal properties across the solid-liquid interface. The energy conservation equation of the condensed material in temperature form includes three domains of interest, viz., the solid phase, the liquid phase and the moving phase front,

$$\begin{cases} \rho_s C_{Ps} \dfrac{\partial T}{\partial t} = k_s \nabla^2 T - q_c w_c, & solid \\ \rho_l C_{Pl} \dfrac{\partial T}{\partial t} = k_l \nabla^2 T - q_c w_c, & liquid \end{cases}, \quad y < 0 \qquad (3\text{-b})$$

$$\begin{cases} -(k \dfrac{\partial T}{\partial n^*})_s + \rho L_s v_{n^*} = -(k \dfrac{\partial T}{\partial n^*})_l, & phase\ front, \quad y < 0 \\ T_\Sigma = T_m \end{cases} \qquad (3\text{-c})$$

Equations (3-b i, ii) are the energy conservation equations for the solid and liquid respectively. Equation (3-c) is the Stefan condition in vector form, where n^* denotes the unit vector normal to the moving solid-liquid phase front Σ, and v_{n^*} denotes the phase front velocity.

At the gas/condensed phase interface, the mass transfer mechanism is pure diffusion

---

[6] The melting point of the polymer is different from the 'glassy point' temperature that frequently appears in the literature, and normally has a larger value.

of the net norm

include conduct

environment, an

removed thereaf

always equilibra

In equations (4-a

virtual mass flo

form as $\int_{,\Gamma} w$

used to adjust th

This equation i

because no stor

Equation (3-b),

mechanism, ma

acknowledges th

contains a unifor

There is a unifo

of the net normal flow comprising pyrolysis products. The heat transfer mechanisms include conduction in the gas, conduction in the solid, surface radiation to the environment, and transient ignition heat flux $\dot{q}_{ig}$, which is applied before ignition and removed thereafter. The species and energy transport processes are assumed to be always equilibrated, whereby

$$\begin{cases} -\rho_g D \dfrac{\partial Y_f}{\partial y}\Big|_{0+} = (1 - Y_f|_{0+})\dot{m}, \\ -\rho_g D \dfrac{\partial Y_o}{\partial y}\Big|_{0+} = (0 - Y_o|_{0+})\dot{m}, \\ -k_s \dfrac{\partial T}{\partial y}\Big|_{0-} = -k_g \dfrac{\partial T}{\partial y}\Big|_{0+} + \varepsilon\sigma(T^4 - T_\infty^4) - \dot{q}_{ig}. \end{cases} \tag{4-a}$$

In equations (4-a i, ii, iii), the mass flow rate $\dot{m}$ arises from the pyrolysis products. The virtual mass flow rate of condensed phase pyrolysis products can be written in integral form as $\int_{\ell_{sy}}^{0} w_c dy$. A permeability factor K_e with range between zero and unity is used to adjust the magnitude of this mass flow rate. Hence,

$$\dot{m} = \mathrm{K}_e \int_{\ell_{sy}}^{0} w_c dy. \tag{4-b}$$

This equation implies that the transport of gas through the liquid is a steady process, because no storage effect or time derivative appears. The heat transfer described by Equation (3-b), however, is unsteady. Usually, when diffusion is the transport mechanism, mass transfer through liquids is slower than heat transfer. Our model acknowledges this limitation, but is applicable (valid) in the limit that the liquid layer contains a uniformly distribution of "gas" molecules that finally escape from the surface. There is a uniform and continual migration of monomer molecules toward the surface.

Of course, this is ar

degradation is bett

molecules of mono

from the surface In

integral of w_s over

cell after the reacti

inflow boundary co

$x = 0,\ 0 < y < l_g$

linear dimension of

applied at the uppe

conditions include

$$x = 0,\ 0 < y$$

The adiabatic condi

Of course, this is an idealization that is, in principle, removable when the solid phase degradation is better understood. The "gas" in this model may be interpreted as molecules of monomers, which form in the liquid layers of thickness l_{sy} that escape from the surface. In other words, Equation (4-b) states that $\dot{m}$ is proportional to the integral of w_c over the solid thickness, but the mass, in fact, escapes from the surface cell after the reaction *polymer* $\rightarrow$ *monomer* has taken place. In the gas, an isothermal inflow boundary condition and an adiabatic outflow boundary condition are applied at $x=0,\ 0<y<\ell_{gy}$ and at $x=\ell_x,\ 0<y<\ell_{gy}$, respectively, where ℓ denotes the linear dimension of the computational domain. A closed adiabatic boundary condition is applied at the upper wall $y=\ell_{gy}, 0<x<l_x$, as indicated below. Other boundary conditions include

$$x=0, 0<y<\ell_{gy}\begin{cases} T=T_\infty \\ Y_o=Y_{o\infty}\ ;\ x=\ell_x, 0<y<\ell_{gy}\begin{cases}\dfrac{\partial T}{\partial x}=0 \\ \dfrac{\partial Y_i}{\partial x}=0, i=o,f\end{cases} \\ Y_f=0\end{cases}$$

The adiabatic condition is written as:

$$y=\ell_{gy}, 0<x<\ell_x\begin{cases}\dfrac{\partial T}{\partial y}=0, \\ \dfrac{\partial Y_i}{\partial y}=0, i=o,f.\end{cases} \qquad (4\text{-}$$

The initial condition

where $Y_{O\infty}$ is the

The conserv

boundary conditio

nonlinear boundar

2.1 Non-Dimensi

The governin

mechanisms that

appropriate refere

the dominant me

thick fuel is solid

and low viscosity

flame spread. Ga

becomes weaker

heat transfer mec

always determine

dimensionalizatio

obtained by mult

factor $\Omega = \alpha_s$

L_s C_{P_s}: the ref

is $Y_{O\infty}$ μ_g

The initial condition is

$$T = T_\infty,\ Y_f = 0 \text{ and } Y_o = Y_{o\infty}, \tag{6}$$

where $Y_{o\infty}$ is the initial or inflow oxidizer mass fraction in the gas.

The conservation Equations (1-3), the gas-condensed interface condition (4), boundary conditions (5) and initial condition (6) together form a well-posed unsteady nonlinear boundary value problem.

2.1.1 Non-Dimensionalization

The governing equations shall be non-dimensionalized in order to analyze physical mechanisms that may subsequently influence flame development. It is difficult to derive appropriate reference variables for dimensional analysis. If phase change is negligible, the dominant mechanism of heat transfer in the solid for flame spread over thermally thick fuel is solid heat conduction [5]. However, for polymers with a low melting point and low viscosity, it was observed [13] that phase change and melt flow may influence flame spread. Gas phase conduction is dominant in thermally thin flame spread and becomes weaker as the fuel thickens [5]. Whatever the relative importance of a certain heat transfer mechanism is, the interactions between the gas and the condensed phases always determines the nature of flame growth and spread. Based on this idea, the non-dimensionalization is carried out as follows: the reference length $\hbar = \alpha_s / u_\infty$ is obtained by multiplying the characteristic thermal length in the gas (α_g / u_∞) by a factor $\Omega = \alpha_s / \alpha_g$; the reference time is $\tau = \hbar / u_\infty$; the reference temperature is L_s / C_{Ps}; the reference oxidizer concentration is $Y_{o\infty}$; the reference fuel concentration is $Y_{o\infty} / \mu_o$.

In summary, th

$\bar{y} = y / h$; time t

dimensionalized a

dimensionalized a

dimensionalized as

boundary and initial

Gas phase,

$$\frac{\partial \bar{Y}_i}{\partial t}$$

Condensed phase (

$$\begin{cases} \dfrac{\partial \bar{T}_s}{\partial t} \\ \bar{\rho}_i \end{cases}$$

$$\begin{cases} - \\ \bar{T}_s \end{cases}$$

Gas condensed

In summary, the coordinates x and y are non-dimensionalized as $\bar{x} = x/\hbar$ and $\bar{y} = y/\hbar$; time t is non-dimensionalized as $\bar{t} = t/\tau$; temperature T is non-dimensionalized as $\bar{T} = C_{ps}(T - T_\infty)/L_s$; the fuel concentration is non-dimensionalized as $\bar{Y}_f = Y_f \mu_o / Y_{o\infty}$; and the oxidizer concentration is non-dimensionalized as $\bar{Y}_o = Y_o / Y_{o\infty}$. The dimensionless equations, interface conditions, boundary and initial conditions are,

Gas phase;

$$\frac{\partial \bar{Y}_i}{\partial \bar{t}} + \frac{\partial \bar{Y}_i}{\partial \bar{x}} = \frac{1}{\Omega Le}\left(\frac{\partial^2 \bar{Y}_i}{\partial \bar{x}^2} + \frac{\partial^2 \bar{Y}_i}{\partial \bar{y}^2}\right) + \bar{w}_g, \quad i = f, o, \quad i = f, o \tag{7}$$

$$\frac{\partial \bar{T}}{\partial \bar{t}} + \frac{\partial \bar{T}}{\partial \bar{x}} = \frac{1}{\Omega}\left(\frac{\partial^2 \bar{T}}{\partial \bar{x}^2} + \frac{\partial^2 \bar{T}}{\partial \bar{y}^2}\right) + \bar{q}_g \bar{w}_g, \quad i = f, o \tag{8}$$

Condensed phase (temperature form);

$$\begin{cases} \dfrac{\partial \bar{T}_s}{\partial \bar{t}} = \dfrac{\partial^2 \bar{T}_s}{\partial \bar{x}^2} + \dfrac{\partial^2 \bar{T}_s}{\partial \bar{y}^2} - \bar{q}_c \bar{w}_c, & \textit{in the solid} \\ \bar{\rho}_l \bar{C}_{Pl} \dfrac{\partial \bar{T}_l}{\partial \bar{t}} = \bar{k}_l \left(\dfrac{\partial^2 \bar{T}_l}{\partial \bar{x}^2} + \dfrac{\partial^2 \bar{T}_l}{\partial \bar{y}^2}\right) - \bar{q}_c \bar{w}_c, & \textit{in the liquid} \end{cases}, \quad \bar{y} < 0 \tag{9-a}$$

$$\begin{cases} -\dfrac{\partial \bar{T}_s}{\partial \bar{n}^*} + \bar{v}_{n^*} = -\bar{k}_l \dfrac{\partial \bar{T}_l}{\partial \bar{n}^*}, & \textit{phase front}, \quad \bar{y} < 0 \\ \bar{T}_\Sigma = St \end{cases} \tag{9-b}$$

Gas/condensed phase interface;

$$\begin{cases} -\dfrac{1}{\Omega Le}\dfrac{\partial \bar{Y}_f}{\partial \bar{y}}\Big|_{0+} = \bar{\dot{m}}\left(\dfrac{\mu_o}{Y_{o\infty}} - \bar{Y}_f\big|_{0+}\right) \\ -\dfrac{1}{\Omega Le}\dfrac{\partial \bar{Y}_o}{\partial \bar{y}}\Big|_{0+} = \bar{\dot{m}}(0 - \bar{Y}_o\big|_{0+}), \quad y = 0 \\ \dfrac{\partial \bar{T}}{\partial \bar{y}}\Big|_{0-} = -\dfrac{k_g}{k_s}\dfrac{\partial \bar{T}}{\partial \bar{y}}\Big|_{0+} + \varpi[(\bar{T} + \tilde{T}_\infty)^4 - \tilde{T}_\infty^4] - \bar{q}_{ig} \end{cases} \tag{10}$$

Boundary conditions;

$$\bar{x} = 0, 0 < \bar{y} < \bar{\ell}_{gy} \begin{cases} \bar{T} = 0 \\ \bar{Y}_f = 0; \ \bar{x} = \bar{\ell}_x, 0 < \bar{y} < \bar{\ell}_{gy} \\ \bar{Y}_o = 0 \end{cases} \begin{cases} \dfrac{\partial \bar{T}}{\partial \bar{x}} = 0 \\ \dfrac{\partial \bar{Y}_i}{\partial \bar{x}} = 0, i = o, f \end{cases};$$

$$\bar{y} = \bar{\ell}_{gy}, 0 < \bar{x} < \bar{\ell}_x \begin{cases} \dfrac{\partial \bar{T}}{\partial \bar{y}} = 0 \\ \dfrac{\partial \bar{Y}_i}{\partial \bar{y}} = 0, i = o, f \end{cases} \tag{11-a}$$

$$\bar{x} = 0, -\bar{\ell}_{sy} < \bar{y} < 0 \ or \ \bar{x} = \bar{\ell}_x, -\bar{\ell}_{sy} < \bar{y} < 0 \ or$$
$$\bar{y} = -\bar{\ell}_{sy}, 0 < x < \bar{\ell}_x \ \frac{\partial \bar{T}}{\partial \hat{l}} = 0 \tag{11-b}$$

Initial conditions;

$$\bar{T} = 0, \ \bar{Y}_f = 0 \text{ and } \bar{Y}_o = 1. \tag{12}$$

Here $\bar{w}_g = \bar{Y}_o \bar{Y}_f \bar{A}_g \exp(-\dfrac{\bar{E}_g}{\bar{T} + \tilde{T}_\infty})$, $\bar{w}_c = \bar{A}_c \exp(-\dfrac{\bar{E}_c}{\bar{T} + \tilde{T}_\infty})$,

$\bar{\dot{m}} = \mathrm{K}_e \int_{-\bar{\ell}_{sy}}^{0} \bar{\rho}_c \bar{w}_c d\bar{y}$, and $\tilde{T}_\infty = C_{Ps} T_\infty / L_s$.

The dimensionless groups are listed in table 2.

2.1.2 Numerical

The compu

direction and tr

phase and a 5(

grid spacing is

uniform with

(y = 0) with a

The neighborir

reaction-intensi

systems were a

The finite

control volume

providing exa

condensed mat

convective term

performance. T

of source terms

the partial der

term is left un

enhance the a

computational

employed: the

The techniques

2.1.2 Numerical Approach

The computational domain of approximately $15mm \times 15mm$, in the streamwise (x) direction and transverse (y) direction consists of a 50×50 mesh system in the gas phase and a 50×40 mesh system in the condensed material. Along the x direction the grid spacing is uniformly 0.3 mm. Along the y direction the grid spacing is non-uniform with the minimum spacing (0.025mm) near the gas-condensed interface ($y = 0$) with an exponential increase in the two opposite (y_{0+} and y_{0-}) directions. The neighboring increment ratio is 1.07. This treatment is intended to resolve the reaction-intensive region close to the interface. The mappings between the two mesh systems were accomplished by appropriate coordinate transformations.

The finite difference method is used to solve the numerical model [46]. First, the control volume formulation is used in the discretization because of its ability for providing exact tracking of the solid-liquid interface during phase change in the condensed material. The diffusion terms are treated by the central difference method; the convective term by the up-wind scheme, which in low flow velocity provides acceptable performance. To treat the chemical (source) terms, the guideline of positive derivatives of source terms is followed. Negative chemical terms are linearized by preserving only the partial derivatives with respect to the primary variable, while the positive source term is left unchanged. In addition, a special treatment of the chemical term is used to enhance the accuracy and stability of the solution procedure [47]. To minimize computational time and storage, the ADI (Alternate Direction Implicit) method is employed: the independent variables are solved alternately in the x and y directions. The techniques used in solution of the phase change process in the condensed phase is a

special form of th

aforementioned er

across the solid-li

[49] of the therma

The run time

umerical model.

terms in the gas a

umerical experir

determined mainl

change even at hi

model, the iterati

finite difference e

The computa

the energy equati

interface pyrolysi

fed into the boun

interface tempera

gas. After the gas

the interface is c

computational pro

values of T, Y_O

normally chosen a

2.2 Theoretical (S

special form of the Enthalpy Method, the ADI Source Update Method, as well as the aforementioned enthalpy-temperature relationship. In addition, property discontinuities across the solid-liquid interface are averaged by using the harmonic mean formulation [48] of the thermal properties for any grid encompassing this interface.

The run time is influenced by three major non-linearities that are present in the numerical model. These non-linearities are the interface condition, the chemical reaction terms in the gas and condensed material, and the Stefan condition. It was determined by numerical experiments that the stiffness of the overall equations, hence the run time, is determined mainly by the chemical reactions. This overshadows the influence of phase change even at high Stefan numbers. In views of the non-linear nature of the numerical model, the iterative Newton-Raphson scheme is applied in semi-implicit form to the finite difference equation.

The computational cycles are constructed according to the physical process. First the energy equation of the condensed phase is solved, which produces the gas-condensed interface pyrolysis product flow rate and the interface temperature. Next this flow rate is fed into the boundary conditions of the two species equations, and the gas-condensed interface temperature is fed into the boundary condition of the energy equation in the gas. After the gas phase temperature is solved from the energy equation, the heat flux of the interface is obtained as a further input into the condensed phase. The iterative computational process continues until the relative error of the two most recent iterative values of T, Y_O, Y_f and h_c fall into the convergence range, the limit of which is normally chosen as 0.0001.

2.2 Theoretical (Simple) Model

The mode

coordinate syst

the energy equ

Wichman and

the "flame sp

convection (in

removed by e

balance princip

other, whereas

surfaces of inc

solid-phase co

across the flam

global energy b

models should

has been dem

spread, gas-pha

where the visc

detail. The au

recirculation ce

In applyin

The flame she

transition from

front located a

The model configuration for theoretical analysis is shown in Figure 3. The coordinate system is flame-fixed, hence a streamwise convection term is introduced in the energy equation of the condensed phase. The global energy balance principle of Wichman and Williams [43] is applied. The global energy balance principle states that the "flame spread rate must be sufficient to remove by downstream solid-phase convection (in flame fixed coordinates) the heat that is generated by combustion and not removed by either downstream gas-phase convection or conduction". This global balance principle is valid when either solid or gas phase conduction overpowers the other, whereas a simplified energy balance for heat flow to unignited fuel across surfaces of incipient fuel [34] can be used only when gas–phase conduction overpowers solid-phase conduction. Thus, flame spread models that employ an energy balance across the flame leading edge (and in its vicinity) are not so generally applicable as the global energy balance. With gas-phase domination both leading edge and global balance models should give approximately identical predictions. For most leading-edge models it has been demonstrated [1,43,49] that under most conditions encountered in flame spread, gas-phase domination is the norm. Exceptions to this norm are discussed in [50], where the viscous-invisid region near the point of flame attachment is examined in detail. The authors of [50] demonstrated that an upstream gas-phase fluid dynamic recirculation cell could alter flame spread behavior.

In applying the energy balance principle, the Oseen approximation is employed. The flame sheet is hypothesized to lie along the gas-condensed material interface. The transition from solid material to liquid is assumed to occur across an infinitesimally thin front located at the locus of a parabolic arc $y/\sqrt{x} = const$. All of the latent heat is

presumed to be c

sufficiently viscou

light, hydrocarbor

formula (see Appe

$$\frac{u_s}{u_\infty}$$

where T_f is the

c is the value of

As $c \to 0$ and T

When phase

as one of the nor

the heat required

melting temperat

Only $St > 0$ is c

A derivation of t

2.2 Simplified I

In this section, a

Equation (13). A

scaling analysis s

in [1, 43, 49] tha

In this model, the

presumed to be consumed along this arc. In addition, the liquid is presumed to be sufficiently viscous that internal, circulating flows do not occur as they do for certain light, hydrocarbon liquids. The analytical solution yields the following spread rate formula (see Appendix II),

$$\frac{u_s}{u_\infty} = \frac{\rho_g C_{Pg} k_g}{\rho_l C_{Pl} k_l} \cdot \left(\frac{T_f - T_i}{T_i - T_m}\right)^2 \cdot erf\left(c\sqrt{\frac{1}{2}\cdot\frac{\alpha_s}{\alpha_l}}\right)^2, \tag{13}$$

where T_f is the flame temperature, T_i is the interface temperature (see Figure 3), and c is the value of the numerical constant defining the locus of the liquid-solid interface. As $c \to 0$ and $T_m \to T_i$, Equation (13) reduces to the thick fuel deRis formula [21].

When phase change occurs, the Stefan number[7] $St = C_{Ps}(T_m - T_\infty)/L_s$ appears as one of the non-dimensional parameters of the problem. Physically, St is the ratio of the heat required to raise a unit mass of the solid from the ambient temperature to its melting temperature to the heat required to transform this unit mass of solid into liquid. Only $St > 0$ is of interest to us since St is positive when phase change is endothermic. A derivation of the preceding results is presented in the Appendix II.

2.2.1 Simplified Derivation of Flame-Spread Equation

In this section, a simple, physically-motivated-scaling-argument derivation is given for Equation (13). A full description is presented in the Appendix II. The simplicity of the scaling analysis sheds light on the important approximations of the analysis. It was shown in [1, 43, 49] that for a basic understanding of the overall flame spread process only the

---

[7] In this model, the definition of St is inverse to those appearing in [1] and [28].

energy conservation.

balance between s

formulation) captur

numerous original w

"Stokes region" nea

formulation produce

We proceed b

then the boundary

them. In the ga

$$\rho_g C_{P_g} u_g \Delta T_g \quad L$$

i.e., uniform coor

$$\alpha_g = k_g \quad \rho_g C_{P_g}$$

$$\rho_s C_{P_s} u_s \partial T_s \quad \partial x$$

$$\rho_s C_{P_s} u_s \Delta T_s \quad L_s$$

gas-phase control

Similarly, the liqu

$$\rho_l C_{P_l} u_l \Delta T_l \quad L_{lx}$$

$$L_{lx} = L_{gx} = L_g \quad a$$

We now exam

flame attachm

energy conservation equations of both media were needed, and that in these equations a balance between streamwise convection and traverse diffusion (a boundary-layer formulation) captured most of the physics. The full problem is elliptic, as shown in numerous original works [21, 51], but the region of pure ellipticity is confined to a small "Stokes region" near the flame attachment point. Outside of that small region, a parabolic formulation produces useful results. We follow the scaling analysis outlined in [1, 50].

We proceed by first scaling the three energy equations (gas, liquid melt, and solid), then the boundary conditions along the interfaces (gas-liquid, liquid-solid) that separate them. In the gas energy equation $\rho_g C_{Pg} u_g \partial T_g / \partial x = k_g \partial^2 T_g / \partial y^2$ scales to $\rho_g C_{Pg} u_g \Delta T_g / L_{gx} \sim k_g \Delta T_g / L_{gy}{}^2$. Imposition of the criterion $L_{gx} = L_{gy} = L_g$, i.e., uniform coordinate scaling in the flame attachment region gives $L_g = \alpha_g / u_g$, $\alpha_g = k_g / \rho_g C_{Pg}$. In the solid the energy equation is $\rho_s C_{Ps} u_s \partial T_s / \partial x = k_s \partial^2 T_s / \partial y^2$, which scales to $\rho_s C_{Ps} u_s \Delta T_s / L_{sx} \sim k_s \Delta T_s / L_{sy}{}^2$. We let $L_{sx} = L_{gx} = L_g$ in order to emphasize gas-phase control of the spread process. We then find $L_{sy} = [\alpha_s \alpha_g / u_s u_g]^{1/2}$. Similarly, the liquid-phase energy equation $\rho_l C_{Pl} u_l \partial T_l / \partial x = k_l \partial^2 T_l / \partial y^2$ scales to $\rho_l C_{Pl} u_l \Delta T_l / L_{lx} \sim k_l \Delta T_l / L_{ly}{}^2$, which yields $L_{ly} = [\alpha_l \alpha_g / u_l u_g]^{1/2}$ when we use $L_{lx} = L_{gx} = L_g$ as for the solid. Clearly $u_l = u_s$.

We now examine the two interfaces. Along the solid-gas interface upstream of the flame attachment point, the conductive energy balance gives

$k_s(\partial T_s \ \partial y)_s$

$L_{sl} \ L_g = k_s$

complicated. I

coordinate to t

the locus $y =$

$\bar{x} = x \ L_{sl} =$

parallel to the

the nondime

$k_s \Delta T_s \ L_{sl}$

In our derivat

overall spread

we substitute

energy equatio

The expres

$\Delta T_l \ \Delta T_s =$

$\Delta T_l \ \Delta T_s$ in

$k_s(\partial T_s/\partial y)_{y=0} \sim k_g(\partial T_g/\partial y)_{y=0}$, which yields $k_s\Delta T_s/L_{sy} \sim k_g\Delta T_g/L_{gy}$ or $L_{sy}/L_g = k_s\Delta T_s/(k_g\Delta T_g)$. Along the liquid-solid interface, the situation is more complicated. Here we have $k_s(\partial T_s/\partial n^*) \sim k_l(\partial T_l/\partial n^*)$, where n^* is the normal coordinate to the parabolic arc along which phase change occurs. This arc is given by the locus $y = -b_l x^2$, which nondimensionalizes to $\bar{y} = -\bar{x}^2$ with $\bar{y} = y/L_{ly}$, and $\bar{x} = x/L_{lx} = x/L_g$ and $L_{ly} = b_l L_g^2$. In the case that the parabolic arcs lie nearly parallel to the horizontal plane, the derivatives $\partial T/\partial n$ approximate to $\partial T/\partial y$. Thus, the nondimensionalization of the interface condition yields, approximately, $k_s\Delta T_s/L_{sy} \sim k_l\Delta T_l/L_{ly}$. Use of $L_{ly} = b_l L_g{}^2$ gives

$$k_s\frac{\Delta T_s}{L_{sy}} \sim \frac{k_l}{b_l L_g}\frac{\Delta T_l}{L_g} \tag{14}$$

In our derivation this interface condition is considered to be more important to the overall spread process than the solid-gas interface condition derived previously. Hence we substitute the relationship $L_{sy} = [\alpha_s\alpha_g/u_s u_g]^{1/2}$ derived from the solid-phase energy equation into Equation (14) to obtain

$$u_s = u_g\frac{\alpha_s}{\alpha_g}\frac{k_l^2}{k_s^2}\left(\frac{\Delta T_l}{\Delta T_s}\right)^2\frac{1}{b_l L_g} \tag{15}$$

The expression for $\Delta T_l/\Delta T_s$ is now written in the following form: $\Delta T_l/\Delta T_s = (\Delta T_g/\Delta T_l)(\Delta T_l/\Delta T_s)^2(\Delta T_s/\Delta T_g)$. Then we use Equation (14) for $\Delta T_l/\Delta T_s$ in the right-hand side (square) term, and the upstream interface condition

$k_s \Delta T_s \sqrt{L_{gs}} = k_g$

Equation (15) yield

The quantity in sq

$L_{gs} = b_i L_g^2$ is en

parabolic isotherm

used in the solid T

We compare this r

small c (

$\mathrm{erf}[c\sqrt{\alpha_s / 2\alpha_l}]$

n square brackets

formulas is exact w

$\Delta T_g = T_f - T_s$,

and liquid phases.

This simplifie

flame spread. Fir

$L_{gs} = L_{gs} = L_g$.

$k_s \Delta T_s / L_{sy} = k_g \Delta T_g / L_{gy}$ for $\Delta T_s / \Delta T_g$. These expressions substituted into Equation (15) yield

$$\frac{u_s}{u_g} = \frac{\rho_g C_{Pg} k_g}{\rho_l C_{Pl} k_l} \left(\frac{\Delta T_g}{\Delta T_l}\right)^2 \left[\frac{\alpha_s}{\alpha_l} (b_l L_g)^2 \frac{L_g^{\,2}}{L_{sy}^{\,2}}\right].$$

The quantity in square brackets reduces to $(\alpha_s / \alpha_l)(L_{ly} / L_{sy})^2$ when the relationship $L_{ly} = b_l L_g^{\,2}$ is employed. When we observe that both liquid and solid must produce parabolic isotherms, we find $(L_{ly} / L_{sy})^2 = (b_l / b_s)^2 = \kappa^2$, where $L_{sy} = b_s L_g^{\,2}$ was used in the solid. The constant factor κ is nondimensional. Thus, our final result is

$$\frac{u_s}{u_g} = \frac{\rho_g C_{Pg} k_g}{\rho_l C_{Pl} k_l} \left(\frac{\Delta T_g}{\Delta T_l}\right)^2 \left[\kappa^2 \frac{\alpha_s}{\alpha_l}\right] \tag{16}$$

We compare this result to Equation (13), the exact formula, by considering the limit of small c (high sweep-back of the isotherms) to find $erf[c\sqrt{\alpha_s / 2\alpha_l}] \approx (2\sqrt{\pi})[c\sqrt{\alpha_s / 2\alpha_l}]$. This yields Equation (16) with the quantity in square brackets replaced by $(2c^2 / \pi)\alpha_s / \alpha_l$. The correspondence between the two formulas is exact when we identify $\kappa^2 = 2c^2 / \pi$. We note finally that in Equation (16) $\Delta T_g = T_f - T_s$, $\Delta T_l = T_s - T_m$ are the characteristic temperature difference in the gas and liquid phases, respectively.

This simplified analysis illustrates important features of the phase change model of flame spread. First, the gas phase is elliptic near the flame leading edge because $L_{gx} = L_{gy} = L_g$, i.e., all characteristic lengths in the 2-D plane are identical. Second, in

the limit being con

processes. Third,

streamwise diffusi

$\partial^2() / \partial y^2$ Fourt

and liquid and so

change enthalpy, w

of the two interfac

than the solid-gas

spread process.

$u_s = K^2 u_g [(\rho_g C$

in proportion to $\bar{k}_l$

are not considered

reckoning, whereas

concept of "gas-ph

imposition of the g

Eighth, the liquid

occurs. Although

interface can ind

motions in our sca

be removed as dis

spread rate are th

the limit being considered chemistry is very fast compared with convection and diffusion processes. Third, the solid and liquid phases are fundamentally parabolic, with streamwise diffusion $\partial^2(\cdot)/\partial x^2$ negligible in comparison with transverse diffusion $\partial^2(\cdot)/\partial y^2$. Fourth, conduction across the interfaces between gas and solid (upstream) and liquid and solid (downstream) dominates streamwise convection and the phase change enthalpy, which appears only implicitly in the parameter c of Equation (13). Fifth, of the two interfaces, the energy balance across the solid-liquid interface was used more than the solid-gas interface balance, indicating its greater importance in the overall flame spread process. Sixth, simple rearrangement of Equation (16) gives $u_s = \kappa^2 u_g[(\rho_g C_{Pg} k_g)/(\rho_s C_{Ps} k_l)]\bar{k}_l^{-1}(\Delta T_g/\Delta T_l)^2$, suggesting that u_s decreases in proportion to $\bar{k}_l^{-1}$ and in proportion to C_{ps}^{-1}, if their influences on other parameters are not considered. Our subsequent evaluations demonstrate that $u_s \propto \bar{k}_l^{-1}$ is a good reckoning, whereas $u_s C_{Ps} \sim$ constant is not (see Figures 4(b) and (c)). Seventh, the concept of "gas-phase dominance" of the spread process is implicitly understood by the imposition of the gas-phase length L_g on L_{lx} and L_{sx}; i.e., the use of $L_{lx} = L_{sx} = L_g$. Eighth, the liquid layer is highly viscous so that no internal convection or recirculation occurs. Although surface tension gradients produced by temperature gradients along the interface can induce circulatory liquid movement [52], we have not included these motions in our scaling analysis. Ninth, subject to the constraint of Oseen flow (which can be removed as discussed in [49]) and fast chemistry, the largest influences on the flame spread rate are the thermal properties of gas, solid and liquid, and the Stefan number,

whose magnitude

3. Results and

The thermal

heat flux from t

of the condens

dimensional pa

change, and $\bar{k}$

Variation of S

k_f or $C_{P,f}$ wh

3.1 Flame Spr

The thick

where T_v de

parameters th

kinetics, and s

values have to

of the interf

[a] The vaporiza

temperature T_v i

surface although sp

whose magnitude controls the multiplicative factor κ^2 in (16) (c in Equation (13)).

3. Results and Discussions

The thermal and flow properties are listed in Table 1. Ignition is established if the heat flux from the gas phase excluding external radiation is over 10 W/cm^2. The effects of the condensed material on flame spread are investigated by varying three non-dimensional parameters, St, $\bar{k}_l$, and $\overline{C}_{Pl}$, in which St denotes the influence of phase change, and $\bar{k}_l$ and $\overline{C}_{Pl}$ denote the relative influence of liquid thermal properties. Variation of St, $\bar{k}_l$ and $\overline{C}_{Pl}$ is accomplished by changing only one single property L_s, k_l or C_{Pl} while keeping the rest fixed.

3.1 Flame Spread Rate

The thick fuel spread rate of deRis 's formula [21] is

$$\frac{u_s}{u_\infty} = \frac{\rho_g C_{Pg} k_g}{\rho_s C_{Ps} k_s} \left(\frac{T_f - T_v}{T_v - T_\infty}\right)^2, \tag{17}$$

where T_v denotes the vaporization temperature[8]. Since T_f and T_v are theoretical parameters that correspond approximately to real condensed-phase and combustion kinetics, and since they are in fact not constant in the numerical model, representative values have to be selected in order to make a comparison. Based on the numerical results of the interfacial temperature (see Figure 8(a)) and on previous experimental

---

[8] The vaporization temperature T_v in deRis 's formula is essentially equivalent with the surface temperature T_i in Equation (13) as the latter denotes the constant temperature of the non-vaporizing surface although the former denotes solid-to-gas "vaporization" (actually sublimation).

measurement (T_v =

extract T_f from

$S_f \to \infty$, since S_f

is the flame spre

worth pointing ou

(13) and the num

manipulation is n

we obtained the

following ratio of

We note that this

physically reason

flame temperatur

introduced that n

of the flame spr

numerical model

the dependence

computational re

the spread rate o

(**) and theor

represented by a

measurement ($T_v = 665K$ for PMMA), it is a reasonable guess to fix T_v at 700K. We extract T_f from Equation (13) by letting the u_s equal the numerical flame spread at $St \to \infty$, since $St \to \infty$ corresponds exactly to flame spread without phase change, that is, the flame spread problem is essentially characterized by deRis 's formulation. It is worth pointing out that this treatment helps to make a comparison between Equation (13) and the numerical model. This comparison is justifiable in that no artificial manipulation is involved for situations of widely varying thermal properties. Therefore we obtained the following representative values, $T_f = 1730\,\mathrm{K}$, thus resulting in the following ratio of the right hand side of Equation (14)

$$(\frac{T_f - T_v}{T_v - T_\infty}) = 2.58\,.$$

We note that this ratio remained fixed in all cases considered, and that $T_f = 1730\,\mathrm{K}$ is a physically reasonable flame temperature estimated in flame spread since the maximal flame temperature in the numerical results is 1630K. In effect, a scaling factor has been introduced that makes the case $St \to \infty$ agrees with the deRis formula. The dependence of the flame spread rate on St, which is obtained from Equations (13), (17) and the numerical model, is plotted separately in Figures 4(a) through 4(c). Figure 4(a) reports the dependence of flame spread on St by presenting the formulas of and eleven computational results. It appears that the formula provides an almost an exact solution to the spread rate of the numerical model, since agreement between the numerical results ('*') and theory (dotted curve) is observed. However, Equation (17), which is represented by a horizontal solid line above the '*' and dotted lines, results in a constant

value higher tha

of St, the spre

which is illustra

addition, St is

spread rate and

L_s is almost c

We can es

of phase chang

and nearly ne

found that if S

No flame spre

initiated in the

flame cannot s

The contr

Figures 4(b) a

the increase o

condensed ph

is lower than

Equation (13)

formulation.

three cases c

Equation (13

value higher than both the numerical result and theory. Qualitatively, with the increase of St, the spread rate increases. The sensitivity of the spread rate with respect to St, which is illustrated by the slope of the curve in Figure 4(a), diminishes for larger St. In addition, St is inversely proportional to L_s, and an almost linear relationship between spread rate and L_s is found. As a result, the aforementioned sensitivity with respect to L_s is almost constant.

We can estimate the influence of phase change on the spread rate. The contribution of phase change can be as much as a 40% change of the flame spread formula at $St = 1$ and nearly negligible influence at $St = 100$. Through numerical experiments, it was found that if St is lower than 0.667, only ignition is observed, followed by extinction. No flame spread occurs. Since the external heat flux is removed as soon as ignition is initiated in the numerical model (for all St cases), the above finding indicates that the flame cannot support itself if St is too low.

The contributions of $\bar{k}_l$ and $\overline{C}_{Pl}$ to the flame spread rate for $St = 2$ are reported in Figures 4(b) and Figure 4(c), respectively. Good agreement is observed. Qualitatively, the increase of either the conductivity or the thermal capacity of the liquid layer in the condensed phase decreases the flame spread rate. Similarly, extinction is observed if $\bar{k}_l$ is lower than approximately 1.0, or $\overline{C}_{Pl}$ is higher than approximately 1.25. Again, Equation (13) does not provide any indication of extinction because of the steady state formulation. However, one may conjecture that certain limits can be derived from the three cases of varying St, $\bar{k}_l$ and $\overline{C}_{Pl}$. Therefore extinction occurs if the ideal (Equation (13)) spread rate decreases below these limits. These rate limits are dependent

on parametric val

of Figure 4(a), 4

to determine thes

in the numerical

procedure may

necessary, theref

analytical studies

defined quantity

3.2 Transient Sp

Figure 5(a)

for $St = 2$. Thi

and fully develo

spread rate arou

The transition s

over the preheat

The final stage

between the pri

with constant ra

front arrival alon

compared to the

the movement

A very detailed an

neluding thermal exp

on parametric values. This viewpoint is partly supported by observing that the rate limits of Figure 4(a), 4(b) and 4(c) differ from each other significantly. However it is difficult to determine these rate limits quantitatively since extinction is not a well-defined event in the numerical model[9]. One reason is that the control of grid size or convergence procedure may influence and substantially alter such unstable phenomena. It may be necessary, therefore, to examine flame extinction at least partly analytically. Even in analytical studies, however, the precise definition of the moment of ignition is an ill-defined quantity.

3.2 Transient Spread Process

Figure 5(a) reports the progress of flame spread rate along the streamwise distance for $St = 2$. Three stages of transient evolution are observed, viz., ignition, transition and fully developed (or steady) spread. Ignition is characterized by sharp slopes of flame spread rate around a peak point, indicating the impulsive nature of the ignition process. The transition stage, which occurs after ignition, allows the flame to stabilize mainly over the preheated region (9-12 mm). Its behavior is characterized by smaller slopes. The final stage of the spread is established after the flame moves across the boundary between the pristine polymer and preheated region ($x = 9\,\text{mm}$), and the flame spreads with constant rate. Figure 5(b) reports the time histories of both flame front and phase front arrival along the polymer surface. It is observed that the interval of transition (2s), compared to the ignition delay time (10s), is relatively short. Another observation is that the movement of the phase front started much earlier than the flame front. This

[9] A very detailed analysis of flame spread initiation was carried out in [40], where all gas-phase processes including thermal expansion were retained.

phenomenon ari

flame front, sin

In Figure 5(c)

streamwise pro

initial heating

preheating reg

Between this

flux applied o

still stays put

is too weak to

the flame surv

Thereafter, p

spread is atta

phase front, a

Figures

temperature

ignition (10s

surface, the

temperature,

and an abrup

rapid change

The heat
```
```

phenomenon arises from the fact that the phase front is established much earlier than the flame front, since the melting temperature is much lower than the ignition temperature. In Figure 5(c), the phase front leads the flame in the region 9mm<x<10mm. The streamwise progress of the phase front is the described as follows: shortly after the initial heating the phase front starts to move, then it approaches the boundary of the preheating region, shown in Figure 5(a) at the location between x=9 and x=12mm. Between this time and ignition, the phase front can not move because there is no heat flux applied outside the preheating region. Even with ignition initiated, the flame front still stays put because the external heat flux is removed and the self-supportive heat flux is too weak to push it forward. The resumption of movement is not accomplished until the flame survives the transition and spread near the boundary of the preheating region. Thereafter, phase spread is driven by the combustion heat from the gas phase and steady spread is attained. This steady stage is characterized by the same spread rate as for the phase front, as is seen by the two parallel lines in Figure 5(b).

Figures 5(c) and 5(d) report the streamwise evolution of heat flux[10], mass flux and temperature at the interface during three stages of flame spread. At the time of pre-ignition (10s), an external heat flux of $5W/cm^2$ is applied to the preheating region of the surface; the mass flux of pyrolysis products is low because of the low condensed phase temperature, see Figure 5(d). Once ignition is initiated, the external heat flux is removed, and an abrupt change of flame environment occurs. The plume of the flame adapts to the rapid change of the heat flux, during which transition occurs. If, for example, the heat

[10] The heat flux here denotes the net heat flux feeding the condensed phase, which is obtained by subtracting the surface radiation loss from gas phase conduction to the interface.

flux generated
through the ga
as was observ
self-supportive
plume and ste
the heat flux d
heat flux. How
by a factor of
pyrolysis layer
and heat flux a

As far as
ignition, whos
the leading ed
increase of d
assumption of
invalidity of th
effects of ph
downstream of
as 20% for th
eventual agree
vaporization
conceptual pic

3.3 Flame Str

flux generated from the combustion reaction cannot compete with the loss of heat through the gas and the condensed phase, the plume shrinks and extinction takes place, as was observed in Section 3.2. The transition stage determines whether the flame is self-supportive or not. Figures 5(c) and 5(d) illustrate the successful survival of the plume and steady spread thereafter. It is observed in Figure 5(c) that the magnitude of the heat flux during the steady spread stage is approximately one tenth of the external heat flux. However, the mass flux shows a reverse trend with an increase of magnitude by a factor of ten because the low mass flux of the initial stage results from the thin pyrolysis layer. Steady spread is attained when the mass flux attains the highest value and heat flux attains the lowest value among the three stages.

As far as the interface temperature is concerned, a leading edge appears after ignition, whose magnitude slightly increases to attain the steady state. Downstream of the leading edge during the steady spread stage, the surface temperature decreases with increase of distance from the leading edge. This observation disagrees with the assumption of a constant surface vaporization temperature discussed at length in [1]. The invalidity of the assumption was discussed in numerical studies (that did not consider the effects of phase change) such as [38, 32]. The divergence of the temperature downstream of flame front from an assumed constant value at the leading edge is as high as 20% for the case $St = 2$. Apparently such a deviation is not crucial, given the eventual agreement between numerical results and theory. For this reason, the constant "vaporization temperature" hypothesis has survived and, in fact, represents an important conceptual piece of the overall flame spread model.

3.3 Flame Structure

The detailed

contours of con

combustion reac

temperature from

From the viewp

qualitatively the

opposed flow, t

oxidizer gas in t

6(b)) From Figu

shows the nature

reactive region

temperatures ar

maximum, as ob

It is intere

structure. A re

observed from

$\bar{C}_{Pl} = 0.125$

fuel concentra

concentration

$k_l = 3$. The s

shape and ori

examined; ho

The detailed flame structure is obtained from the numerical model by examining contours of constant temperature, fuel concentration, oxidizer concentration, and combustion reaction rate in four cases of interest (see Figure 6). The non-dimensional temperature from the numerical model is divided by St in order to make comparisons. From the viewpoint of physics, the flame structure displayed in Figure 6 shows qualitatively the same characteristic as reviewed in [1]. Under the influence of an opposed flow, the diffused fuel gas from the interface (Figure 6(c)) reacts with the oxidizer gas in the mainstream (Figure 6(d)), thereby forming a reaction region (Figure 6(b)). From Figure 6(b) we see that the thickness of the reactive region is finite, which shows the nature of finite-rate reaction in the gas. In addition, the temperature of this reactive region is the highest in the field, as shown in Figure 6(a). The highest temperatures are displaced from the surface somewhat downstream of the reactivity maximum, as observed in previous studies of flame near cold surfaces [53, 54, 31].

It is interesting to evaluate the influence of the condensed phase on the flame structure. A reference state of $St = 2$ is chosen for these comparisons. First, it is observed from Figure 6(a) that $St = 100$ and $\bar{k}_l = 3$ produce bigger flames. However, $\bar{C}_{Pl} = 0.125$ produces a smaller flame. This observation is confirmed by comparing fuel concentration constant contours in Figure 6(c). The same constant contour of fuel concentration is pushed further downstream of the flame leading edge if $St = 100$ or $k_l = 3$. The second observation is from Figure 6(b). Near the flame leading edge, the shape and orientation of the reactive region does not change for the four cases we examined; however, farther downstream of the flame leading edge, the reactive region

tends to be sligh

becomes smaller

3.4 The Conden

The temper

numerical mode

isotherms are pa

numerical soluti

parabola except

downstream of t

Good agreemen

edge of the pha

the leading edg

therefore some

The influe

stage is show

condensed pha

interface temp

flame front ar

$St = 100$ pro

$C_{Pl} = 0.125$

and the net

presented in

tends to be slightly raised if St or $\bar{k}_l$ becomes larger, or slightly pressed down if $\overline{C}_{Pl}$ becomes smaller.

3.4 The Condensed Phase

The temperature profile (including location of the phase front) from both the numerical model and theory are compared in Figure 7. Theory predicts that the isotherms are parabolas with the origins located at the leading edge ' o ' in Figure 7. The numerical solution, however, predicts that the isotherms do not resemble the shape of parabola except near the flame leading edge. The isotherms deviate from parabolas downstream of the leading edge. The thickness of the liquid layer shrinks downstream. Good agreement between the numerical result and theory is observed near the leading edge of the phase change point ' o '. The behavior of the liquid thickness downstream of the leading edge suggests a connection to the surface temperature or heat flux at ignition, therefore some other parameters of interest are investigated.

The influence of the condensed phase on flame spread during the steady spread stage is shown in Figure 8 by investigation of interface temperature, mass flux, condensed phase heat conduction and the phase front locations. As is shown by the interface temperature in Figure 8(a), there is negligible difference downstream of the flame front among four cases except $\bar{k}_l = 3$. In addition, upstream of the flame front, $St = 100$ produces a shallower gradient of the interface temperature than $St = 2$, and $C_{Pl} = 0.125$ makes this gradient even lower. Distributions of the interface mass flux and the net heat flux into the condensed phase along the streamwise distance are presented in Figures 8(c) and 8(d). Among the four cases, $\bar{k}_l = 3$ stands out having the

highest mass fl

phenomenon is

mechanism in t

corresponds to a

extent of the m

significantly enl

the other cases a

A simple an

liquid layer in th

which is subject

subjected to the

condensed phase

neglected.

where δ denot

and T_{lg} do

relationship o

$\bar{k}_l = 3$ is alm

The strea

characterize

highest mass flux and lowest heat conduction into the condensed phase. This phenomenon is well understood if we recall that we used the in-depth pyrolysis mechanism in the condensed phase. As a result, the larger pyrolysis area in general corresponds to a higher mass flow rate. The extent of the pyrolysis area is related to the extent of the melting region, as shown in Figure 8(b). It is observed that $\bar{k}_l = 3$ significantly enlarges the liquid region, thus resulting a higher pyrolysis region, while in the other cases a smaller difference is observed.

A simple analysis illustrates that $\bar{k}_l$ controls the thickness of the liquid phase. The liquid layer in the condensed phase can be looked on as a plane plate, the upper side of which is subjected to the ignition temperature T_{ig}, and the lower side of which is subjected to the melting temperature T_m. If $\bar{q}_{ig}$ denotes the heat conduction into the condensed phase, then a simple heat conduction relation applies if the transient effect is neglected,

$$\delta = k_l \frac{T_{ig} - T_m}{\bar{q}_{ig}}, \tag{18}$$

where δ denotes the average thickness of the liquid layer. Since the magnitudes of $\bar{q}_{ig}$ and T_{ig} do not depend significantly on the magnitude of $\bar{k}_l$, an approximate relationship of $\delta \propto k_l$ is determined. This explains why the liquid layer thickness of $\bar{k}_l = 3$ is almost three times as large as $\bar{k}_l = 1$.

The streamwise evolution of the phase front location and pyrolysis front location (characterized by $\bar{w}_c = 1.5 \times 10^{-7}$) is shown in Figure 9. The liquid region

encompasses alm

slight intrusion

pyrolysis temper

the pyrolysis re

front and fits we

of the pyrolysis r

3.5 Mechanism

Generally, n

conclusions on

dependence of t

5.7mm×4.5mm

$\bar{k}_l = 3$, $\bar{C}_{Pl} =$

balance accoun

evaluated by nu

An energy

gas phase upstr

condensed pha

control volume

important comp

the total heat ob

and should be

Table 3 indica

higher spread ra

encompasses almost the entire pyrolysis region during all three stages. In addition, the slight intrusion of the pyrolysis front out of the phase boundary indicates that the pyrolysis temperature is slightly lower than the melting temperature. Also the shape of the pyrolysis region is not a parabola. Its thickness shrinks downstream of the flame front and fits well with the shape of phase front. In addition, the reaction intensive part of the pyrolysis region has the highest temperature, and lies below the flame front.

3.5 Mechanism of Steady Flame Spread

Generally, many different mechanisms contribute to the flame spread process, and conclusions on which mechanism is dominant (if any) are difficult to make. The dependence of flame spread on St, $\bar{k}_l$, and $\overline{C}_{Pl}$ is analyzed below. Control volumes of $5.7mm \times 4.5mm$ upstream of the flame leading edge are chosen for cases $St = 100$, $\bar{k}_l = 3$, $\overline{C}_{Pl} = 0.125$ as well as the reference state in order to construct a local energy-balance accounting. Different heat transfer mechanisms in non-dimensional from are evaluated by numerical integration, see Table 3.

An energy balance can be constructed for this control volume. The heat from the gas phase upstream of the flame leading edge plus the streamwise conduction in the condensed phase are responsible for the pyrolysis process and enthalpy rise of the control volume. Pyrolysis and streamwise conduction in the condensed phase are not important compared with the upstream conduction from the gas phase [34]. Physically, the total heat obtained in Table 3 is responsible for enthalpy rise of the control volume, and should be connected to the spread rate. Comparison of $St = 2$ and $St = 100$ in Table 3 indicates that with the increase of St, the total heat increases, resulting in a higher spread rate. However, for cases of variable thermal conductivity and variable heat

capacity, the m

the spread rate

the spread rate

The ratio

energy barrier

for the four cas

of preheating t

the temperatu

justifiable ded

$St = 100$, $\bar{C}$

therefore comp

for $St = 100$

the latent heat

reference state

barrier. A diff

many differen

$\bar{k}_l = 3$ result

$\bar{k}_l = 3$

ratio in Table

however, tend

The overall in

supported by

capacity, the magnitudes of the total heat do not necessarily measure the magnitudes of the spread rate. This phenomenon can be explained by a ratio between the total heat and the spread rate.

The ratio of the total heat to the spread rate, presented in Table 3, denotes the energy barrier for flame propagation with a spread rate of unity. We compare this ratio for the four cases we examined, since it reflects physically the ratio of relative difficulty of preheating the condensed phase to the ignition temperature. This ignition temperature (the temperature at the flame leading edge), should be identical for different cases if justifiable deductions are made. Observation of Figure 8(a) indicates that $St = 2$, $St = 100$, $\overline{C}_{Pl} = 0.125$ have identical flame temperatures at the leading edge, therefore comparisons between these three cases are made below. From Table 3 the ratio for $St = 100$ has a lower value than for $St = 2$, indicating a lower energy barrier when the latent heat is decreased. Similarly, the ratio for $\overline{C}_{Pl} = 0.125$ is lower than for the reference state, because the lower thermal capacity is consistent with the lower energy barrier. A different interpretation for the last case $\overline{k}_l = 3$ is needed because it shows many different characteristics from the other cases. From Figure 8(a), it is observed that $\overline{k}_l = 3$ results in a lower flame temperature at the leading edge. Second, from Figure 8(b), $\overline{k}_l = 3$ results in a larger liquid thickness. The first influence tends to lower the ratio in Table 3 because a lower ignition temperature is required. The second influence, however, tends to increase the ratio because a thicker liquid layer requires more energy. The overall influence of $\overline{k}_l = 3$ seems to be controlled by the second influence, as is supported by Table 3: the ratio of the total heat to the spread rate is larger than for the

reference state.

4. Conclusions

A new num

in the condense

to-liquid phase

processes in th

transfer, fuel a

between the

constructed by

radiant emissi

The influ

flame spread

interest, $St_$

numerical mo

It is found th

variable St

spread formu

result and Eq

Some ob

stages are ob

spread. In ad

ignition dela

certain limits

reference state.

4. Conclusions

A new numerical model of flame spread is constructed by introducing phase change in the condensed phase. The processes considered in the condensed phase include solid-to-liquid phase change, an in-depth pyrolysis reaction and heat conduction. The processes in the gas phase, after applying the Oseen-flow approximation, include heat transfer, fuel and oxidizer transfer, and finite-rate combustion kinetics. At the interface between the gas phase and the condensed phase, the heat and mass balance is constructed by incorporating heat conduction into both gas and condensed phases, radiant emission from the surface, and diffusion of pyrolysis products into the gas.

The influence of phase change and thermal properties of the condensed phase on flame spread are investigated by introducing three non-dimensional parameters of interest, St, $\bar{k}_l$, and $\overline{C}_{Pl}$. Quantitative comparisons of spread rate between the numerical model and theory outlined in Section 2.3, 2.2.1, and Appendix II are obtained. It is found that the numerical model provides almost exact correspondence to [28] for variable St and $\overline{C}_{Pl}$, and 90% agreement for cases of variable $\bar{k}_l$. DeRis 's flame spread formula, which results in a constant spread rate value higher than the numerical result and Equation (13), is independent of phase change.

Some observations are made about the transient process of flame spread. (1) Three stages are observed: ignition, transition, and fully developed (or steady state) flame spread. In addition, the interval of transition is found to be very short compared to the ignition delay time. (2) Extinction is observed if St, $\bar{k}_l$ go below, or $\overline{C}_{Pl}$ goes beyond, certain limits. Quantitative values of these limits are not precisely known. (3) The rates

of spread of the

The depen

increase of St

results are cons

rate on the thre

means a lower

$\bar{k}_f$ on the oth

results in a low

at the interface

The mech

found that a r

the flame lead

the preheating

this basis is c

discussed ori

$q = \rho_s u_f \Delta h$

upstream unb

difference b

$q\ u_f = \rho_s$

relevance to

varying St

preheating of

of spread of the phase and flame fronts differ until the steady spread stage is attained.

The dependence of flame structure on St, $\bar{k}_l$, and $\overline{C}_{Pl}$ were studied. With the increase of St or $\bar{k}_l$, or with the decrease of $\overline{C}_{Pl}$, the flame size increased. These results are consistent with the qualitative nature of the dependence of the flame spread rate on the three parameters. Physically, a lower latent heat or a lower thermal capacity means a lower energy barrier for the flame, hence a larger spread rate. The increase of $\bar{k}_l$, on the other hand, denoting the diffusion away of the thermal energy for preheating, results in a lower spread rate. The study of heat flux, mass flux and surface temperature at the interface provides additional information on the mechanisms of flame spread.

The mechanisms of flame spread are interpreted by energy balance analysis. It is found that a ratio between the total heat applied to the condensed material upstream of the flame leading edge and the spread rate reveals the physical mechanisms that control the preheating of the condensed material to the ignition temperature. A comparison on this basis is consistent with the notion of a "fundamental equation of flame spread" as discussed originally in [34] and in Section 3.1.5 of [1]. This equation is written as $q = \rho_s u_f \Delta h$, where q is the energy flux transported across the flame front to upstream unburned fuel, ρ_s is the fuel density, and Δh is the fuel thermal enthalpy difference between ignition and ambient temperature. Clearly, the quantity $q/u_f = \rho_s \Delta h$ was evaluated in our work, and this quantity has the direct physical relevance to the propensity for flame spread. Comparisons of this ratio in situations of varying St, $\bar{k}_l$, and $\overline{C}_{Pl}$ reveals the difference in physical mechanisms that control the preheating of the condensed phase to the ignition temperature. Although the theoretical

result (Equation

where predictio

numerical resul

principle [49].

examined in ter

globally derived

Extension o

extinction limit

addition, detailed

needed. More at

phase change p

attempted by in

longer horizonta

result (Equation (13)) on which much of the numerical comparisons were based and where predictions were, in same cases, remarkably accurate when compared with numerical results, if was derived from the application of the global energy balance principle [49], The general result it produces (Equation (13)) can subsequently be examined in terms of local energy balances. Thus, there is no contradiction between a globally derived formula and its subsequent local interpretation.

Extension of the current work is needed. The transient flame behaviors, such as extinction limit or ignition limit with phase change, leave room for future research. In addition, detailed analysis of the mechanisms of flame spread over a melting polymer is needed. More attention may be given to combination of the gas phase influence with phase change processes in the condensed material. Further modeling efforts may be attempted by incorporating the melt flow phenomena when the burning material is no longer horizontal.

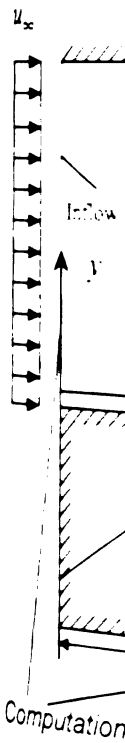

Figure 1 Sch

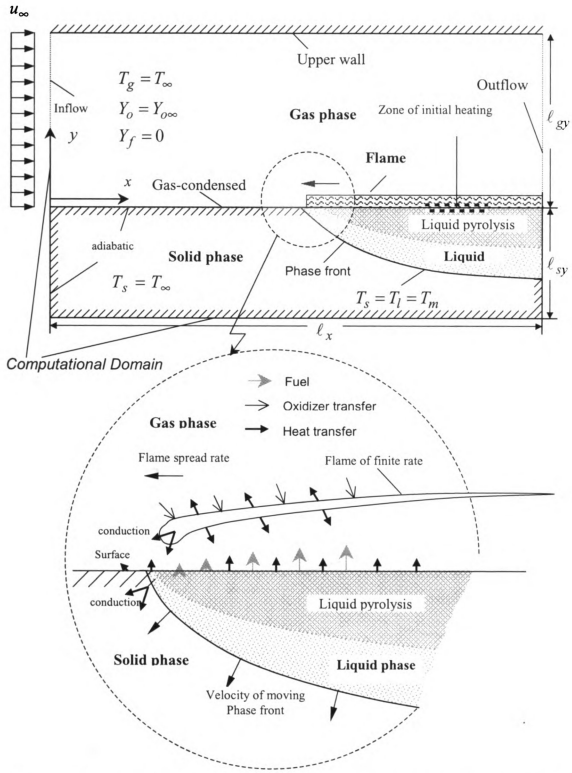

Figure 1 Schematic description of diffusion flame spread over polymers in an opposed-flow

Figure 2 T

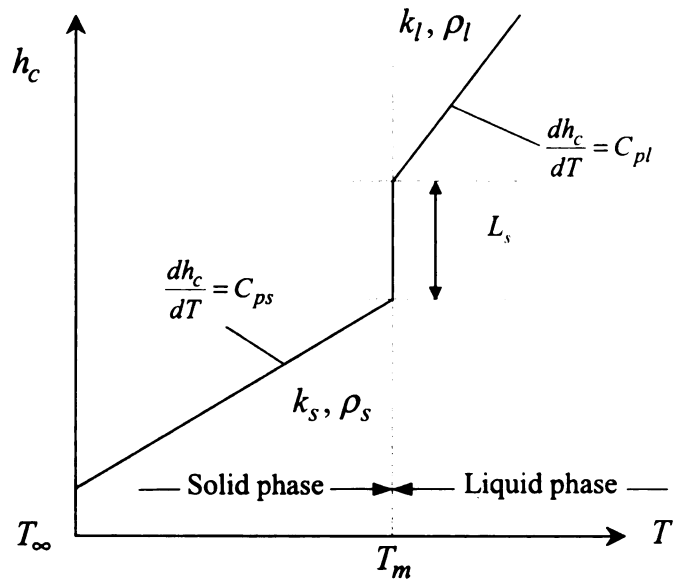

Figure 2 The enthalpy-temperature relationship used in the numerical model.

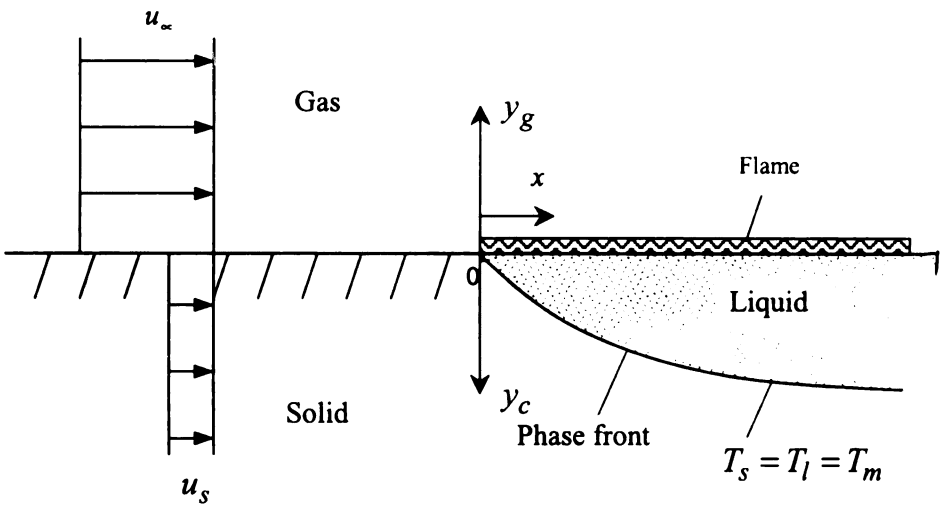

Figure 3 The simplified flame-spread model for steady flame spread.

Flame spread rate (mm/s)
0.4
0.35
0.3
0.25
0.2
0.15
0.1
Flame spread rate (mm/s)
0.45
0.4
0.35
0.3
0.25
0.2
0.15

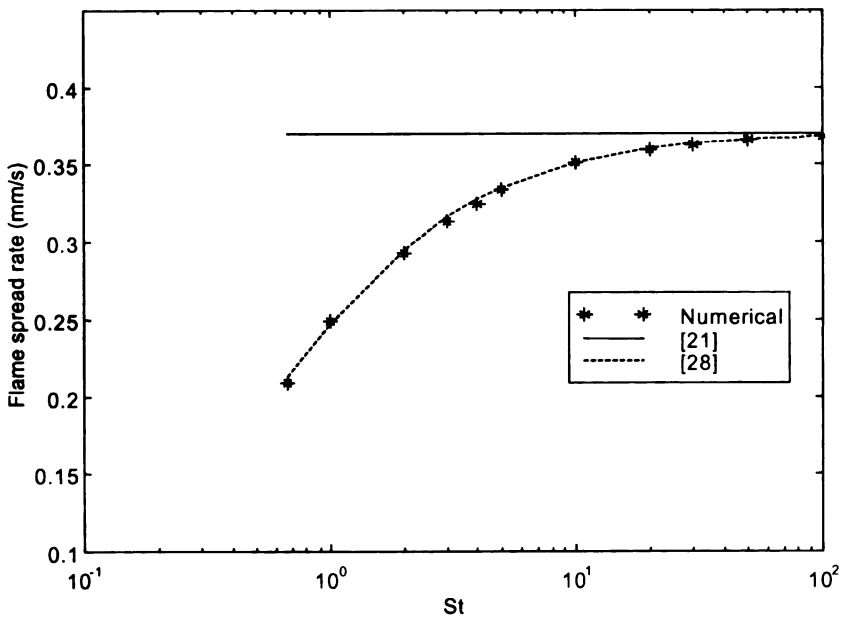
Flame spread rate (mm/s)
0.4
0.35
0.3
0.25
0.2
0.15
0.1
10^{-1}
10^{0}
10^{1}
10^{2}
St
Numerical
[21]
[28]

(4-a)

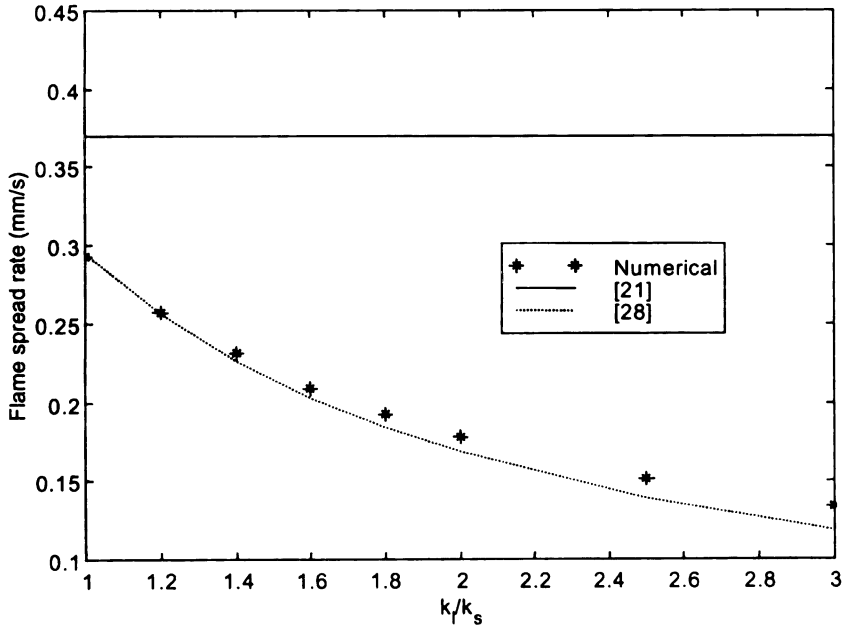
Flame spread rate (mm/s)
0.45
0.4
0.35
0.3
0.25
0.2
0.15
0.1
1
1.2
1.4
1.6
1.8
2
2.2
2.4
2.6
2.8
3
k_f/k_s
Numerical
[21]
[28]

(4-b)

Figure 4 (a) Flar
spread rate vs. C

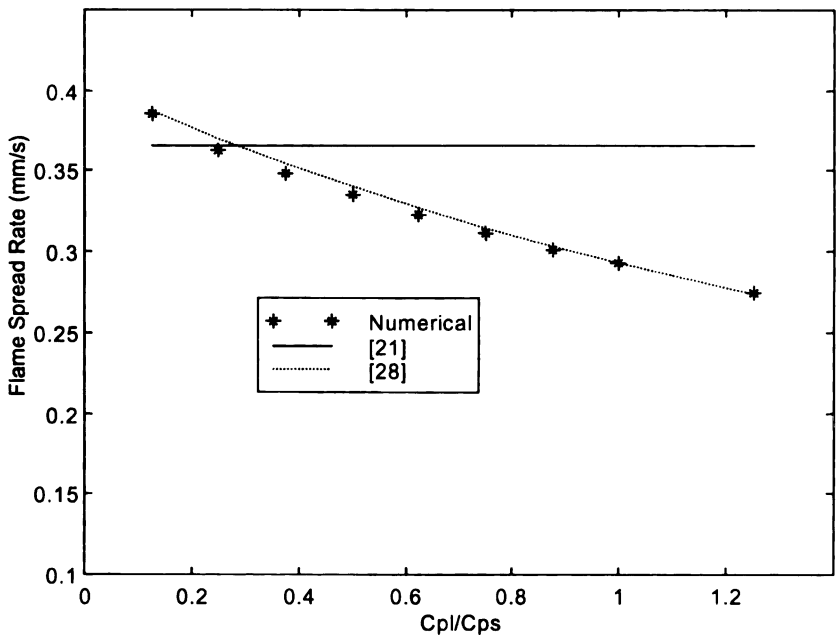

(4-c)

Figure 4 (a) Flame spread rate vs. St; (b) Flame spread rate vs. $\overline{k_l}$ at $St = 2$; (c) Flame spread rate vs. $\overline{C_{Pl}}$ at $St = 2$.

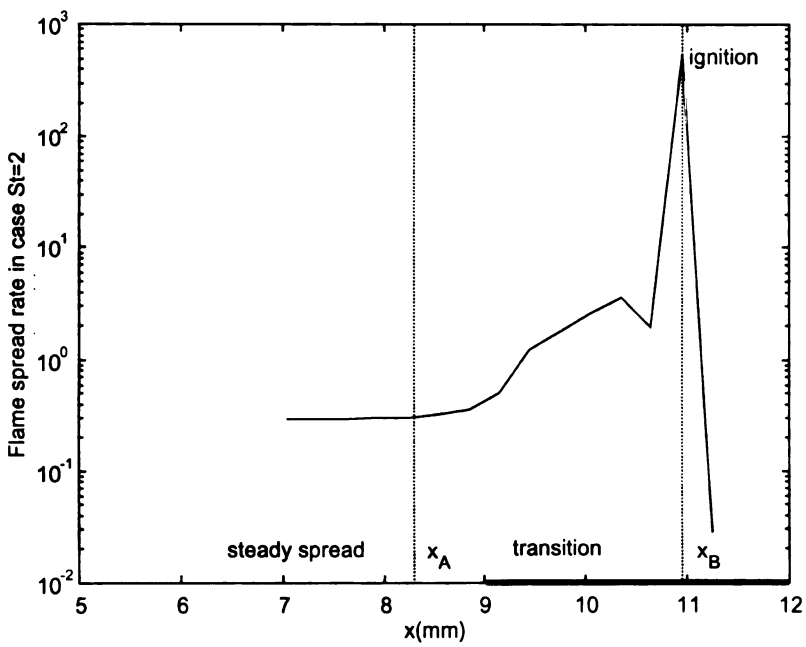

(5-a)


mass or heat flux at the
front arrival time in case St 2

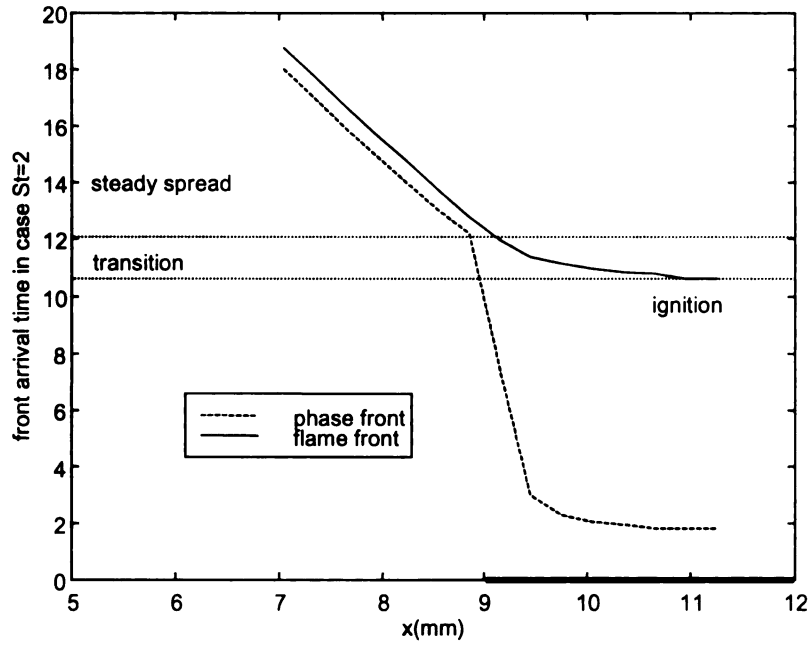
front arrival time in case St=2
steady spread
transition
ignition
phase front
flame front
x(mm)

(5-b)

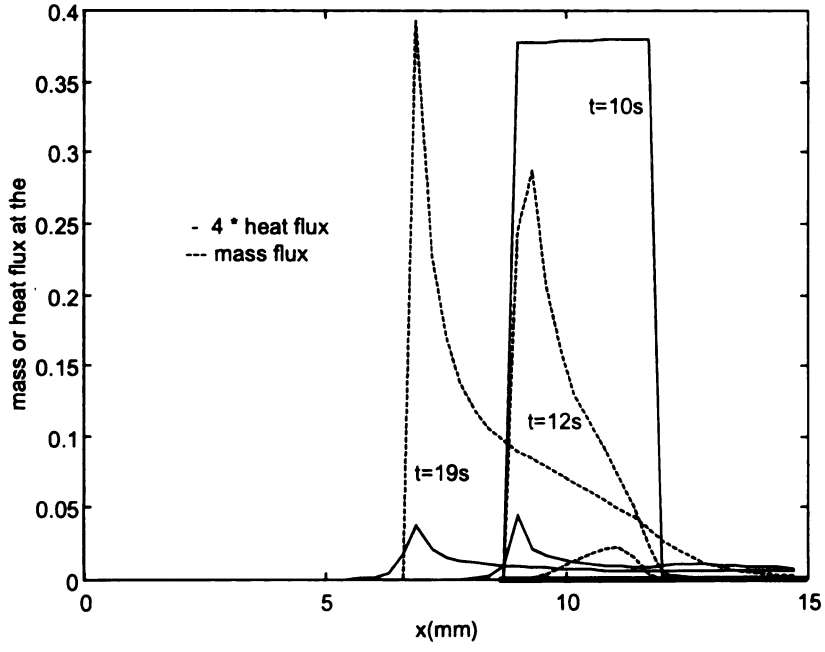
mass or heat flux at the
- 4 * heat flux
--- mass flux
t=10s
t=12s
t=19s
x(mm)

(5-c)

Figure 5 (a) Fla
the left); (b) Ar
streamwise ev
transition (12s)
temperature be

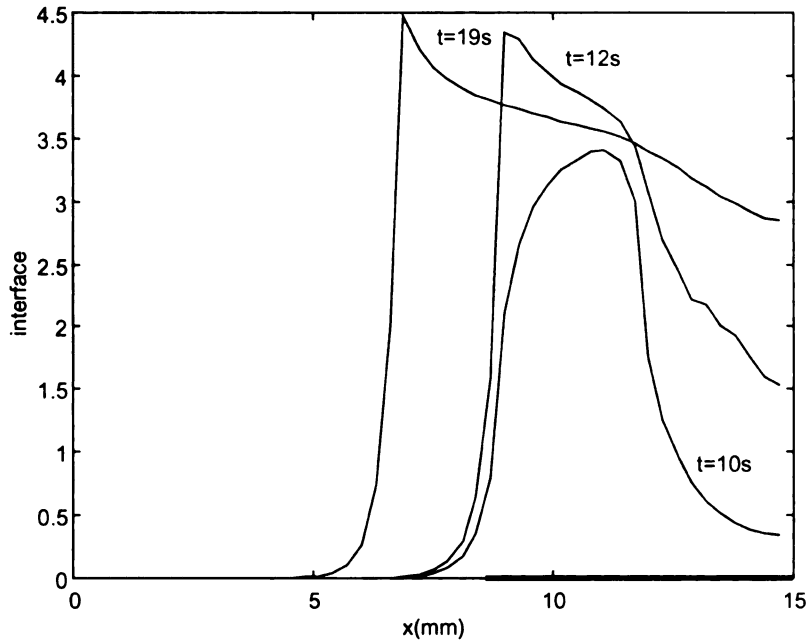

(5-d)

Figure 5 (a) Flame spread rate vs. streamwise distance at $St = 2$ (the front propagates to the left); (b) Arrival times of flame front and phase front vs. streamwise distance; (c) The streamwise evolution of heat and mass flux at the interface before ignition (10s), during transition (12s) and during steady spread (19s); (d) The streamwise evolution of interface temperature before ignition (10s), during transition (12s) and during steady spread (19s).

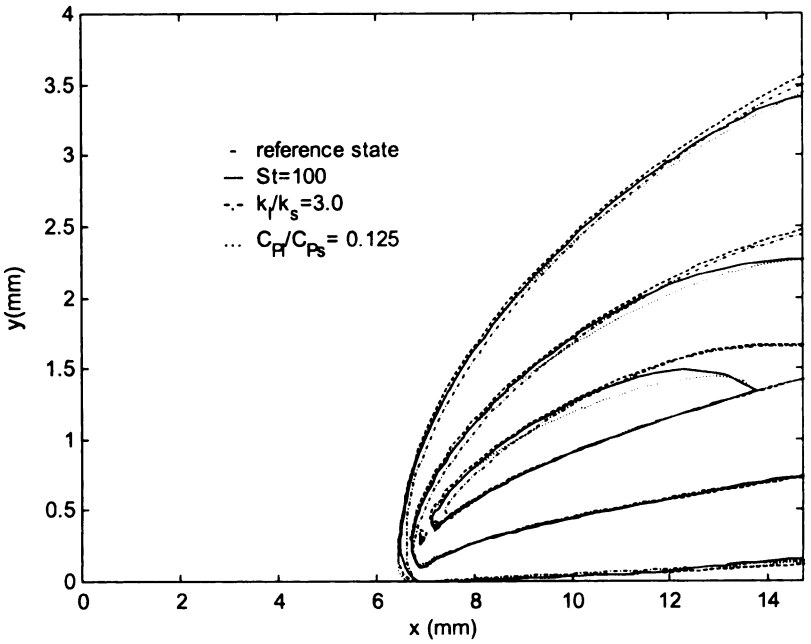
- reference state
— St=100
-.- k_f/k_s=3.0
... C_{Pf}/C_{Ps}= 0.125
y(mm)
x (mm)
0
0.5
1
1.5
2
2.5
3
3.5
4
0
2
4
6
8
10
12
14

(6-a)

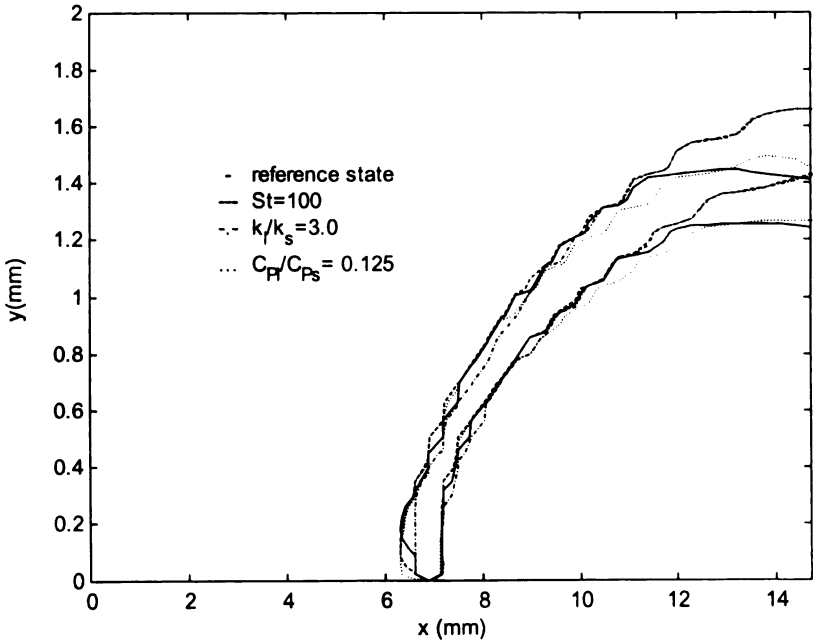
- reference state
— St=100
-.- k_f/k_s=3.0
... C_{Pf}/C_{Ps}= 0.125
y(mm)
x (mm)
0
0.2
0.4
0.6
0.8
1
1.2
1.4
1.6
1.8
2
0
2
4
6
8
10
12
14

(6-b)

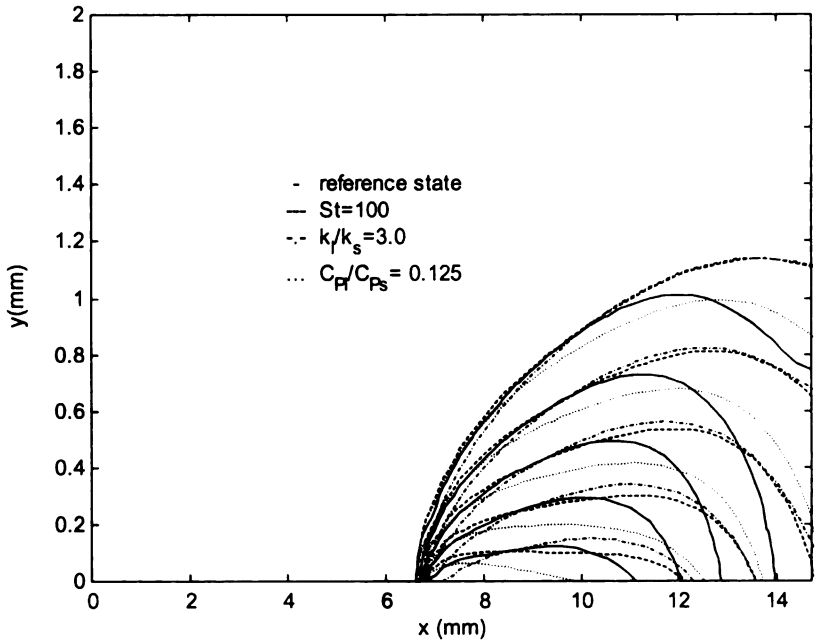
- reference state
— St=100
-.- k_l/k_s=3.0
... C_{Pl}/C_{Ps}= 0.125
y(mm)
x (mm)
0
0.2
0.4
0.6
0.8
1
1.2
1.4
1.6
1.8
2
0
2
4
6
8
10
12
14

(6-c)

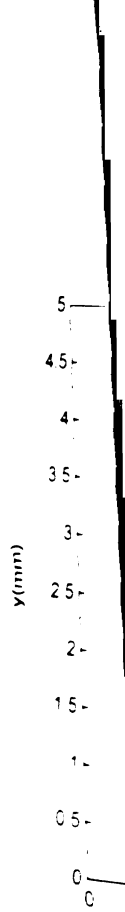

Figure 6 Compar
concentration an
material. The re
increment 2.0 bet
0.2 with increm
characterized by

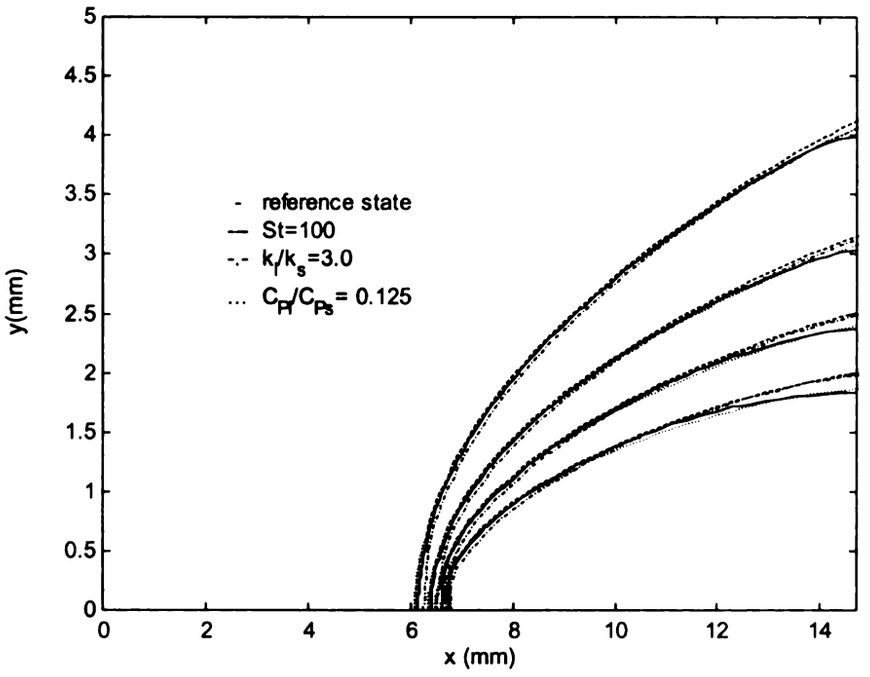

(6-d)

Figure 6 Comparisons of non-dimensional (a) temperature/St, (b) reaction rate, (c) fuel concentration and (d) oxidizer concentration for four conditions of the condensed material. The reference state denotes $St = 2$. The outermost isotherm is 2.0 with increment 2.0 between two adjoining contours; the innermost isoline of oxidizer or fuel is 0.2 with increment 0.2 between two adjoining contours; the reaction profile is characterized by reaction rate 0.0001.

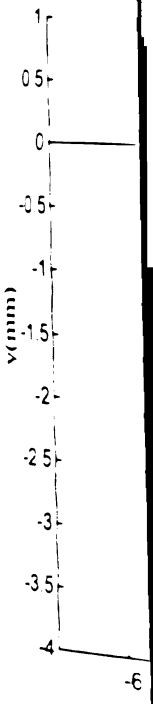

Figure 7 Comparis
profiles and phase
coincides with the
1.0 between two a
straight line of the

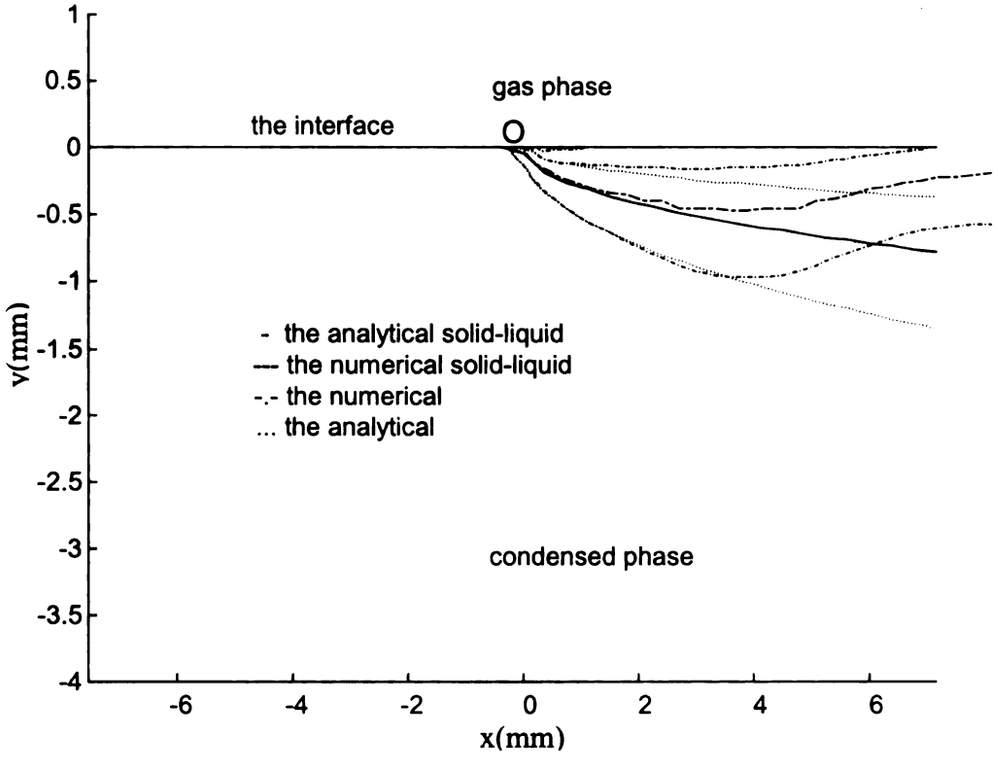

Figure 7 Comparison of numerical model and theory (Appendix II) for the temperature profiles and phase fronts in the condensed phase at $St = 2$. The location of phase change coincides with the constant profile $\overline{T} = St$. The lowest isotherm is 1.0 with increment 1.0 between two adjoining contours. The analytical isotherm of $\overline{T} = 4$ coincides with the straight line of the gas-condensed interface.

25
2
15
y(mm)

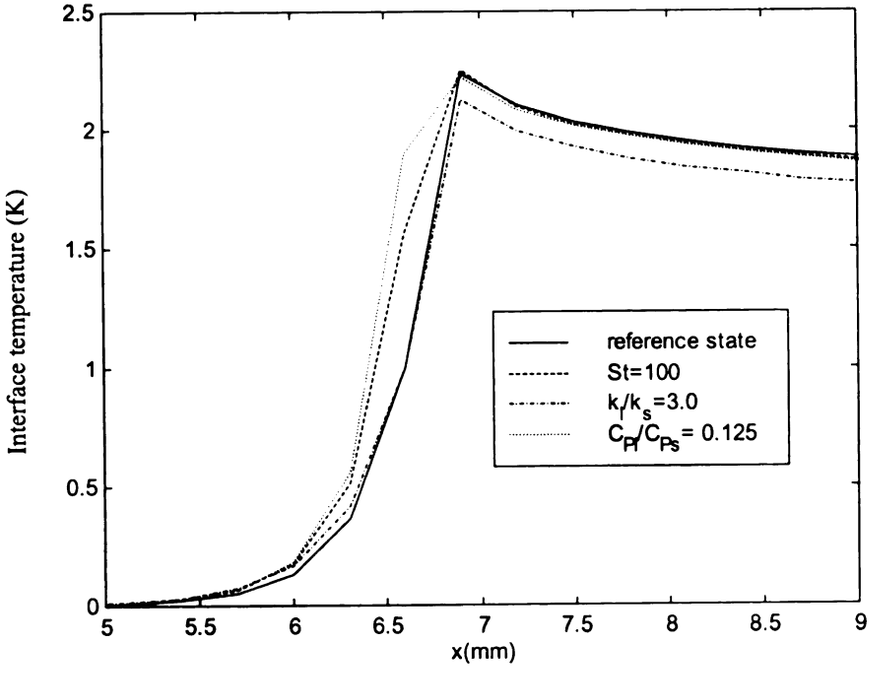
Interface temperature (K)
x(mm)
reference state
St=100
k_f/k_s=3.0
C_{Pf}/C_{Ps}= 0.125

(8-a)

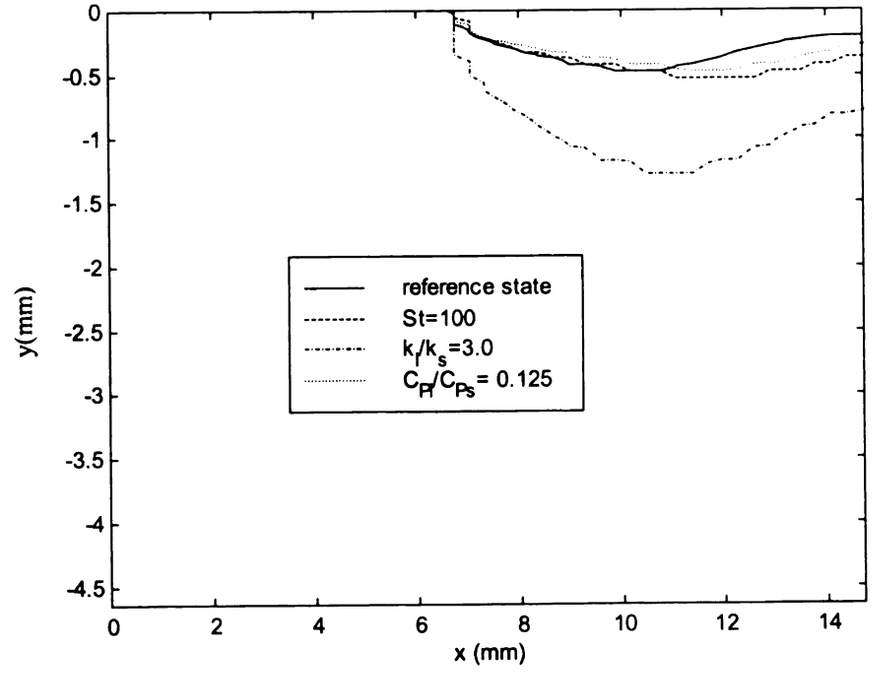
y(mm)
x (mm)
reference state
St=100
k_f/k_s=3.0
C_{Pf}/C_{Ps}= 0.125

(8-b)

Interface mass flux (Kg m^{-2} s)

6 x 10^{-5}

5

4

3

2

1

0

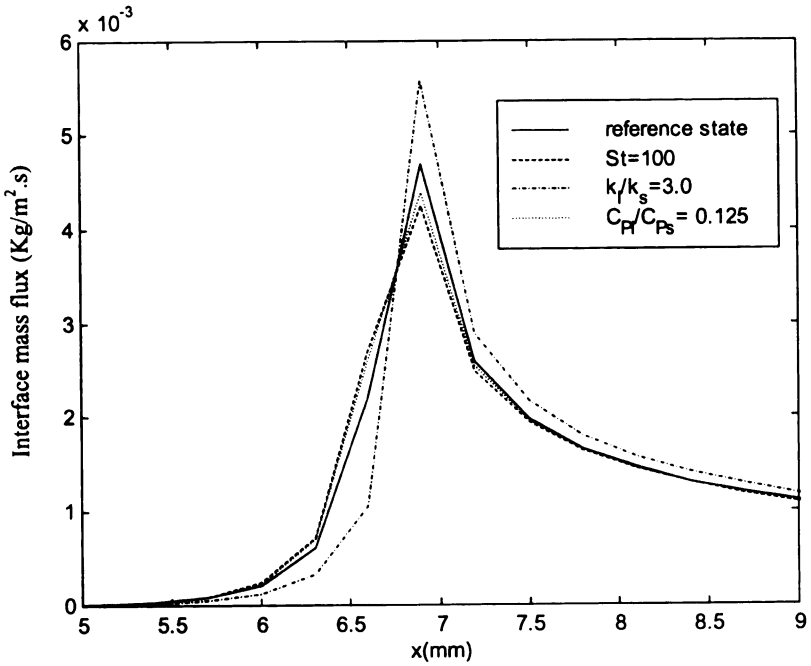
x 10^-3
Interface mass flux (Kg/m^2.s)
x(mm)
reference state
St=100
k_l/k_s=3.0
C_Pl/C_Ps= 0.125

(8-c)

Figure 8 Compa
flux and (d) inte

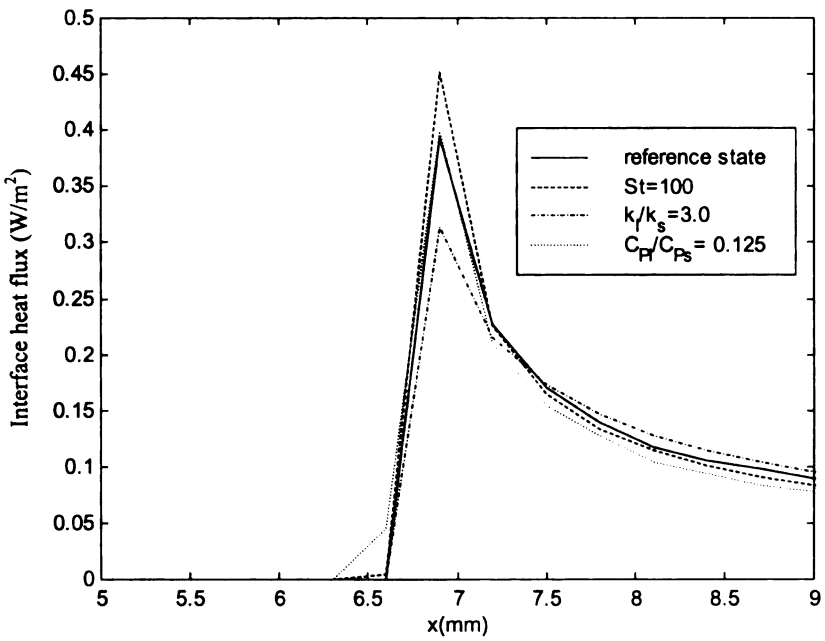

(8-d)

Figure 8 Comparisons of (a) interface temperature, (b) phase location, (c) interface mass flux and (d) interface heat flux in four situations of the condensed phase.

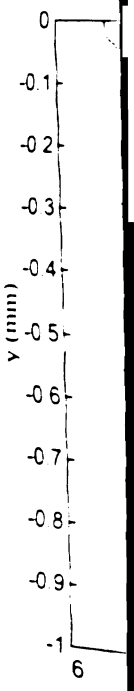

Figure 9 The e
ignition (10s), d
is characterized

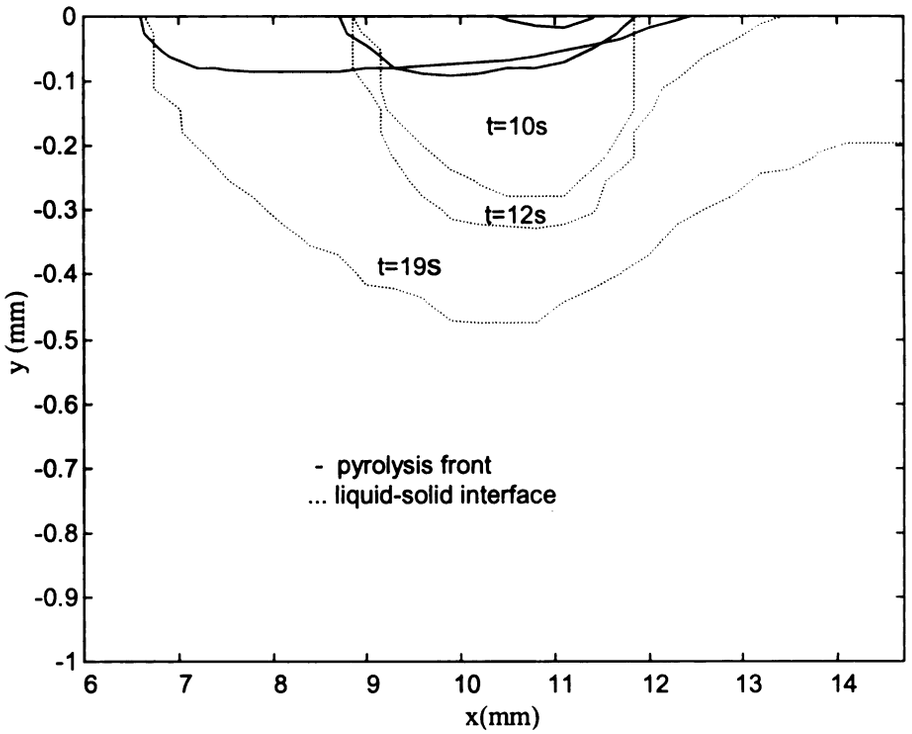

Figure 9 The evolution of solid-liquid interface and pyrolysis front locations before ignition (10s), during transition (12s) and during steady spread (19s). The pyrolysis front is characterized by $\overline{w}_c = 1.5 \times 10^{-7}$ in the numerical model.

Table 1.

$k_s = 0.05$ W (m·K)
$T_m = 500$ K
$K_c = 0.5$
$D = 3.514 \times 10^{-5}$ m² s
$u_\infty = 0.1$ m s

Table 1. Major properties and kinetic data used for the numerical model.

$k_s = 0.05$ W/(m·K)	$C_{ps} = 1460$ J/(kg·K)	$\rho_s = 1190$ kg/m^3	$\rho_l = 1190$ kg/m^3
$T_m = 500$ K	$A_c = 2.82 \times 10^9$ s^{-1}	$E_c = 129580$ J/mol	$q_c = 1113.5$ kJ/kg
$K_e = 0.5$	$k_g = 0.0411$ W/(m·K)	$C_{pg} = 1007$ J/(kg·K)	$\rho_g = 1.16$ kg/m^3
$D = 3.514 \times 10^{-5}$ m^2/s	$A_g = 1.6 \times 10^{15}$ m^3/(kg·s)	$E_g = 155000$ J/mol	$q_g = -15539.4$ kJ/kg
$u_\infty = 0.1$ m/s	$T_\infty = 300$ K	$Y_{O\infty} = 0.31$	$Y_{f\infty} = 0.0$

Ta

Symbol
$\bar{A}_g$
$\bar{q}_g$
$\bar{E}_g$
Le
$\bar{C}_{Pl}$
$\bar{\rho}$
$\bar{v}_n$
$\bar{q}_{ig}$

Table 2. Dimensionless parameters for the numerical model.

Symbol	Parameter group	Symbol	Parameter group
$\overline{A}_g$	$\frac{A_g \rho_g \alpha_s Y_{o\infty}}{u_\infty^2}$	$\overline{A}_c$	$\frac{A_c \alpha_s}{u_\infty^2}$
$\overline{q}_g$	$\frac{q_g Y_{o\infty} C_{Ps}}{\mu_o C_{Pg} L_s}$	$\overline{q}_c$	$\frac{q_c C_{Ps}}{C_{ps} L_s}$
$\overline{E}_g$	$\frac{E_g C_{Ps}}{R L_s}$	$\overline{E}_c$	$\frac{E_c C_{Ps}}{R L_s}$
Le	$\frac{\alpha_g}{D}$	St	$\frac{C_{Ps}(T_m - T_\infty)}{L_s}$
$\overline{C}_{Pl}$	$\frac{C_{Pl}}{C_{Ps}}$	$\overline{\rho}_l$	$\frac{\rho_l}{\rho_s}$
$\overline{\rho}_c$	$\frac{\rho_c}{\rho_g}$	$\overline{k}_l$	$\frac{k_l}{k_s}$
$\overline{v}_{n^*}$	$\frac{v_{n^*}}{u_\infty}$	$\overline{\ell}_{sy}$	$\frac{u_\infty \ell_{sy}}{\alpha_s}$
$\overline{q}_{ig}$	$\frac{\dot{q}_{ig} \alpha_s C_{Ps}}{u_\infty k_s L_s}$	ϖ	$\frac{\varepsilon \sigma \alpha_s L_s^3}{k_s u_\infty C_{Ps}^3}$

Table 3. Differe
serves as the refe

(Heat conduct
– radiation
Streamwise
conde
Heat of p
conde
The
Spread r
The total h

Table 3. Different heat transfer mechanisms in four cases of interest, in which $St = 2$ serves as the reference state.

	$St = 2$	$St = 100$	$\bar{k}_l = 3$	$\bar{C}_{Pl} = 0.12$
(Heat conduction from gas phase – radiation at the interface)	2.497	2.828	1.406	2.231
Streamwise conduction in the condensed phase	3.229	4.279	11.042	1.965
Heat of pyrolysis in the condensed phase	0.0000	0.0000	0.0000	0.0000
The total heat	5.727	7.107	12.448	4.196
Spread rate (10^{-4} m/s)	2.926	3.677	1.316	3.852
The total heat / Spread rate	1.957	1.932	9.458	1.089

MODELING O

S

1. Introduction

Flame spre

combustion con

in much greate

complete mode

energy, species

form. Several n

phase was sim

boundary cond

equation; see t

that could acco

confined to sir

complex phen

desirable to de

realistic phen

model that inc

spread formul

numerical res

terms of flam

CHAPTER 4

MODELING OF FLAME SPREAD OVER MELTING POLYMERS WITH NAVIER STOKES FLOW CALCULATION IN THE GAS PHASE

1. Introduction

Flame spread over polymers has received extensive attention by researchers in the combustion community. In previous research efforts, the gas phase has been investigated in much greater detail compared to the condensed phase. In the gas phase, the most complete model to date consists of the two-dimensional Navier Stokes momentum, energy, species, and continuity equations together with chemical kinetics in simplified form. Several models (see review [4]) have employed such formulations. The condensed phase was simplified in such a manner that early investigations normally used it as a boundary condition. Later it was described by a two-dimensional heat conduction equation; see the review of [1]. Although some other more advanced models appeared that could account for the in-depth reaction, material property change, etc., they are still confined to single-phase heat conduction. Normally they do not consider melting and complex phenomena such as bubble formation and sub-surface liquid flow. It is desirable to develop a condensed phase sub-model in order to essentially describe such realistic phenomena. As one step forward toward this goal, we propose a flame spread model that incorporates condensed phase melting phenomena [55]. In addition, a flame spread formula was examined for melting polymers and very good agreement with the numerical results was obtained. Various new findings on the influence of melting in terms of flame behavior were provided in [55].

The numeri

gas flow across t

situations. The

calculation by s

treatment, thou

may interact wi

behavior by cou

is not clear whe

accurately calcu

goal of this ch

incorporate the

extension of th

numerical mod

phenomena. F

subject of this

2. The Math

A flame s

established in

requires a set

differential fo

fields. A nur

reduce the co

between the

The numerical model in [55], however, employed the Oseen approximation for the gas flow across the condensed field sample, which makes it undesirable for realistic flow situations. The Oseen approximation was proposed originally to eliminate the flow field calculation by simply applying an external velocity profile of much simpler form. This treatment, though convenient for calculation purposes, is very coarse since the gas phase may interact with the condensed phase through the boundary layer, and influence flame behavior by coupling the temperature and species fields. For flame spread with melting, it is not clear whether previous results will still be accurate when the flow field is more accurately calculated. By acknowledging the drawback of the previous flame model, the goal of this chapter is to extend it to a realistic flow situation. The gas phase will incorporate the Navier Stokes momentum and continuity equations as well as the related extension of the interface conditions with flow complications. Therefore the complete numerical model will predict the interaction of the flow characteristics and the melting phenomena. Flame behavior subject to complexities of melting and flow will be the subject of this chapter.

2. The Mathematical Model

A flame spread model including both gas phase flow and condensed phase melting is established in order to describe the flame behavior in a more realistic manner. This requires a set of conservation equations for continuity, momentum, energy and species in differential form. An equation of state is also needed to link the pressure and the density fields. A number of assumptions (A) and restrictions (R) are used to in order to further reduce the complexities and make the formulation more tractable. A distinction is made between the "restriction" (R) [defined as clear and unambiguous limitation of the

analysis, remova

statements conc

physical quantit

loss to the envir

because of the

applied to the p

heat, constant

important (A);

liquid layer form

of the surface t

to highly viscou

are written in a

The flame

the unburned

initial condition

Gas Phase:

Continuity:

Momentum e

$$\frac{\partial \rho_g}{\partial t}$$

Momentum e

analysis, removable by a more detailed analysis] and "assumptions" (A) [defined as statements concerning the functional dependence and order of magnitude of various physical quantities]. They are: (1) Radiation heat transfer only includes surface radiation loss to the environment (R); (2) Viscous dissipation and compressive work are neglected because of the low velocity of induced or external flow (R); (3) The ideal gas law is applied to the pressure-density relationship of the gas phase (R); (4) Constant specific heat, constant binary diffusion coefficients (R); (5) Soret and Dufour effects not important (A); (6) One step global reaction mechanism in the gas phase (R); (7) The liquid layer formed by heating of the solid does not "flow" in the sense that the gradients of the surface tension do not produce circulating motion. This is a limitation of our work to highly viscous melt layers that has been acknowledged previously [55]. The equations are written in an unsteady form.

The flame survives ignition and gradually attains a steady state while approaching the unburned end of polymer material. The complete system of equations along with initial conditions and boundary conditions is:

Gas Phase:

Continuity:

$$\frac{\partial \rho_g}{\partial t} + \frac{\partial \rho_g u}{\partial x} + \frac{\partial \rho_g v}{\partial y} = 0 \tag{1}$$

Momentum equation in x direction:

$$\frac{\partial \rho_g u}{\partial t} + \frac{\partial (\rho_g u^2)}{\partial x} + \frac{\partial (\rho_g uv)}{\partial y} = -\frac{\partial p}{\partial x} + \frac{4}{3}\mu \frac{\partial^2 u}{\partial x^2} + \mu \frac{\partial^2 u}{\partial y^2} + \frac{1}{3}\mu \frac{\partial^2 v}{\partial x \partial y} \tag{2}$$

Momentum equation in y direction:

$$\frac{\partial \rho_g v}{\partial t}$$

Energy equation

$$\frac{\partial \rho_g C_{P,i}}{\partial t}$$

Species equation

$$\frac{\partial \rho_g Y_i}{\partial t} + \frac{\partial \rho_g}{\partial}$$

where $w_g = -$

Condensed Pha

Energy equation

where $w_c = -$

Solid-Liquid In

Gas-Condens

$$\frac{\partial \rho_g v}{\partial t}+\frac{\partial(\rho_g uv)}{\partial x}+\frac{\partial(\rho_g v^2)}{\partial y}=-\frac{\partial p}{\partial y}+\mu\frac{\partial^2 v}{\partial x^2}+\frac{4}{3}\mu\frac{\partial^2 v}{\partial y^2}+\frac{1}{3}\mu\frac{\partial^2 u}{\partial x\partial y} \quad (3)$$

Energy equation:

$$\frac{\partial \rho_g C_{Pg} T}{\partial t}+\frac{\partial(\rho_g C_{Pg} uT)}{\partial x}+\frac{\partial(\rho_g C_{Pg} vT)}{\partial y})=k_g(\frac{\partial^2 T}{\partial x^2}+\frac{\partial^2 T}{\partial y^2})+w_g q_g \quad (4)$$

Species equations of fuel and oxidizer:

$$\frac{\partial \rho_g Y_i}{\partial t}+\frac{\partial \rho_g uY_i}{\partial x}+\frac{\partial(\rho_g vY_i)}{\partial y}=D[\frac{\partial}{\partial x}(\rho_g\frac{\partial Y_i}{\partial x})+\frac{\partial}{\partial y}(\rho_g\frac{\partial Y_i}{\partial y})]+w_g\Xi_i \quad i=f,o. \quad (5)$$

where $w_g=-\rho_g^2 Y_o Y_f A_g e^{-E_g/RT}$ and $\Xi_i=\frac{M_i\nu_i}{M_f\nu_f}$, $i=f,o$.

Condensed Phase

Energy equations:

$$\begin{cases}\rho_s C_{Ps}\dfrac{\partial T}{\partial t}=k_s\nabla^2 T-q_c w_c, & solid\\ \rho_l C_{Pl}\dfrac{\partial T}{\partial t}=k_l\nabla^2 T-q_c w_c, & liquid\end{cases} \quad (6)$$

where $w_c=-\rho_c A_c e^{-E_c/RT}$.

Solid-Liquid Interface

$$\begin{cases}-(k\dfrac{\partial T}{\partial n^*})_s+\rho L_s v_{n^*}=-(k\dfrac{\partial T}{\partial n^*})_l, & phase\ front\\ T_\Sigma=T_m\end{cases} \quad (7)$$

Gas-Condensed Interface

where $\dot{m} = K_e$

Equation of Sta

The initial cond

In addition, at
applied. Initial
from x=9mm
outlined below
flow channel
computation
flow field is
techniques [4
Kirchoff form
term treatmer
for flow calcu

$$\begin{cases} -\rho_g D\dfrac{\partial Y_f}{\partial y}\Big|_{0+} = (1 - Y_f\big|_{0+})\dot{m} \\ -\rho_g D\dfrac{\partial Y_o}{\partial y}\Big|_{0+} = (0 - Y_o\big|_{0+})\dot{m} \\ -k_s\dfrac{\partial T}{\partial y}\Big|_{0-} = -k_g\dfrac{\partial T}{\partial y}\Big|_{0+} + \varepsilon\sigma(T^4 - T_\infty^4) - \dot{q}_{ig} \\ \dot{m} = \rho_g v \\ u = 0 \end{cases} \tag{8}$$

where $\dot{m} = \mathrm{K}_e \int_{\ell_{sy}}^{0} w_c dy$.

Equation of State:

$$p = \rho_g R_u T \tag{9}$$

The initial condition:

$$T = T_\infty,\ Y_f = 0 \text{ and } Y_o = Y_{o\infty}, \tag{10}$$

In addition, at the inlet of the channel, a condition of uniform flow velocity profile is applied. Initially an external radiation heat flux of ($5W/m^2$) is imposed over at the region from x=9mm to x=12mm. The problem is solved by using the numerical methods outlined below. The computational domain is composed of a cartesian-based gas phase flow channel and a condensed phase domain; see Figure 1 in [55]. The overall computation is an iterative alternate direction implicit (ADI) procedure. The gas phase flow field is calculated by using a SIMPLEC-based scheme and under-relaxation techniques [46]. The melting phenomenon is solved by the source update method with Kirchoff formulation for discontinuous thermal conductivity [48]. The combustion source term treatment is implemented by special techniques [47]. Detailed numerical methods for flow calculation is given in Appendix IV.

3. Re

3.1 Ph

Th

case is

The ki

using t

flame b

explos

render

limit ig

In

dimen

repeat

sensib

define

chang

3.2 F

T

chose

interf

form

3. Results

3.1 Physical Properties

The physical properties are listed in Table 1. Note that the magnitude of q_g in this case is significantly larger than the Oseen model [55]; and E_g is significantly smaller. The kinetic data are used for supporting a larger flame which cannot be established by using the kinetic data employed in the Oseen flow case [55]. It is observed again that the flame behavior is sensitive to the combustion kinetics. Too large a value of q_g results in explosive behavior, which makes the computation too costly, and too small a value renders the incipient flame unable to survive after ignition. When q_g is below a certain limit ignition cannot be attained.

In addition, in order to evaluate the influence of material properties, three non-dimensional parameters are derived, they are St, $\overline{C}_{Pl}$ and $\overline{k}_l$ [55]. Their definitions are repeated here. St, which is defined by $C_{Ps}(T_m - T_\infty)/L_s$, represents the ratio of sensible heat and latent heat in the condensed phase. $\overline{C}_{Pl}$ is defined as C_{Pl}/C_{Ps}; $\overline{k}_l$ is defined as k_l/k_s. The variation of the three non-dimensional parameters is attained by changing only L_s, C_{Pl}, and k_l respectively, while keep the other properties fixed.

3.2 Flame Spread Rate

To compare with the analytical formula, a flame temperature value T_f of 1870 K is chosen by taking the largest temperature in the gas phase from the numerical results. The interface temperature T_i of 673 K is chosen from the numerical results. The flame spread formula is presented here [28]. (See also the appendix of [55] for a concise derivation,

and th

The fl

observ

becau

larger

From

analyt

analyt

analyt

be exp

additi

flame

[55].

diffus

3.3. T

In

repres

and st

times,

The fl

and the text of [55] for a derivation using scaling analysis)

$$\frac{u_s}{u_\infty} = \frac{\rho_g C_{Pg} k_g}{\rho_l C_{Pl} k_l} \cdot \left(\frac{T_f - T_i}{T_i - T_m}\right)^2 \cdot erf\left(c\sqrt{\frac{1}{2} \cdot \frac{\alpha_s}{\alpha_l}}\right)^2,$$

The flame spread rate as a function of St, $\bar{k}_l$ or $\overline{C}_{Pl}$ is shown in Figures 1-3. The first observation is that the magnitude of the flame spread rates are larger than those in [55] because new chemical kinetics are employed, the ratio $(T_f - T_i)/(T_i - T_\infty)$ is 3.21, larger than the value 2.58 in the previous work, where $T_i = 673\,\mathrm{K}$ and $T_f = 1730\,\mathrm{K}$. From Figures 1-3, good agreement is observed between the numerical results and the analytical formula. The physical trends follow well the analysis given in [55]. Since the analytical formula provides agreement with the numerical results, the structure of the analytical formula, as well as its restrictions and assumptions upon which it is built, will be explored later. In addition, because of the newly selected E_g and q_g values, and the addition of the influence of the flow field, the range of $\overline{C}_{Pl}$ and $\bar{k}_l$ that could support flame spread is much smaller compared to the computation with the Oseen approximation [55]. The explanation may relate to the transient stability characteristics of a spreading diffusion flame, which is beyond the scope of this chapter.

3.3. Transient Flame Development

In order to study the transient behavior of the flame, $St = 2$ is selected as a representative case. Overall flame development includes preheating, ignition, transition and steady flame spread. Based on the calculated ignition time of 4.76s, four different times, 3s, 5s, 10s and 15s, are chosen to illustrate the history of the flame development. The flame behavior is characterized by the temperature field and the flow field (Figure

4), pres

(Figure

10). Ot

better e

field at

fuel an

Examir

(1) Up

burnin

flow d

observ

expan

interfa

gradie

produ

forme

of ma

some

near

temp

the s

of th

strea

4), pressure field (Figure 5), fuel and oxidizer concentrations (Figure 6), reaction rate (Figure 7), mass flux (Figure 8), heat flux (Figure 9), and surface temperature (Figure 10). Other figures that show snapshots at different times are also obtained in order to better explain some interrelated physical phenomena. These are the pressure and velocity field at 15s (Figure 11), temperature and velocity field at 15s (Figure 12), reaction rate, fuel and oxidizer at 8.5s (Figure 13), and mass and heat flux at 15s (Figure 14). Examination of these figures reveals interesting phenomena, as explained below:

(1) Upstream from the pyrolysis front, the flow of ambient air accelerates toward the burning region. As it approaches the vicinity of the leading edge of the fuel surface, the flow deflects slightly outward and the streamlines are raised from the heated surface, as observed in Figure 4(b and c). This deflection occurs by two mechanisms: (1) the thermal expansion of the gas phase; (2) fuel vapor generated by pyrolysis flow away from the interface. The former is due to density changes resulting from the high temperature gradient near the flame tip or leading edge. The latter is driven by buoyancy forces produced by density stratification near the reaction zone. The outward streamlines are formed by the convergence of the vapor fuel flow and enforced channel flow. The point of maximal deflection, which corresponds to the maximal streamline slope, is observed some distance ahead of location of maximum temperature. The latter maximum occurs near the flame leading edge. This indicates that the *temperature gradient*, not the temperature magnitude, determines the deflection of the streamlines. The deflection of the streamlines becomes less significant downstream of the flame leading edge because of the comparatively lower temperature gradient. With time, it is found that the degree of streamline deflection near the heated interface increases with the development of the

flame.

with t

further

from

surfac

expan

conve

well

predi

Note

over

deve

tends

dow

upstr

the

inter

isoth

one

dom

(2)

and

appl

flame, which is obvious since the corresponding interface temperature becomes higher with time because of the increasing supply of heat from the flame leading edge. This further facilitates the increase of fuel mass flux; thereby deflecting the streamlines further from the interface. In terms of the transport mechanism, the fuel transport from the surface to the reaction region by diffusion and normal convection, as well as the gas expansion due to temperature increase. Oxidizer is transported to the reaction region by convection and diffusion parallel to the interface. The predictions presented here agree well with the velocity pattern in previous experimental observations and numerical predictions [29]. Figure 4 also shows the temperature pattern in the condensed phase. Note that the thickness and parallel extent of the liquid corresponds to the temperature over 500K. It is obvious that the thickness and extent of the liquid grow with the development of the flame. Downstream of the flame front, especially the liquid layer tends to extend far beyond the limit of initial heating region mainly because the downstream flame envelops a much larger area of the condensed phase compared to the upstream. The thickness of the liquid layer attains a maximum somewhere downstream of the leading edge, and then decreases gradually downstream as a result of the decreased interface heat flux, see Figure 9. This difference of the downstream contours of the isotherms between the numerical results and steady state theory (see [1]) is an important one and cannot be ignored when examining flame spread energy influences in finite domains.

(2) The velocity field can be explained by means of the relative pressure field in Figure 5 and Figure 11 because of their functional inter-dependence. Because a channel flow is applied in the gas phase, four stagnation points are identified at the corners of the

channe

pressur

the lor

evolve

produc

the flar

well-de

there i

elevati

from t

reactio

injectio

surface

melting

pattern

terms

pressur

during

and 5(

and be

levels,

maxim

injectio

channel. Pressures at these locations normally exceed those at the interior, forming pressure sources, as seen from Figure 5. Downstream, a pressure gradient develops along the longitudinal direction. The pattern of pressure decreasing downstream ceases to evolve in the vicinity of the flame leading edge, where an elevated pressure region is produced upstream of the pyrolysis front and a low-pressure region is produced behind the flame. The most obvious evidence is a pressure source appearing at the interface for a well-developed flame, as observed in Figures 5 (b, c and d). However, before ignition there is no evidence indicating such a "pressure source". This mechanism of pressure elevation was well explained in [29], which pointed out that the elevated pressure arises from two types of triggering mechanisms. One is upstream heat diffusion from the reaction region that produces the hot gas expansion ahead of the flame. Another is the injection of fuel vapor at the surface that reduces the shear stress and the velocity near the surface ahead of the pyrolysis front. Although the situation here is different (for the melting case), the explanation is still valid since melting does not change qualitatively the patterns of heat diffusion and injection mass flow though quantitatively they do change in terms of energy redistribution. From the time history of the pressure field, the elevated pressure region does not appear before ignition (Figure 5(a)). It then forms and expands during ignition (Figure 5(b)) and retains a well-developed shape afterwards (Figures 5(c) and 5(d)). The pressure gradient in the vicinity of the heated region increases with time and becomes a constant when the flame is stabilized. The "kinks" of the constant pressure levels, as observed in Figure 5(c) and (d), are located in the region corresponding to the maximum temperature gradients, which is seen also in Figure 12. Since the vapor injection effect is not important at the locations of "kinks" because they are distance

away from the interface, it is obvious that these" kinks" are produced by the thermal expansion of gaseous products due to large temperature gradients. Plots of the velocity vectors in Figure 11 and Figure 12 show that the region of elevated pressure near the flame front causes the velocity to deflect in two directions. The first deflection is outward away from the surface, which is easily observed. Another deflection is inward toward the surface and is not easily observed (actually there is only one vector that points inward in Figure 11 and 12). Downstream of the flame front, there is a low pressure region as well as an accelerated velocity region. The expansion of the gas results in a significant acceleration of the longitudinal velocity in this region. The low pressure draws the external oxidizer into the reaction region, though it is not obvious from the figures shown here. There is no re-circulation flow observed in Figure 11, as was previously reported in [31]. It is conjectured that the thick polymer with melting yields a much lower rate of fuel gas production; therefore the resulting adverse pressure against the main flow is too small to support a re-circulating cell. The reproduction of the re-circulation flow has not been previously reported in numerical studies for thermally thick polymers, even for pure solid conduction without liquid-layer formation.

(3) The time histories of fuel (dashed line) and oxidizer (solid line) profiles are presented in Figure 6. Before ignition, gradients of fuel and oxidizer concentrations in the gas phase are insignificant since the vapor generation is too small because of the low interface temperature. Shortly after ignition (5s), as seen in Figure 6(a), well-mixed gases are present near the heated surface. Note that mixing does not take place along the locations in the interface where fuel injection occurs. In fact, the injected fuel vapor pushes the oxidizer longitudinal flow away from the surface. The mixing, which is basically a

diffusion p

Figure 6(b

oxidizer ca

premixed f

Figure 6(b

identified.

is observed

a maximu

of the the

reaction m

a flame sh

with a flar

an "edge-f

flame lead

the interfa

sufficientl

establishm

oxidizer a

This phen

et al. and

different ti

contours c

reaction re

diffusion phenomenon, occurs in a layer between the oxidizer and fuel regions, as seen in Figure 6(b and c). At 10s, when the flame is stabilized, the patterns of the fuel and oxidizer can be categorized into two regions. In the region that lies near the flame front, a premixed flame is observed where the fuel and oxidizer mix ahead of the flame front. In Figure 6(b), a partially premixed region that is occupied by both fuel and oxidizer is identified. In the region that lies downstream of the flame front, a diffusion flame region is observed where the fuel and oxidizer attain contiguous minima and reaction rate attains a maximum. The appearance of an upstream premixed region contradicts the assumption of the theoretical formula of de Ris and others [21], who postulated an infinite rate reaction mechanism at the flame leading edge. The theoretical flame structure resembles a flame sheet that attaches to the interface (also named "attached" flame), as compared with a flame zone with finite thickness that is suspended above the interface (also called an "edge-flame" or a "flame leading edge") in this case, as seen in Figure 6 (b). The flame leading edge results from the finite-rate reaction scheme since the temperature of the interface is sufficiently low; the reaction rate in the vicinity of the interface is sufficiently small, allowing leakage of both oxidizer and fuel through the flame tip. The establishment of a mixing region ahead of the flame front occurs where both fuel and oxidizer are present, because the quench layer allows the fuel and oxidizer to diffuse. This phenomenon was proposed by Ray and Glassman [30], and later confirmed by Mao et al. and others [29]. The reaction rate time history is presented in Figure 7 for three different times. In addition, fuel concentration, oxidizer concentration and reaction rate contours computed from a finer grid system are presented in Figure 13. At 3s, the reaction region is a small envelope covering the preheated area. At 5s, the reaction rate is

strong enough to support itself by supplying heat to the condensed fuel while consuming fuel and oxidizer. Downstream of the flame front the reaction rate decreases by consumption of fuel and oxidizer from upstream, showing an enlarged downstream open-tip. This phenomenon has been investigated by Di Blasi [4], who chose the reaction rate envelope to describe the transient behavior of a flame. The results here are similar to those of Di Blasi. When the flame is stabilized, the downstream reaction envelope fully disappears, and only a half-arc exists representing the upstream reaction envelope. From curves of reaction rates in Figure 7, an open-tip flame is observed, which is characterized by a discernable distance between the flame leading edge and the interface (also called the "stand-off distance" or "quench layer thickness"). This distance, interestingly, is smaller during the preheating period than during ignition and steady flame spread. This, again, explains the influence of the combined effects of fuel vapor injection and thermal expansion. This phenomenon indicates that the quench layer thickness is controlled more by gas phase expansion and normal convection than by the chemical kinetics used in the current research. Note that in the flame model using the Oseen approximation (Figure 8 in [55]), there is no perceptible distance between the flame tip and the interface. This indicates that a higher reaction rate is used in [55], resulting in a closed-tip flame. Figure 13 gives the fuel, oxidizer, and reaction rate profiles in a refined grid system where the x direction grid size is reduced to 0.00015m. The diffusion flame characteristics are confirmed in the reaction region where the fuel and oxidizer become a minimum as the reaction rate goes to a maximum. In the reaction region, the maximal reaction rate is found to be in the upstream part. In Figure 13 (b), the temperature profile and reaction rate profile indicate that the location of the *maximal temperature* in the entire domain is

not th

tempe

interf

tempe

and b

13(b)

the hu

(4) T

level

show

and t

the

gener

deve

regio

energ

flam

preh

decr

of th

repre

time

surro

not the location of the *maximal reaction rate*. The upstream reaction region has a lower temperature and a higher reaction rate mainly due to the higher supply of fuel near the interface pyrolysis front. However, the downstream reaction region has a higher temperature partly because the gas is already preheated by the upstream reaction region and because heat losses there are negligibly small. In addition, it is observed from Figure 13(b) that the maximal temperature in the computational domain is located well beyond the high reaction region along the flame arc.

(4) The time history of the mass flux is presented in Figure 8 for four different time levels. Before ignition (3s), the mass flux is so low that its magnitude is almost zero, as shown by a line close to the interface. After ignition, the mass flux peak increases (at 10s) and then decreases (at 15s). The rise and fall of the mass flux peak can be explained by the influence of the preheating region spanning the region 0.009-0.012m. Fuel generation, which is an in-depth mechanism, requires a heated layer before any developed flame proceeds. In terms of an energy barrier, soon after ignition occurs, the region nearby the preheating region has received substantial heat so that most of its energy barrier is cleared. Therefore when it is subjected soon to an incoming moving flame, the mass flux develops in an accelerating manner until the flame moves out of the preheating region. Once the flame moves to an "unprepared" region, the mass flux decreases since the heat from the flame is the sole heating source for the polymer ahead of the flame. The mass flux gradually increases with time and attains a constant value, as represented at 15s. The interface heat flux history is given in Figure 9 for four different times. Here the heat flux is defined as the net heat flux into the condensed phase by the summation of gas conduction, radiation, and external heat flux (existing during

preheating). At 3s, the heat flux is like a jump function, the magnitude of which is almost eighty percent of the total external heat flux. The other twenty percent is composed of the gas conduction heat loss and radiation heat loss. After ignition, the heat flux peak "rises and falls" too, resembling the behavior of the mass flux. Note that at 5s, the heat flux from the gas phase at the boundaries of the preheating region is negative since the combustion induced heat flux is not high enough to surmount the heat losses. After ignition, the interface heat flux peak is significantly larger (1 or 2 times higher) than before ignition. It is the combustion reaction that produces the sharp gradient of the heat and mass flux near the flame leading edges. The interface temperatures at four different times are presented in Figure 10. It is found that the maximal interface temperature remains nearly constant after ignition. Downstream of the flame front, the surface temperature decreases gradually. This contradicts the assumptions of theoretical models based on the "ideal vaporizing solid" [21], and has been discussed in [1, 55]. An interesting finding is presented in Figure 14 where the heat flux and mass flux are co-plotted. It is observed that the heat flux front is upstream of the mass front. This phenomenon cannot be observed in the flame model calculations that use the Oseen Approximation [55], where the heat flux front and mass flux front occupy the same location, see Figure 8-B in [55]. The finite distance between the two fronts results from gas phase blowing and expansion, which push the fuel vapors upstream ahead of the reaction region. Since the location of the heat flux front corresponds to the flame leading edge, it can be deduced the flame tip is located ahead of the mass flux front producing "flame overhang". This phenomenon is in qualitative agreement with experimental measurements by Chu et. al [56] and was explained by others [1].

(5) Phase Front ar

In the flame mod

located downstre

model. it is obse

of $St = 2$. $St =$

exception where

generalize that t

without influenc

farthest upstrean

of gas expansion

downstream of t

processes such

upstream expan

explained in [55

3.4. Flame Struc

Flame struc

compare the fla

reference state.

is represented b

temperature lev

be used to char

increase of $\bar{k}_l$.

(5) Phase Front and Flame Front

In the flame model that uses the Oseen approximation, we observed that the flame front is located downstream of the phase front. With the real flow effects added into the current model, it is observed that the flame front actually precedes the phase front in three cases of $St = 2$, $St = 100$ and $\overline{C}_{Pl} = 0.5$, as can be seen in Figure 15. There is only one exception where the phase front precedes the flame front, that is, $\bar{k}_l = 2.5$. One can generalize that the flame front is stretched upstream significantly compared to the case without influence of the flow. Even for $\bar{k}_l = 2.5$, because its phase front location is the farthest upstream (because it has the largest thermal conductivity), the stretching effects of gas expansion are so significant that the phase front is located nearly imperceptibly downstream of the phase front. The finding here restates the importance of the gas phase processes such as thermal expansion and injection flow, which contributes to the upstream expansion of the flame front. The qualitative nature of the phase front is explained in [55], and not further explained here.

3.4. Flame Structure

Flame structures for four cases are compared in Figure 16. It is not meaningful to compare the flame structure without a reference state, so the case $St = 2$ serves as our reference state. From the constant temperature constant contours in Figure 16(a), $St = 2$ is represented by solid constant contours. If we take the innermost lines of the flame temperature levels, which correspond to 1500K as given in Figure 16(a), these levels can be used to characterize the vaporizing flame sizes. By comparison, it is found that with increase of $\bar{k}_l$, or with decrease of $\overline{C}_{Pl}$, or increase of St, the flame size increases. The

finding here is c

$\bar{C}_{pl} = 0.5$ and

$\bar{k}_l = 2.5$ has t

conduction due

profiles in the co

almost the same

region. The $\bar{k}_l$ =

resulting in a mu

contour does no

the relatively sm

leading edge. F

(d). The qualit

Actually a bou

contours, whi

consumed, wh

of spatial dim

conclusion of

the constant te

3.5. Energy B

In order

energy balan

changing con

finding here is consistent with the analysis in [55]. The physical explanations are that $\overline{C}_{Pl} = 0.5$ and $St = 100$ have a lower energy barrier than the reference state, while $\bar{k}_l = 2.5$ has the same energy barrier but magnified lateral and transverse heat conduction due to increased thermal conductivity. Figure 16 (b) gives the temperature profiles in the condensed phase. The three cases $St = 2$, $\overline{C}_{Pl} = 0.5$ and $St = 100$ have almost the same distributions of temperature, and therefore the same size of the liquid region. The $\bar{k}_l = 2.5$ case has a liquid layer with a thickness almost proportional to $\bar{k}_l$, resulting in a much thicker liquid layer. Downstream of the flame front, the temperature contour does not resemble that of parabola, instead it shrinks in thickness. This is due to the relatively small heat flux from the flame to the interface compared to that at the flame leading edge. Fuel and oxidizer concentration levels are presented in Figure 16 (c) and (d). The qualitative behavior is consistent with [55], characterizing a diffusion flame. Actually a boundary exists between the constant fuel and oxidizer concentration constant contours, which characterize the region where both species are almost completely consumed, while the reaction rate attains a maximum, see also Figure 13(a). Comparisons of spatial dimensions of fuel and oxidizer regions can lead one to arrive at the same conclusion of the diffusion flame as characterized by the size of the flame provided by the constant temperature contours.

3.5. Energy Balance Analysis During Steady Flame Spread

In order to understand the flame spread mechanism in terms of heat transfer, an energy balance analysis is numerically implemented by choosing a continuously changing control volume with the left boundary fixed at x=0 and right boundary moving

from left to righ

may quantitative

different heat tra

steady state flam

streamwise cond

conduction and

streamwise cond

applied to the c

mechanisms in t

phase, thereby a

layer, and the p

mechanisms tha

the mechanisms

with the except

$St = 100$, $\bar{k}_l$

comparisons b

cases. They are

non-zero arou

slope of the o

control volum

the flame lead

maximal heat

maximal slope

from left to right. In this way, the spatial variance of a typical heat transfer mechanism may quantitatively reveal the influence of combustion and melting. Figure 17 presents different heat transfer mechanisms as a function of the size of the control volume during steady state flame spread. The mechanisms under consideration are: (1) In the gas phase: streamwise conduction and convection and combustion heat; (2) At the interface: gas conduction and condensed phase conduction; (3) In the condensed phase: pyrolysis and streamwise conduction. In addition, an important heat transfer quantity, the total heating applied to the condensed phase, can be obtained by summation of the all heat transfer mechanisms in the condensed phase. It is directly related to the heating of the condensed phase, thereby also to controlling properties such as the thickness of the polymer liquid layer, and the pyrolysis in the condensed phase. In order to make the plots clear, the mechanisms that relate to the condensed phase phenomena are plotted below the abscissa; the mechanisms that relate to the gas phase phenomena are plotted above the abscissa with the exception of gas convection, as seen in Figure 17. Four cases including $St = 2$, $St = 100$, $\bar{k}_l = 2.5$ and $\overline{C}_{Pl} = 0.5$ are presented in Figure 17 in order to make comparisons between these cases. Some general observations are obtained for all four cases. They are: (1) the combustion heat, as represented by a series of bold dots, becomes non-zero around the flame leading edge and increases its magnitude downstream. The slope of the overall combustion heating denotes the rate of the heat addition into the control volume by combustion. The maximum slope is expected to locate itself around the flame leading edge, where the reaction rate is the maximum and corresponds to the maximal heat release. It is observed to be so for one can match the location of the maximal slope to that of the reaction rate. (2) Streamwise gas conduction, as represented

by a series of d

here indicates th

as seen in Figur

(in turn the stre

of the tempera

conduction curv

(3) Gas convect

first non-zero s

with constant slo

volume. the left

contributions for

solely dependen

temperature sin

temperature has

convection ter

significantly ar

its relation to

resembles that

the flame leadi

mirrors the he

explained in (

times larger th

The energy ba

by a series of dash dots, shows a peak downstream of the flame front. The observation here indicates that the streamwise temperature distribution resembles that of the interface, as seen in Figure 10. In fact, upstream of the temperature peak, the temperature gradient (in turn the streamwise heat conduction) shows a positive value. However, downstream of the temperature peak, the gradient shows a negative value. The streamwise gas conduction curve simply states that there exists a temperature peak in the reaction region. (3) Gas convection, as represented by a dashed line below the abscissa, shows that it is first non-zero somewhere before the flame leading edge, and then gradually increases with constant slope downstream of the flame front. Because of the selection of the control volume, the left boundary of the control volume is the incoming air, thus does make contributions for all cases on the convection calculation. Therefore the convection term is solely dependent on the fluid flow out of the right boundary, to be specific, on the temperature since the flow rate is constant. As explored before in Figure 10, the temperature has a peak, downstream of which the temperature tends to be stabilized. The convection term indicates that the heat loss out of the control volume increases significantly around the flame reaction region and then stabilizes downstream, explaining its relation to the temperature field. (4) Interface conduction in the condensed phase resembles that of the combustion heat, with the maximal absolute slope located around the flame leading edge. This is obvious since the gas temperature gradient at the interface mirrors the heating. The mirroring of condensed phase and gas phase conduction is explained in (5) below. In addition, the magnitude of the interface conduction is many times larger than streamwise heat conduction. This was also found to be true in [55]. (5) The energy balance at the interface states that the conduction from the gas phase is equal

to the conductio

loss, which is

conduction). Th

conduction. (6)

condensed phas

downstream of

constant temper

downstream. Th

examines the te

it is an exponen

is negligible, ma

mentioned befor

from sources in

conduction in

conduction, mal

phase. Note tha

boundary of the

flame spread r

upstream, flam

the condensed

spread rate. S

starting point.

experimentall

to the conduction in the condensed phase plus the radiation heat loss. The radiation heat loss, which is not plotted here, is normally very small (approximately 10% of gas conduction). That is why interface gas conduction nearly mirrors condensed phase conduction. (6) The pyrolysis reaction is dependent on the temperature profiles in the condensed phase. From Figure 16, it is observed that there are no noticeable changes downstream of the flame leading edge. This can be explained if we recall from the constant temperature contours in Figure 16 (b), where the liquid thickness shrinks downstream. Though the temperature farther downstream is still negligibly small if one examines the temperature profiles, the pyrolysis reaction is not significant simply because it is an exponential function of the temperature. Below some temperature limit, pyrolysis is negligible, making the total pyrolysis heat in the control volume nearly constant. (7) As mentioned before, the total heat in the control volume is a combination of contributions from sources including condensed interface conduction, pyrolysis, and streamwise heat conduction in the condensed phase. The major contributor is interface-condensed conduction, making it resemble the shape of the interface conduction in the condensed phase. Note that the total heat given here is a function of the position of the right boundary of the control volume. At the leading edge, the total heat can be related to the flame spread rate. In the case that gas phase heating dominates solid phase heating upstream, flame spread theory [1] states that the net heat applied to a control volume in the condensed phase ahead of the flame leading edge can be used to determine the flame spread rate. Some efforts have been carried out in [55], which uses this theory as a starting point. However, it tends to be a difficult theory to apply either numerically or experimentally mainly because of the absence of detailed temperature and heat flux

information nea

the leading edg

maximal interfa

the unsteady co

near the flame l

cost. Therefore

investigated. Th

spread rate mig

patching to the

the physical me

By selecti

$St=100$, $\bar{k}_l$ =

an almost unn

four cases exc

phase is much

The higher the

layer (almost

conductivity. T

streamwise co

same. For the

higher than t

temperature. T

conductivity is

information near flame leading edge. Fundamental questions concerning the definition of the leading edge are of critical importance since it can be defined as the location of the maximal interface heat flux, or the maximal reaction rate. In the current model, we utilize the unsteady configuration, and we do not employ a grid-adapting scheme. A fine grid near the flame leading edge is not employed because of considerations of computational cost. Therefore only the spatial variation of the total heat in the control volume is investigated. The subject of a preheated control volume as the determinant of the flame spread rate might better be investigated with a fine grid. Computationally, adaptive grid patching to the flame region is very promising if accurate quantitative interpretation of the physical mechanisms is sought.

By selecting the reference state as $St = 2$, the heat transfer mechanisms for $St = 100$, $\bar{k}_l = 2.5$, and $\overline{C}_{Pl} = 0.5$ can be compared with the reference state. There is an almost unnoticeable difference among the various heat transfer mechanisms for the four cases except for $\bar{k}_l = 2.5$, where streamwise heat conduction in the condensed phase is much more significant than in the reference state. This is mainly caused by (1) The higher thermal conductivity in the liquid, (2) The enlarged thickness of the liquid layer (almost 2.5 times that of the reference state) as a result of the high thermal conductivity. The former is obvious since a higher conductivity in the liquid increases streamwise conduction heat transfer as long as the temperature distribution is almost the same. For the latter, this enlarged liquid layer occupies a region where temperature is higher than the average temperature, thereby resulting in a higher gradient of temperature. The former is thought to be the major influence since the thermal conductivity is related to heat conduction rather than the temperature field (see Figure

17(b)). For the r

condensed phase

4. Conclusion

A flame spr

in a channel flo

high external ra

a transition stag

the gas phase

injection flow

physical phenor

melting as we

conductivity) ac

Navier Stokes

energy equation

loss but not ir

previous work

examined in

model and t

presented, de

The effect

attention giv

combustion

are interpr

17(b)). For the rest of the three cases, in which $\bar{k}_l$ is unity, streamwise conduction in the condensed phase is not significant.

4. Conclusions

A flame spread model is established which describes transient flame spread behavior in a channel flow over a melting polymer. Ignition is initially established by applying a high external radiation heat flux to the surface. Afterwards the transient flame undergoes a transition stage and then attains a steady state. The physical phenomena considered in the gas phase include channel flow, gas expansion due to high temperature, and gas injection flow from the fuel that is generated from condensed phase pyrolysis. The physical phenomena considered in the condensed phase include heat conduction and melting as well as discontinuous thermal properties (heat capacity and thermal conductivity) across the phase boundary. The numerical computation involves solution of Navier Stokes momentum, species, energy, and continuity equations in the gas phase; energy equations for the melting condensed phase; and an interface capable of radiation loss but not in-depth radiation absorption. This work is an important extension to the previous work that employed the Oseen approximation [55]. A flame spread formula is examined in the new situation and good agreement is obtained between the numerical model and the flame spread formula. The transient flame development history is presented, described in terms of three stages: ignition, transition, and steady flame spread. The effect of the gas phase on the flame spread behavior is explored with specific attention given to the injection flow from the interface and gas expansion due to the high combustion temperature gradient. Parameters such as pressure, velocity, and streamlines are interpreted in terms of their coupling to the temperature, species field and interface

conditions. Flan

compared to a r

balance analysis

to understand

discussed as to

heat conduction

interface conde

theory [55]. Th

and the model

between phase

and the quenc

Oseen model

formulation is

ahead of the

These discre

interface inj

melting in

influences.

conditions. Flame structures in three cases $St = 100$, $\overline{C}_{pl} = 0.5$ and $\overline{k}_l = 2.5$ are compared to a reference state $St = 2$ with $\overline{C}_{Pl} = 1$ and $\overline{k}_l = 1$. In addition, an energy balance analysis of a spatially-varying control volume is applied to the four cases in order to understand the flame spread mechanism. Different heat transfer mechanisms are discussed as to their respective contributions to flame spread. It is found that streamwise heat conduction in the condensed phase has a very small magnitude compared to the interface condensed-phase heat conduction. This result is in agreement with previous theory [55]. The comparison between the model with the Navier Stokes flow calculation and the model with the Oseen approximation is made with respect to the relationship between phase and flame front, the relationship between heat flux and mass flux front, and the quench layer thickness. It is found that quench layer thickness is smaller in the Oseen model than in the Flow model, mainly because a much stronger reaction rate formulation is used in the former. In addition, it is found that the flame front is located ahead of the phase front, and the heat flux front is located ahead of the mass flux front. These discrepancies can be explained in terms of gas phase thermal expansion and interface injection flow. Analysis was also carried out on the influences of gas flow and melting in order to understand the flame spread mechanisms associated with their influences.

0.5
0.45
0.4
0.35
0.3
0.25
0.2
0.15
0.1
Flame Spread Rate (mm/s)
10
0.5
0.45
0.4
0.35
0.2
Flame Spread Rate (mm/s)

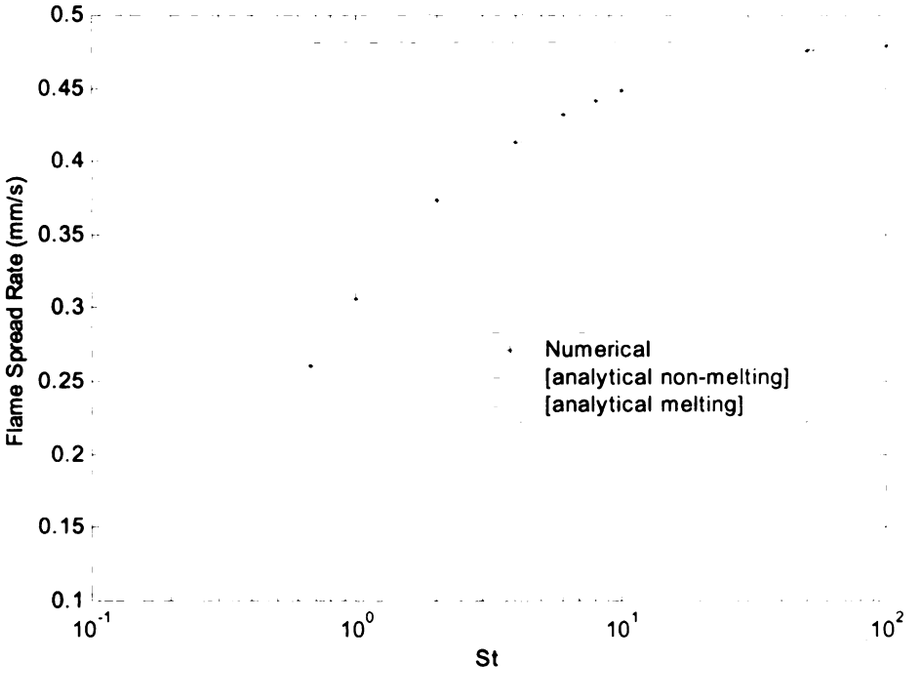

Figure 1 Flame spread rate vs. St

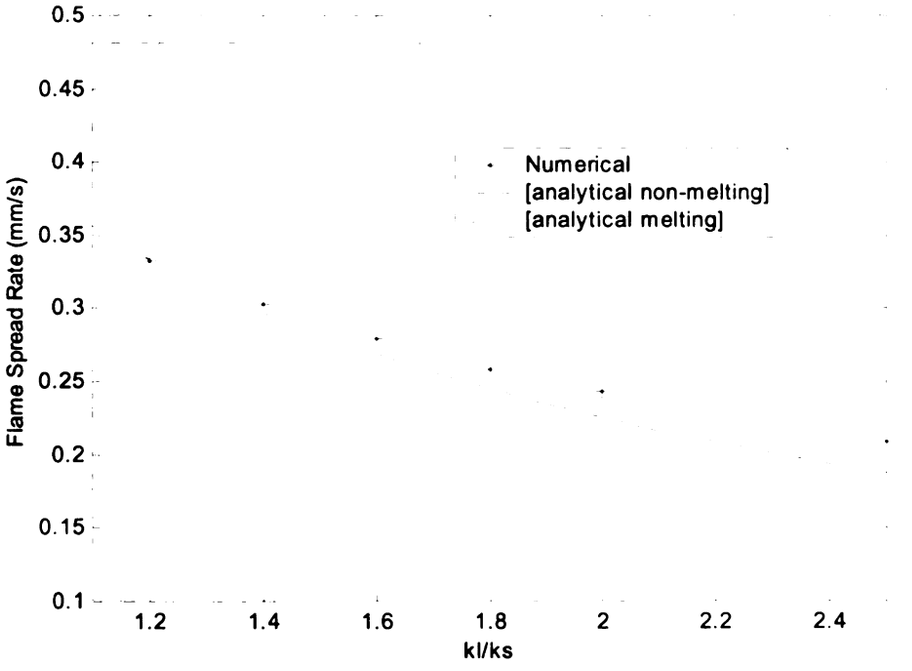

Figure 2 Flame spread rate vs. $\bar{k}_l$

Flame Spread Rate (mm/s)

0.5
0.45
0.4
0.35
0.3
0.25
0.2
0.15
0.1

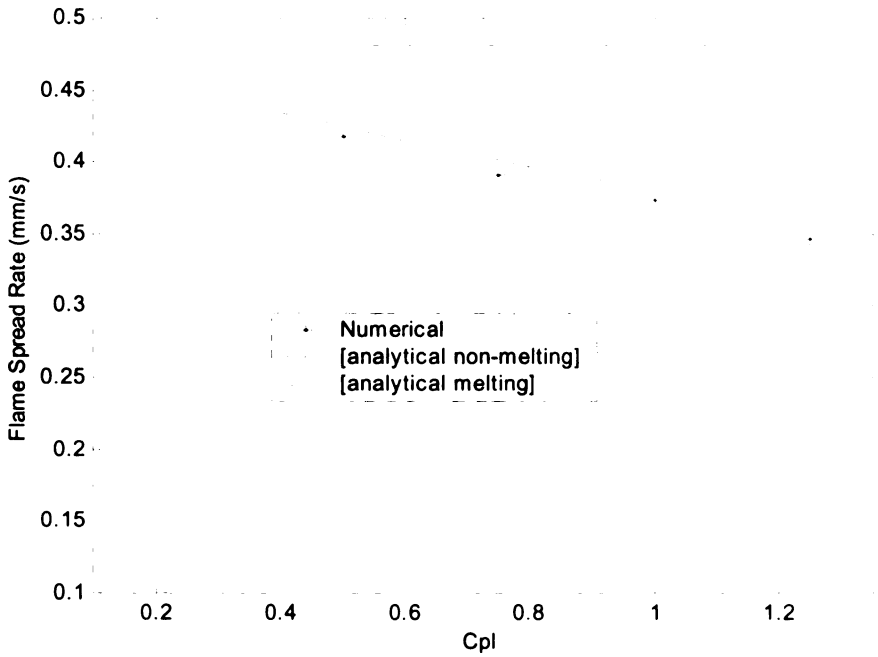

Figure 3 Flame spread rate vs. $\overline{C}_{Pl}$

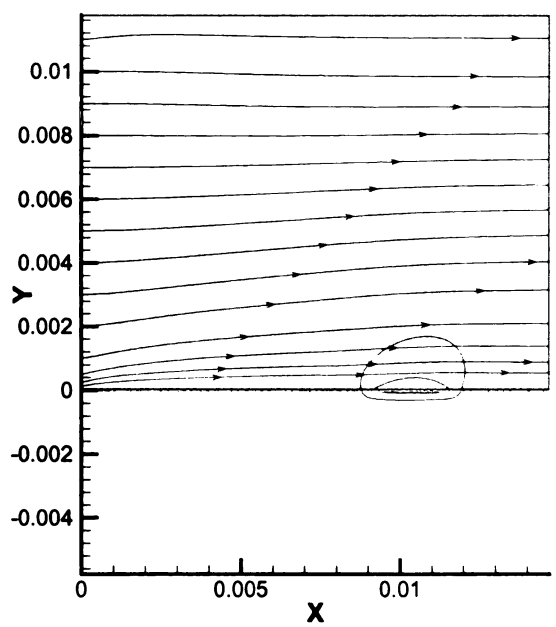

(4-a)

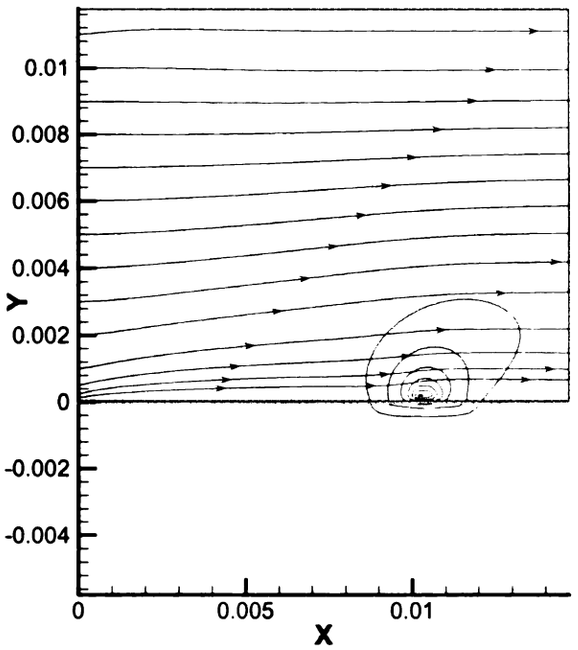
0.01
0.008
0.006
0.004
Y
0.002
0
-0.002
-0.004
0
0.005
0.01
X

(4-b)

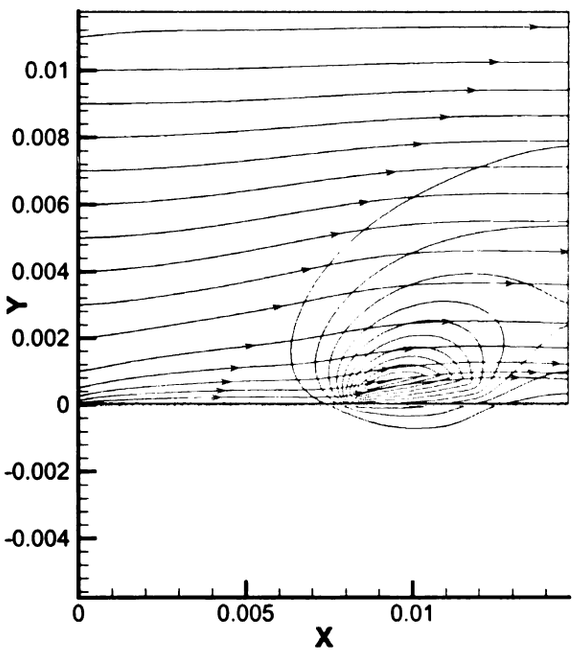
0.01
0.008
0.006
0.004
Y
0.002
0
-0.002
-0.004
0
0.005
0.01
X

(4-c)

Figure 4 Cons
streamlines at
have units of (

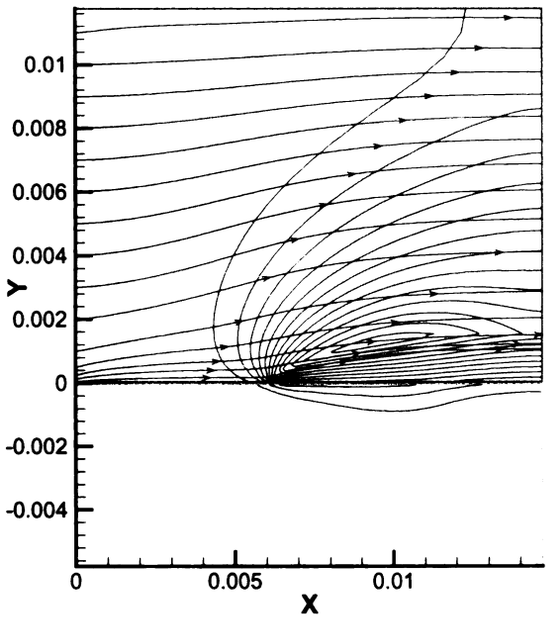

(4-d)

Figure 4 Constant temperature levels (starting from 400 K with step 100 K) and flow streamlines at (a) $t = 3s$, (b) $t = 5s$, (c) $t = 10s$ and (d) $t = 15s$. The coordinate X and Y have units of (m). Note that temperatures are evaluated in both gas and condensed phases.

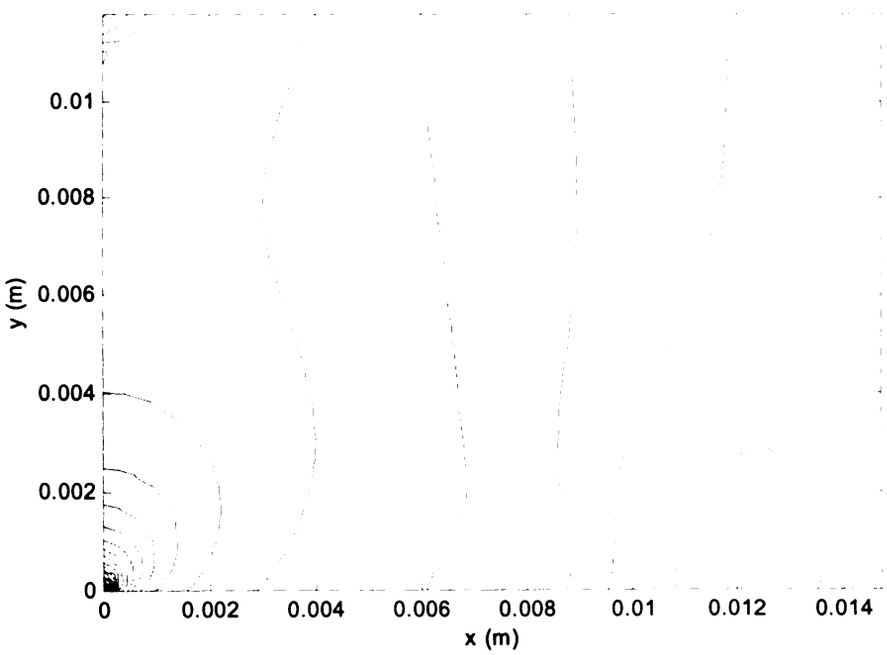

(5-a)

0.01
0.008
y (m) 0.006
0.004
0.002
0
0.01
0.008
y (m) 0.006
0.00
0.00

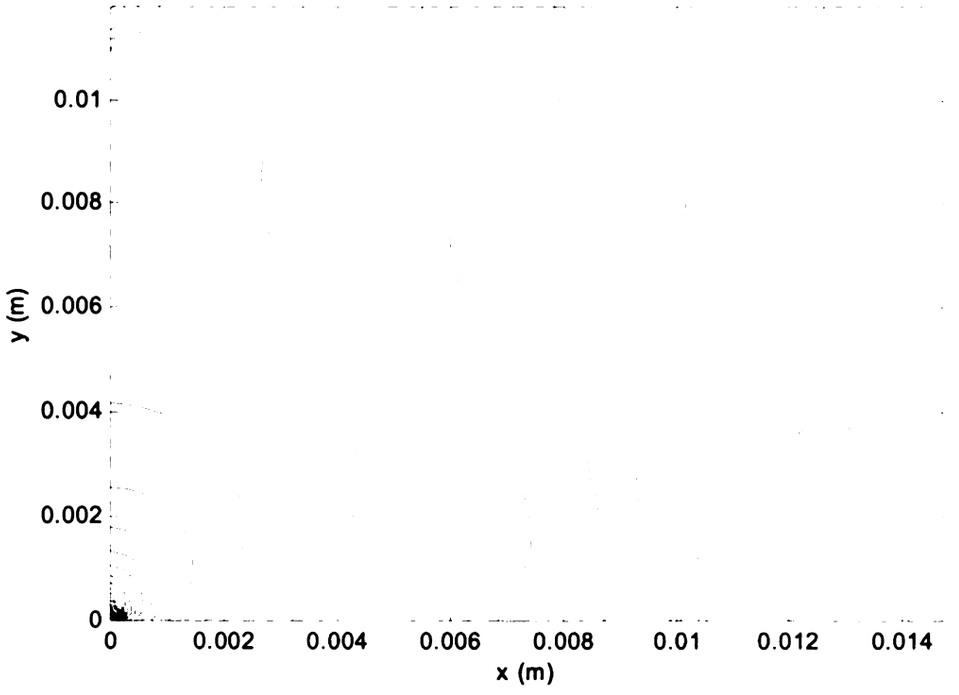
0.01
0.008
0.006
0.004
0.002
0
y (m)
0
0.002
0.004
0.006
0.008
0.01
0.012
0.014
x (m)

(5-b)

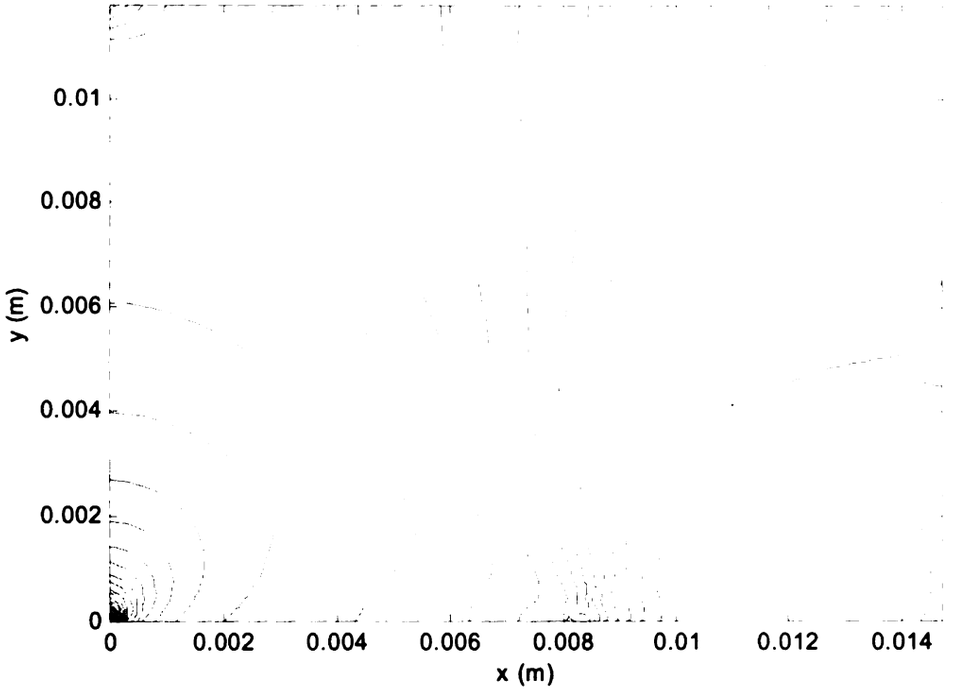
0.01
0.008
0.006
0.004
0.002
0
y (m)
0
0.002
0.004
0.006
0.008
0.01
0.012
0.014
x (m)

(5-c)

Figure 5 Press
contour level is
stagnation poir

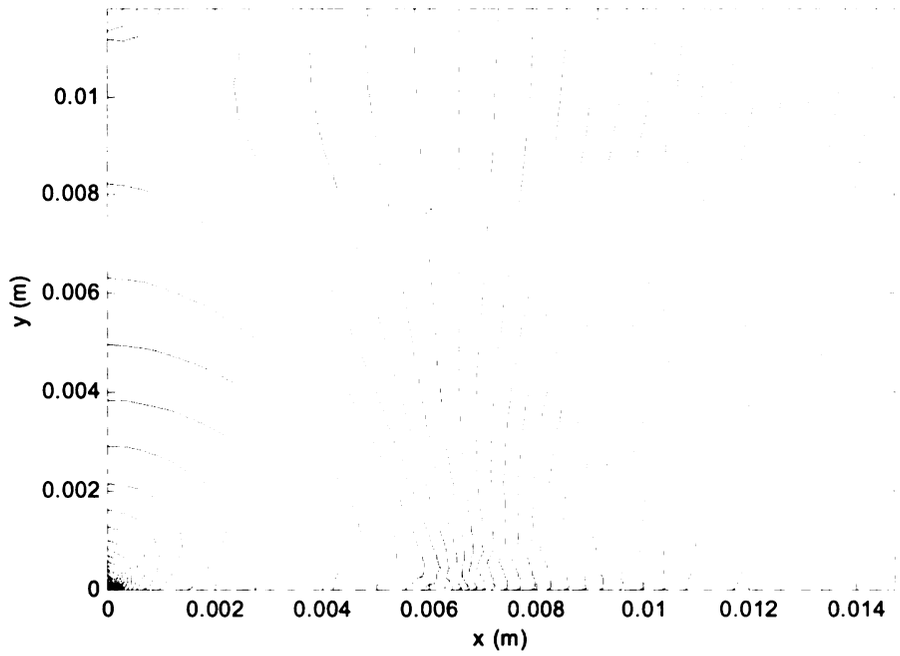

(5-d)

Figure 5 Pressure distributions at (a) 3s, (b) 5s, (c) 10s, and (d) 15s. The rightmost contour level is 0.001 with increase of step of 0.001 from right to left. The corners are the stagnation points with elevated pressures.

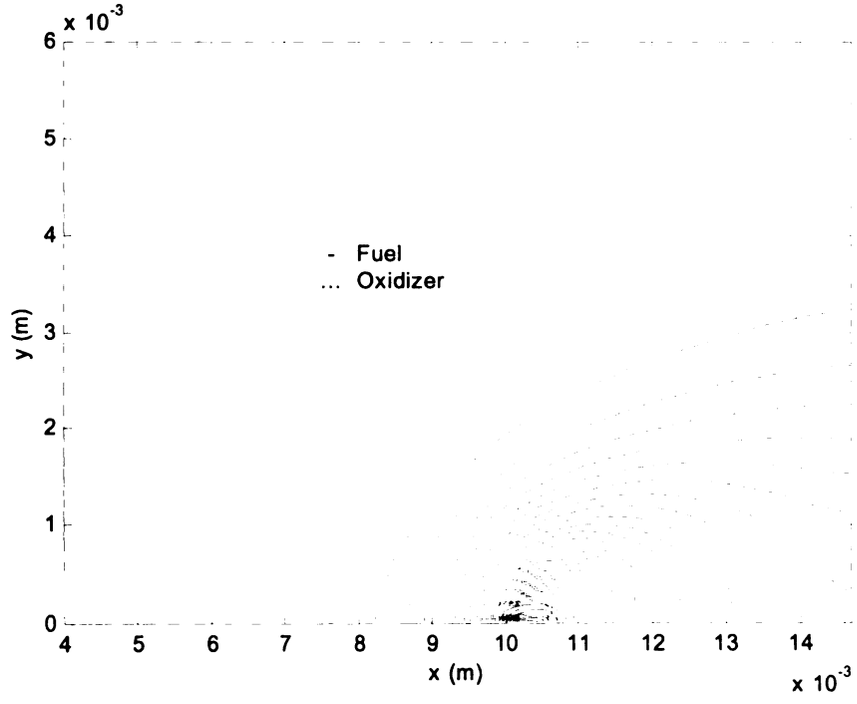

(6-a)

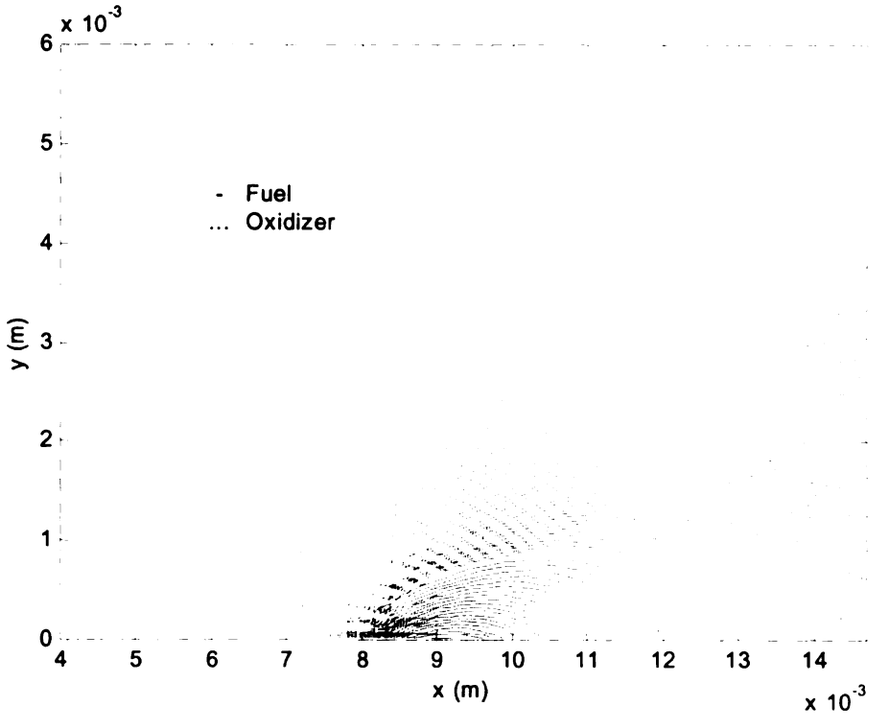

(6-b)

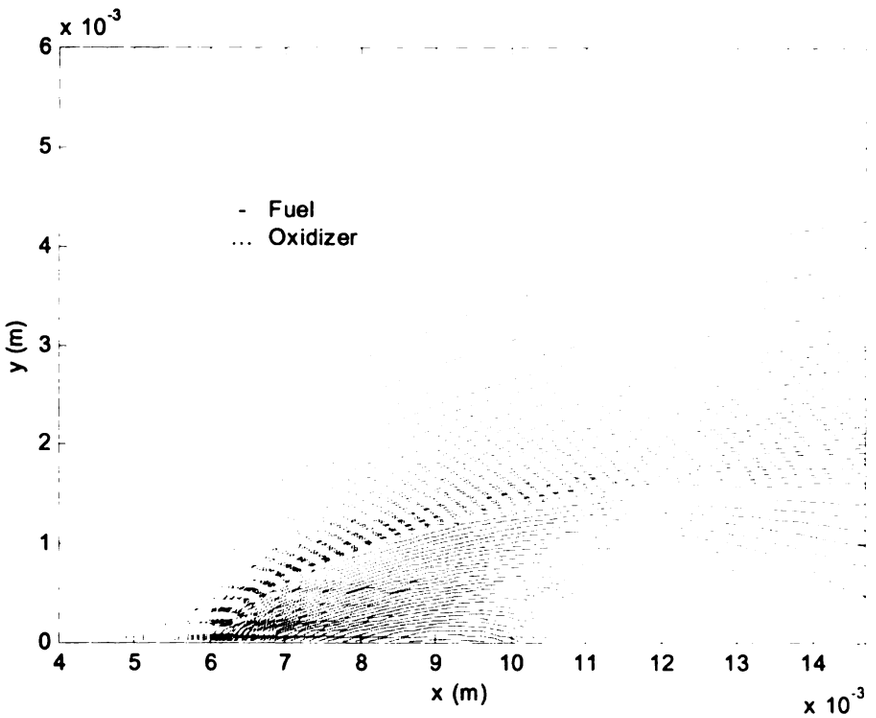

(6-c)

Figure 6 Constant fuel and oxidizer concentration levels for $St = 2$ at 5s (a) and 10s (b) and 15s (c). Solid lines start from outermost 0.01 with step of 0.01, dotted line start from outermost line of 0.30 with step of -0.01. A small partial premixing region exists near the flame leading edge but otherwise the reactants are essentially separate.

x
2
1.5
1
0.5
0
-0.5
-1
-1.5
-2
y (m)
0
x
2
1.5
1
0.5
0
-0.5
-1
-1.5
-2
y (m)

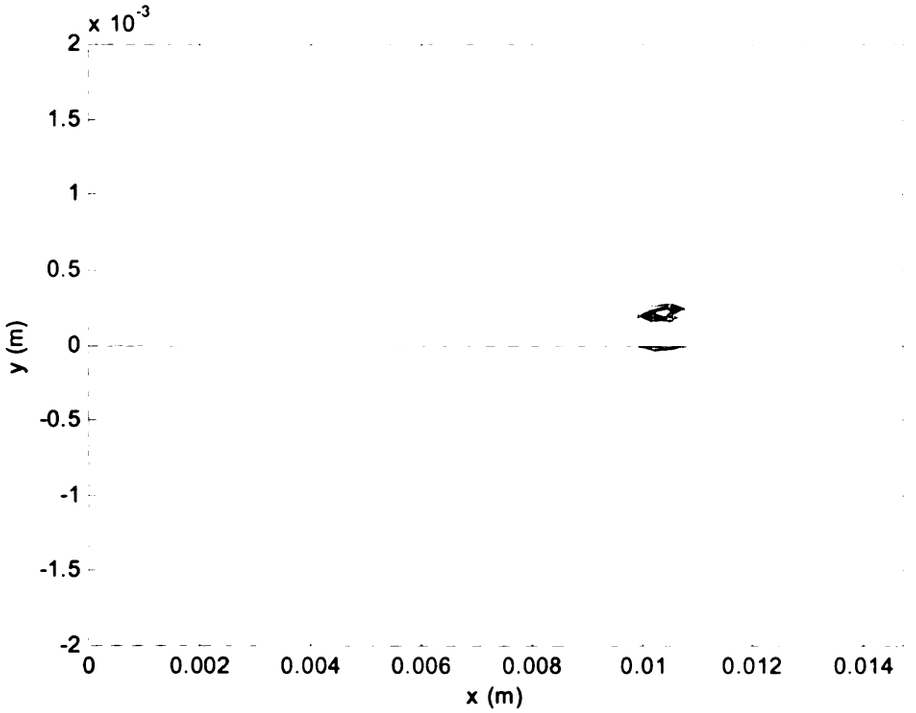
x 10^-3
2
1.5
1
0.5
0
-0.5
-1
-1.5
-2
y (m)
0
0.002
0.004
0.006
0.008
0.01
0.012
0.014
x (m)

(7-a)

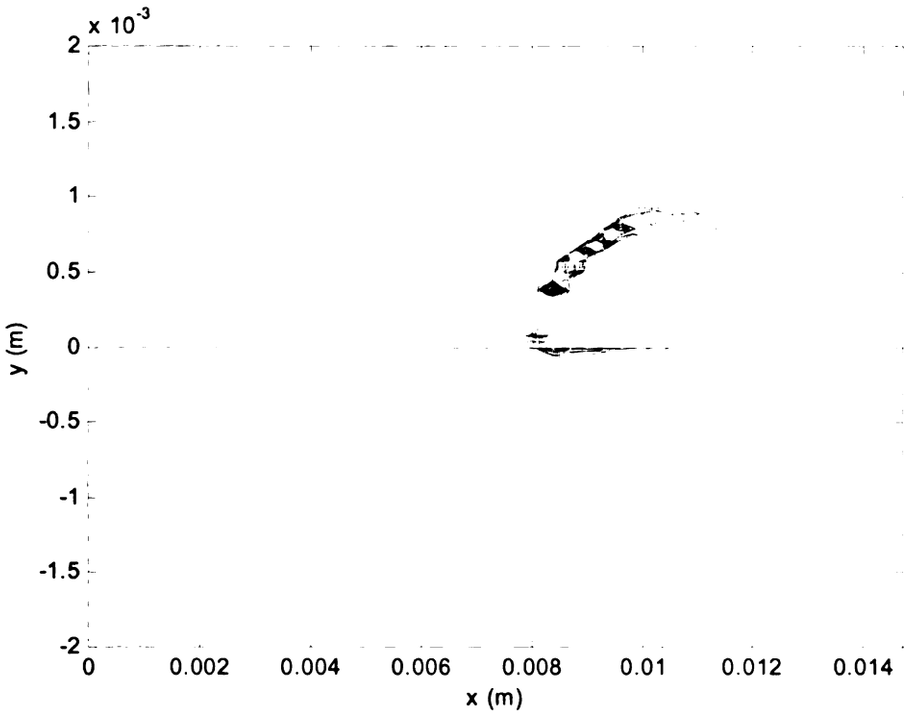
x 10^-3
2
1.5
1
0.5
0
-0.5
-1
-1.5
-2
y (m)
0
0.002
0.004
0.006
0.008
0.01
0.012
0.014
x (m)

(7-b)

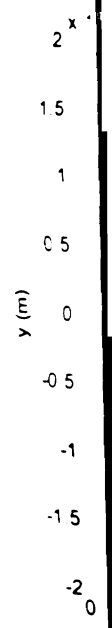

Figure 7 Combu
(b) and 15s (c
reaction rate co

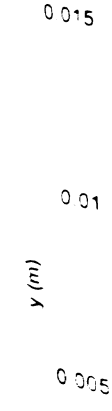

Figure 8 Ma
the evolution

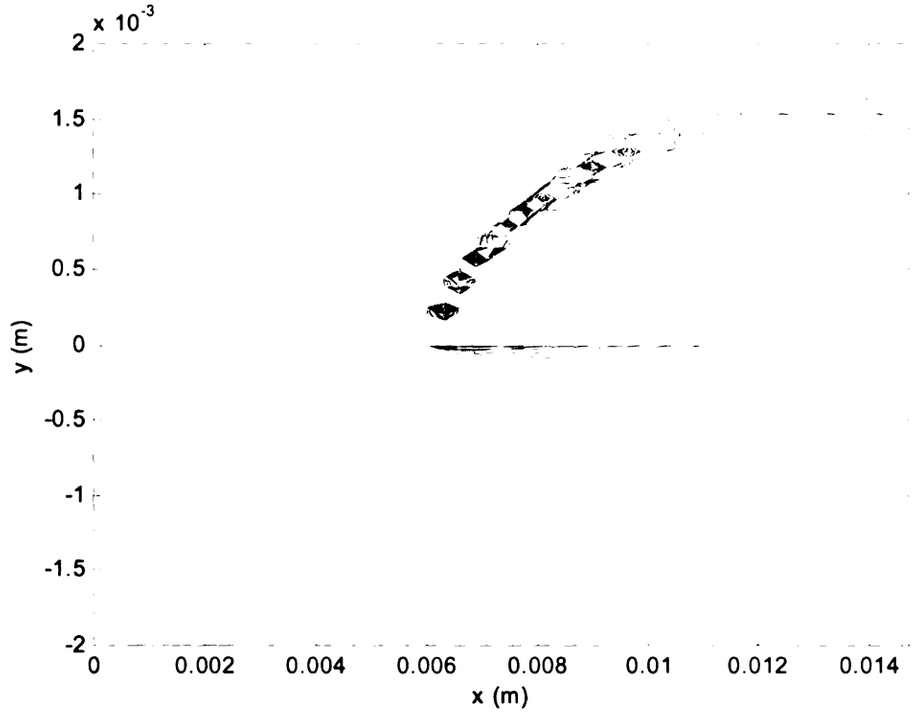

(7-c)

Figure 7 Combustion reaction and pyrolysis reaction constant levels for $St = 2$ at 5s, 10s (b) and 15s (c). Constant lines start from 25 with step 25. The discontinuity in the reaction rate contours come from the insufficiently fine grid near the flame front.

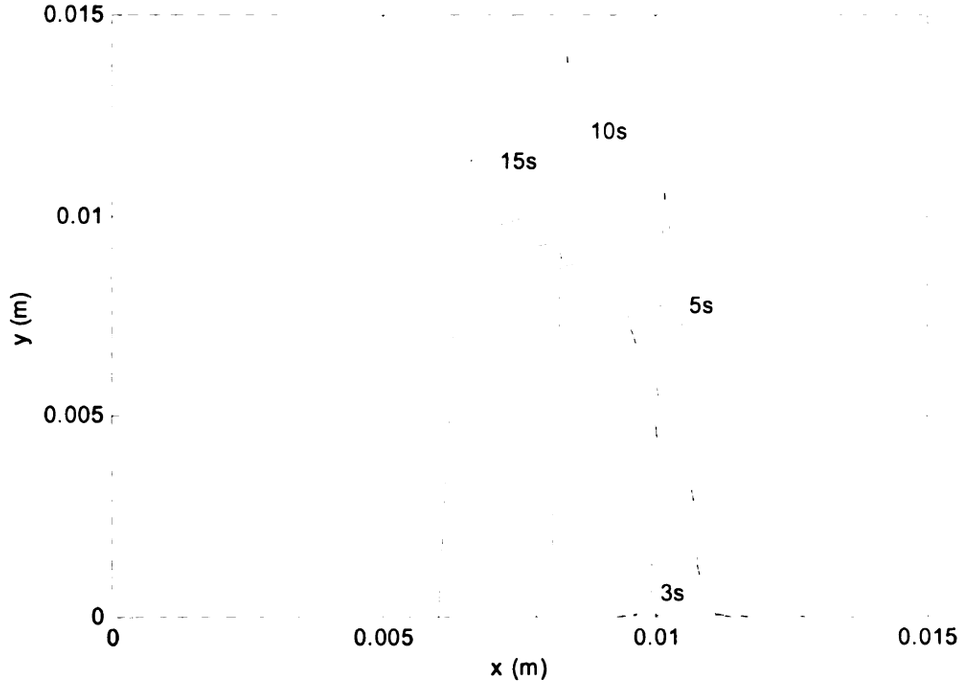

Figure 8 Mass flux along the interface at four different time (3s, 5s, 10s, 15s), showing the evolution from ignition to steady spread.

Figure 9 Net he
5s, 10s, 15s).

Figure 10 Su
consistency
constant wit

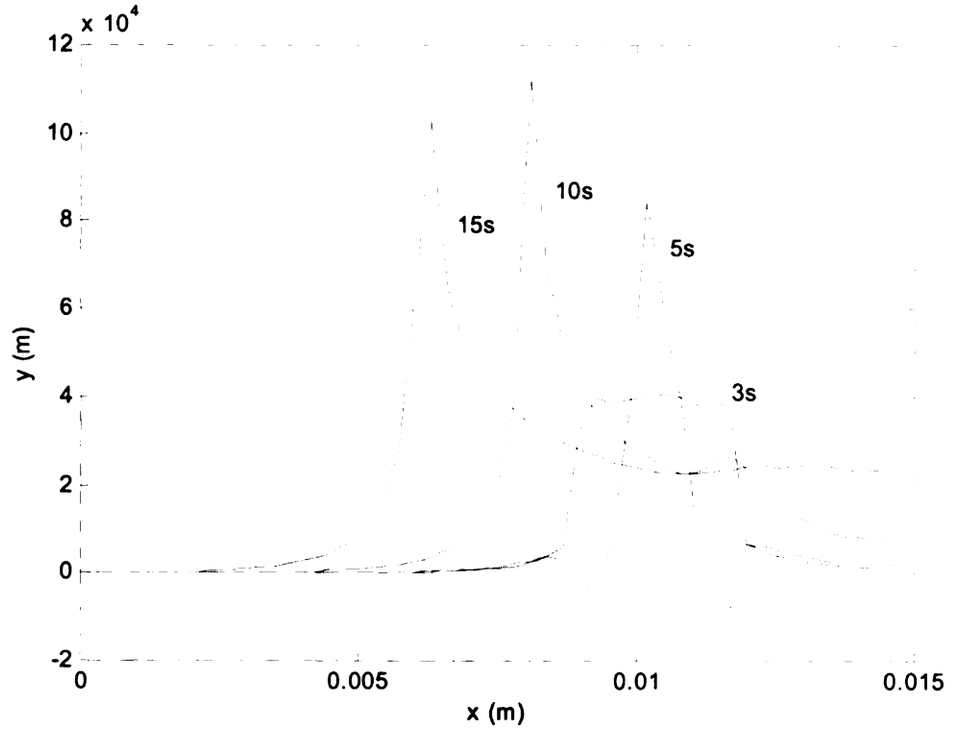

Figure 9 Net heat fluxes from the gas phase along the interface at four different time (3s, 5s, 10s, 15s).

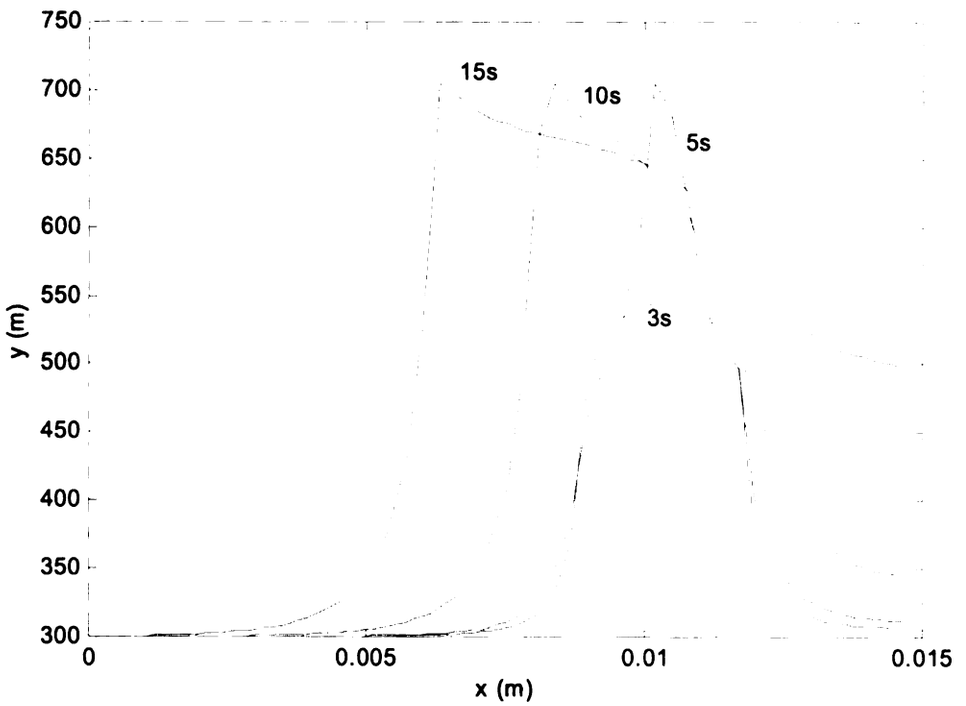

Figure 10 Surface temperatures at four different times (3s, 5s, 10s, 15s). Note the non-consistency of the surface temperature behind the spreading flame front at 15s, and the constant with the "ideal vaporizing solid" of [55].

0.011
0.01
0.009
0.008
0.007
0.006
0.005
0.004
0.003
0.002
0.001

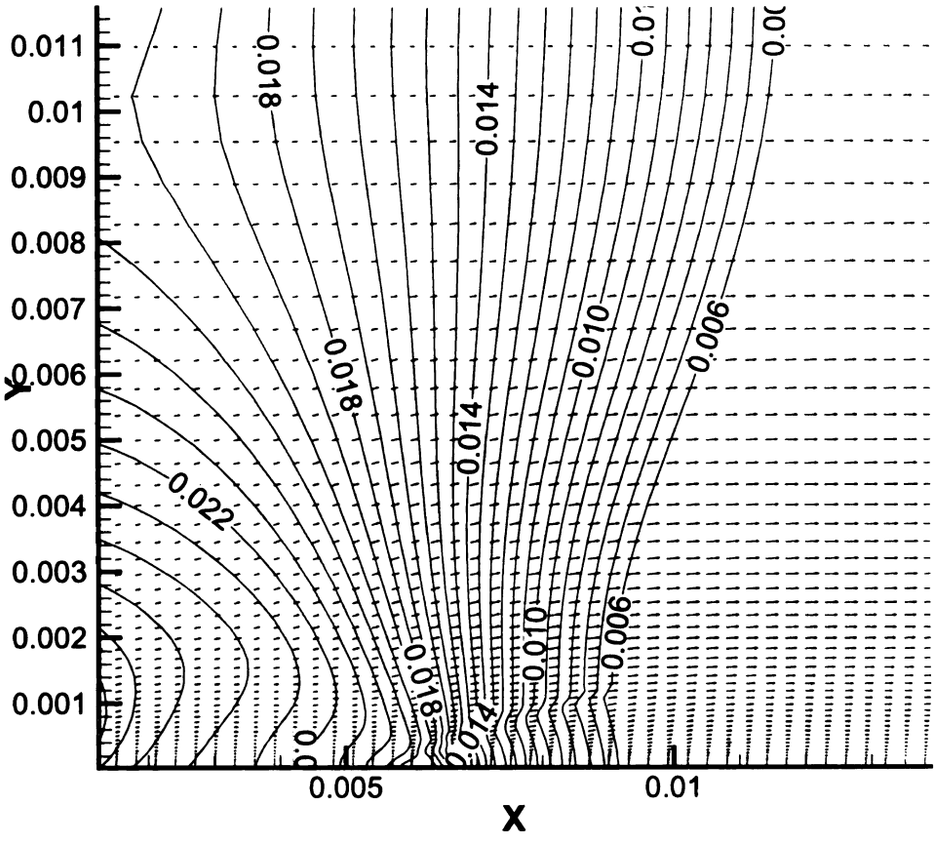

Figure 11 Pressure and velocity fields at 15s.

Figure 12 Te
acceleration

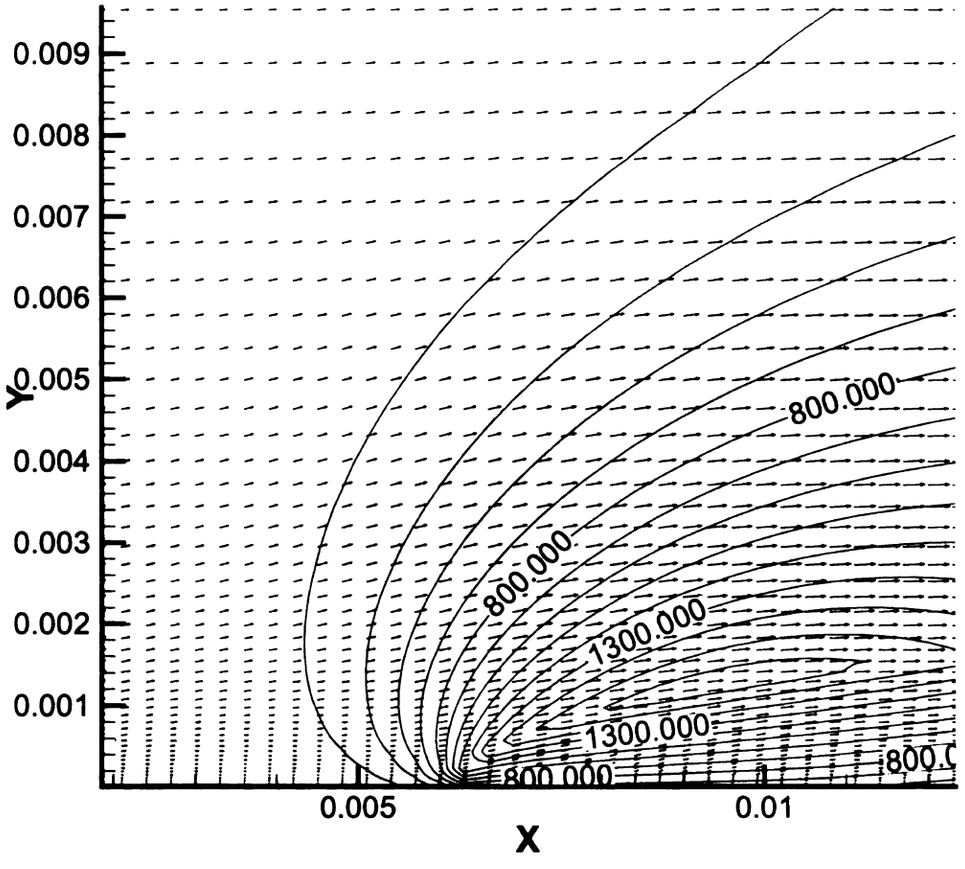

Figure 12 Temperature and velocity fields at 15s. Thermal expansion and associated flow acceleration occur near the flame locus.

Figure 13(a).
refined grid s

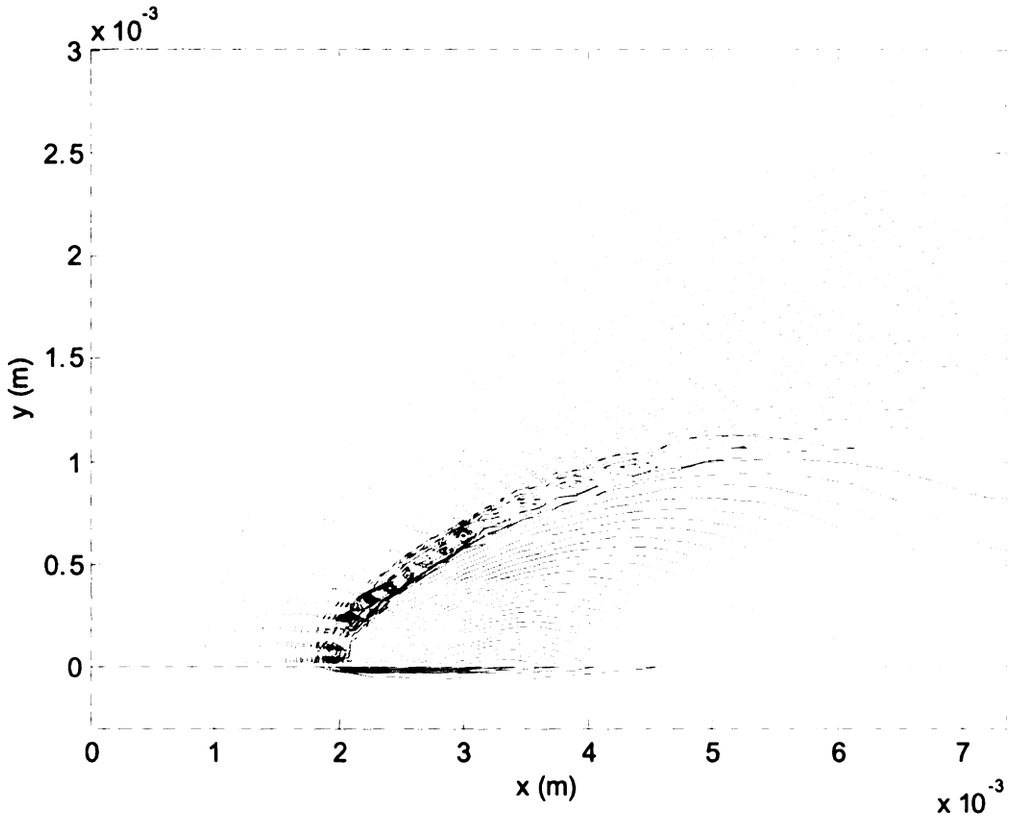

Figure 13(a). Reaction rate, fuel concentration and oxidizer concentration at 8.5s in a refined grid system that has $\Delta x = 0.15\,\text{mm}$.

Figure 13(b).
$\Delta x = 0.15$ mm

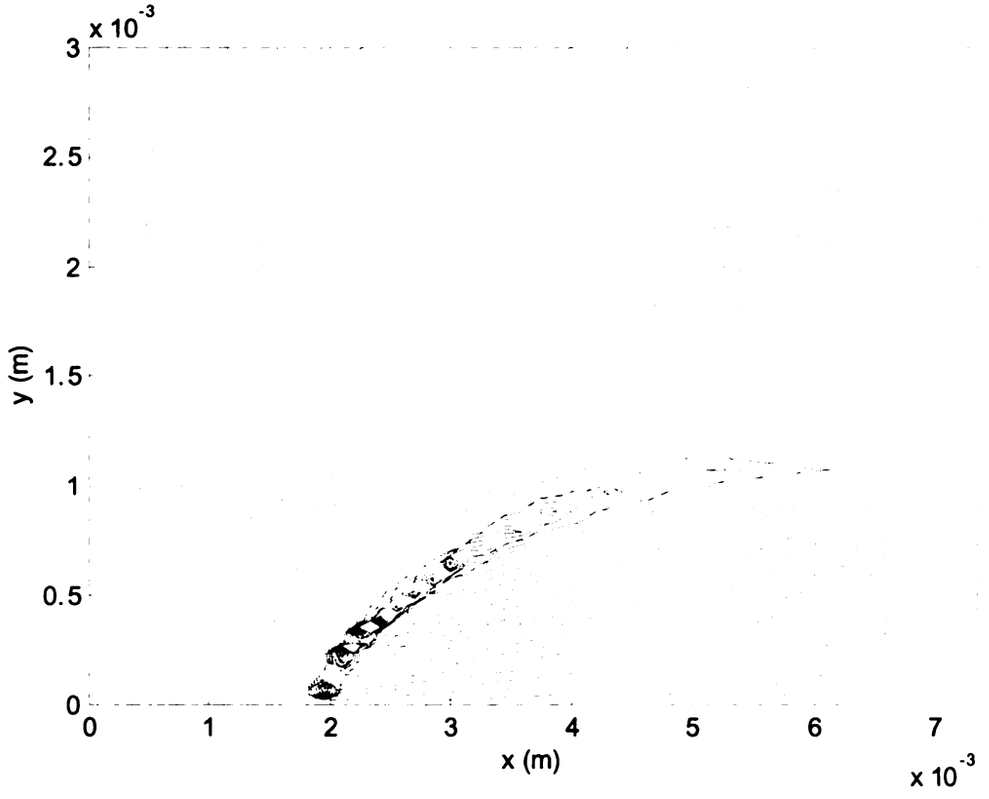

Figure 13(b). Reaction rate and temperature at 8.5s in a refined grid system that has $\Delta x = 0.15\,\text{mm}$. The grid still does not produce continuous reactivity contours.

Figure 14 Ma
latter with res

Figure 15 (
The flame
advances to

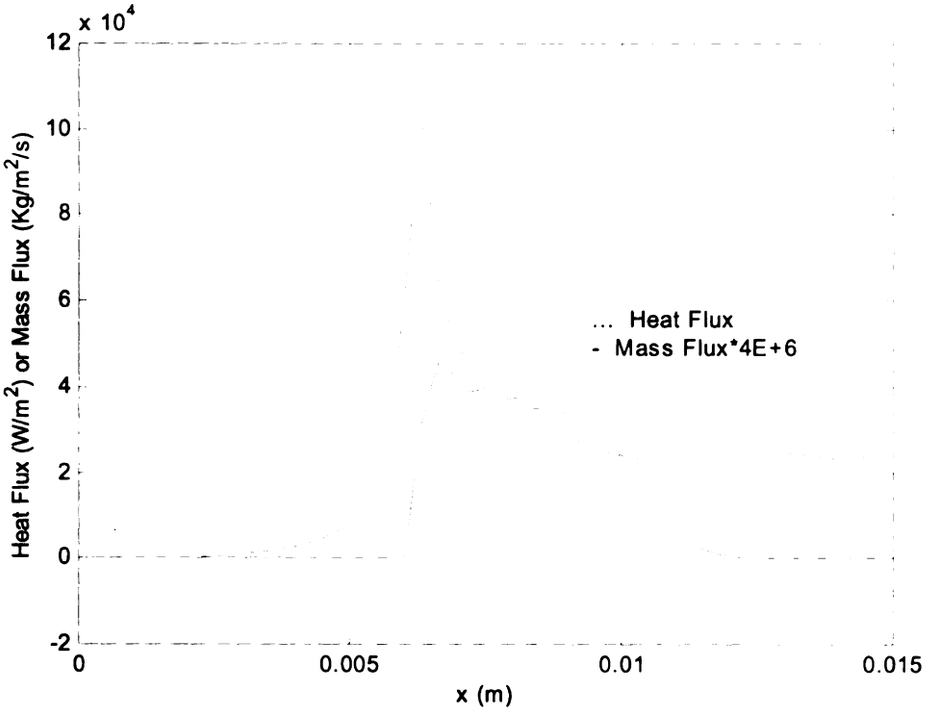

Figure 14 Mass flux and heat flux at 15s, indicating the upstream displacement of the latter with respect to the former.

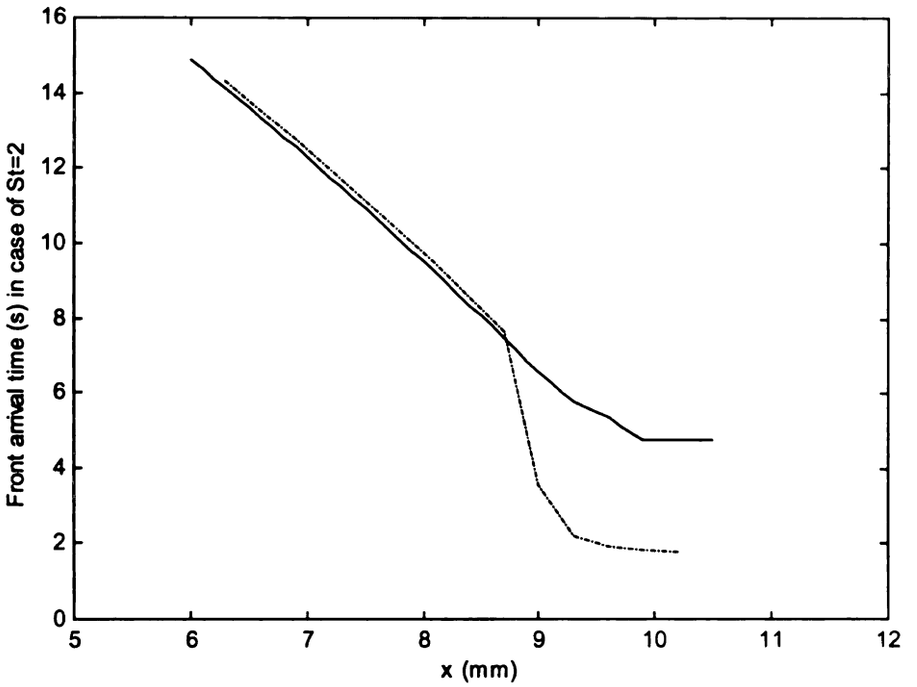

Figure 15 (a) Flame front (solid line) and phase front (dash dot) vs. x distance at St=2. The flame front very slightly precedes the phase front after $x \approx 8.75mm$ as the flame advances toward decreasing x (vice versa for $x \geq 8.75mm$).

Figure 15 (b

Figure 15 (
The phase

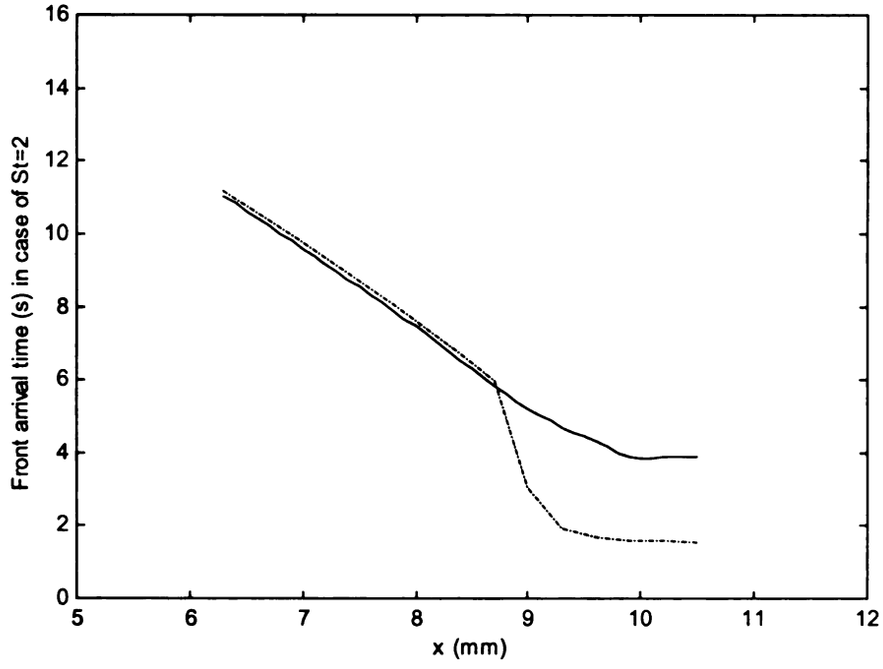

Figure 15 (b) Flame front (solid line) and phase front (dash dot) vs. x distance at St=100

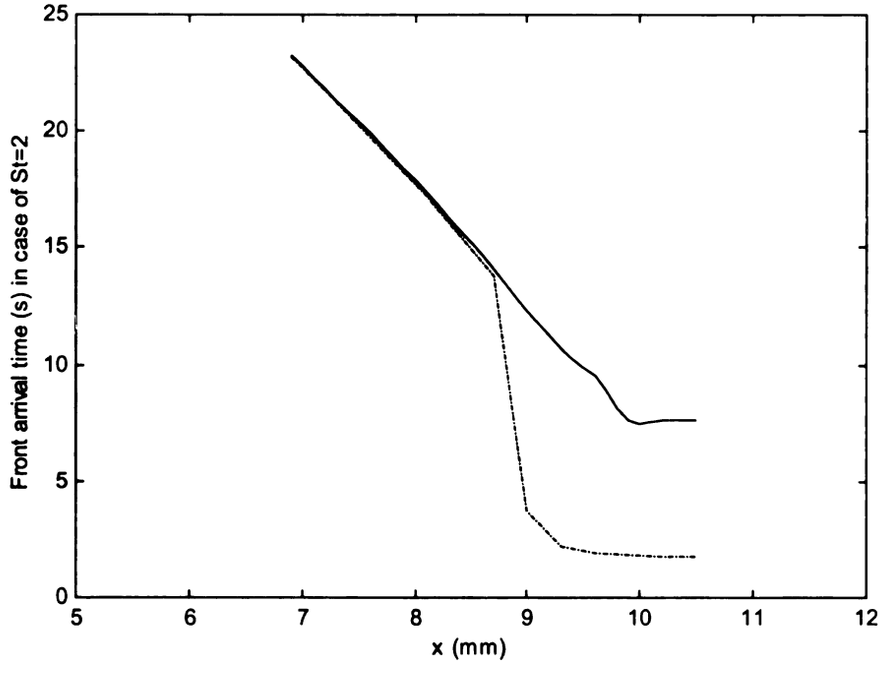

Figure 15 (c) Flame front (solid line) and phase front (dash dot) vs. x distance at $\bar{k}_l = 2.5$. The phase front precedes the flame front very slightly when $x \leq 8.75mm$.

Front arrival time (s) in case of St=2

Figure

y (mm)

Fig

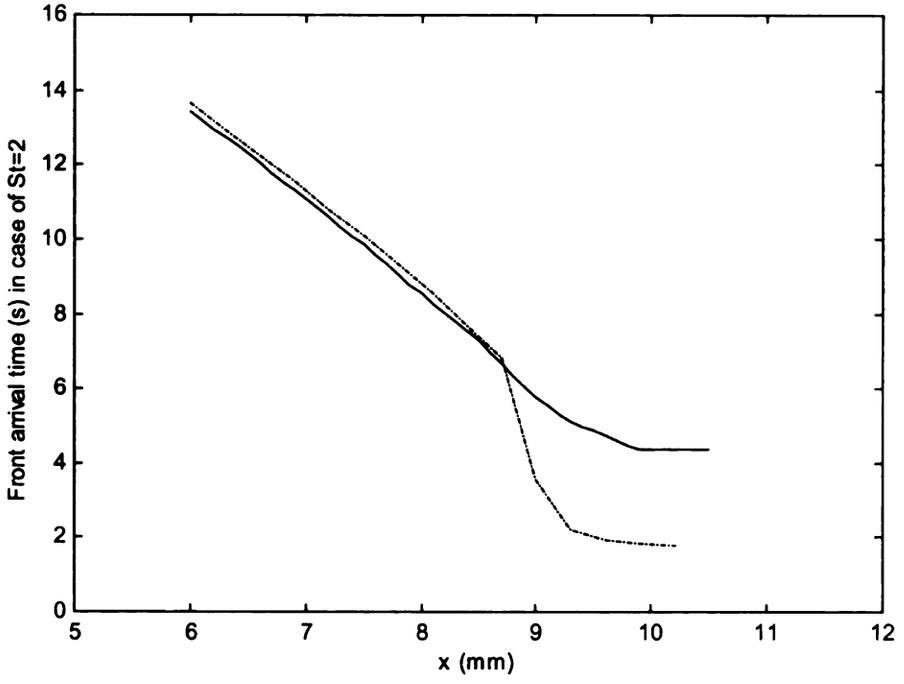

Figure 15 (d) Flame front (solid line) and phase front (dash dot) vs. x distance at $\overline{C}_{Pl} = 0.5$.

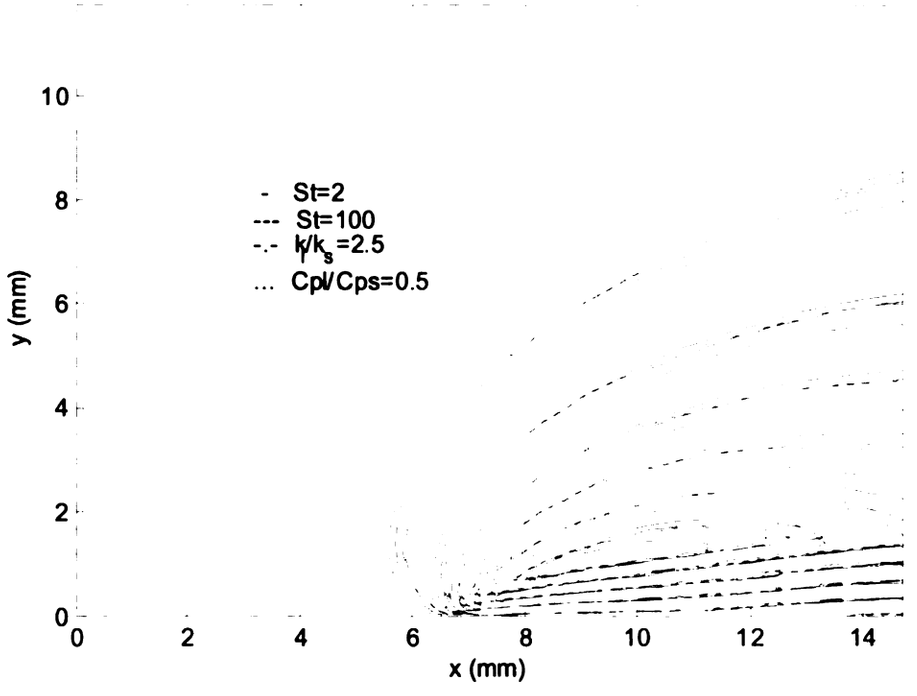

Figure 16 (a) Temperature Profiles for four different cases examined herein.

y (mm)

Figure 16 (
edge at x =
down).

y (mm)

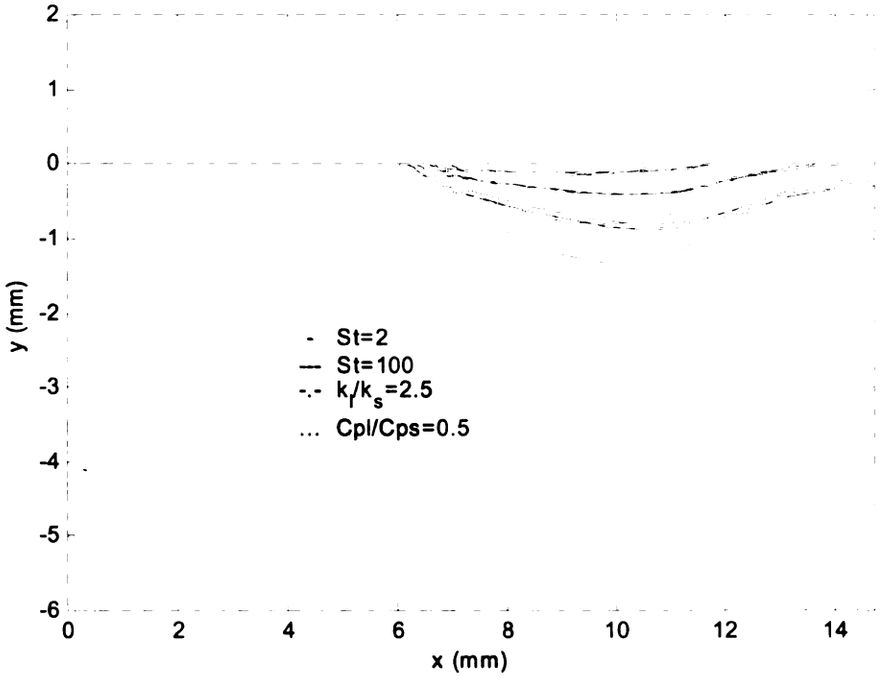

Figure 16 (b) Temperature distribution in the condensed phase. Near the flame leading edge at $x \approx 6mm$ it is self-similar. Downstream (at $x \approx 10mm$ self-similarity breaks down).

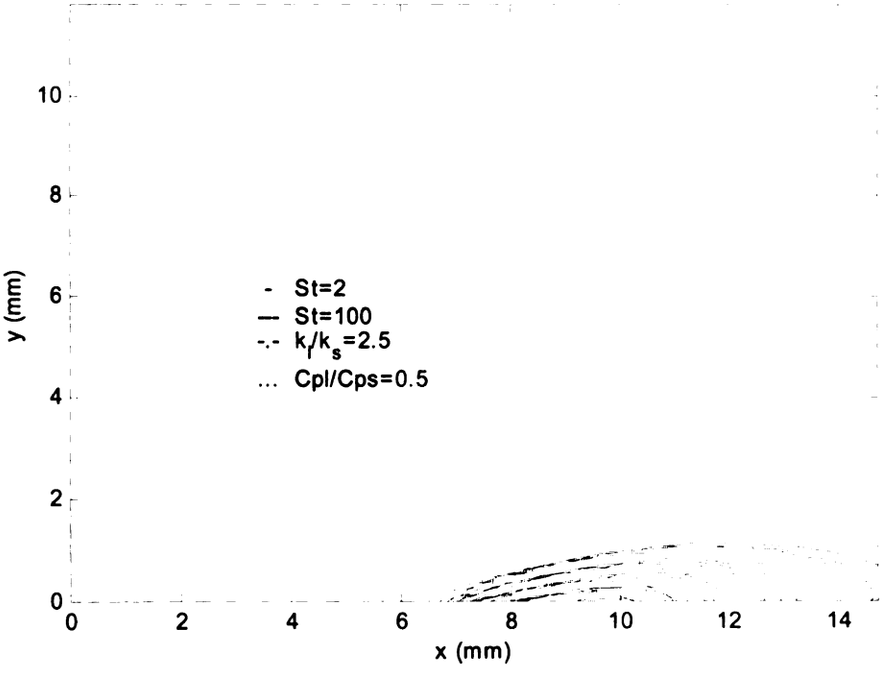

Figure 16 (c) Fuel concentration profile in the gas phase.

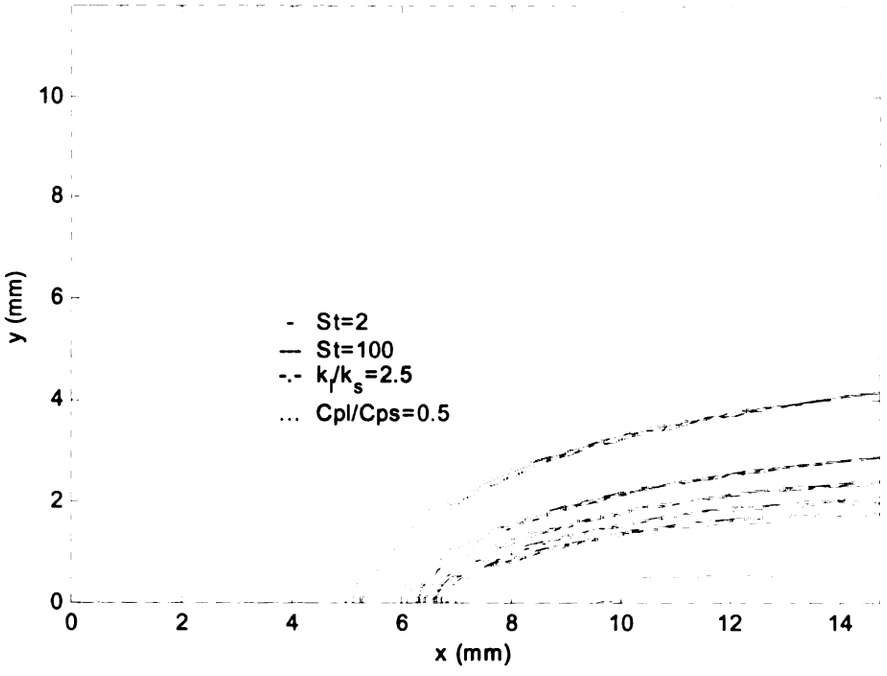

Figure 16 (d) Oxidizer concentration profiles in the gas phase.

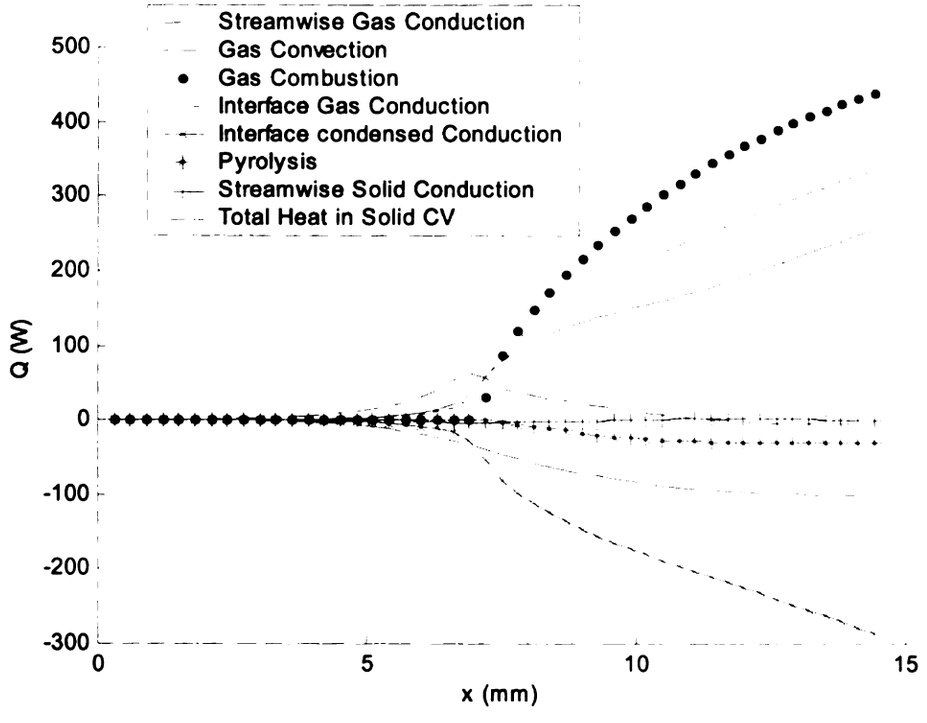

(17-a)

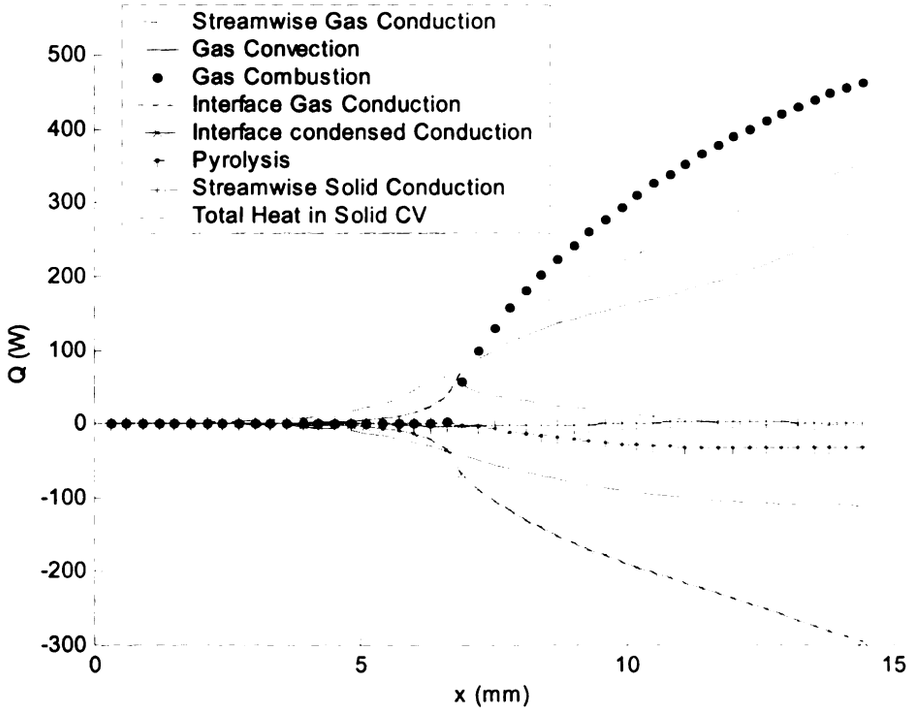
Streamwise Gas Conduction
Gas Convection
Gas Combustion
Interface Gas Conduction
Interface condensed Conduction
Pyrolysis
Streamwise Solid Conduction
Total Heat in Solid CV
500
400
300
200
100
0
-100
-200
-300
Q (W)
0
5
10
15
x (mm)

(17-b)

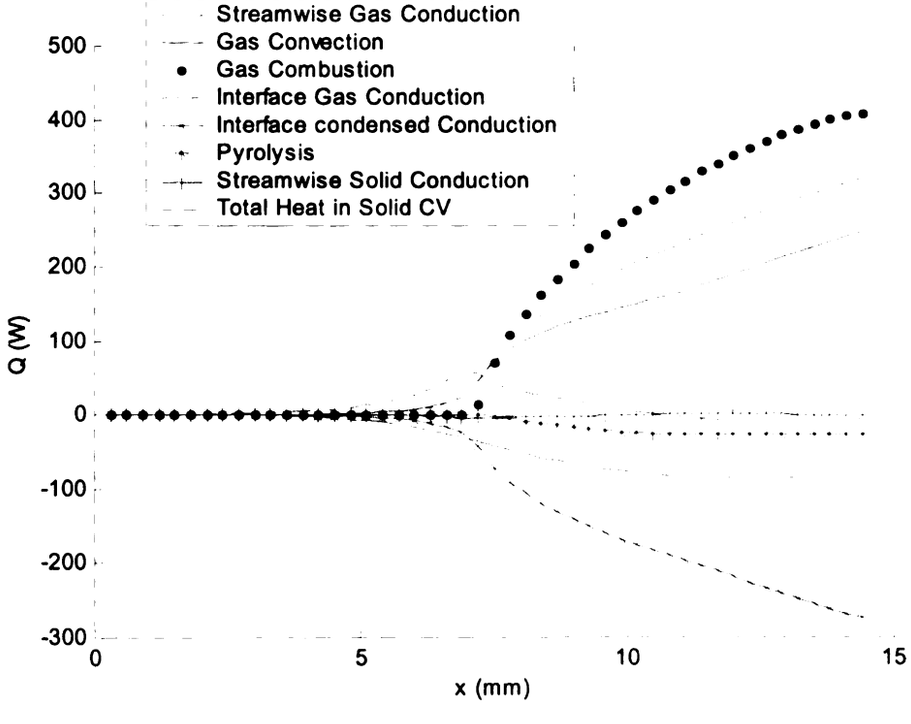
Streamwise Gas Conduction
Gas Convection
Gas Combustion
Interface Gas Conduction
Interface condensed Conduction
Pyrolysis
Streamwise Solid Conduction
Total Heat in Solid CV
500
400
300
200
100
0
-100
-200
-300
Q (W)
0
5
10
15
x (mm)

(17-c)

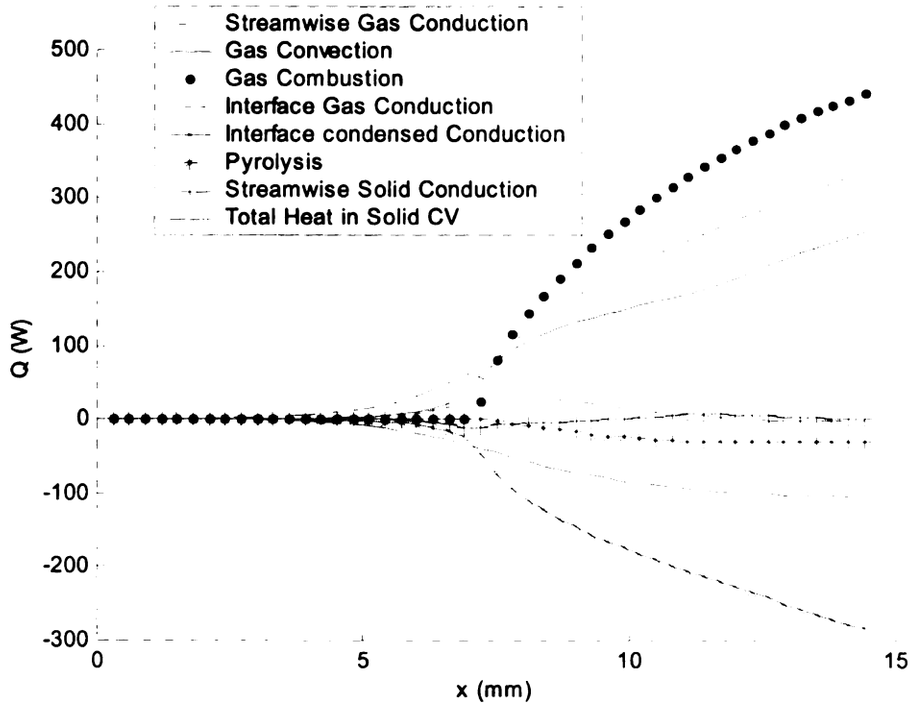

(17-d)

Figure 17 Distribution of heat flow rate (W) for a control volume in the gas phase and a control volume in the condensed phase ahead of the flame along the polymer surface for four Cases: (a) $St = 2$; (b) $St = 100$; (c) $\overline{k}_l = 2.5$ at $St = 2$; (d) $\overline{C}_{Pl} = 0.5$ at $St = 2$. In this figure, for the purpose of clarity, positive values are assigned to $\dot{Q}_{cg}$, $\dot{Q}_{com}$, $\dot{Q}_{wg}$, and $\dot{Q}_T$ (above $y = 0$); and negative values are assigned to $\dot{Q}_{cvg}$, $\dot{Q}_{py}$, $\dot{Q}_{ws}$ and $\dot{Q}_{cs}$ (below $y = 0$).

Table 1. Major properties and kinetic data used for the numerical model.

$k_s = 0.05$ W/(m·K)	$C_{Ps} = 1460$ J/(kg·K)	$\rho_s = 1190$ kg/m^3	$\rho_l = 1190$ kg/m^3
$T_m = 500$ K	$A_c = 2.82\times10^9$ s^{-1}	$E_c = 129580$ J/mol	$q_c = 1113.5$ kJ/kg
$K_e = 0.5$	$k_g = 0.0411$ W/(m·K)	$C_{Pg} = 250$ J/(kg·K)	$\rho_{g0} = 1.16$ kg/m^3
$D = 2.2\times10^{-5}$ m^2/s	$A_g = 1.6\times10^{15}$ m^3/(kg·s)	$E_g = 135730$ J/mol	$q_g = -51798$ kJ/kg
$u_\infty = 0.1$ m/s	$T_\infty = 300$ K	$Y_{O\infty} = 0.31$	$Y_{f\infty} = 0.0$

CHAPTER 5

REVISIT OF THE INFLUENCE OF SOLID ANISOTROPY ON FLAME SPREAD OVER MELTING POLYMERS

1. Introduction

Anisotropy of the solid phase influences flame spread behavior by possibly exaggerating the non-uniformity of heat conduction into the condensed phase. Chapter 2 investigated the anisotropic properties of a pure solid in a simplified flame spread situation. This work, however, did not consider the influence of a realistic flow and the melting behavior of thermoplastic solid. In addition, the influences of the material properties were investigated in a restrictive manner. In this work, we examine the full range of conductivity variation.

We have also significantly improved the previous numerical model by adding more realistic physical mechanisms. These include a Navier-Stokes flow and melting solid–liquid in the heated layer of the condensed phase. It allows us to explore the behavior of flame spread for melting thermoplastic materials.

When an anisotropic solid polymer undergoes external heating or responds to flame combustion heat it may undergo a phase change that alters the material properties. The resulting condensed phase contains an isotropic liquid region with uniform conductivities and an anisotropic solid region that is located below the liquid layer (and which was once solid and anisotropic). Generally, for the configuration we shall examine, theoretical investigations are absent because of the complexity of the condensed phase calculation. An exception exists, of course, for the simple case when spread is steady and no phase

change occurs [1, 43, 49].

The purpose of this Chapter is two fold: First, the flame spread rate will be obtained with respect to a varying transverse conductivity or a varying longitudinal conductivity; Second, we will explore the flame spread characteristics as reflected by the influence of the conductivities, such as the field parameters, interface parameters, and the heat transfer mechanisms. The last influence is accounted for by using energy balance numerical techniques. Afterwards the flame spread rate is discussed by using a global energy balance principle [43,49,55].

2. Results

The mathematical model uses an energy equation in the condensed phase that incorporates anisotropic conduction in the solid, which is the same as Chapter 4. In order to evaluate the influence of the anisotropic conductivity, a reference state is selected where $k_{sx} = k_{sy} = 0.05$ W/(m·K), $k_l = 0.05$ W/(m·K), and $L_s = 438000$ (W/kg). Note that $k_{sx} = k_{sy} = 0.05$ are the conductivities at ambient temperature. To analyze the influence of longitudinal conductivity k_{sx}, we change its magnitude in a range from 1/10 of the reference value (0.05) to 10 times of the reference value (0.5) with k_{sy} being fixed to the reference value. Similarly, the influence of the transverse conductivity k_{sy} is evaluated in a range from 0.005 (10 times of the reference value) to 0.1 (2 times of the reference value) while keeping k_{sx} fixed to the reference value.

2.1 Flame Spread Rate

The dependence of the flame spread rate on k_{sx} and k_{sy} is plotted in Figure 1(a) and Figure 1(b), respectively. The dots in figures represent the numerical results and the

solid line is the corresponding linear interpolation.

There is no theoretical formula available for flame spread over a melting polymer with solid phase anisotropy; however, we can find some comparable cases similar to our studies here in order to estimate the influence of these conductivities. For a range of k_{sx}, a comparable case is flame spread over anisotropic solid polymers. Without melting, the de Ris formula can be applied to the anisotropic case by showing that a variable k_{sx} does not change the flame spread rate [21]. This was verified in [43], where the streamwise conductivity could be eliminated from the spread formula. Interpretation of these results was aided considerably by the energy balance principle. This energy balance principle was applied to flame spread over melting polymers in [55]. Numerical investigation [57] has shown that the flame spread rate is weakly affected by k_{sx} except for large values of k_{sx}. Beyond certain magnitude of k_{sx}, the flame spread rate decreases with increasing k_{sx}. A comparison of Figure 1 of [57] to Figure 1(a) here indicates that a similar trend holds true for the melting case with anisotropic solid properties. A quantitative comparison will not be attempted because a different set of kinetic data is used here. As observed from Figure 1(a), there exists an asymptote for the spread rate when k_{sx} approaches zero, whose value is approximately 0.36 mm/s. In addition, the slope of the flame spread rate with respect to k_{sx} diminishes when k_{sx} decreases to small values. The range of k_{sx} corresponding to a constant spread rate will not be examined here since it is case dependent. A very small range is expected by observing a small slope at $k_{sx} \approx 0$.

The similarity between the numerical results with and without melting indicates that

the melt layer does not change the qualitative nature of the flame spread vs. k_{sx} relationship. Quantitatively it changes the magnitude of the flame spread rate [55]; for example, $St = 2$ results in a much lower spread rate than $St = 100$. Most of the computations are outside of the flat flame spread rate versus k_{sx} regime, which is near $k_{sx} \approx 0$. Similar to [57], for the range of k_{sx} employed in this model, there is no indication that spread rate increases with k_{sx} [58] for an intermediate range of streamwise conductivity. The physical explanation is that the higher k_{sx} results in a higher streamwise conduction, which serves to enhance heat losses more than it enhances upstream heat transfer to the unburned material.

The dependence of the flame spread rate on the transverse conductivity k_{sy} is plotted in Figure 1 (b). The dashed line represents the de Ris formula and the solid line is the numerical result. Qualitatively, both spread rates decrease with increasing k_{sy}, with a much stronger dependence than k_{sx}. The melt layer therefore does not change the qualitative nature of the spread rate vs. k_{sy}. In addition, the decline of u_s with k_{sy} in the de Ris formula is much steeper because we have a melting layer in the numerical model, which serves as an energy barrier (with the latent heat corresponding to $St = 2$). The de Ris formula [21,43,49] gives $u_s \propto 1/k_{sy}$. The numerical trend in Figure 1(b) coarsely resembles $u_s \propto 1/k_{sy}$ as suggested by Figure 1 in [57]. We obtain $u_s \propto 1/k_{sy}^n$ with $n \approx 0.2$ which is a substantially weaker dependence than the de Ris case with $n = 1$ Physically, an increasing k_{sy} lowers the spread rate by magnifying the heat loss through transverse conduction. There may be some other complications of melting such as the

layer thickness for example. They will be examined in more detail later.

2.2 Phase Front

Melting introduces the complication of the liquid layer in addition to those introduced by the anisotropy of the solid polymer. The spatial locations of phase interfaces between the solid phase and liquid phase are plotted in Figure 2 for two cases: (1) one with varying k_{sx} (2-a), and (2) one with varying k_{sy} (2-b). Since the process is transient, we take a snapshot of the phase front approximately 6 seconds after ignition. In this way, the condensed phases in each case receives almost the identical heating from the combustion reaction, thereby enabling a comparison of the influence of the condensed phase properties. An interesting observation from Figure 2 is readily obtained in terms of the size of the liquid layer. It is found that both the thickness and the streamwise extent of the liquid layer decrease with increasing k_s in each case. This seems to contradict the intuitive notion that a higher conductivity enhances the heat conduction rate, thereby increasing the net heat flux into the condensed phase from the gas phase reaction, and subsequently increasing the size of the liquid region. This intuition seems reasonable in that in the extreme case of zero conductivity the condensed phase does not receive any heat by conduction, thus rendering impossible any flame spread. A larger conductivity might be expected to better preheat the condensed phase to a high temperature and better support a spreading gas-phase flame. This speculation is invalid because, in this model, heat conduction serves not to accumulate thermal energy but to redistribute it inside the thermally thick polymer. For an otherwise identical situation for the thermally thin case, the polymer could be heated in a shorter time, thereby enhancing the flame spread rate. For the thick material considered here, however, the enhanced heat loss by conduction

reduces the size of the liquid layer, giving an inverse trend for the liquid layer size with respect to k_{sx} and k_{sy}. To compare the influences of k_{sx} and k_{sy}, we choose two parallel cases with $k_{sx} = 0.005$ and $k_{sy} = 0.005$, with each having conductivity of 0.05 in the other direction. From these two cases, it is found that the latter not only results in a larger liquid layer thickness, it also results in a larger streamwise extent of the liquid layer. This example indicates that k_{sy} is the more important factor in determining the size in all directions of the liquid layer.

2.3 Interface Parameters

The interface temperature, the mass flux, and the heat flux are plotted in Figure 3, Figure 4, and Figure 5 for two cases. The surface temperatures, as observed from Figure 3, show almost the same peak value for the different cases. The size of the heated surface can be characterized by a spatial span in which the temperature is above a certain magnitude along the interface. If we take this magnitude as 600K, it is observed that the size of the heated surface decreases with increasing k_{sx} or k_{sy}. This supports the heat loss effect of both k_{sx} and k_{sy}; the larger conductivity produces a smaller heated surface region. Comparison of Figure 3(b) and Figure 3(a) indicates consistency with Figure 2(a) and Figure 2(b) in that the k_{sy} not only expands the transverse extent of the liquid layer but also expands the streamwise extent, when using the size of the heated surface as a measure.

The interface heat flux is defined as the net heat flux into the condensed phase, namely, gas conduction minus interfacial radiation loss. This is plotted in Figure 4. In order to make comparisons, their peak values are fixed to the same location. It is

observed that the peaks have almost the same magnitudes no matter which values k_{sx} or k_{sy} take. Downstream of the peak, there are discernable decreases of the heat flux with increasing k_{sx} or k_{sy}. Interestingly, there is a more significant influence of k_{sx} on the heat flux far downstream. If we use the $2W/(m^2s)$ to characterize the heat flux region in which the heat flux exceeds this value, the size of the region has a decrease of approximately 4mm between $k_{sx} = 0.005$ and $k_{sx} = 0.5$. Smaller k_{sx} results in a larger heat flux region downstream of the flame front. The case of varying k_{sy} shows a similar influence although the influence of k_{sy} is not significant except for large magnitudes, as seen for the case $k_{sy} = 0.1$ in Figure 4(b), where a much small downstream heat flux region is obtained compared to the other three cases. The interface mass flux distribution along the interface is plotted in Figure 5 for the two cases. The order of mass flux magnitude with respect to the conductivity in a given direction resembles the heat flux and temperature. The explanation can be obtained readily from Figure 2 by considering the in-depth pyrolysis mechanisms. Again, a lower conductivity in any given direction results in a higher mass flux. The peak value of the mass flux is found to be also dependent on the conductivity, especially in cases of varying k_{sx}. In addition, $k_{sx} = 0.005$ or $k_{sy} = 0.005$ has a significantly larger magnitudes of the mass flux peak compared to the other cases.

2.4 Energy Balance Analysis

Integral numerical methods are used to obtain the magnitudes of various heat transfer mechanisms in a series of varying control volumes for steady flame spread. The control

volume right boundary moves along the interface from left to right, thereby resulting a functional dependence of these heat transfer mechanisms on the longitudinal distance at interface, as given in Figure 6. A general observation is made first by relating the conductivity to the magnitude of the overall scales of these heat transfer mechanisms. That is, the higher k_{sx} or k_{sy} results in lower magnitude of each heat mechanism. From Figure 6, it is observed that the reference state corresponds to the middle position between a smaller conductivity and a higher conductivity in terms of the magnitude of the heat transfer mechanisms. The heat transfer magnitudes actually represent the size of the flame; a higher conductivity corresponds to a smaller flame. One formulation of the flame spread mechanism [34] states that the total heat applied to the condensed phase upstream of the flame front determines the flame spread rate. In [43] the energy balance provided in [34] were clarified in both scope and applicability. The formulation of [34] is consistent with our observations, hence according to [43], the gas phase dominates the spread process. A measure of the relative importance of each phase is the parameter $P_e = (u_f / \alpha_{sx})/(u_g / \alpha_g)$ known as the solid to gas Peclet ratio. When $P_e >> 1$ gas phase forward heat transfer dominates the solid phase heat transfer, and vice versa for $P_e << 1$. In our three cases (Figure 6(a) (b) (c)) we have $P_e = 592$, $P_e = 5.9$, and $P_e = 59$ respectively. By comparing the total heat transmitted to the solid as represented by the solid line in Figure 6 for all cases, one sees that its order is consistent with the order of the flame spread rate. The total heat carried upstream of the flame front also follows this rule.

Another observation concerns streamwise conduction in the condensed phase. Since

this is related to k_{sx}, Figures 6(a), 6(b), and 6(c) are chosen for comparison. It is found that when $k_{sx} = 0.5$ the streamwise conduction shows a totally different behavior from the other cases. First and foremost, conduction in the solid has a higher magnitude compared to that of streamwise conduction in the gas phase. In this case, the forward heat transfer in the solid is less dominated by the gas, as indicated by the parameter $P_e = 5.9$ [43]. Second, the conduction magnitude first increases by forming a peak when it approaches the flame front and decreases downstream, similar to the other cases. Downstream of the flame front, however, it continues to decrease at almost a constant rate and finally attains a peak again. This second peak is downstream of the flame front. Here the heat loss term due to streamwise conduction in the condensed phase has a negative value, whose magnitude is comparable to that of the streamwise gas conduction, or one tenth of the combustion heat in the control volume. This result indicates the important role played by the downstream heat conduction loss for high k_{sx}. For the other cases, streamwise heat conduction in the condensed phase is not as significant. The influence of k_{sy} can also be found by examining Figures 6(c), 6(d) and 6(e). Compared to k_{sx}, k_{sy} does not substantially alter the trends of the overall heat transfer mechanisms. The variation of k_{sy} supports the observation made before, that is, higher k_{sy} results in both a smaller flame and heat transfer magnitude.

2.5 Flame Size

The flame size increases as the conductivity in any given direction decreases. Figure 7 shows another perspective for the same purpose. The temperature is plotted at a line through both the gas and condensed phase, the location of which is selected as the center

of the heated surface. The temperature pattern shows first an upslope, then a peak and finally a down-slope with y=0 serving as the boundary between the gas and condensed phases. The peak of the temperature may not correspond to the maximum flame temperature in the gas because the selection of the cutting line may not exactly match the location of maximum temperature. The influence of k_{sx} on the temperature is observed from Figure 7 (a), where higher k_{sx} corresponds to a lower gas temperature. The order of the temperature peaks obeys the observations made before. That is, the flame size has an inverse dependence on k_{sx}. Similarly, Figure 7(b) shows the temperature along a slice for four k_{sy} values. The temperature peak depends inversely on k_{sy}. Figure 7 clarifies the dependence of the flame size on conductivity in a given direction by the graphed temperature pattern.

2.6 Ignition Delay Time

Finally the influence of the conductivities on the ignition delay time is given in Figure 8. A higher k_{sx} results in an increased ignition time (Figure 8(a)), and similarly a higher k_{sy} results in a higher ignition delay time (Figure 8(b)). These results restate yet again the heat loss effect of the conductivities. With increasing magnitude of conductivity, the energy loss via conduction makes high surface temperatures harder to attain, thus requiring longer ignition times. Other aspects of ignition behaviors will not be explored here since we are mainly interested in the steady spread of the flame. The ignition delay time provides consistent results that improve our understanding of the energy redistribution aspects of k_{sx} and k_{sy}.

A general discussion is now provided on the dependence of the flame spread rate on

k_{sy}. In a flame-fixed coordinate system, the global energy balance principle [43] states that the spread rate must be sufficient to remove the combustion heat by downstream condensed phase (solid and liquid) and conduction in addition to downstream gas phase convection and conduction. Here we provide a conceptual explanation. A mathematical deduction is not attempted because of the introduction of the phenomenon of a liquid layer, as compared to a much simpler configuration described by Equations (3) and (4) in [43]. The role played by k_{sy} is to distribute a proportion of the combustion heat released by the flame to the condensed phase. With diminished k_{sy}, since the gas carries away less heat due to the limitation of the diffusivity, the condensed phase must increase its velocity in order to carry away its share of the combustion heat. Therefore with the decrease of k_{sy}, the flame spread rate (the convection of the solid phase) increases. This behavior is similarly observed for flame spread over pure solid fuels. There are several additional complications that enter in attempts to rigorously use the principle for cases with varying conductivity. One is that the combustion heat is not constant but depends on the conductivity (see Figure 7). Another is that the condensed phase enthalpy is dependent on the conductivity (see Figure 2). Interpretation of the flame spread rate with case-dependent combustion heat and streamwise condensed phase convection introduces an interesting problem. The resolution of this problem is beyond the scope of this chapter.

3. Conclusions

The problem of flame spread over an anisotropic polymer solid is investigated again with the introduction of a realistic flow field accompanied by melting of the anisotropic solid. The condensed phase therefore consists of an isotropic liquid near the heated interface and an anisotropic solid surrounding it. The flame spread rate is computed and

compared to a numerical case without melting and an analytical formula for a pure solid. It is found that the flame spread rate resembles the former case by producing an almost inversely decreasing curve with respect to the transverse conductivity. The analytical formula has a sharper rate of decrease with increasing transverse conductivity. At the reference state where only the isotropic solid and the liquid are present, the flame spread rate is lower than the analytical formula, indicating that the energy barrier of the melting lowers the flame spread rate. In addition, the flame spread rate generally does not show independence of the longitudinal conductivity in that it actually decreases with increasing k_{sx}. A very weak dependence of the spread rate is found near $k_{sx} \approx 0$, indicating that it is possible that a small range of k_{sx} exists where the flame spread rate is essentially independent of k_{sx}. The discussion of [43] considered primarily the limit of vanishing streamwise conductivity, demonstrating convincingly that in the limit the influence of the conductivity is nil. There was no detailed discussion of large streamwise conductivity except to note that it does not appear in the theoretically derived flame spread formulas. In addition, the size of the liquid layer was found to be larger when a lower k_{sx} or k_{sy} value was employed. This indicates that the lower conductivity in any direction results in a lower rate of heat loss by condensed phase conduction. The interface phenomena are also investigated by means of the interface temperature, the mass flux, and the net heat flux to the condensed phase. It is found that a smaller size of the heated region or heat flux region results from a higher magnitude of k_{sx} or k_{sy}. Energy balance analysis is also applied to the flame spread process. It is observed that the magnitude of each heat transfer mechanism depends inversely on k_{sx} and k_{sy}. In general, a higher magnitude of

either k_{sx} or k_{sy} results in a smaller flame size. Another interesting phenomenon is found with respect to the importance of the streamwise conduction in the condensed phase. When k_{sx} has a large magnitude (0.5 W/(m.s)), the streamwise heat conduction in the condensed phase has a peak value near the flame front. This peak represents the heat gain of the control volume and its magnitude is comparable to the magnitude of streamwise convection in the gas phase. Downstream a peak of nearly the same magnitude (but of course opposite sign) is found for the heat loss. A low k_{sx} value does not result in high streamwise conduction in the condensed phase.

Although the dependence of the spread rate and other quantities on k_{sx} was generally significantly weaker than the dependence on k_{sy} (see e.g. Figure 1), the influence of k_{sx} on the overall flame character (size, shape, temperature distribution) is very important. The streamwise conductivity is a significant determinant of melt layer thickness and extent (inverse relationship) and, therefore, both flame size and flame strength.

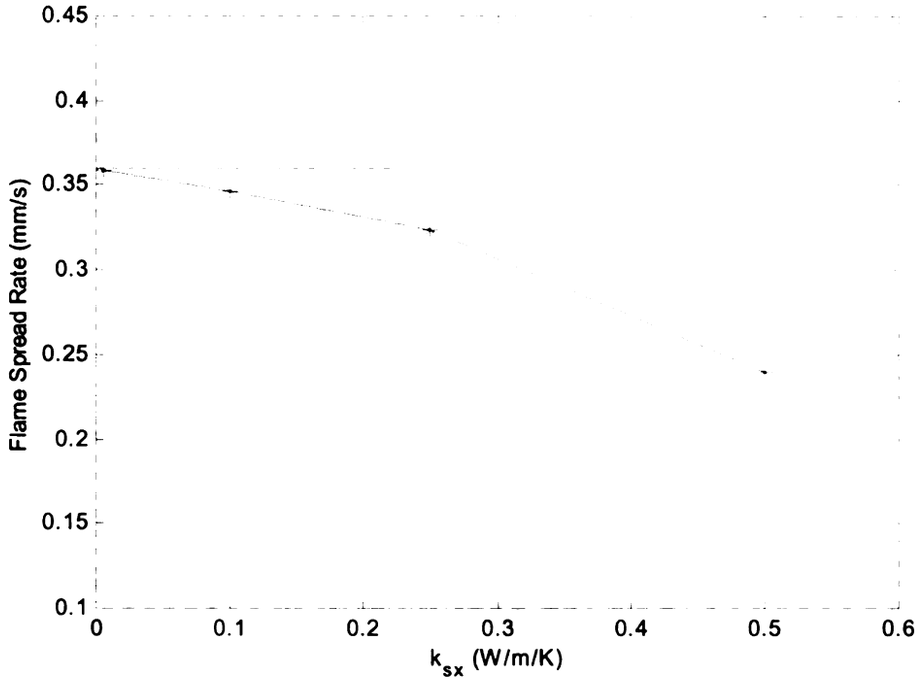

Figure 1 (a) Flame spread rate vs. k_{sx} while k_{sy} is kept constant.

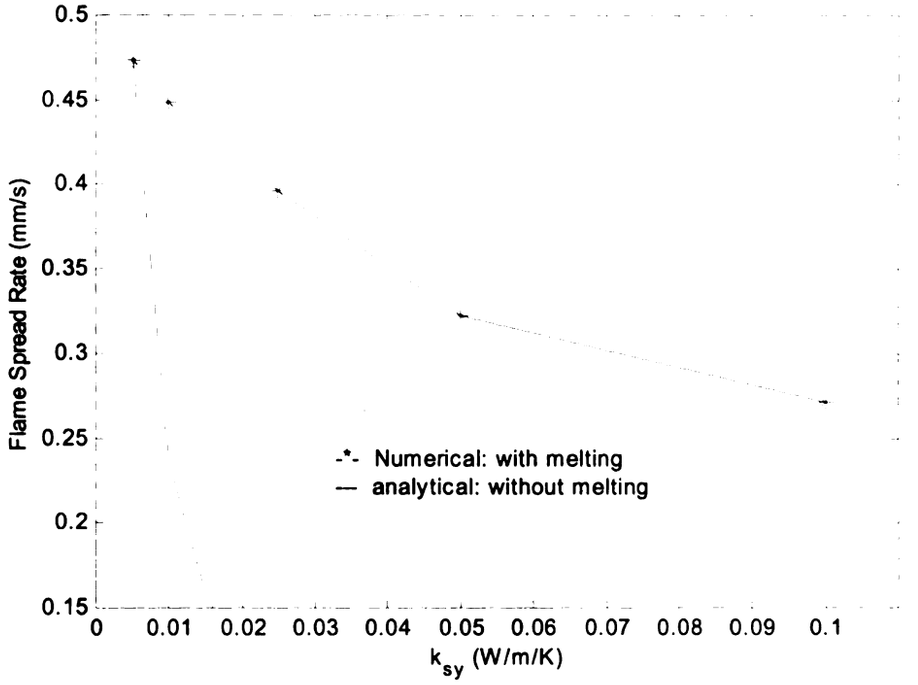

Figure 1 (b) Flame spread rate vs. k_{sy} while k_{sx} is kept constant. The analytical result comes from de Ris formula for flame spread over pure solid.

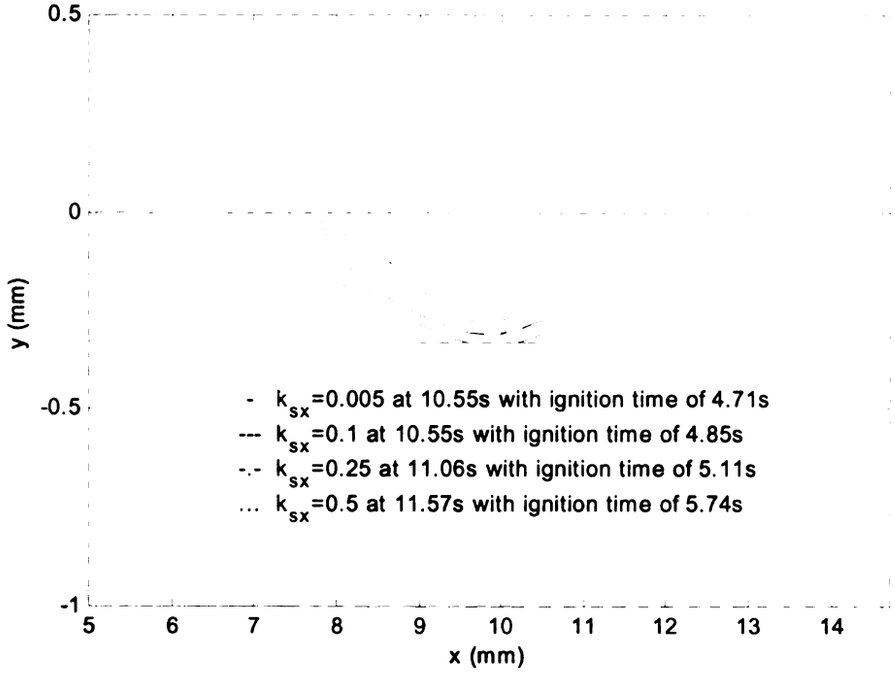

Figure 2 (a) The phase contours for four cases with different k_{sx}.

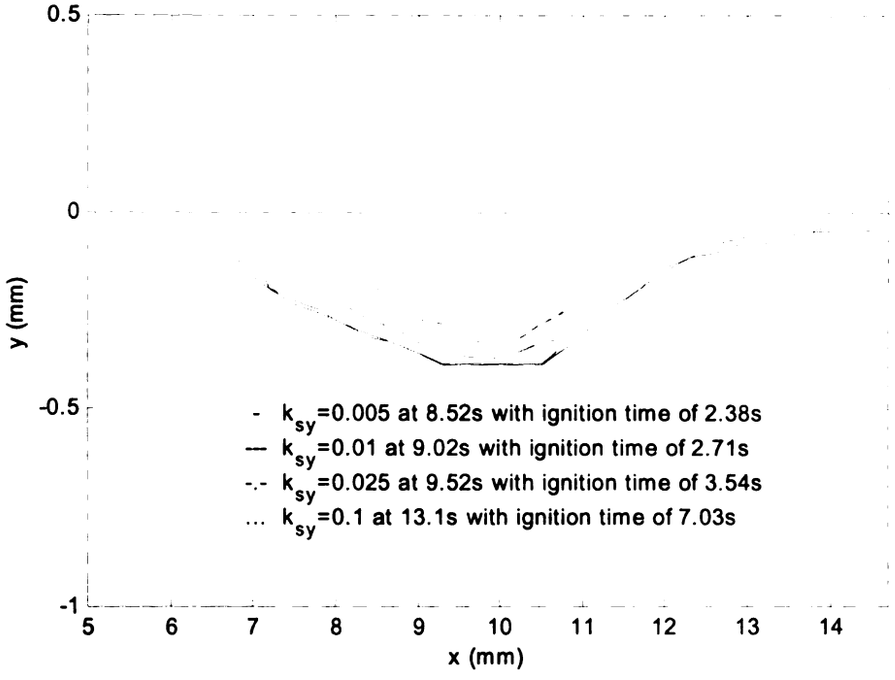

Figure 2 (b) The phase contours for four cases with different k_{sy}. Note that k_{sy} also expands the streamwise extent of the liquid layer.

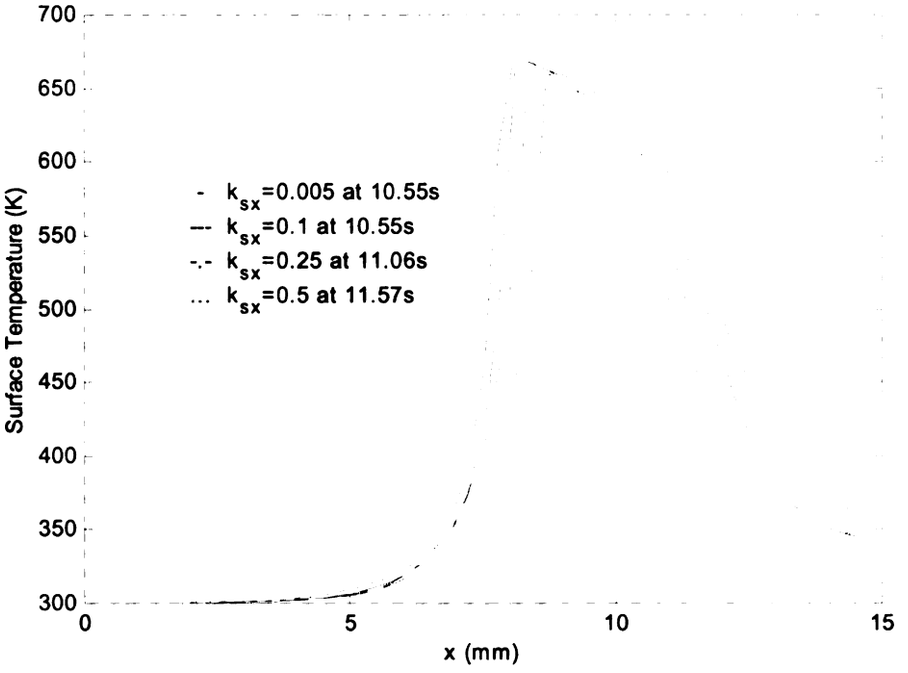

Figure 3(a) The surface temperature for four cases with different k_{sx}.

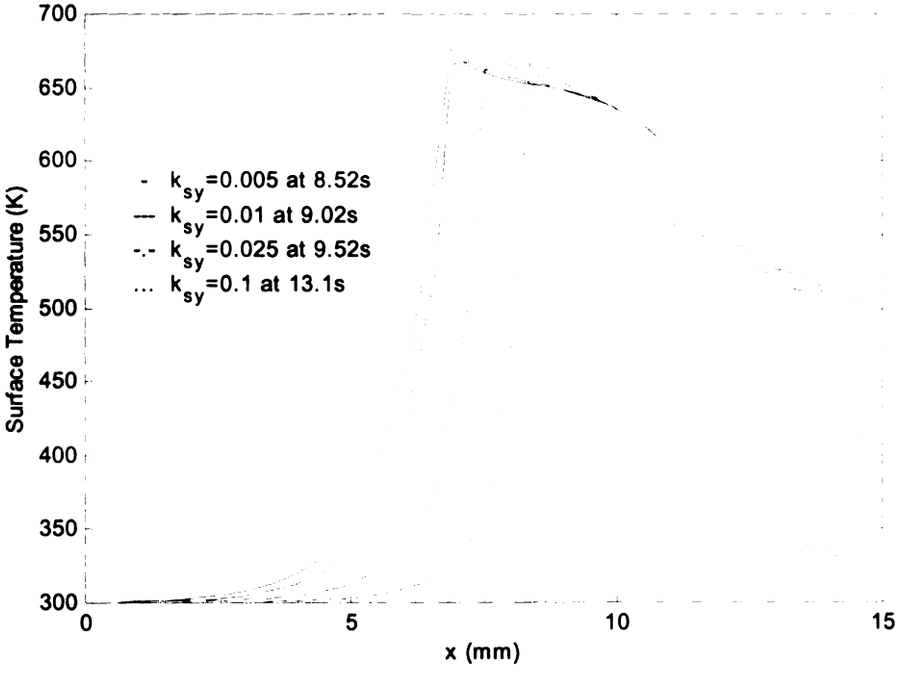

Figure 3(b) The surface temperature for four cases with different k_{sy}.

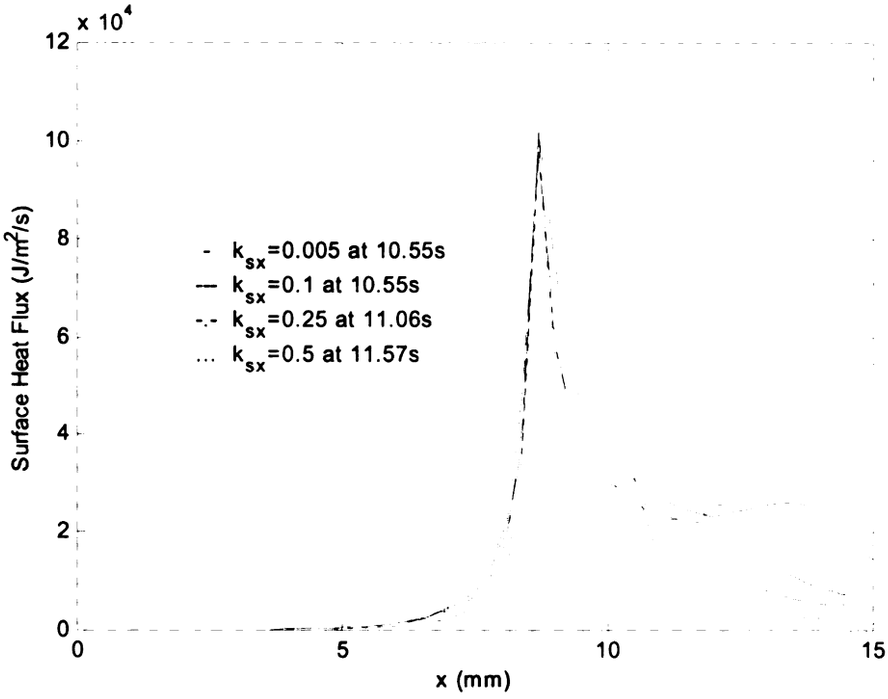

Figure 4(a) The surface heat flux for four cases with different k_{sx}.

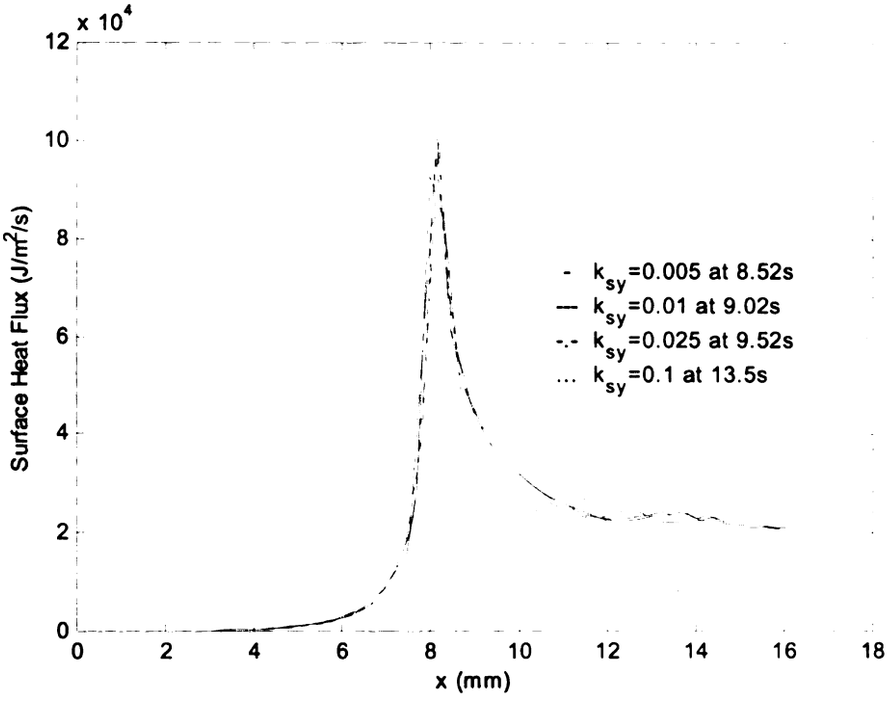

Figure 4(b) The surface heat flux for four cases with different k_{sy}.

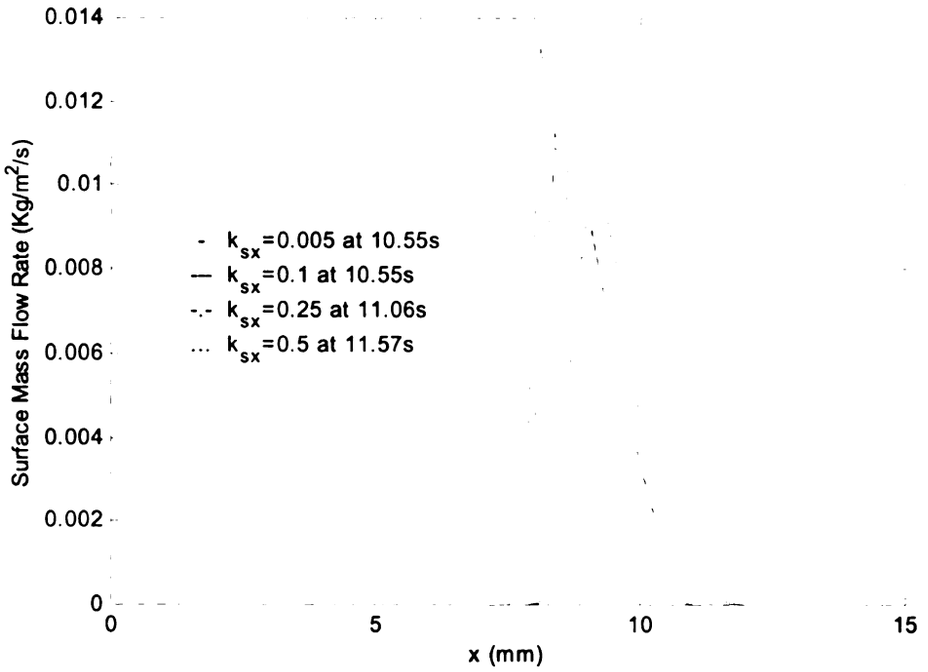

Figure 5(a) The surface mass flux for four cases with different k_{sx}.

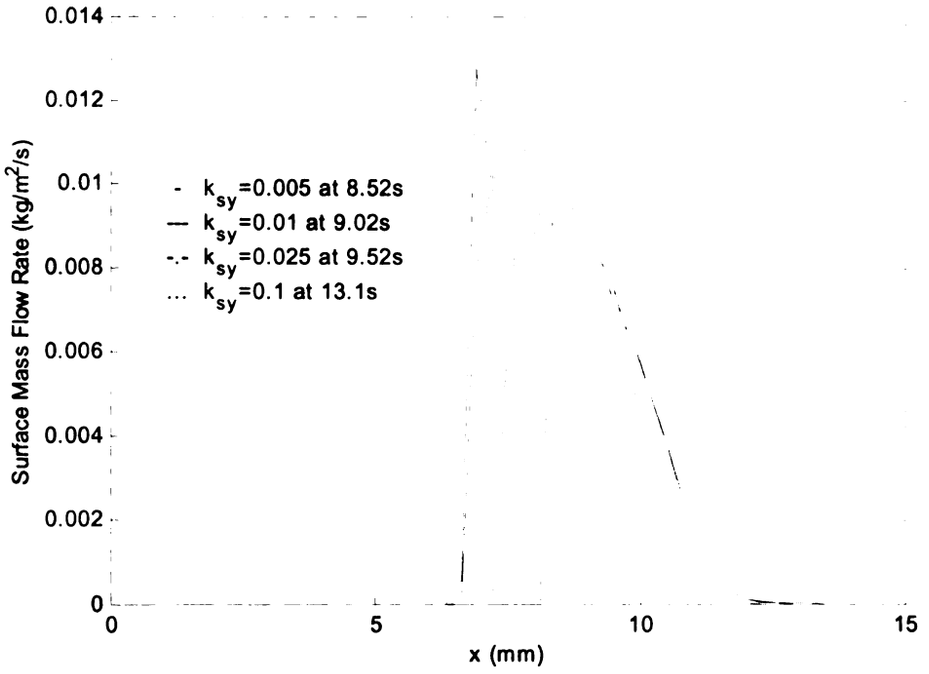

Figure 5(b) The surface mass flux for four cases with different k_{sy}.

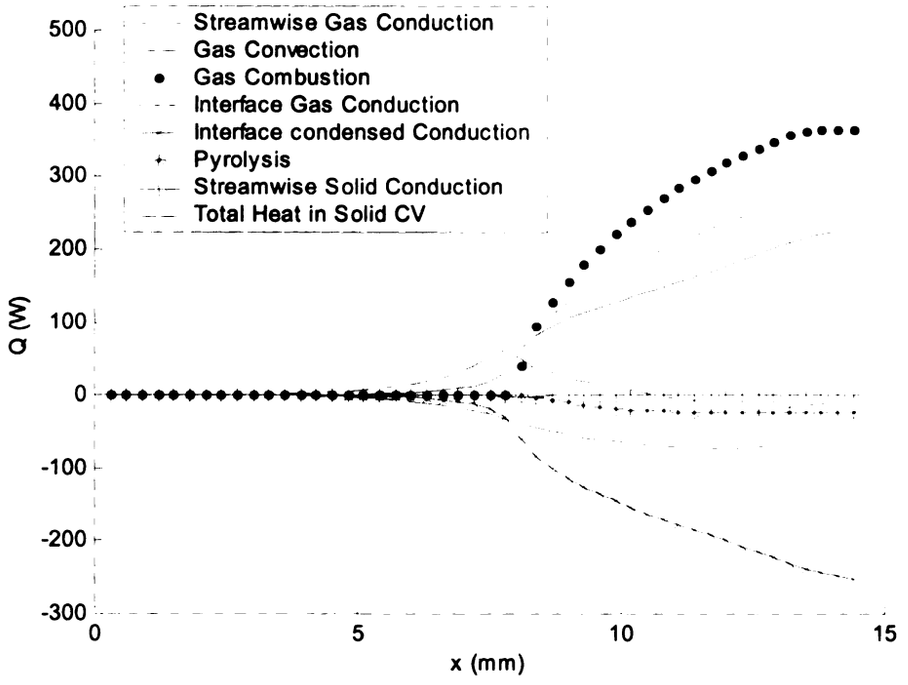

(6-a) $k_{sx} = 0.005$

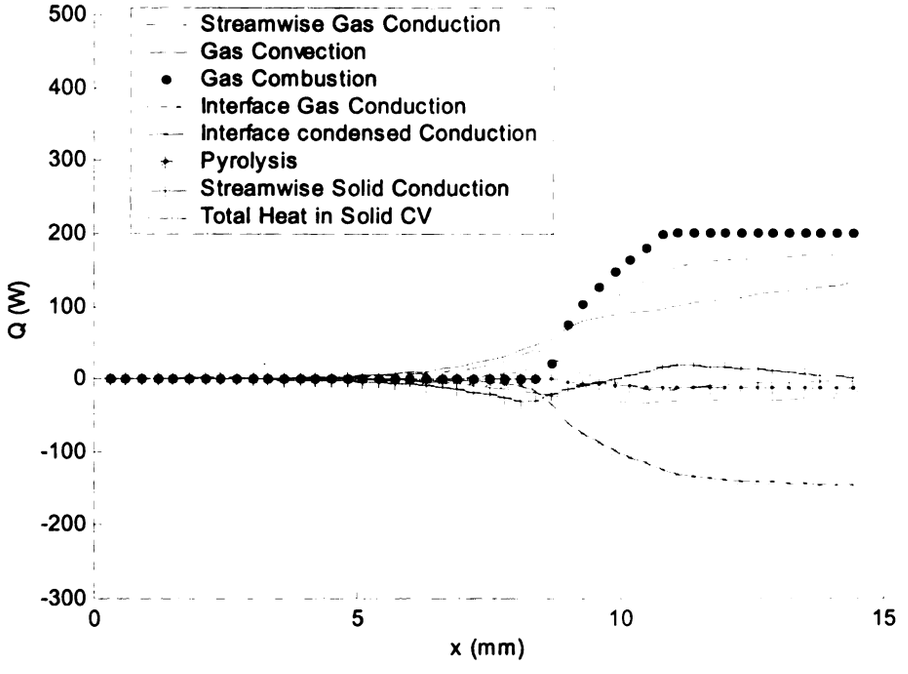

(6-b) $k_{sx} = 0.5$

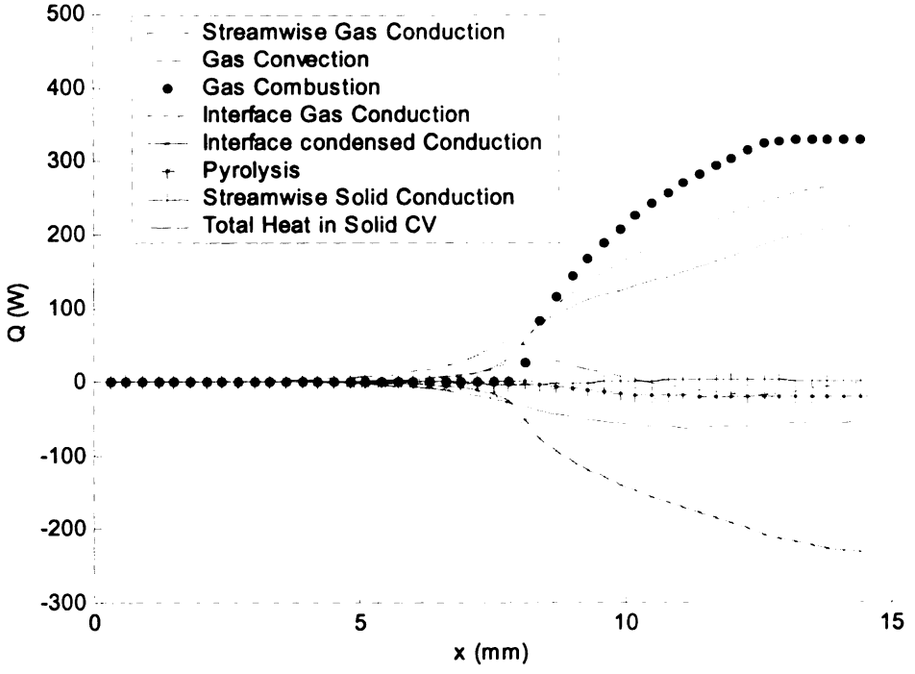

(6-c) Reference state

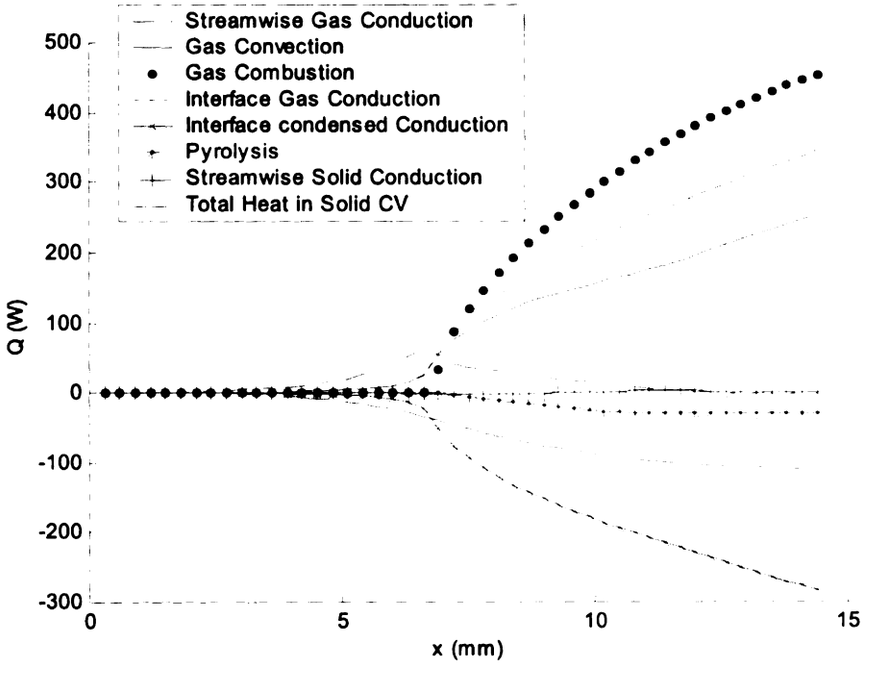

(6-d) $k_{sy} = 0.005$

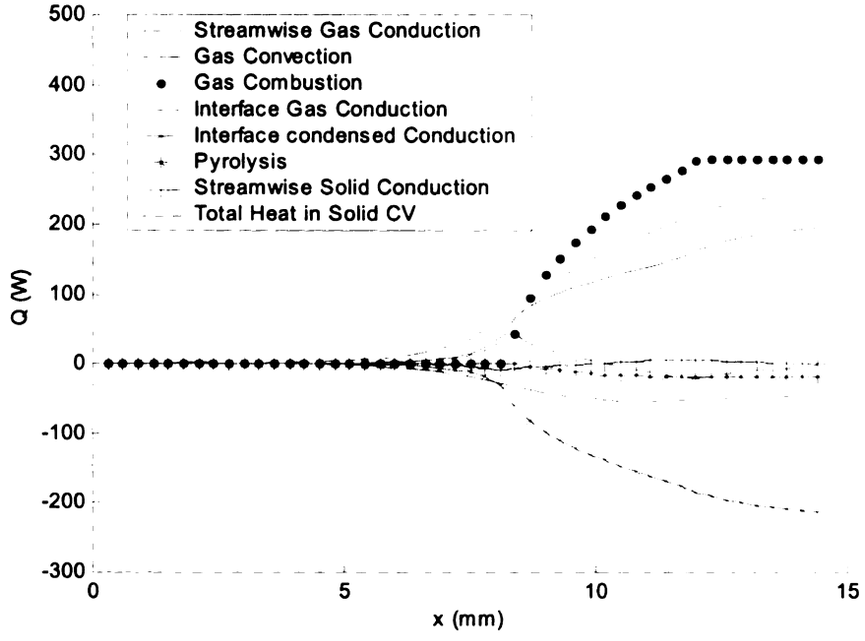

(6-e) $k_{sy} = 0.1$

Figure 6. Distribution of heat flow rate (W) for a control volume in the gas phase and a control volume in the condensed phase ahead of the flame along the polymer surface for three cases: (a) $k_{sx} = 0.005$; (b) $k_{sx} = 0.5$; (c) reference state; (d) $k_{sy} = 0.005$; (e) $k_{sy} = 0.1$. In this figure, for the purposes of clarity, positive values are assigned to $\dot{Q}_{cg}$, $\dot{Q}_{com}$, $\dot{Q}_{wg}$, and $\dot{Q}_T$ (above $y = 0$); and negative values are assigned to $\dot{Q}_{cvg}$, $\dot{Q}_{py}$, $\dot{Q}_{ws}$ and $\dot{Q}_{cs}$ (below $y = 0$).

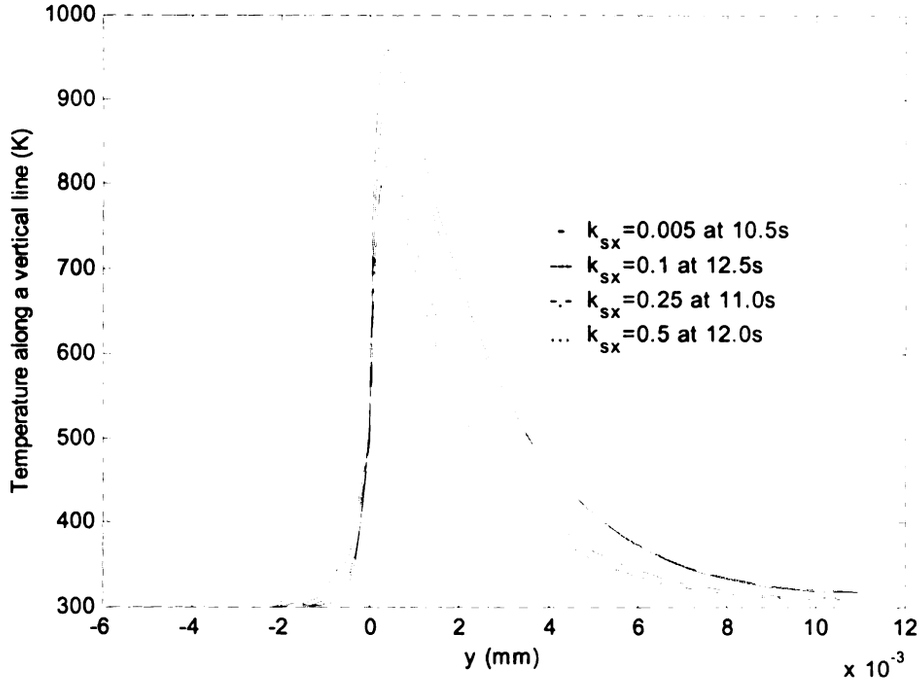

(7-a)

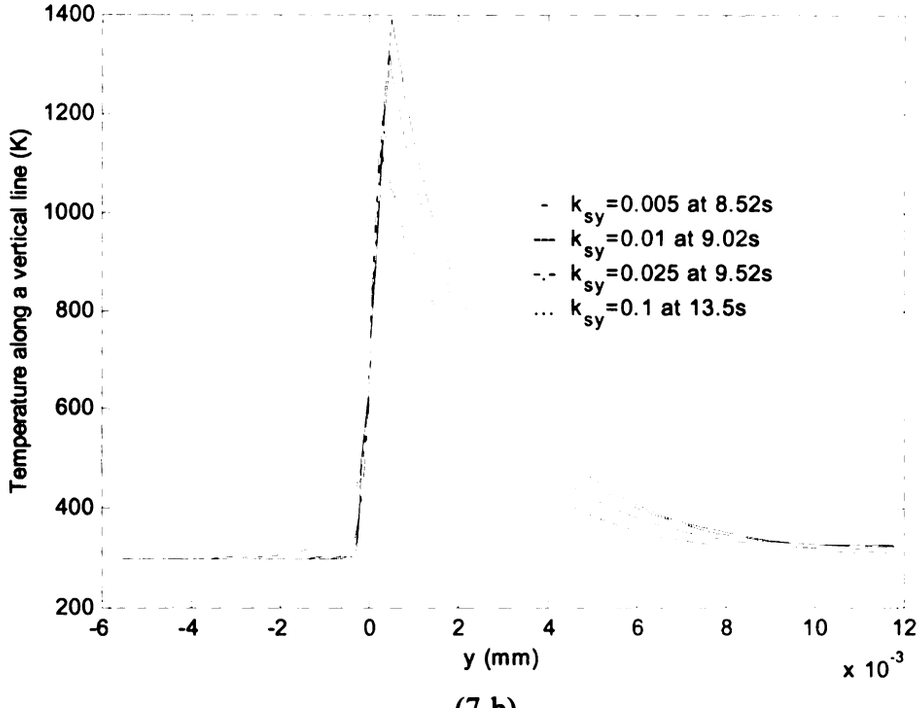

(7-b)

Figure 7 Temperature along a slice at the center of the heat surface with both the gas phase and the condensed phase plotted. Two cases are for (a) k_{sx} (b) k_{sy}.

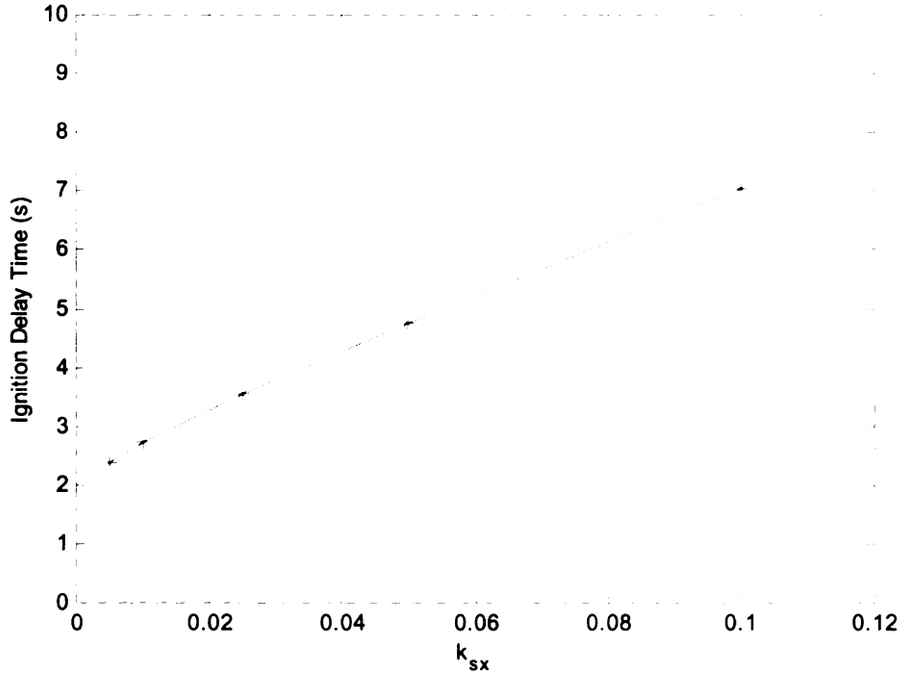

Figure 8 (a) Ignition delay time vs. k_{sy} while k_{sx} is kept constant.

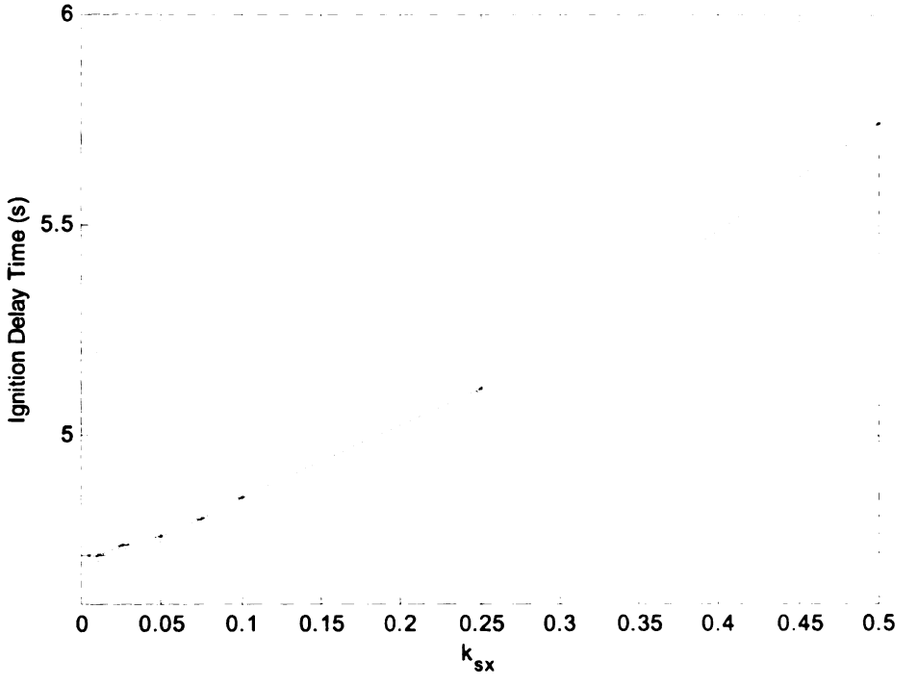

Figure 8 (b) Ignition delay time vs. k_{sx} while k_{sy} is kept constant.

Chapter 6

ENERGY BALANCE ANALYSIS OF IGNITION OVER A MELTING POLYMER SUBJECTED TO A HIGH RADIATION HEAT FLUX IN A CHANNEL FLOW

1. Introduction

In describing the flammability of combustible materials one attempts to answer the question "How does the heated surface ignite into flame?." Four explanations have been proposed. Two are based on attainment of a critical surface temperature or a minimum volatile mean flux into the adjacent gas. The remaining two explanations require a minimum oxygen concentration and a minimum external heat flux. Complications arise because these four criteria are closely related. The surface temperature and mass flux depend on the oxygen mass fraction and heat flux, and the surface mass flux may be a function of the surface temperature. The incident heat flux – the sole initial "stimulus" or "cause" – is the most primitive flammability "property". The practical measure of interest is the time to ignition. Most tests of material flammability specify the oxygen concentration (air) and applied external heat flux[11].

Heated gaseous fuels and warm air, mixed to the correct proportions, can be self-ignited. In many fires with thermal radiation from existing flames, a nearby layer of hot product gases, or hot walls in close proximity to the surface are the primary reasons why as-yet-unburned material ignites into flame. This ignition may be spontaneous (self-ignition) or piloted. The most rigorous test (for the material) exposes the heated surface

---

[11] This discussion is taken almost verbatim from I.S. Wichman's unpublished report "A Review of the Literature of Material Flammability, Combustion and Toxicity Related to Transportation".

to a pilot flame. The two kinds of pilot flames are continuous and intermittent. Unless a gas flow is present, the continuous pilot may alter the energetics of the flammability test, bathing the sample in an additional stream of heat. For "static" flammability tests, the intermittent pilot test is preferred. Recent work in flammability analysis and testing, however, has emphasized the greater reality of the continuous pilot and the gas cross flow [40,42].

In Refs. [59,60], explanations are provided for the differences in the dependence of the critical heat flux for thermally thick and thin materials. The model of [60] is more detailed as it considers convective cross flow. For incident heat flux below the critical value, the heated surface will not undergo piloted ignition even if heated indefinitely. Above the critical heat flux, ignition is possible. The explanation in [59] rested on the formulation of a simple model consisting of an energy equation in the heated solid integrated over the heated surface. For thin fuels of thickness l

$$\tau_{ig} = \rho_s C_{ps} l (T_{ig} - T_\infty) / \dot{q}_{ig},$$

while for thick fuels of infinite thickness

$$\tau_{ig} = \rho_s C_{ps} \lambda_s (T_{ig} - T_\infty)^2 / \dot{q}_{ig}^{\,2}$$

for piloted ignition with continuous external flux $\dot{q}_{ig}$. The temperatures T_∞ and T_{ig} denote values of the ambient and surface at the moment of ignition, respectively. Experimental data plotted in this manner fall accurately into straight lines conforming both the qualitative and quantitative accuracy of the theory [59]. The critical heat flux is obtained by extrapolating these straight-lines plots to $\tau_{ig} = \infty$. The more detailed examination of [60], however, indicates that simple extrapolation is often inaccurate

because other physics, such as convective flow, became important. Thus, the preceding conclusions break down near the critical flux, $\dot{q}_{crit-ig}$.

The above correlations relate τ_{ig} and $\dot{q}_{ig}$. If in addition to the fuel surface: 1) The narrow nearby gas region is also heated to T_{ig}; (2) The concentration of the reactants – including the gaseous oxidizer – renders this heated layer of gas flammable; (3) The mass gasification rate is sufficiently high, then a self-sustaining flame may be produced over the heated combustible surface. Transition from ignition to flaming will occur, resulting in fire initiation.

Many experimental methods have been developed for investigating the ease of ignition and material flammability. Generally the fuel sample, whether in a vertical or horizontal position, is exposed to external radiation in the presence of the pilot flame. The time required to initiate sustained flaming is measured along with the sample surface temperature [61]. These data are correlated to produce an empirical ignition criterion. The ignition criteria proposed to date are several: critical surface temperature T_{ig} at ignition; critical fuel mass flux [62]; critical mean solid temperature [63]; for cellulosic or charring materials, critical char depth [64]. According to [61], "The critical fuel mass flux at ignition seems to be physically the most correct, but surface temperature has proved to be the most useful since it can be conveniently related to the fire spread rate". These four criteria are indirect measures of ignition, though they are presumed to be closely related to ignition. The actual ignition requires first that the heated solid fuel chemically decompose, resulting in the injection of fuel gases into the surrounding oxidizer to produce a flammable mixture that is ignited by the nearby pilot flame or which can self-

ignite. In order to achieve sustained ignition, the fuel production rate from the decomposing condensed fuel must be sufficient to produce a flame with a heat release large enough to overcome heat losses to the surface and ambient surroundings.

A full computational description of material ignition requires a transient multidimensional model for the simultaneous processes of solid phase thermophysical decomposition and gas phase mixing, transport and combustion. Progress toward such computationally intensive models has been made [40,42]. According to [61] the "absence of such comprehensive models has necessitated the various attempts to develop the (empirical) ignition criteria" that have been described above. Our intention in this chapter is to continue the further development of such full, computational models with especial emphasis in processes occurring in the condensed phase. In-depth material phenomena have been included with notable successes for charring materials [65] in which an important component of the model is the solid advection term representing the transient in-depth mass loss. The latter model, we note is considered in isolation from the adjacent gas phase except through the action of interface boundary conditions.

Our work is preceded by others examining similar questions. In [60] the focus was on convective influence and their effect on ignition in the difficult low-flux, long-ignition-time regime. In [40,42] the emphasis has been on the development of a full, 3-D transient model of ignition by external flux of cellulosic in a cross-flow of gas (oxidizer). In neither of these models was detailed solid (or condensed phase) energy transport considered. In [60] it was not considered at all, thus enabling further theoretical development along the lines of [61]. In [55] the model was used for making comparisons with similar experiments and has provided a detailed examination of condensed-phase

energetics. No analytical correlations were developed. Thus, an approach will be used here to further the development – if possible – of theoretical correlations that can represent solid (condensed) fuel ignition. In our work, the ignition of polymers is investigated in a transient two-dimensional configuration with a channel cross-flow in the gas phase, melting and pyrolysis in the condensed phase, and radiation loss at the interface. The ignition model employs two flow patterns, one from a Navier Stokes calculation, and one using Oseen approximation for the gas flow. The complications they influence for the ignition processes will be compared in terms of different heat transfer mechanisms. The condensed phase influences ignition by changing the conductivity, by adding a latent heat sink in the condensed phase and by changing the latent heat and the heat capacity. The sensitivity of the ignition behavior with respect to the material properties is investigated for each flow pattern. A simple ignition theory is derived to interpret the ignition delay with respect to two non-dimensional material property-based parameters. The ignition theory, by using an energy balance principle, predicts the ignition delay time that is computed from the ignition model.

2. Results and Discussion

The mathematical model is the same as Chapter 4. In addition, initially an external radiation heat flux of ($5W/m^2$) is applied at the region from x=9mm to x=12mm. Two situations of ignition are studied, that is, the one with assumed flow field (Oseen approximation), and the one with realistic flow field (Navier Stokes calculations). The thermal and chemical properties are listed in Table 1 in Chapter 4. The kinetic data in Table 1 are such that they result in the ignition establishments for both cases. It is worth noting that the kinetic data in [55], which employs the Oseen approximation, cannot

support an ignition event for the Navier Stokes model. The kinetic data generally determine the possibility of ignition establishment and they influence the magnitude of the ignition delay time. The selection is such that below a lower limit for the kinetic parameters the heat loss is so high that the ignition cannot be established; beyond a higher limit the reaction overwhelms the heat loss and leads to explosion [66].

2.1 Ignition Delay Time

We first discuss the ignition criteria. These criteria can be defined in several different ways, for example, the gas reaction rate, the surface temperature, the interface heat fluxes, or the mass flux of volatiles from the fuel surface. They may take different forms but must ideally characterize a unique instant of time. In the numerical model, ignition has initiated flame once the "self-supportive" heat flux feeding the condensed phase is "large enough" ($10W/cm^2$). The notion of "self-supportive" indicates that this heat flux comes solely from the gas conduction, not external radiation ($5W/cm^2$), implying that once the external radiation is removed after ignition the flame can propagate itself. As indicated from the chemical kinetics, a higher pre-exponential factor will generate more heat, thus a higher temperature gradient at the interface. A lower activation energy will lower the threshold of the chemical reaction, which results also in a higher temperature gradient. Since the temperature gradient determines the conductive heat flux, the ignition time itself can be characterized by the heat flux. The ignition delay time is defined as the elapsed time to ignition from the moment external radiation was first applied. Figure 1 reports the ignition time vs. (a) $1/St$, (b) $\overline{k}_l$, and (c) $\overline{C}_{Pl}$ for the two numerical models using different flow patterns. It is observed that the ignition delay times for the two flow patterns are different in magnitude for identical values of $1/St$, $\overline{k}_l$ or $\overline{C}_{Pl}$. The

difference arises from the interaction of the flow with the condensed phase, which will be examined later in terms of the global energy balance principle. Examination of the ignition delay time as a function of $1/St$, or $\bar{k}_l$, or $\overline{C}_{Pl}$ in Figures 1 and 2 allows ready explanation of the physical influence of the material properties. First, the ignition delay time increases with $1/St$. The factor $1/St$ is proportional to the latent heat of melting; hence the increase of $1/St$ increases the energy barrier for heating the condensed phase and hinders the ignition. The limit of non-melting is attained when $St \to \infty$, which is the regime of solid ignition. Second, the ignition delay time increases with $\bar{k}_l$. A higher $\bar{k}_l$ denotes a higher liquid thermal conductivity, facilitating the loss of the energy in the condensed phase. The higher liquid conductivity removes the energy accumulation near the interface by conduction, extending the ignition delay time. The ignition delay time increases with $\overline{C}_{Pl}$. A higher liquid heat capacity requires more liquid preheat for the same temperature rise of the condensed phase, thus a longer ignition delay. Figure 1 shows the physical trends as discussed above. Notice that the ignition delay time always shows a linear dependence with respect to the three non-dimensional parameters. These linear relationships between the ignition delay time and $1/St$ and $\overline{C}_{Pl}$ will later be examined by a simple theory that uses an overall or integral energy balance principle. The relationship between the ignition delay time and $\bar{k}_l$ is only qualitatively explained here since it involves more complex phenomena. The $\bar{k}_l$ value changes not only the temperature distribution, but also the liquid thickness, as seen in Figures 9 and 10.

2.2 Heat Transfer Mechanisms at Interface

During pre-ignition, four types of heat transfer mechanisms occur at the interface to

form an energy balance. They are heat conduction from the gas phase, heat conduction from condensed phase, radiation heat loss to the environment, and radiation from the external heat source. The last quantity is assumed to be 100% absorbed at the interface. This treatment of radiation has neglected the effects of volatile radiation absorption from the external radiation source, gas phase radiation emission (and scattering), and the absorption of the gas phase radiation at the surface. These assumptions are introduced for convenience, and have been used in models before [67]. However, Kashiwagi [68] showed that the volatiles might absorb external radiation directed toward the surface up to as much as 70% of the total for both PMMA and red oak in quiescent air. This evaluation of the radiation influx is thought to be not critical in the current modeling since: (1) The longitudinal applied flow field is applied over the polymer surface in this modeling, resembling the situation of a horizontal radiation source applied to a vertical plate. Therefore the radiation absorption via fuel could describe a significantly different situation in that the cross flow sweeps the absorbing and scattering pyrolysis products downstream away from the ignition source; (2) The radiation heat flux in this case is 5 (W/cm^2), which corresponds to a lower external radiation heat flux than in experiments, and represents a less severe case since radiation absorption decreases with the decrease of the external radiant heat flux. The convenience of using the assumptions also stems from the fact that it is not possible to quantitatively identify each radiation mode and its isolated influence on ignition, by either experiment or theory. The authors acknowledge that radiation is so complex an issue that it may deflect attention from the main subject of this paper, that is, the influence on ignition of flow pattern and condensed phase. At the interface only the heat loss of surface re-radiation to the ambient is included, and its

presence does not substantially influence the magnitude of the self-supportive heat flux, as will be seen. The energy balance is constructed such that the external radiation is the sum of the remaining three terms.

Figure 2 and 3 give the dependence of the four heat transfer mechanisms on the three non-dimensional parameters $1/St$, $\bar{k}_l$, and $\overline{C}_{Pl}$. The magnitudes of these mechanisms are obtained by numerical integration over the entire interface and over time. Physically they denote the overall accumulated effects from the start of preheating to the moment of ignition. The numerical derivations of these mechanisms are given in Appendix V. Several useful points can be drawn from these figures. First, the total external radiation behavior is observed to resemble that of the ignition delay time, since it is a linear function of the ignition delay time. Second, solid phase conduction at the interface is the major mechanism that heats the condensed phase, since the combustion reaction is negligible before ignition. It is observed in Figures 2 and 3 that the majority of the external radiation goes from the surface into condensed phase conduction. The rest returns to the gas phase by conduction from the surface, which is used to heat the gas, and to the radiation heat loss to the environment through the surface "re-radiation" term. The heated gas then flows downstream and finally exits the channel. Third, when radiation heat loss and gas phase conduction are compared for Navier Stokes and Oseen approximations, it is found that gas phase conduction is smaller than radiation in the first case and opposite in the second. This can be explained by appealing to the interface temperature (see Figure 13). Since the interface temperature in the first case is larger than in the second case, the radiation. Fourth, condensed phase conduction is almost constant in Figures 2-b and 3-b, unlike the trends with varying St and $\bar{k}_l$. As a coarse deduction,

since higher $\bar{k}_l$ gives higher ignition delay time (Figure 1-b), it appears to have a lower heat flow rate via condensed phase conduction. It is further deduced that the temperature gradient in the condensed phase at the interface is much lower; and the thickness of the liquid layer on average is possibly larger. The implications of this fact on the temperature field and heat flux will be presented later.

2.3 Heat Transfer Mechanisms in Control Volume

Figures 4 and 5 give the heat transfer mechanisms for the two flame models: external radiation, combustion heat, pyrolysis, and gas convection. The gas enthalpy increase is also given with reference to the initial condition. As seen from these figures, both reaction rates of combustion and pyrolysis are negligibly small before ignition. Seeing that the combustion heat will be dominant after ignition, a transition is necessary. The gas enthalpy increase is small compared to the other heat transfer mechanisms, mainly because of the low volume heat capacity of the gas phase. Convection has a magnitude comparable to surface re-radiation. The sum of both constitutes the major heat loss up to 25% of the total radiation influx during ignition. The influences of flow are also compared in Figures 4 and 5. The most salient one is that with the uniform flow pattern (Oseen approximation), the streamwise convection has a higher magnitude (and certainly a higher percentage of the total flux). The reason is straightforward since the Oseen approximation removes the boundary layer, replacing it with a uniform flow velocity at the interface. The resulting convection is larger on average. Another important finding is that the Navier Stokes flow pattern has a larger percentage of the combustion heat in the total flux; and the model with the assumed flow pattern shows the opposite. This phenomenon can be explained by the difference in the flow pattern. The Navier-Stokes

model introduces two new factors. One is the interface boundary layer flow, and another is the normal hot fuel flow from the interface toward the gas into the flame. The former decreases the longitudinal flow velocity, thus increasing the residence time of the fuel and oxidizer, helping maintain higher concentrations of fuel and oxidizer. It also helps to maintain a higher gas temperature because of the reduced convection near the interface. The normal flow out of the interface improves the mixing of the fuel and oxidizer compared to the case without flow at the interface. Remember that the flow out of the interface is hot volatile gaseous fuel; it is one factor that facilitates the establishment of the combustion reaction. Overall, the realistic flow pattern has a higher temperature near the interface, a high reaction rate, and a high heat flux. A higher temperature at the interface is observed in Figure 14(a), where the temperature profile as a function of the transverse distance is plotted. The temperature peak in the realistic flow configuration (Navier Stokes) is almost 100K larger than the Oseen flow. The higher heat flux (observed in Figure 11(b)) will be examined later.

2.4 Enthalpy Increase of Condensed Phase

During the period starting from preheating to ignition, the enthalpy increase of the condensed phase is of direct interest to the ignition delay time. Figures 6 and 7 give the latent enthalpy increase due to melting, the sensible enthalpy increase due to temperature rise of both liquid and solid phase, and the sum of the latent and sensible enthalpy increases, herein named the total enthalpy increase. Analysis of these figures indicates that the sensible enthalpy increase is several times larger than the latent enthalpy increase. This is mainly because low magnitude conductivities are used. The resulting liquid layer is generally small in the model. The temperature field characterizes the liquid

layer thickness in the condensed phase, which is plotted in Figures 9 and 10 where the solid-liquid interface corresponds to the temperature 500K. From Figures 6 and 7, the total enthalpy increase is always a linear function of the abscissas. This important finding helps us to construct a simple theory to account for the ignition delay time vs. $1/St$ and $\overline{C}_{pl}$. Another perspective of the same finding is given in Figure 8 showing the average heat flux for the two cases. They are constant no matter what the values of $1/St$ or $\overline{C}_{Pl}$. Observations indicate that the flow patterns do not change the average heat flux with respect to $1/St$. They do, however, with respect to $\overline{C}_{Pl}$. The latent increase is linear with $1/St$; however, it does not depend on $\overline{C}_{Pl}$. The latter phenomenon indicates that the liquid mass in the condensed phase is nearly a constant regardless of the magnitude of the liquid heat capacity.

A final remark is made here concerning the energy balance in the condensed phase. Recall that the heat conduction at the interface and pyrolysis heat are the major heat transfer mechanisms to the condensed phase. The net heat to the condensed phase can be obtained by simply subtracting the pyrolysis heat from the conduction heat, and is equal to the total enthalpy increase of the condensed phase. This was verified directly from the numerical results.

2.5 Field Phenomena in Condensed Phase and at Interface

The role played by the flow pattern can be observed by comparing Figures 9 and 10, where the isotherms at ignition are given. The gradient of the temperature can be estimated from the number of contours in a given region. The most significant difference is the reactive region, which hangs above the interface. It provides heat after the external

radiation is removed. In the Oseen model, the temperature gradient is lower since the constant levels filling the reactive region are not so densely distributed. Numerically, the resulting net heat flux to the condensed phase is obtained by subtracting radiation from gas conduction. The magnitude of the ignition heat flux peak shows a difference of 2 W/cm^2 by comparing the two models. This observation leads one to relate it to the influence of the flow pattern. Compared to the realistic flow pattern, the use of the Oseen velocity profile decreases the residence time of fuel and oxidizer, and accelerates the rate of heat removal, thus finally strengthening the interface cooling and decreasing the net heat flux to the interface. The surface temperatures are plotted in Figure 12, showing that a lower surface temperature results from the Oseen model. This is consistent with the application of a higher convective cooling rate to the vicinity of the interface. The interface mass flow rates for the two models are plotted in Figure 13. As observed in the figure, the mass flow rate in the Oseen model is so low that its magnitude is almost half of the realistic flow model. The low transverse mass flux again reflects the enhanced streamwise convection near the surface due to the Oseen model. In summary, the Oseen model results in a weaker reactive region, smaller size of flame, and lowered heat and volatile mass flux at interface. This statement is supported by the temperature profile (Figures 9 and 10), heat flux (Figure 11), surface temperature (Figure 12), and mass flow rate (Figure 13).

The relative orders of magnitude between the radiation heat losses at the interface and heat conduction at the interface as seen in Figures 2 and 3, can be explained readily in terms of surface temperature. Obviously the Oseen ignition model has a lower surface temperature, resulting in a lower radiation loss. This is why the order of the magnitude

with respect to gas conduction and radiation loss in Figure 2 is reversed in comparison with Figure 3.

It is interesting to point out that the Oseen approximation, although it enhances convection, yields a lower ignition time. This is contrary to the intuited speculation that enhanced heat loss requires a larger ignition time. The explanation of this behavior must depend on the critical condition of ignition. That is, ignition is established if the overall heat gain surmounts overall heat loss. Notice that the use of the Oseen approximation mainly enhances interface cooling, thus resulting in a lower surface temperature through its contribution to the interface energy balance. The decreased interface temperature significantly decreases the radiation heat loss. The heat flux that is required to overcome this heat loss, therefore, is not as high as the Navier Stokes case. That is why, we believe, we observed a weaker reaction and diminished flame size but shorter ignition delay. In an overall sense, the thermal energy content of a "ball" of gas near the incipient flame is larger than for the realistic flow case. From Figure 11, negative heat flux to the condensed phase is observed around the edges of the preheating region, indicating the effect of the heat loss. The heat loss effect is attained there because the combustion in the gas phase is too small to compensate for the loss of heat by gas conduction and radiation. The heat loss is significant because external radiation has been removed. In addition, the levels of heat flux correspond to the energy barriers that the gas conduction is expected to overcome at ignition. Taking $St = 2$ as the reference state, the other heat fluxes follow well with their corresponding magnitudes for the energy barrier, as analyzed before. The mass flux, as shown in Figure 13, shows that higher $\bar{k}_l$ corresponds to a higher mass flux because $\bar{k}_l$ determines the thickness of the liquid layer and therefore the pyrolyzed mass

flux. As seen from Figures 9 and 10, the $\bar{k}_l$ value does determine the liquid thickness, in contrast to $1/St$ or $\overline{C}_{Pl}$, whose values do not affect the liquid layer thickness.

2.6 Influence of External Radiation

A range of external radiation heat fluxes is selected in order to evaluate their influences on ignition. The range, which is from 1 W/cm^2 to 9 W/cm^2 with a step of 1 W/cm^2, encompasses the range used in [61] in order to make comparisons. To facilitate analysis, the condensed phase is first fixed to the reference state $St = 2$, and then $St = 100$. The relationship between the ignition delay and the external radiation is obtained. From the numerical results, the first observation is that the condensed phase cannot support ignition below a certain limit. For the Navier Stokes model the limit is 4 W/cm^2; for the Oseen model the limit is 3 W/cm^2. Numerically there is no ignition observed for an extremely long time. This result supports observations in experiments and a statement in the introduction, that is, there exists a critical heat flux below which no ignition can be supported. The cases that yield successful ignitions are plotted in Figure 14(a), which presents the calculated ignition delay for two flow models. Four computational cases are plotted with different flow model and St. A general observation is obtained. Qualitatively, with the increase of radiation heat flux $\dot{q}_{ig}$, the ignition delay decreases. The Oseen model results in a lower ignition delay and a smaller range of radiation heat flux yielding ignition. These are consequences of enhanced convection heat loss as discussed before. The second observation is that Figure 14 gives $\tau_{ig} \propto (1/\dot{q}_{ig})^2$ for both $St = 2$ and $St = 100$. The *square* relationship between τ_{ig} and $1/\dot{q}_{ig}$ indicates that the ignition in this modeling is for *thermally thick polymer* [59].

Furthermore, by comparison of $St = 2$ and $St = 100$, melting does not change the qualitative relationship of $\tau_{ig} \propto (1/\dot{q}_{ig})^2$ though yields a less steep curve than the pure solid (as a consequence of higher energy barrier). By observation, the Oseen or Navier Stokes flow pattern does not change this square relation either.

Figure 15 shows the dependence of the surface temperature on the magnitude of external heat flux. It is interesting to point out that a higher radiant flux generates a higher surface temperature, as indicated by the order of the peak temperature from Figure 15. This finding indicates again that the ignition temperature does not stand out as a good sole characteristic of ignition. Instead, ignition is better characterized by coupled parameters between both gas phase and condensed phase. However, the surface temperature is a useful engineering measure due to its simplicity. In Figure 15, the difference between the three cases is small compared to the maximum surface temperature. Figure 16 shows the surface temperature history for three radiation heat fluxes. The curves plotted in Figure 16 resemble Figure 3 in [61]. In addition, the numerical results show that there is a "jump" of temperature during ignition, which breaks the smoothness of the curves in Figure 16. The "jump" indicates the instability of the ignition event as a consequence of the chemical kinetics. The transient instability in fact causes the difficulty in defining the surface ignition temperature. This is possibly the case for the measured surface temperatures at ignition in [61], which did not show complete smoothness and some transient variability appeared.

2.7 Simple Theory for Ignition Delay – Influence of Condensed Phase

In order to investigate the influence of the condensed phase on ignition delay, the external radiation heat flux is fixed while changing the condensed phase properties.

Energy balance analysis is used to quantify the functional dependences of ignition delay on $\overline{C}_{Pl}$ and St. Two radiation heat fluxes, 5 (W/m^2) and 9 (W/m^2), will be used to show the validity of this theory, using the former as an exemplar case to deduce the theory. We first set the scope for the case of varying $\overline{C}_{Pl}$ since it shows a uniform behavior for liquid mass. Taking the whole condensed material as a control volume (see Figure 1), the energy balance states that

$$Q_{tot} = Q_{sen} + Q_{lat}. \tag{1}$$

The sensible heat is defined as a function of temperature increase of both solid and liquid,

$$\begin{aligned} Q_{sen} &= \iint_{CV} \rho_c C_{pc}(T - T_0)dxdy \\ &= \iint_{CVL} \rho_l C_{pl}(T - T_0)dxdy + \iint_{CVS} \rho_s C_{ps}(T - T_0)dxdy \\ &= \Delta H_{liquid} + \Delta H_{solid}. \end{aligned} \tag{2}$$

where CVS and CVL represent the solid and liquid volumes respectively. The latent heat is characterized by formation of the liquid,

$$Q_{lat} = L_s * m_{liquid}, \tag{3}$$

where m_{liquid} is obtained from

$$m_{liquid} = \iint_{CVL} \rho_c dxdy. \tag{4}$$

In order to derive a relation for the ignition delay, three statements are made, among which two are derived from numerical observations; one is used as an assumption. The first statement is that the net heat flow rate (J/s) into the condensed material is identical over a range of $\overline{C}_{Pl}$. That is

$$\overline{q}_{ig} = Q_{tot} / \tau_{ig} \tag{5}$$

where τ_{ig} denotes the ignition time. This is already supported in Figure 8. Note that $\overline{q}_{ig}$ is different from $\dot{q}_{ig}$ in that it is a spatially integral quantity with unit of (J/s). On the contrary, $\dot{q}_{ig}$ has a unit of W/m^2. The second statement is that the liquid is independent of $\overline{C}_{Pl}$, as shown in Figures 6-c and 7-c respectively. Because we use constant latent heat, the liquid mass is independent of $\overline{C}_{Pl}$. We have

$$\tau_{ig} = (\frac{m_{liquid} L_s}{\overline{q}_{ig}} + \frac{\Delta H_{solid}}{\overline{q}_{ig}}) + (\frac{\Delta H_{liquid}}{\overline{q}_{ig}}). \tag{6}$$

where ΔH_{liquid} can be written as $\Delta H_{liquid} = \rho_l C_{Pl} \iint_{CVL} (T - T_0) dxdy$ since ρ_l and C_{Pl} are all constants. By using $C_{Pl} = C_{Ps} \overline{C}_{Pl}$, we deduce the following ignition formula based on the numerical integration.

$$\tau_{ig} = (\frac{m_{liquid} L_s}{\overline{q}_{ig}} + \frac{\Delta H_{solid}}{\overline{q}_{ig}}) + (\frac{\rho_l C_{ps} \iint_{CVL} (T - T_0) dxdy}{\overline{q}_{ig}}) * \overline{C}_{Pl} \tag{7}$$

In order to derive the linear curve in Figure 1(c), a third statement is introduced by assuming that $\iint_{CVL} (T - T_0) dxdy$ is a constant. Its physical meaning is that the temperature distribution in the liquid layer does not depend on C_{Pl}. If the "temperature excess" in the heated volume depended upon $\overline{C}_{Pl}$, its value should appear in this hypothetical relationship. In this way, τ_{ig} can be determined as a linear function of $\overline{C}_{Pl}$. The calculation of this ignition theory is carried out for four different values of $\overline{C}_{Pl}$

including 0.5, 0.75, 1.0, and 1.25. The intercepts and slopes are determined from each case separately. Figure 17 shows the ignition delay time (a lines) calculated from this theory and the direct result (solid line). The agreement is satisfactory since the realistic values lie in the range of predicted sets from the simplified ignition theory. In terms of slope and intercept, the error is within 10%, as observed from Figures 17. The verification of the theory indicates that the energy balance can be very useful for interpretation of the realistic ignition delay time. This analysis also lends support to the numerical model.

The relationship between ignition delay time and St is discussed here. Slight manipulation of Equation (1) yields a linear relationship between the ignition delay time and $1/St$,

$$\tau_{ig} = [\frac{Q_{sen}}{\bar{q}_{ig}}] + [\frac{m_{liquid} C_{Ps} (T_m - T_\infty)}{\bar{q}_{ig}}] * \frac{1}{St} \qquad (8)$$

Another assumption is introduced here by stating that m_{liquid} is independent of St. This assumption is not stringent as will be seen. The numerical calculation of Equation (8) is presented in Figure 18. There exists a broader range of ignition delay time encompassing the realistic case. The slope does not match very well with the predictions. This comes directly from the assumption of constant liquid mass, which in fact is a weak linear function of $1/St$. However, we can use this range of ignition delay time to estimate τ_{ig}. As engineering approximations such estimates appear useful.

The dependence of ignition delay time on $\bar{k}_l$ cannot be obtained directly by this simplified ignition theory. Only qualitative conclusions can be obtained because of the nonlinear behavior of the liquid layer thickness and temperature profiles, as discussed

previously.

It is important to note that the examination of this section differs fundamentally from that of Section 3.6. In Section 3.6 the influence of external radiation on ignition delay was examined by changing the radiant flux $\dot{q}_{ig}$. In this section, the influence of the condensed phase is examined *by fixing* $\dot{q}_{ig}$ and changing only the material properties. In addition, $\overline{q}_{ig}$ is the net heating rate (W) into the condensed phase while $\dot{q}_{ig}$ is the radiation heat flux (W/m^2).

3. Conclusions

A two-dimensional ignition model is examined for two different flow patterns, the one with a realistic flow (Navier Stokes calculation) and the one with an assumed flow (Oseen approximation). The latter model, which eliminates the mass and momentum equations from considerations and eliminates influences of thermal expansion, is of course by far the simpler of the two models. The physical phenomena considered in the models include channel flow and combustion reaction in the gas phase, pyrolysis and melting in the condensed phase, radiation heat loss and mass flow at the interface. Ignition was investigated by means of an integral energy balance analysis. The field parameters such as temperature, heat flux, and mass flux were also used in order to interpret the ignition mechanism. From the numerical results, the flow pattern has an impact on the ignition process. It influences the magnitude of the ignition delay time, the interface heat balance, and the reaction rate. The use of the Oseen approximation enhances interface convection; thereby decreasing the interface temperature. The decreased radiation loss, in turn, helps to produce a shorter ignition delay time. In

general, the Oseen model results in a weaker reactive region, smaller size of flame and lowered heat and mass flux at the interface. The influence of condensed phase material properties such as latent heat, conductivity, and heat capacity are investigated for each flow pattern. A theory to determine the ignition delay time is derived from the numerical observations by employing the energy balance principle. The predicted ignition delay times agree well with the direct numerical results. The theory is useful for interpreting and estimating the ignition delay over a range of values calculated from numerical cases. The influence of the external radiation is investigated by changing its magnitude in a wide range. The numerical results indicate that the ignition time is approximately inverse to the *square* of the radiation heat flux. The square relationship indicates that the ignition under this study is for "thermally thick" polymer [59]. The melting does not change the square relationship though yields a less steep curve than the pure solid as a consequence of higher energy barrier. In addition, the surface temperature at ignition is found to be dependent on the external heat flux. The higher radiant heat flux generates a higher surface temperature. This indicates the limitation of using temperature as the measure of ignition in real multiphase coupled systems.

From computed results, it is clear that the realistic cross flow influences ignition and subsequent flame spread. The qualitative dependence, however, is unchanged except for some isolated (but important) features of the problem. One of these is the reversal of ordering between radiation loss and convective loss, which (apparently) plays a role in the ignition time calculation, producing a slightly shorter delay for the Oseen case as both surface temperature and radiant losses to the surroundings were diminished. We did not quantify the influence of realistic cross flow, nor did we quantify the influence of thermal

expansion in the gas (which effects are permitted when the velocity field is allowed to vary). One might expect that thermal expansion should dissipate the heated layers, making ignition more difficult. In other words, as the layer of gas adjacent to the surface is heated, thermal expansion enlarges this region while simultaneously diminishing its temperature. The result is a larger ignition delay. Our work suggests that before analyzing detailed flow processes, theoretical models of ignition in gases of variable density may yield useful results. The coupling of local thermal expansion with gravitationally induced (buoyant) flow can also substantially influence ignition.

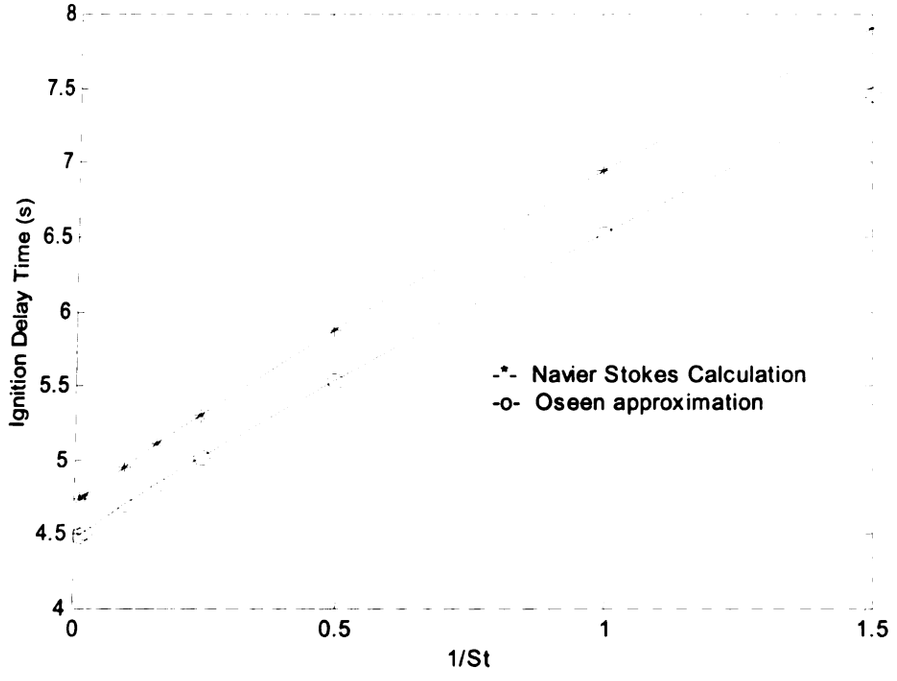
Ignition Delay Time (s)
1/St
-*- Navier Stokes Calculation
-o- Oseen approximation

(1-a)

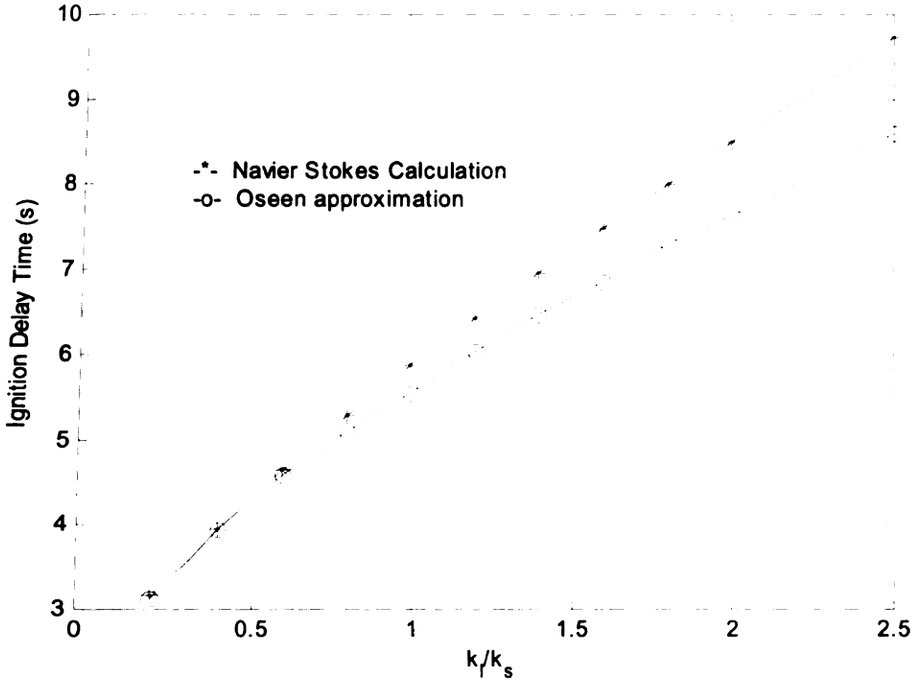
Ignition Delay Time (s)
k_f/k_s
-*- Navier Stokes Calculation
-o- Oseen approximation

(1-b)

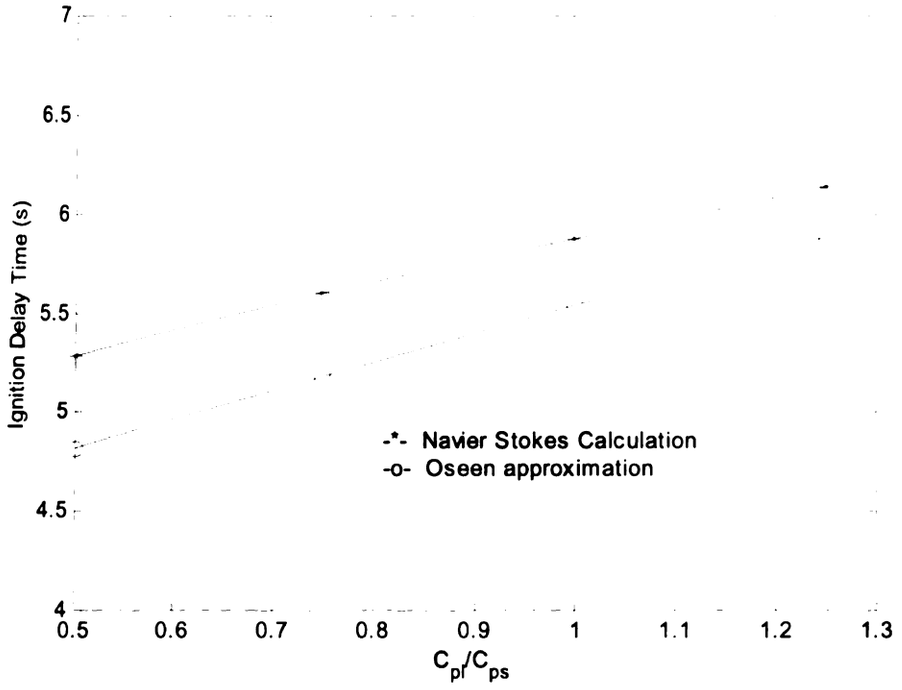

(1-c)

Figure 1 Ignition time vs. (a) $1/St$ (b) $\bar{k}_l$ (c) $\overline{C}_{Pl}$ for the Navier Stokes model and the Oseen model.

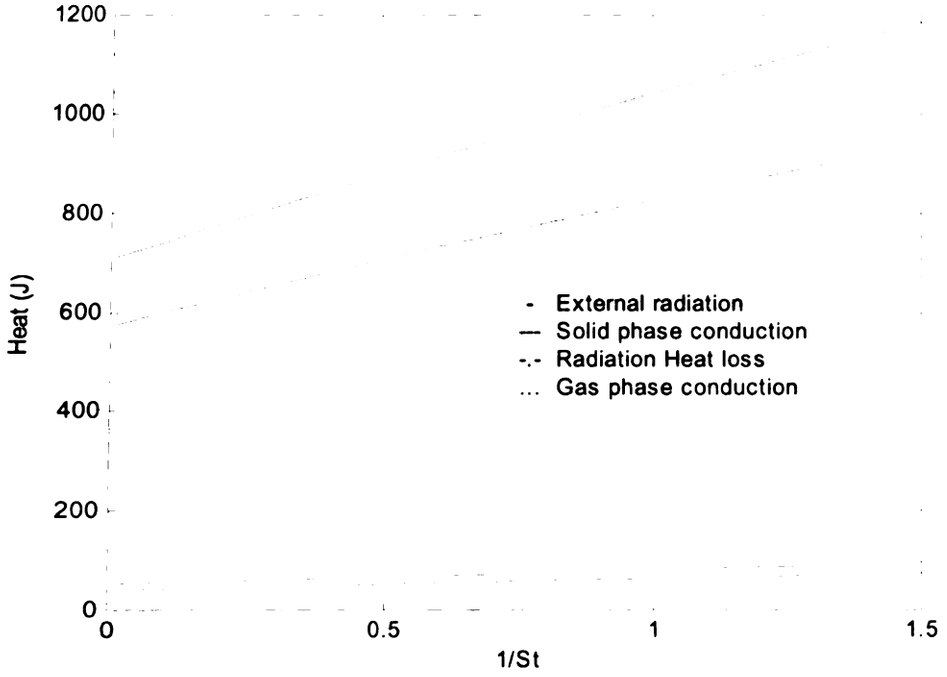

(2-a)

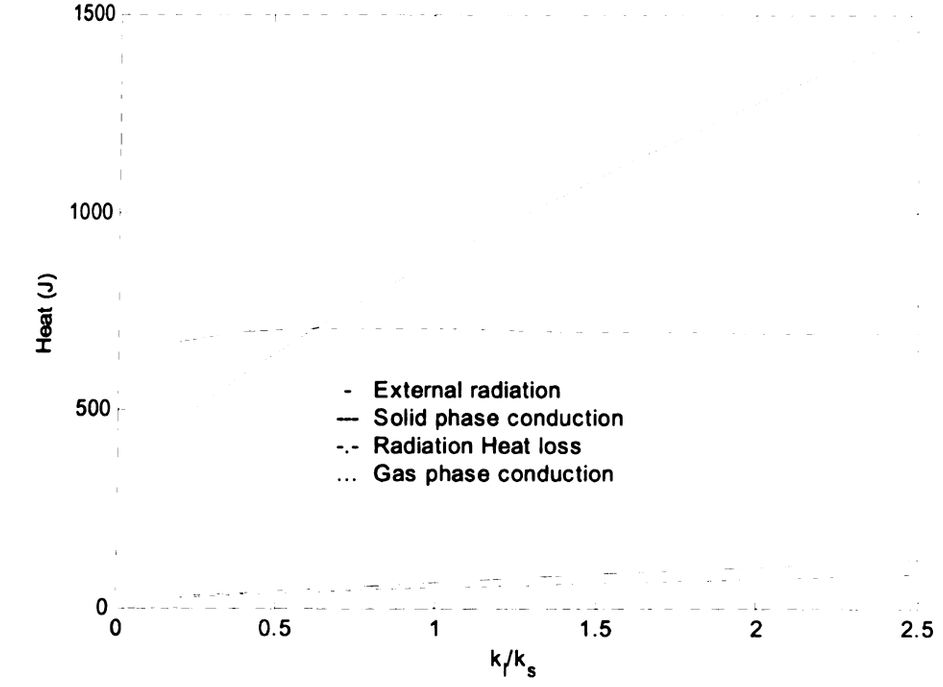

(2-b)

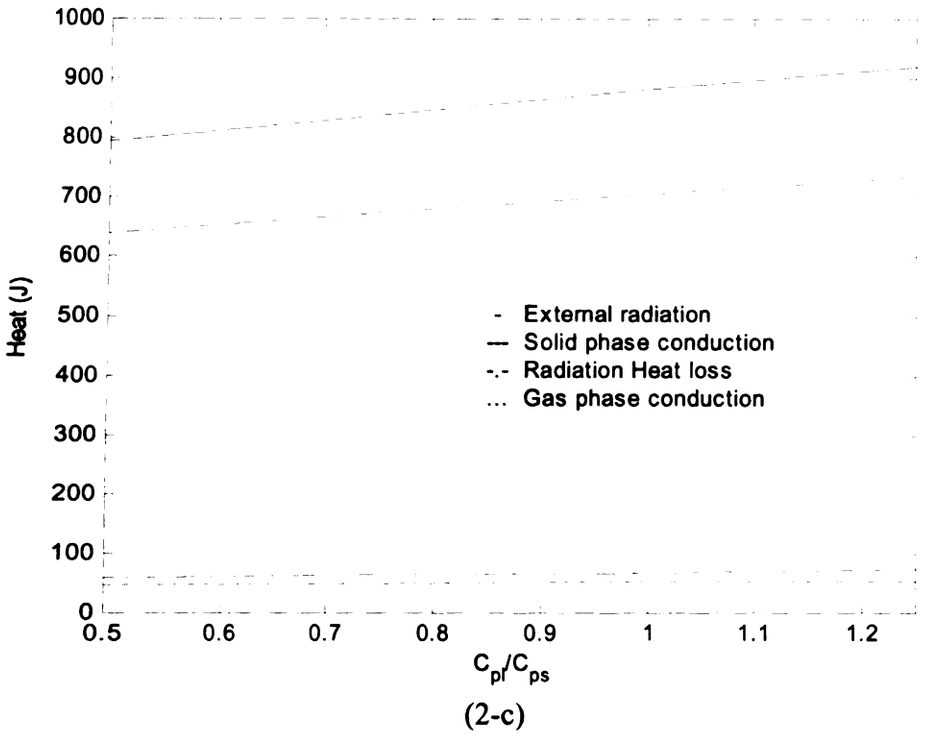

(2-c)

Figure 2 Four heat transfer mechanisms at the interface vs. (a) $1/St$ (b) $\overline{k}_l$ (c) $\overline{C}_{Pl}$ for the Navier Stokes model.

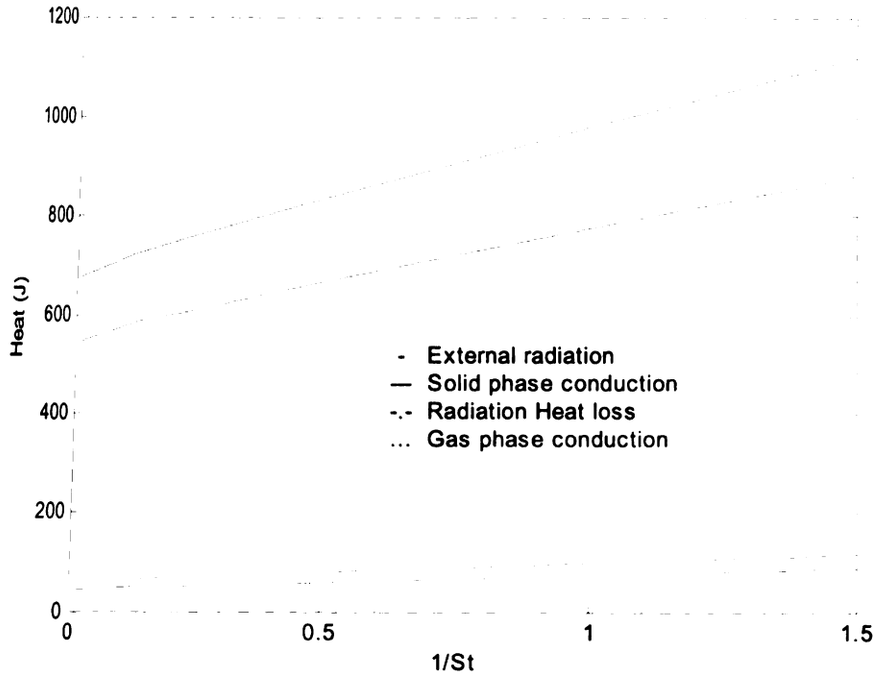
1200
1000
800
600
400
200
0
Heat (J)
0
0.5
1
1.5
1/St
- External radiation
— Solid phase conduction
-.- Radiation Heat loss
... Gas phase conduction

(3-a)

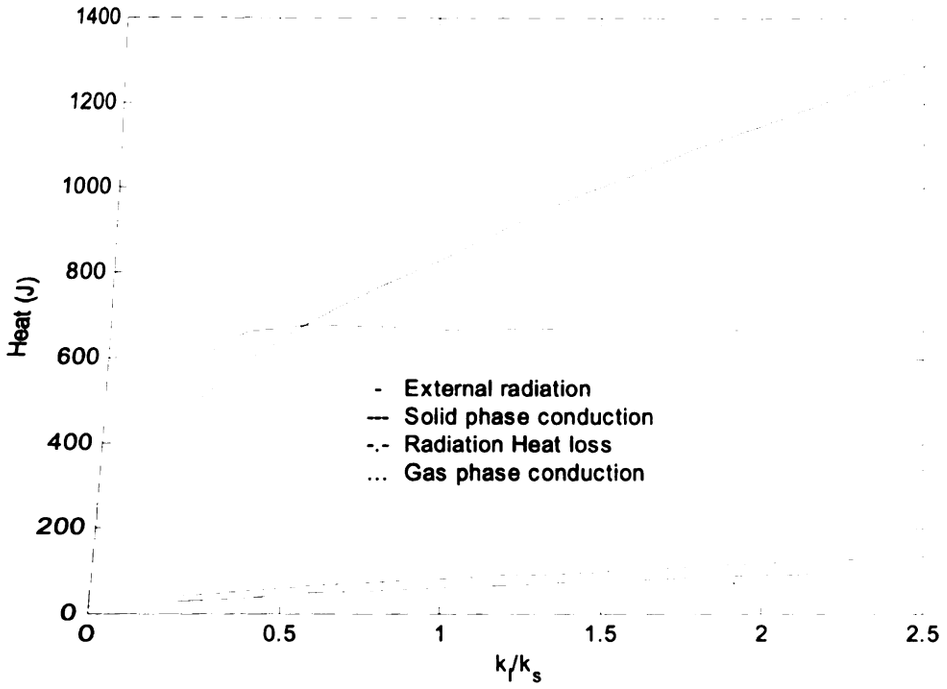
1400
1200
1000
800
600
400
200
0
Heat (J)
0
0.5
1
1.5
2
2.5
k_f/k_s
- External radiation
— Solid phase conduction
-.- Radiation Heat loss
... Gas phase conduction

(3-b)

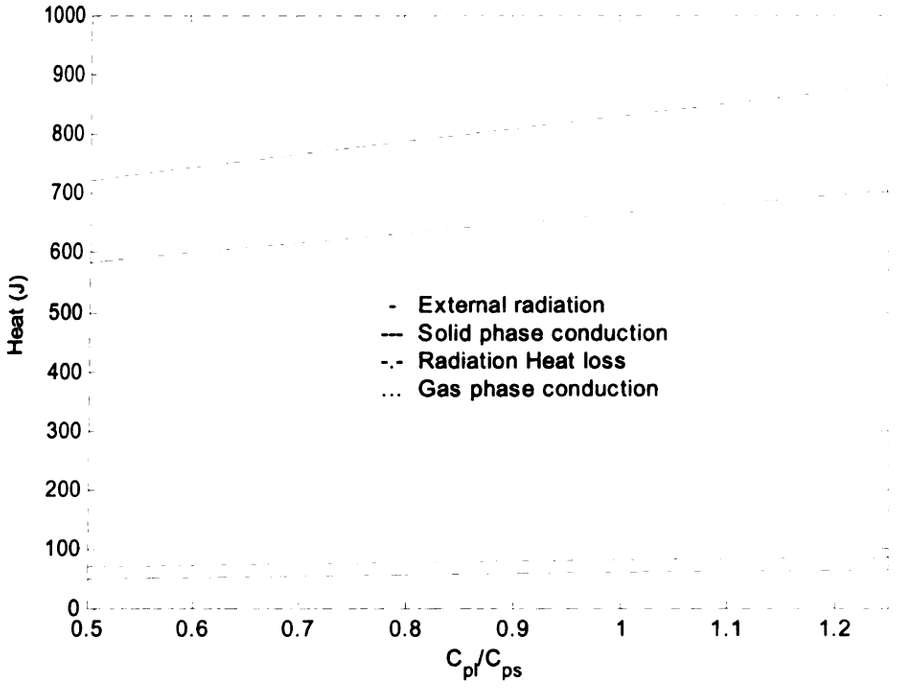

(3-c)

Figure 3 Four heat transfer mechanisms at the interface vs. (a) $1/St$ (b) $\bar{k}_l$ (c) $\overline{C}_{Pl}$ for the Oseen model.

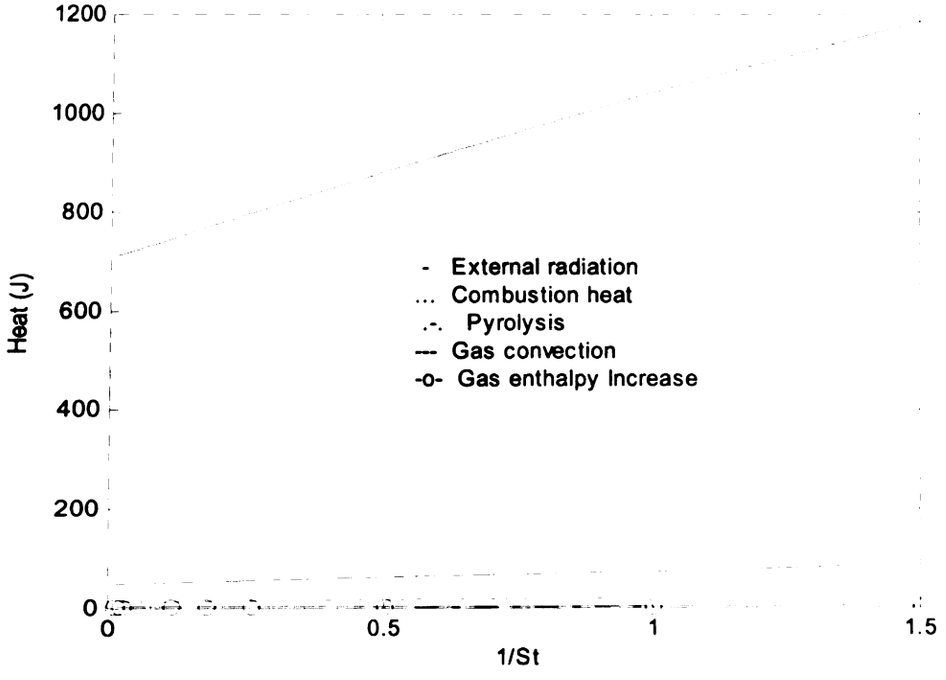

(4-a)

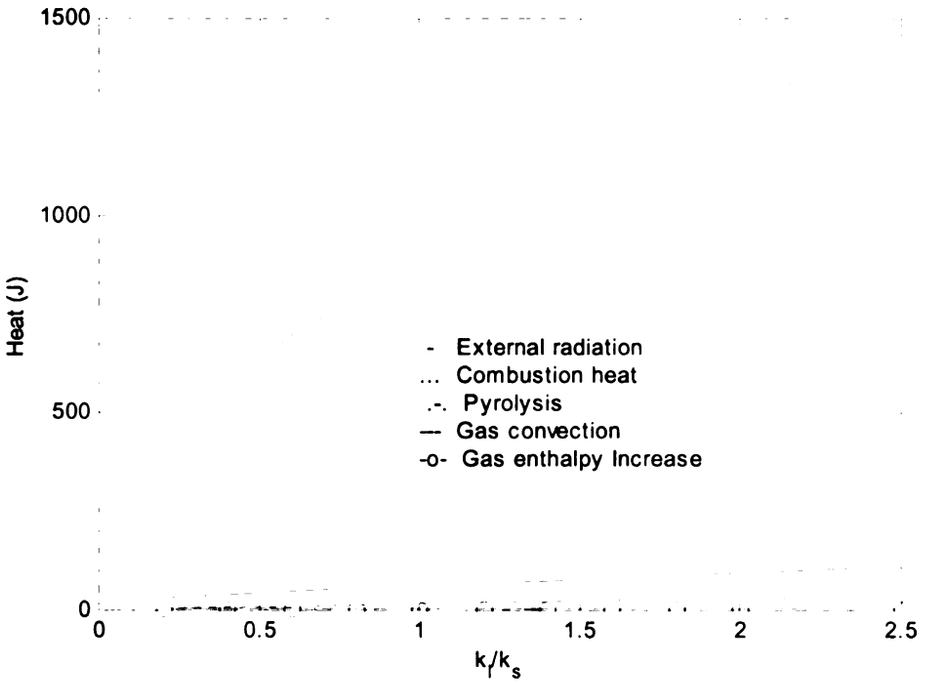

(4-b)

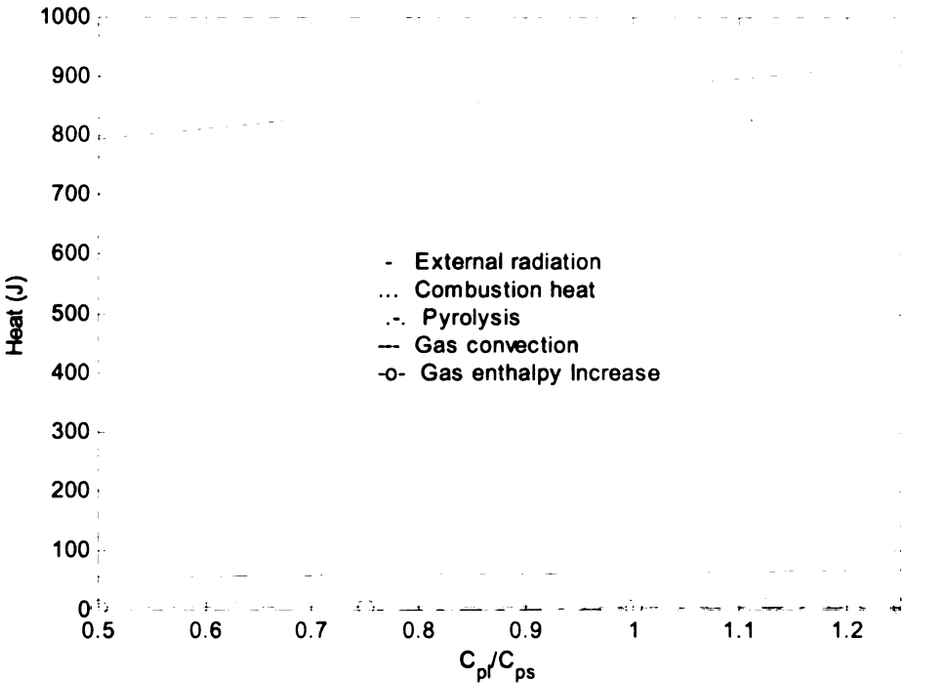

(4-c)

Figure 4 Five heat transfer mechanisms vs. (a) $1/St$ (b) $\bar{k}_l$ (c) $\bar{C}_{Pl}$ for the Navier Stokes model.

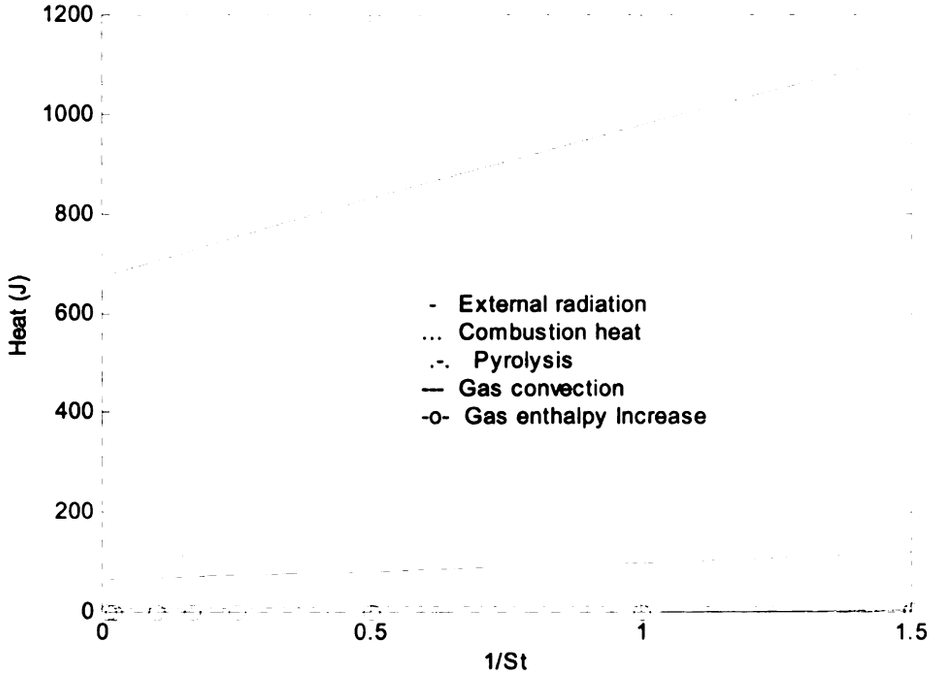
1200
1000
800
600
400
200
0
Heat (J)
0
0.5
1
1.5
1/St
- External radiation
... Combustion heat
.-. Pyrolysis
— Gas convection
-o- Gas enthalpy Increase

(5-a)

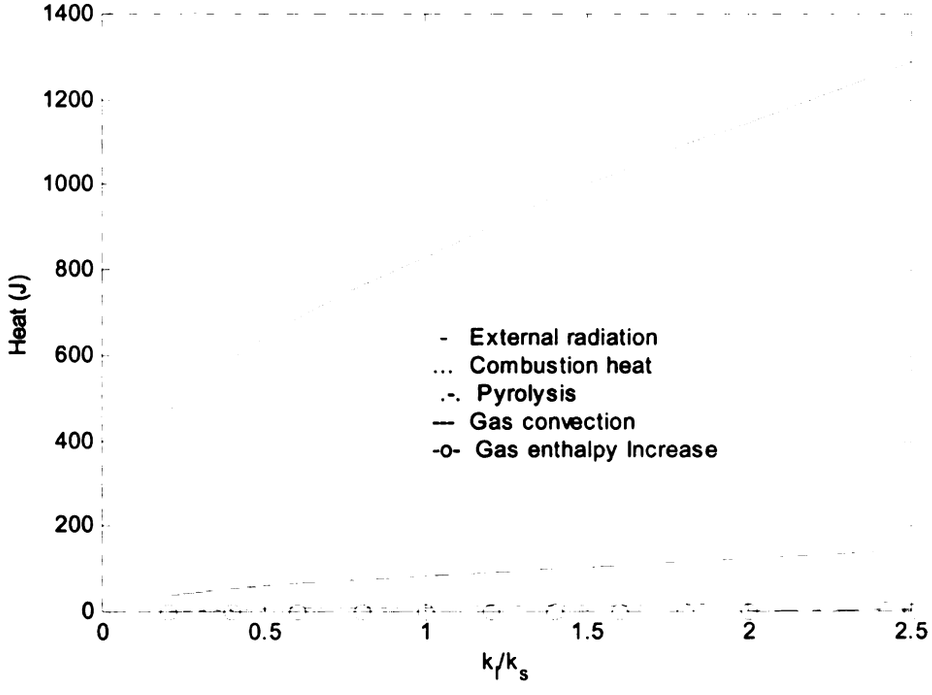
1400
1200
1000
800
600
400
200
0
Heat (J)
0
0.5
1
1.5
2
2.5
k_f/k_s
- External radiation
... Combustion heat
.-. Pyrolysis
— Gas convection
-o- Gas enthalpy Increase

(5-b)

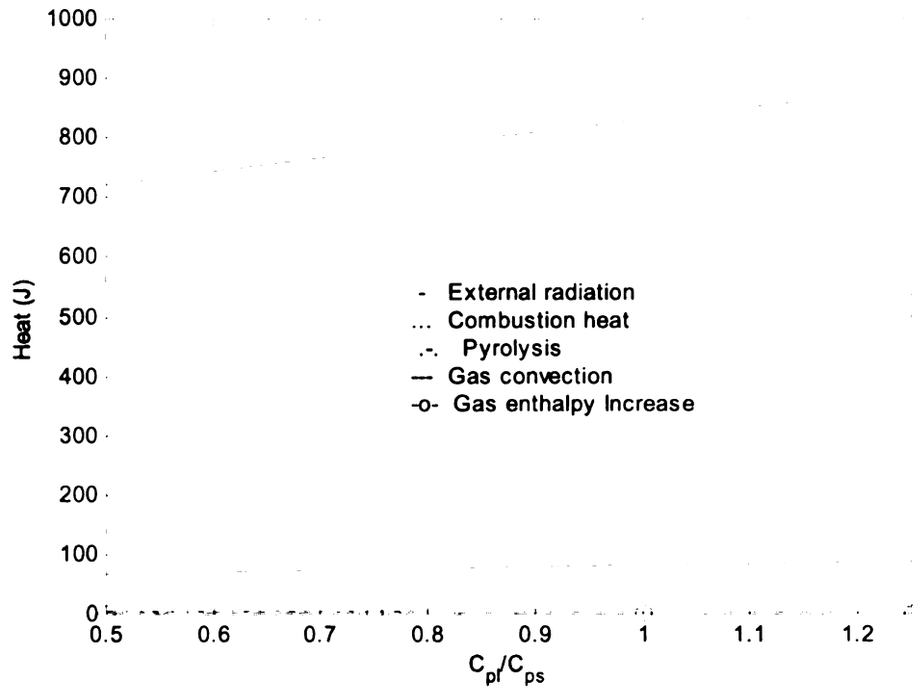

(5-c)

Figure 5 Five heat transfer mechanisms in the control volume vs. (a) $1/St$ (b) $\overline{k}_l$ (c) $\overline{C}_{Pl}$ for the Oseen model.

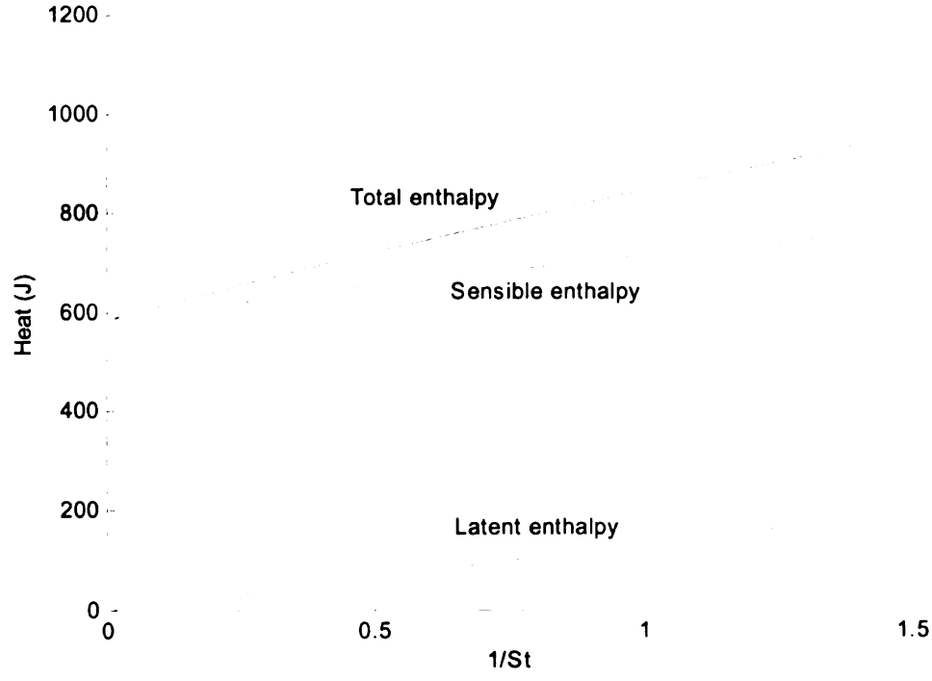

(6-a)

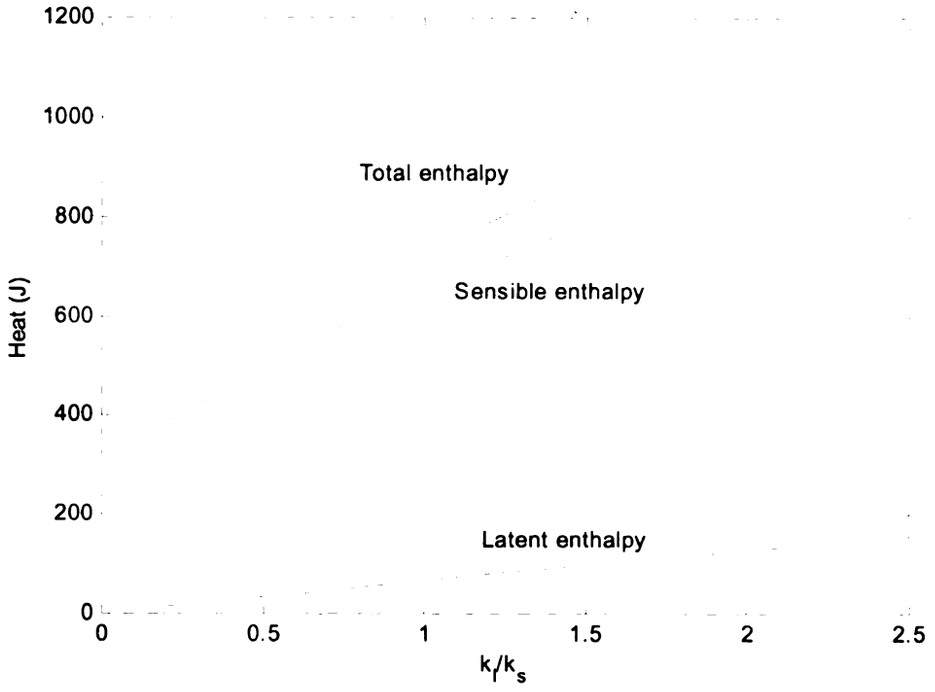

(6-b)

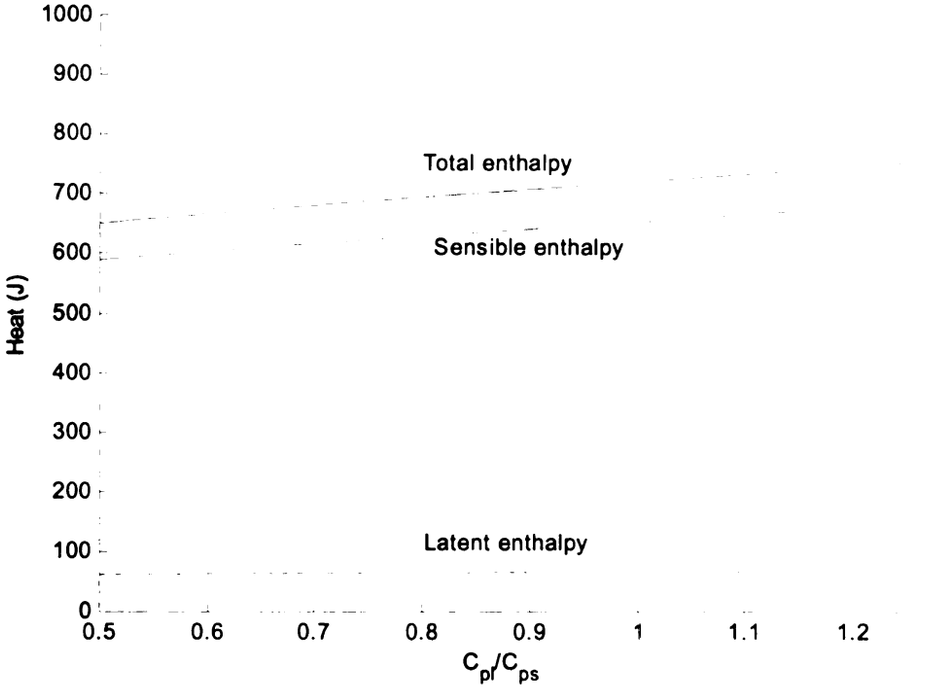

(6-c)

Figure 6 Magnitudes of enthalpy increase of the condensed phase at ignition vs. (a) $1/St$ (b) $\overline{k}_l$ (c) $\overline{C}_{Pl}$ for the Navier Stokes model.

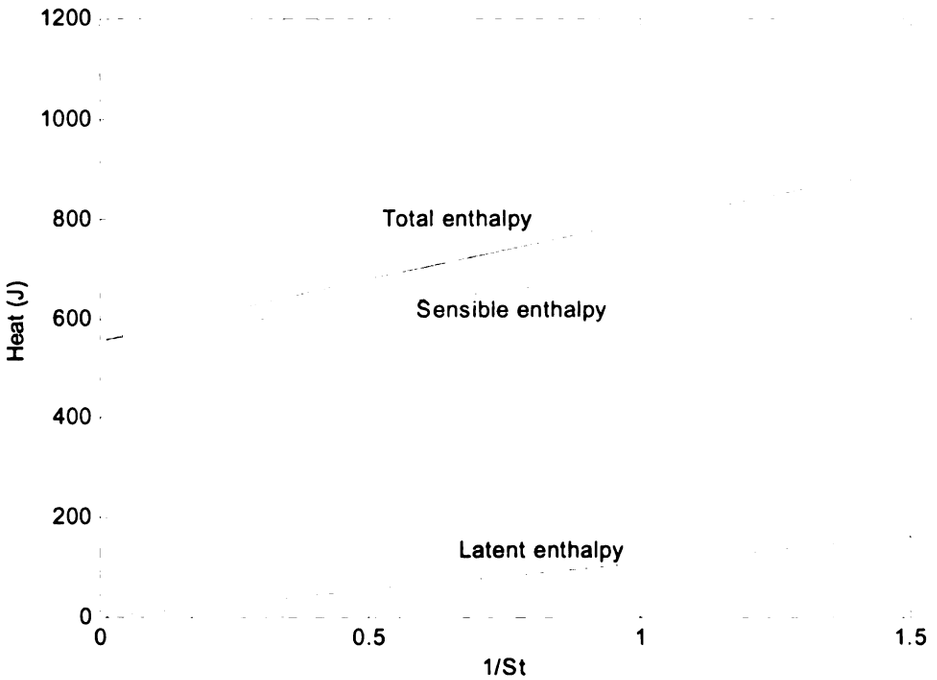
1200
1000
800
600
400
200
0
Heat (J)
Total enthalpy
Sensible enthalpy
Latent enthalpy
0
0.5
1
1.5
1/St

(7-a)

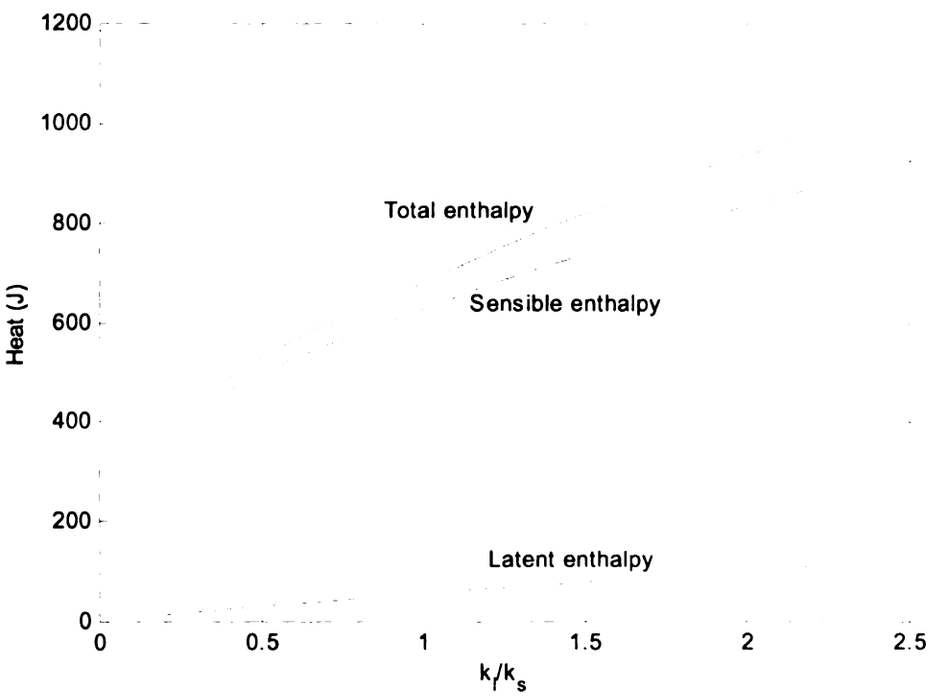
1200
1000
800
600
400
200
0
Heat (J)
Total enthalpy
Sensible enthalpy
Latent enthalpy
0
0.5
1
1.5
2
2.5
k_l/k_s

(7-b)

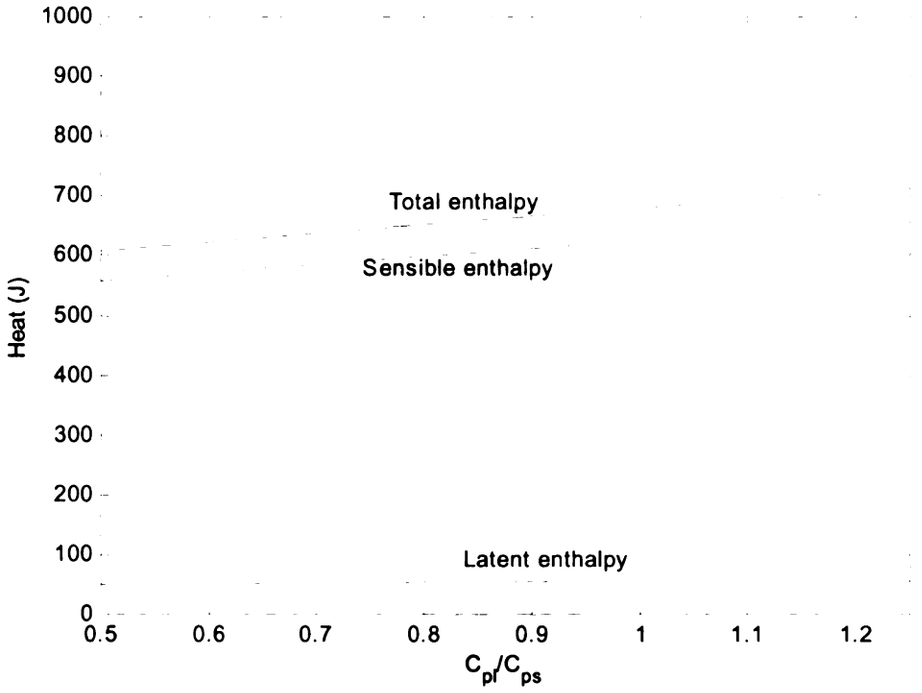

(7-c)

Figure 7 Magnitudes of enthalpy increase of the condensed phase at ignition vs. (a) $1/St$ (b) $\overline{k}_l$ (c) $\overline{C}_{Pl}$ for the Oseen model.

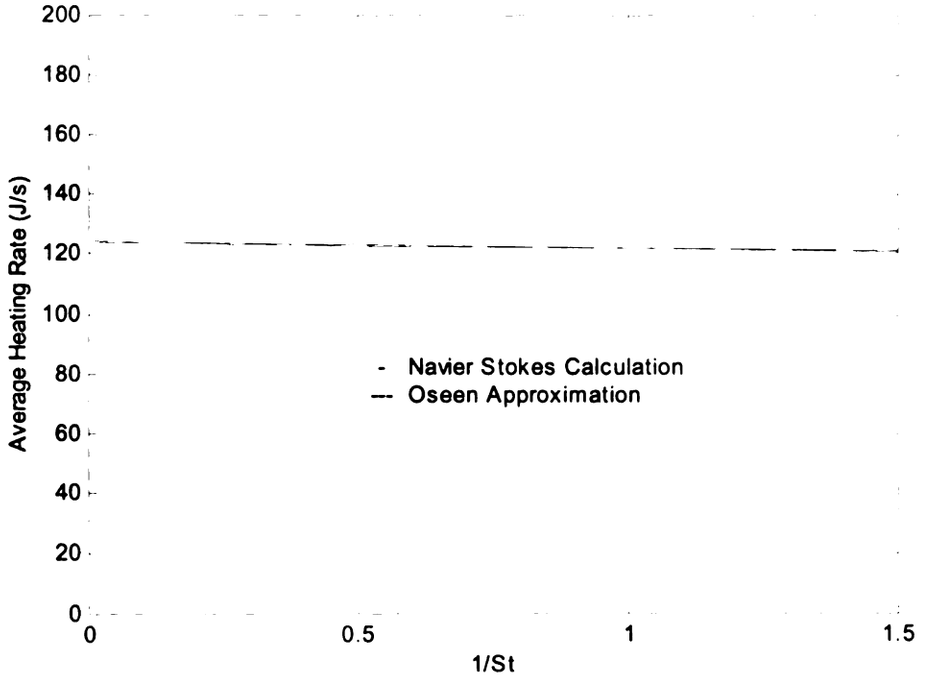

(8-a)

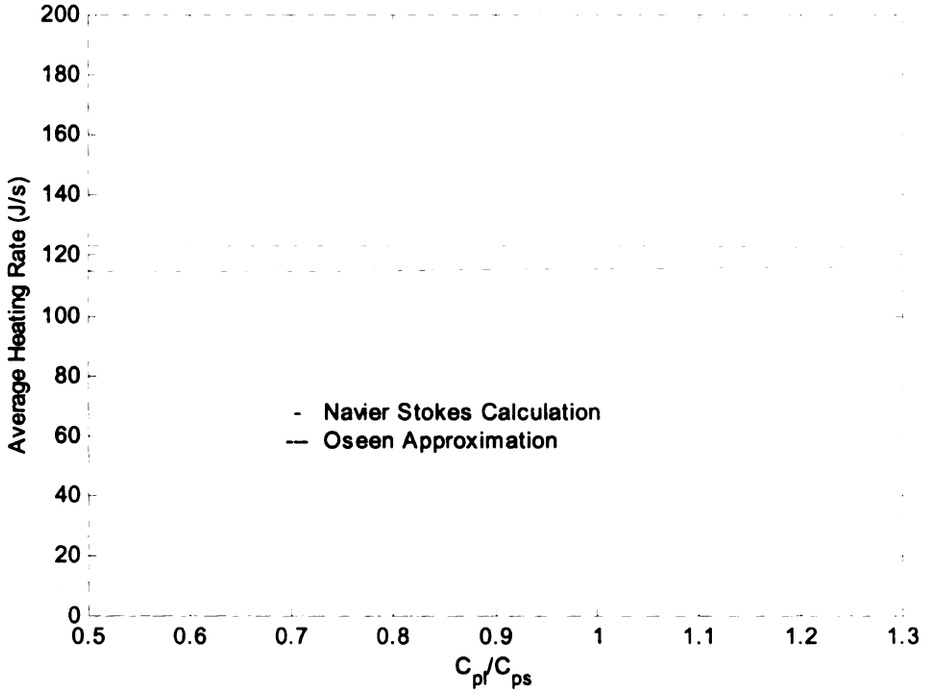

(8-b)

Figure 8 Average heat flow rate during ignition process vs. (a) $1/St$, (b) $\overline{C}_{Pl}$ for the Navier Stokes model.

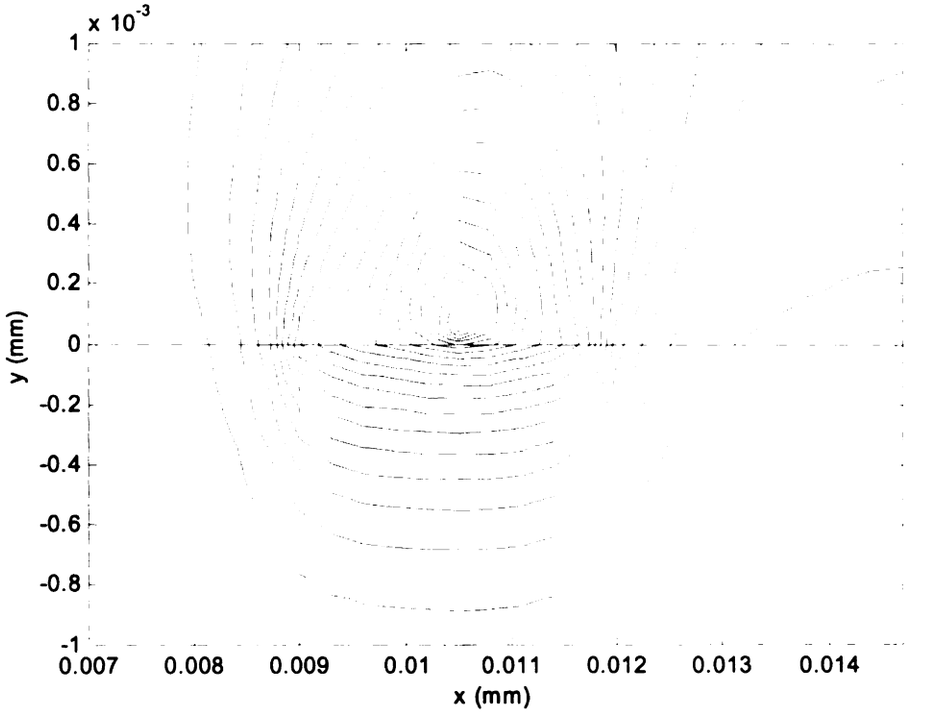

(9-a)

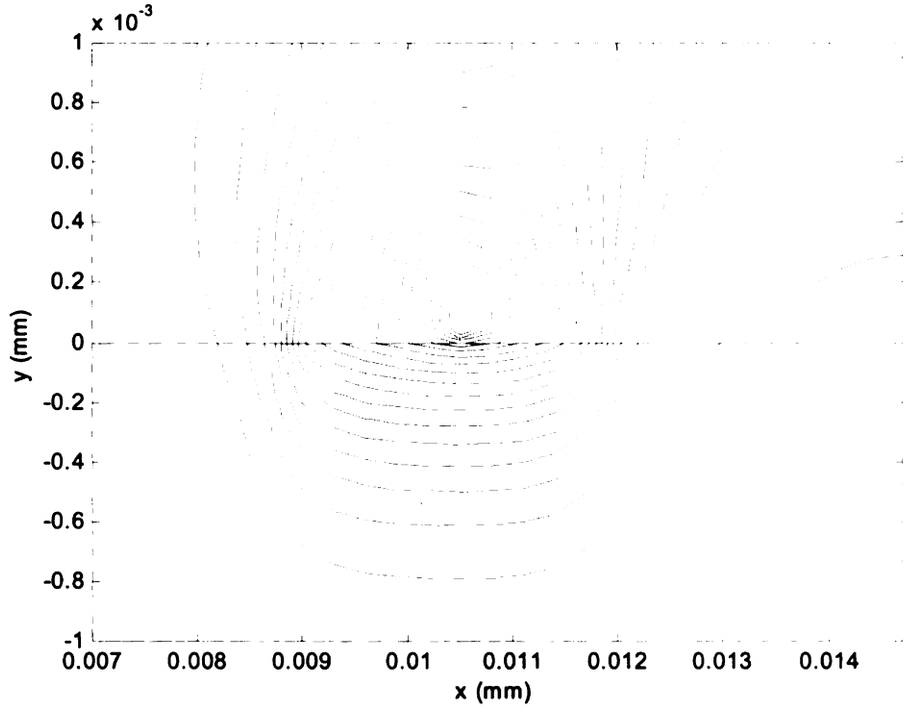
x 10^-3
1
0.8
0.6
0.4
0.2
0
-0.2
-0.4
-0.6
-0.8
-1
y (mm)
0.007
0.008
0.009
0.01
0.011
0.012
0.013
0.014
x (mm)

(9-b)

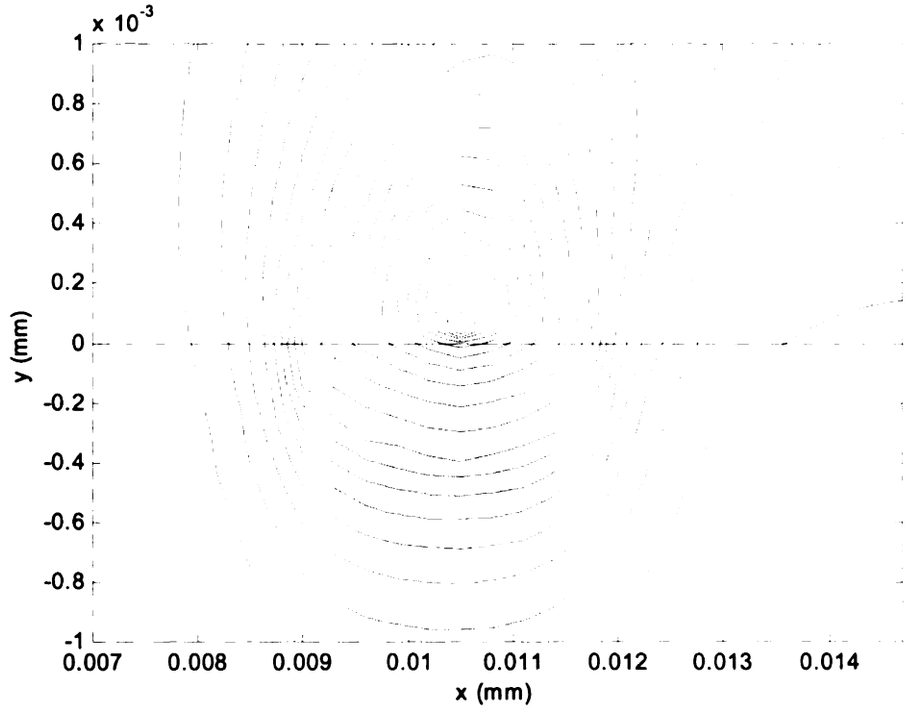
x 10^-3
1
0.8
0.6
0.4
0.2
0
-0.2
-0.4
-0.6
-0.8
-1
y (mm)
0.007
0.008
0.009
0.01
0.011
0.012
0.013
0.014
x (mm)

(9-c)

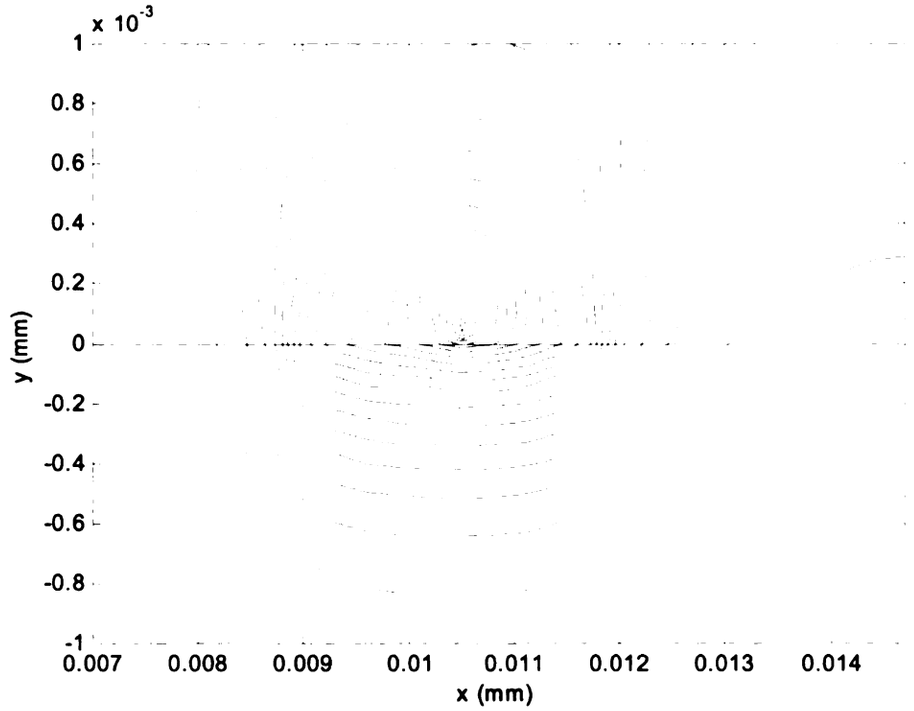

(9-d)

Figure 9 The temperature field vs. (a) $St = 2$ (b) $St = 100$ (c) $\bar{k}_l = 2.5$ (c) $\overline{C}_{Pl} = 0.5$ at ignition for the Navier Stokes model, the outmost line is 325K with step of 25K inward.

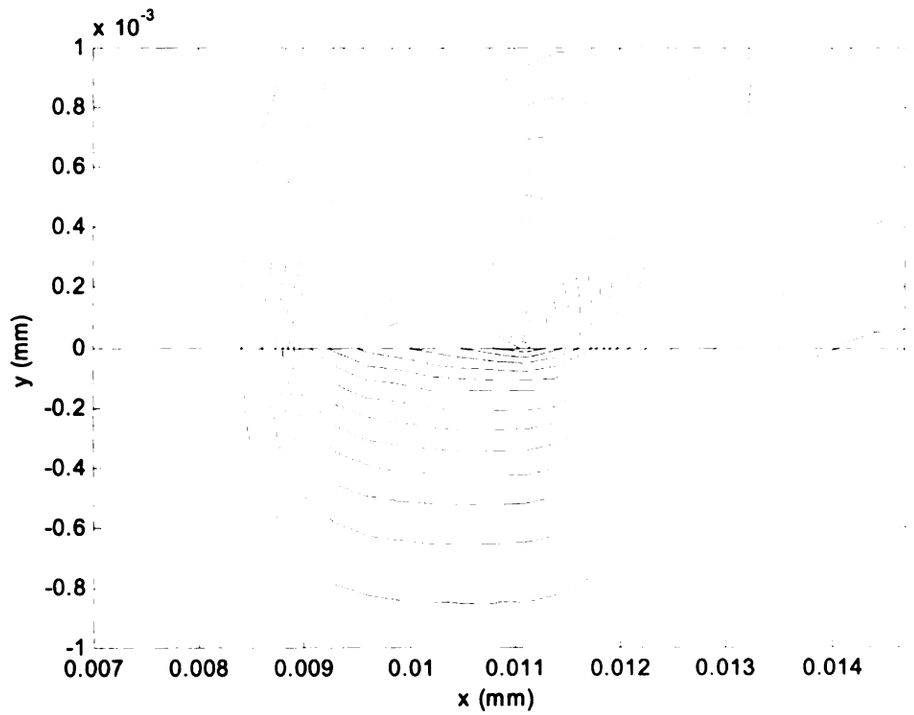

(10-a)

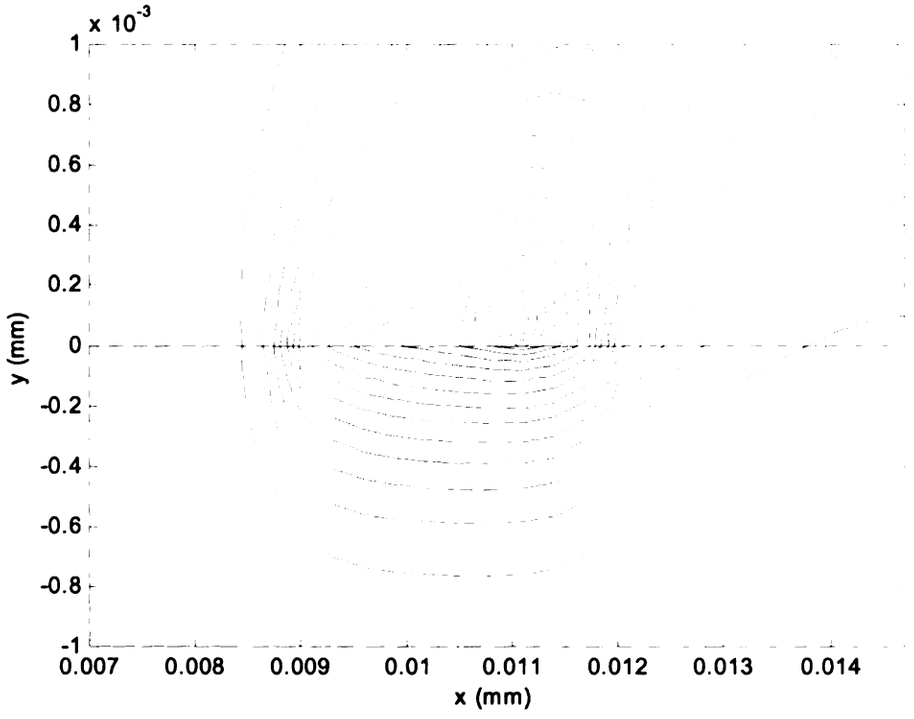
x 10^-3
1
0.8
0.6
0.4
0.2
0
-0.2
-0.4
-0.6
-0.8
-1
y (mm)
0.007
0.008
0.009
0.01
0.011
0.012
0.013
0.014
x (mm)

(10-b)

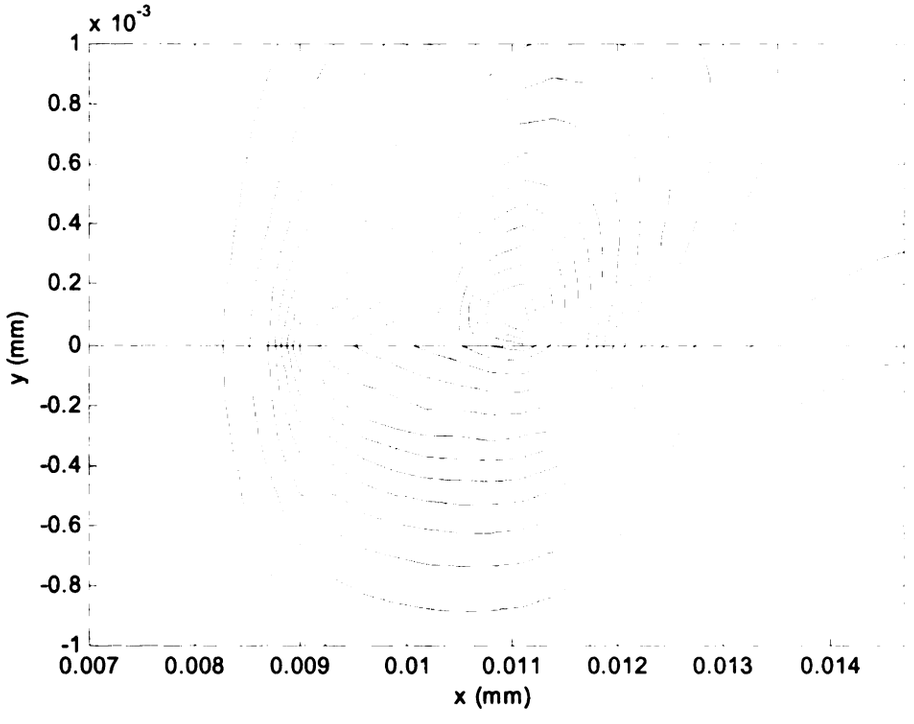
x 10^-3
1
0.8
0.6
0.4
0.2
0
-0.2
-0.4
-0.6
-0.8
-1
y (mm)
0.007
0.008
0.009
0.01
0.011
0.012
0.013
0.014
x (mm)

(10-c)

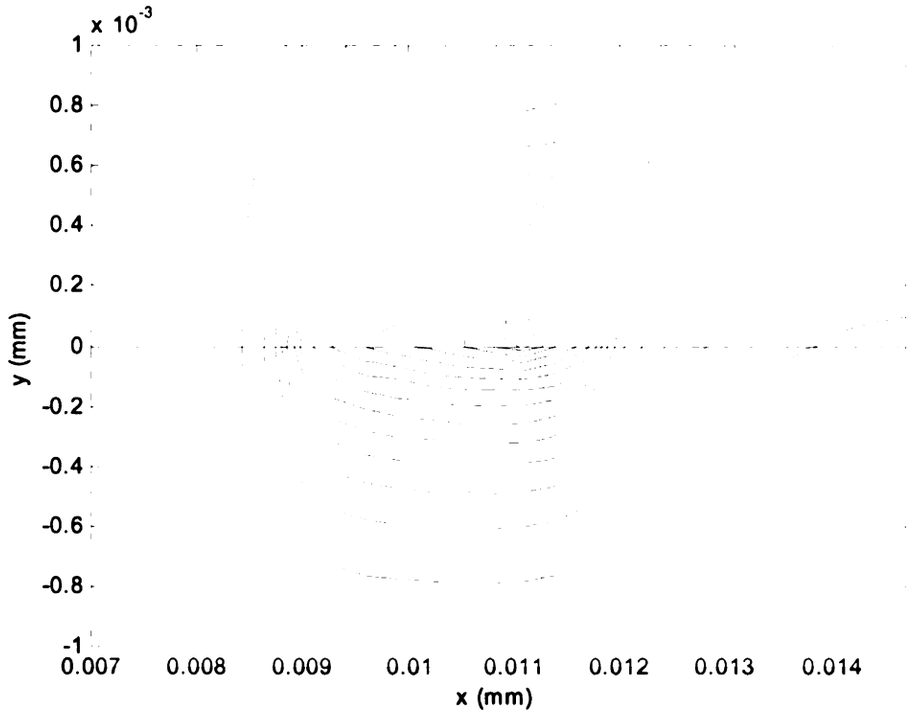

(10-d)

Figure 10 The temperature field vs. (a) $St = 2$ (b) $St = 100$ (c) $\bar{k}_l = 2.5$ (d) $\overline{C}_{Pl} = 0.5$ at ignition for the Oseen model, the outmost line is 325K with step of 25K inward.

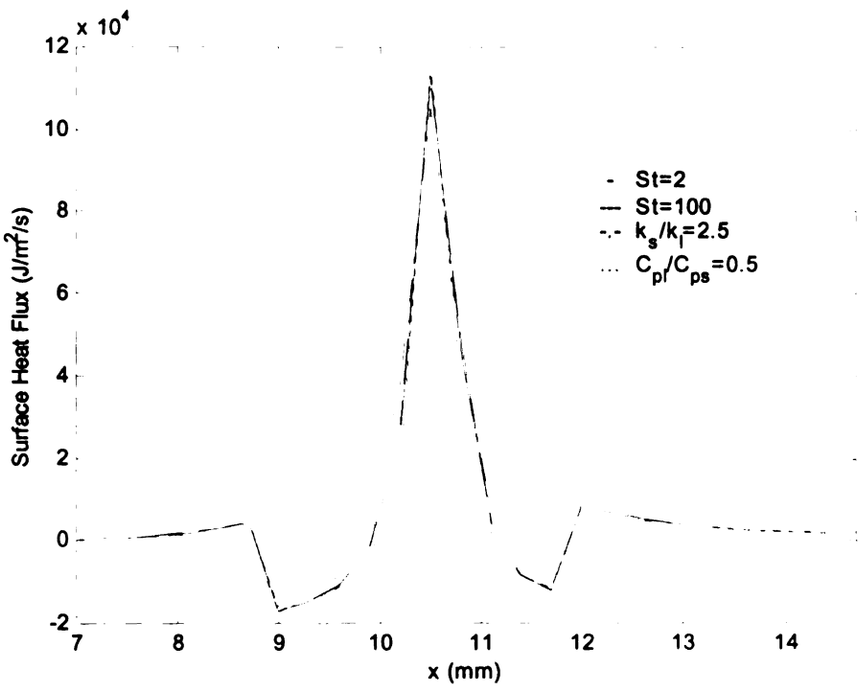

(11-a)

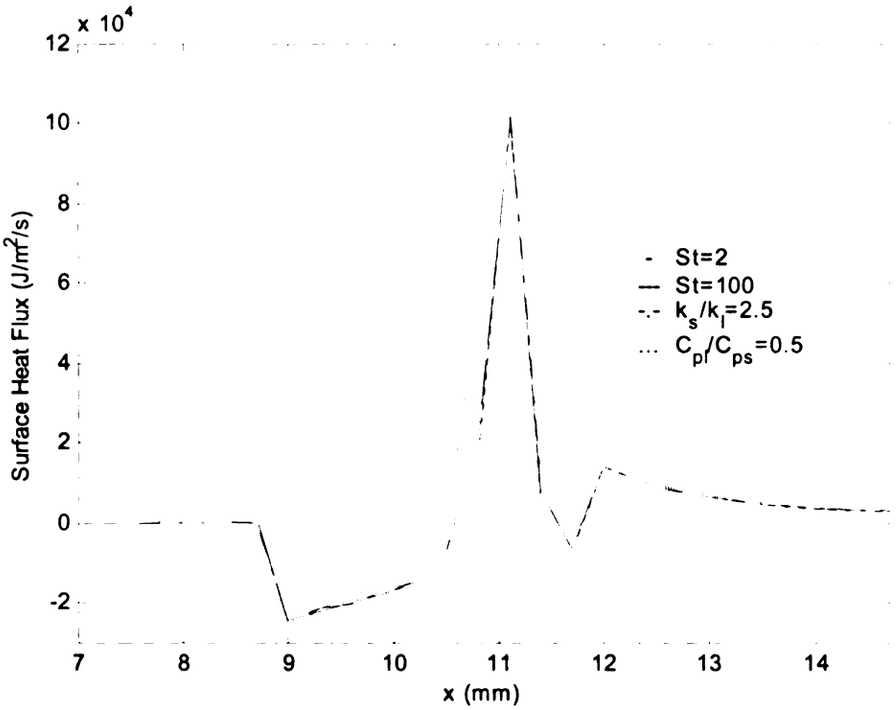

(11-b)

Figure 11 The interface heat flux to the condensed phase at ignition for four different cases for (a) the Navier Stokes model (b) the Oseen model.

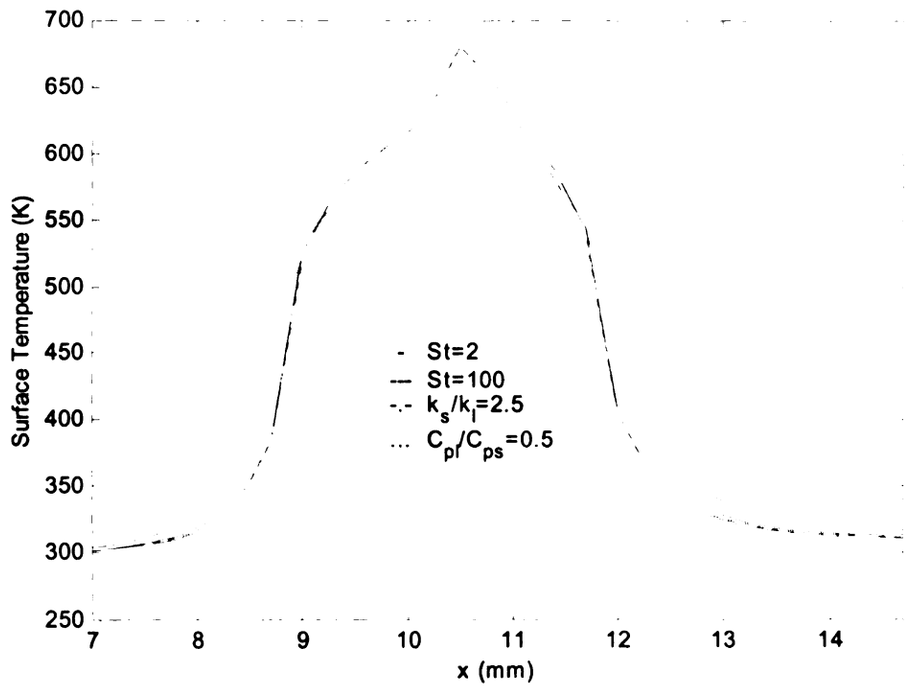

(12-a)

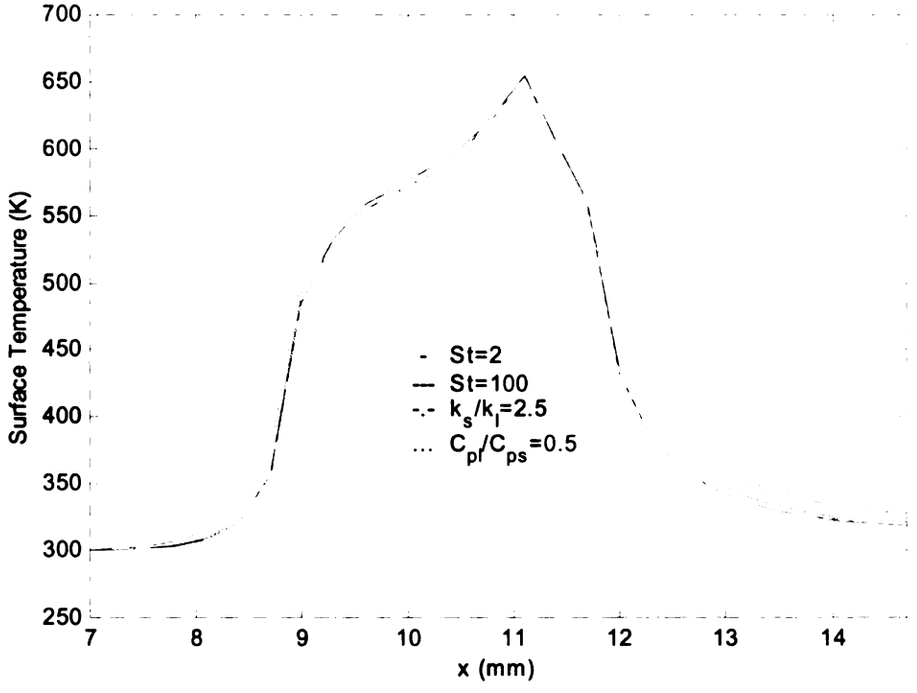

(12-b)

Figure 12 The interface temperature at ignition for four different cases for (a) the Navier Stokes model (b) the Oseen model.

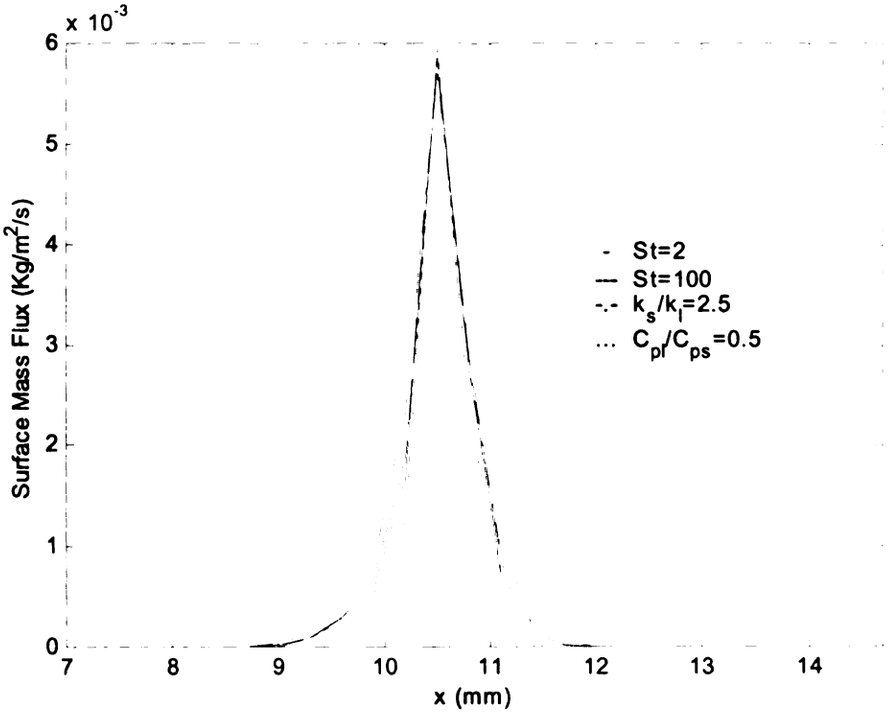

(13-a)

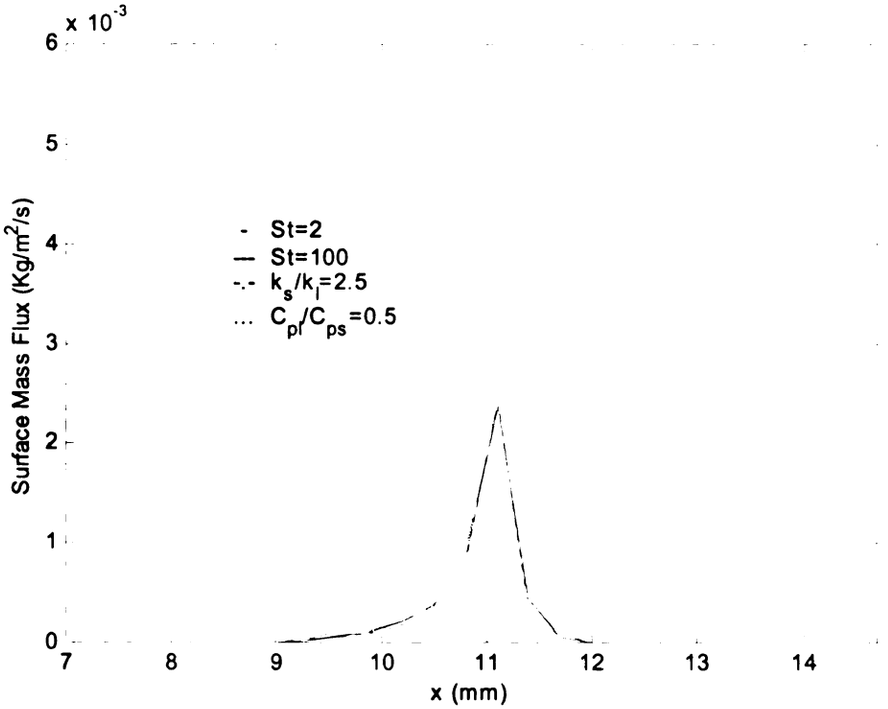

(13-b)

Figure 13 The interface mass flux at ignition for four different cases for (a) the Navier Stokes model (b) the Oseen model.

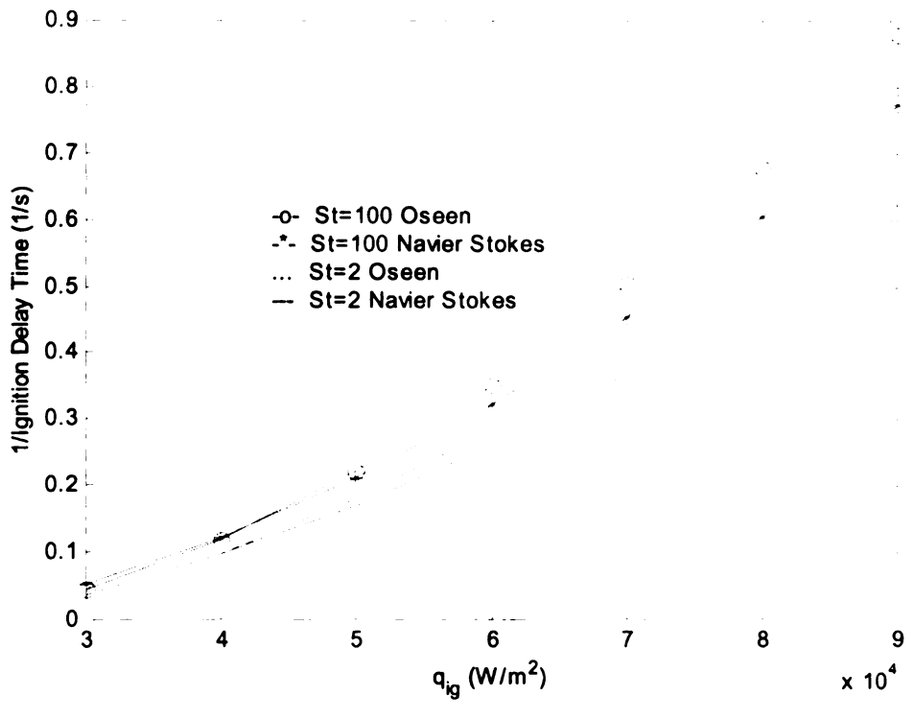

Figure 14 (a) The ignition delay time vs. $1/\dot{q}_{ig}$.

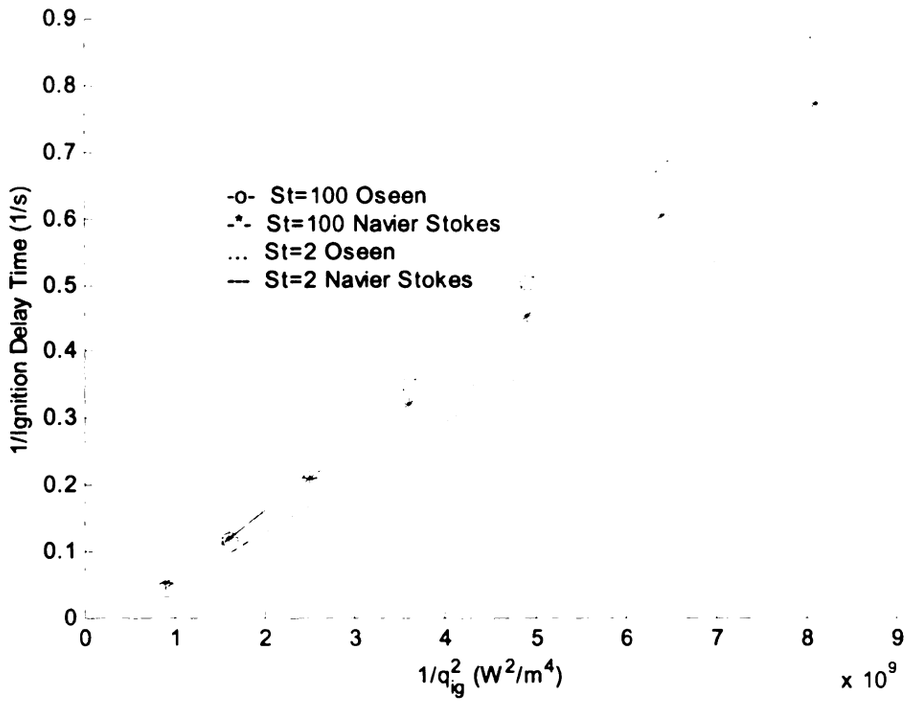

Figure 14(b) The ignition delay time vs. $1/\dot{q}_{ig}^2$.

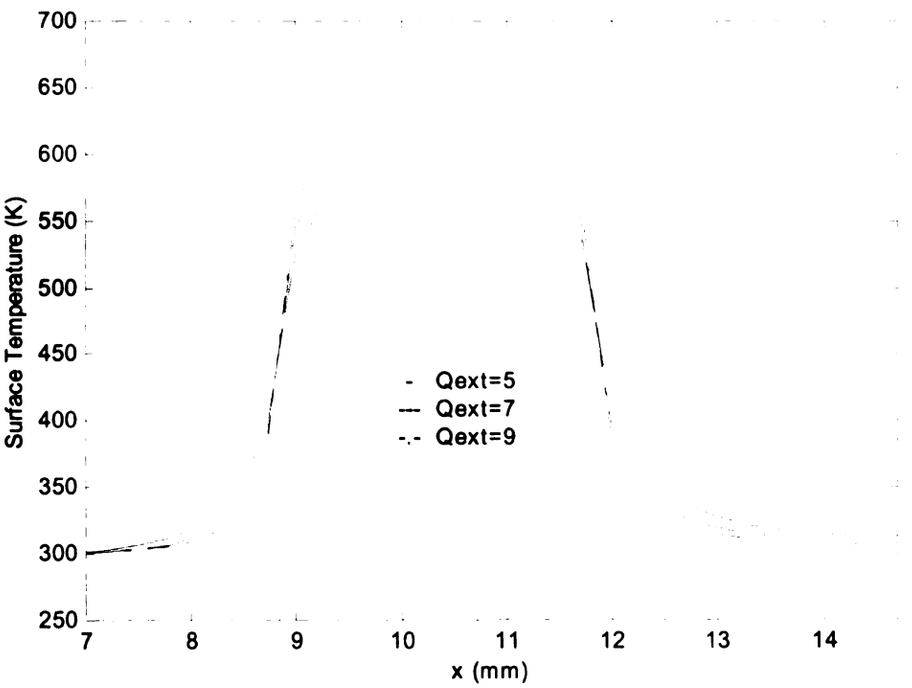

(15-a)

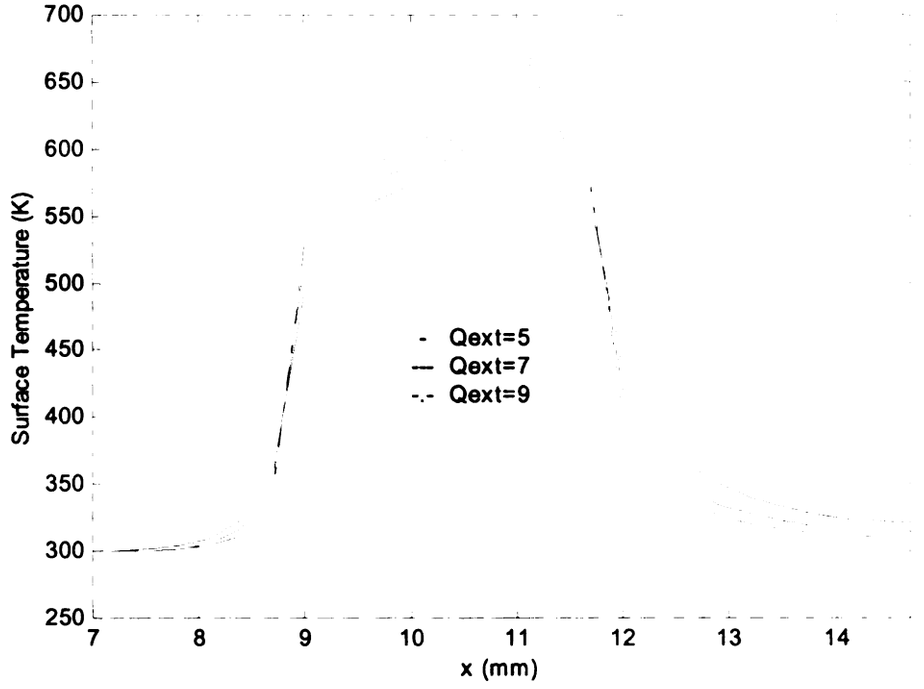

(15-b)

Figure 15 The interface temperature at ignition for three cases of external radiation heat flux. (a) the Navier Stokes model (b) the Oseen model.

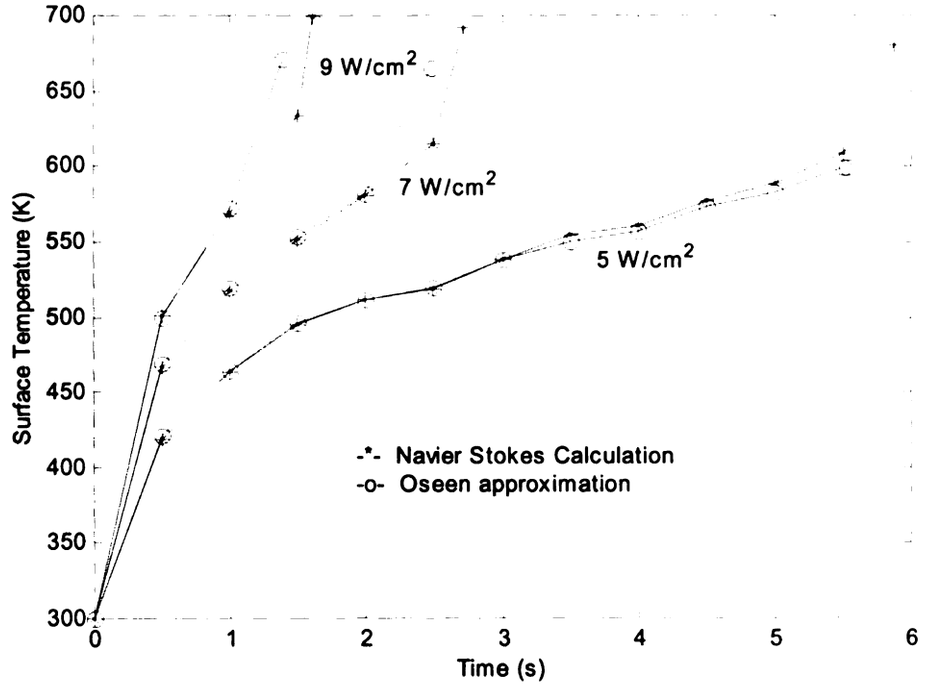

Figure 16 The maximal surface temperature vs. time for three external radiation heat flux in two cases (a) the Navier Stokes model (b) the Oseen model.

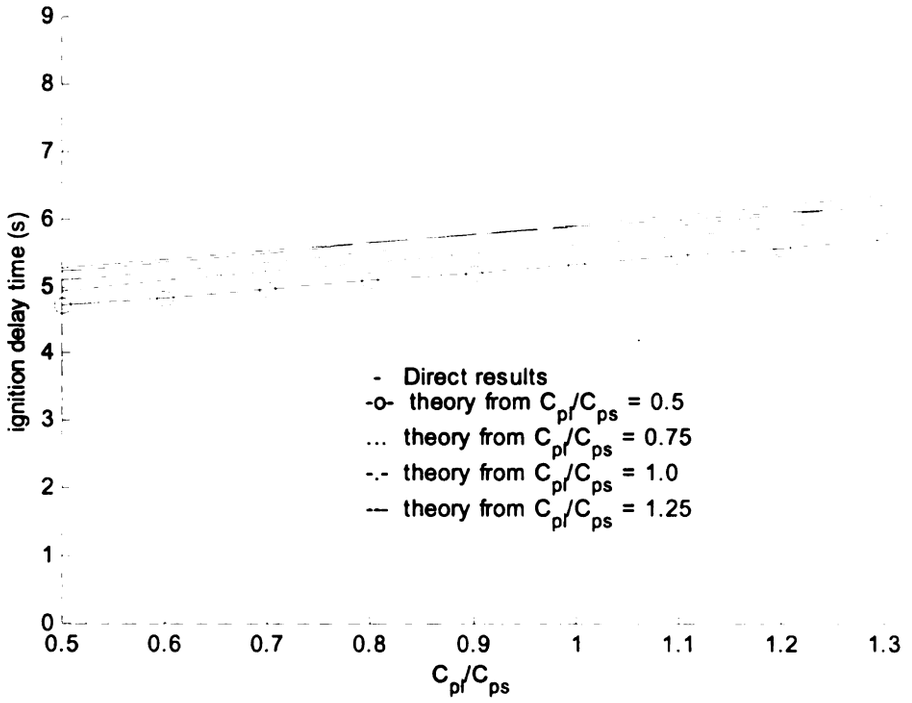
ignition delay time (s)
0
1
2
3
4
5
6
7
8
9
0.5
0.6
0.7
0.8
0.9
1
1.1
1.2
1.3
C_{pf}/C_{ps}
- Direct results
-o- theory from C_{pf}/C_{ps} = 0.5
... theory from C_{pf}/C_{ps} = 0.75
-.- theory from C_{pf}/C_{ps} = 1.0
--- theory from C_{pf}/C_{ps} = 1.25

(17-a)

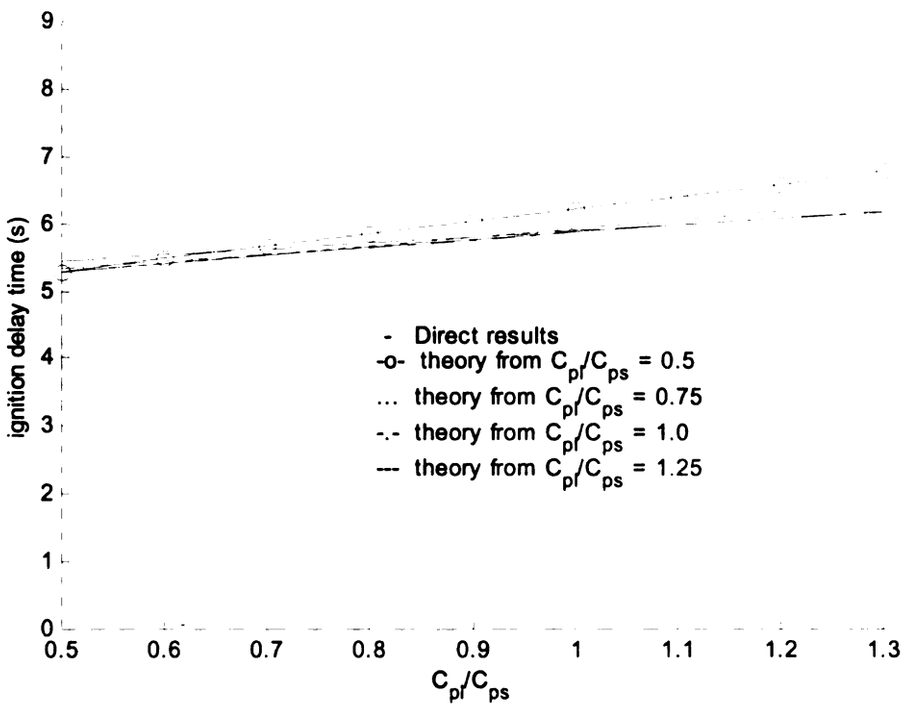
ignition delay time (s)
0
1
2
3
4
5
6
7
8
9
0.5
0.6
0.7
0.8
0.9
1
1.1
1.2
1.3
C_{pf}/C_{ps}
- Direct results
-o- theory from C_{pf}/C_{ps} = 0.5
... theory from C_{pf}/C_{ps} = 0.75
-.- theory from C_{pf}/C_{ps} = 1.0
--- theory from C_{pf}/C_{ps} = 1.25

(17-b)

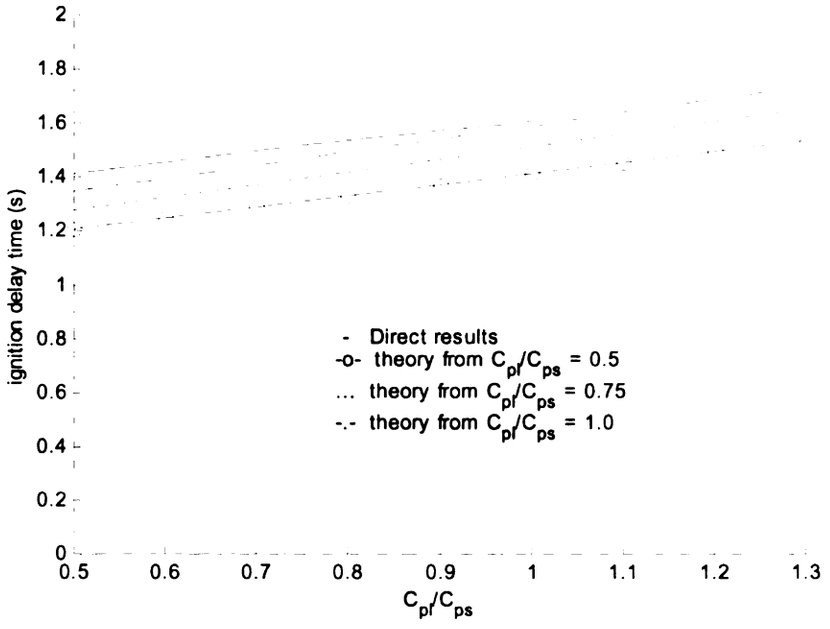

(17-c)

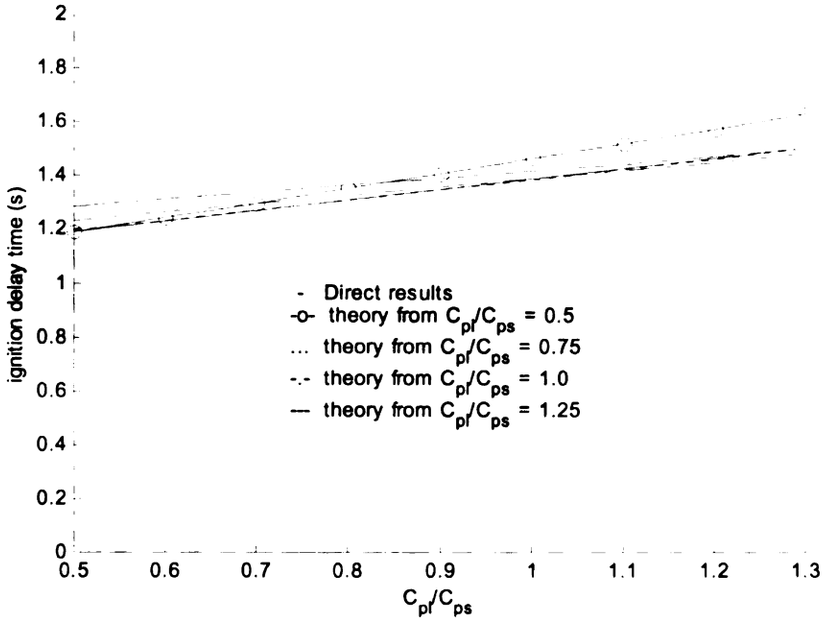

(17-d)

Figure 17 Ignition delay time: a simple theory and direct results (solid line) vs. $\overline{C}_{Pl}$ for (a) the Navier Stokes model with $\dot{q}_{ig} = 5W/m^2$ (b) the Oseen model $\dot{q}_{ig} = 5W/m^2$ (c) the Navier Stokes model with $\dot{q}_{ig} = 9W/m^2$ (d) the Oseen model with $\dot{q}_{ig} = 9W/m^2$.

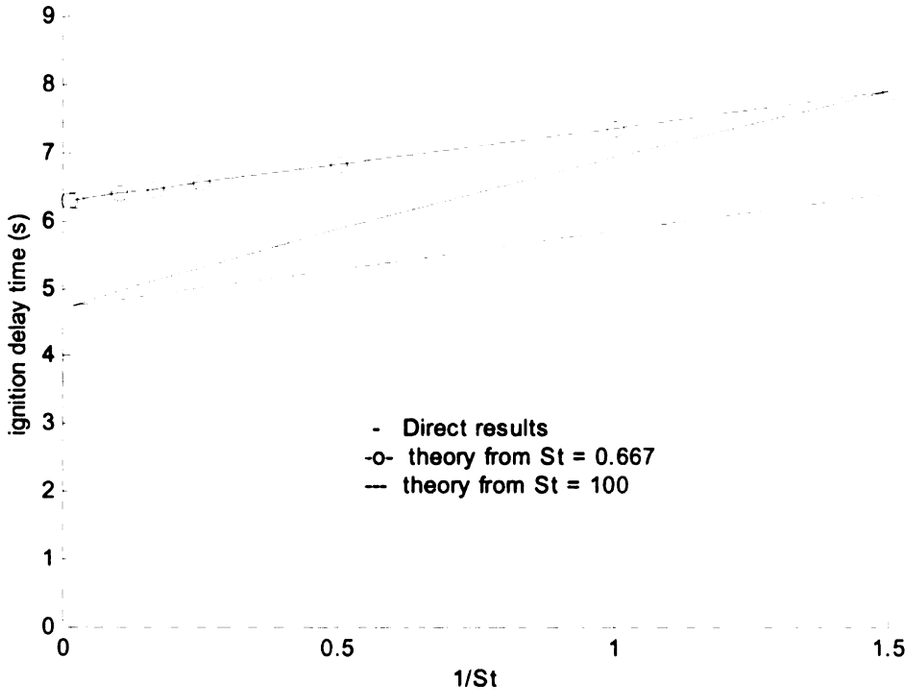
ignition delay time (s)
1/St
- Direct results
-o- theory from St = 0.667
— theory from St = 100

(18-a)

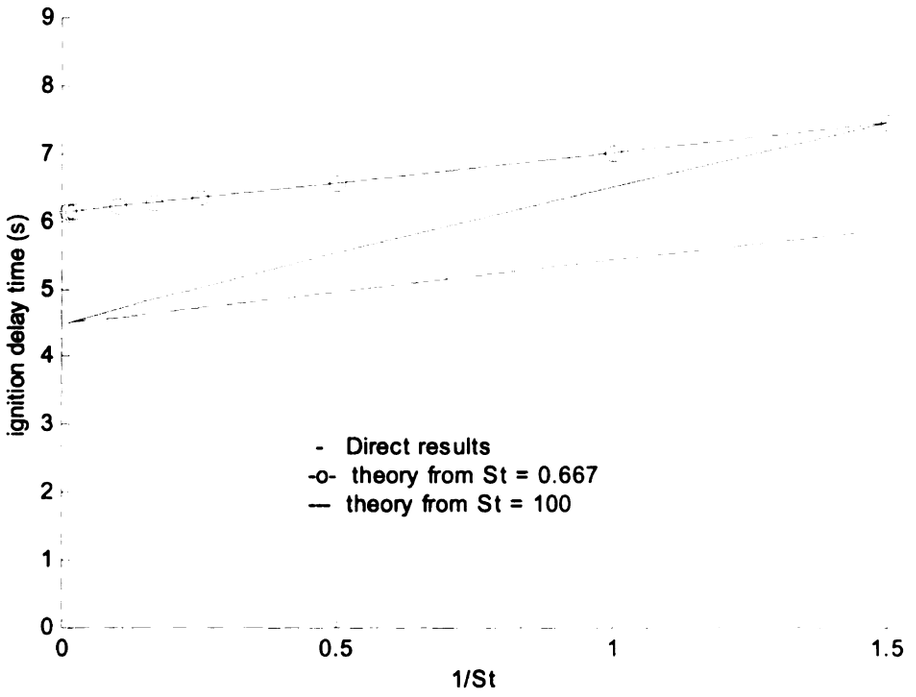
ignition delay time (s)
1/St
- Direct results
-o- theory from St = 0.667
— theory from St = 100

(18-b)

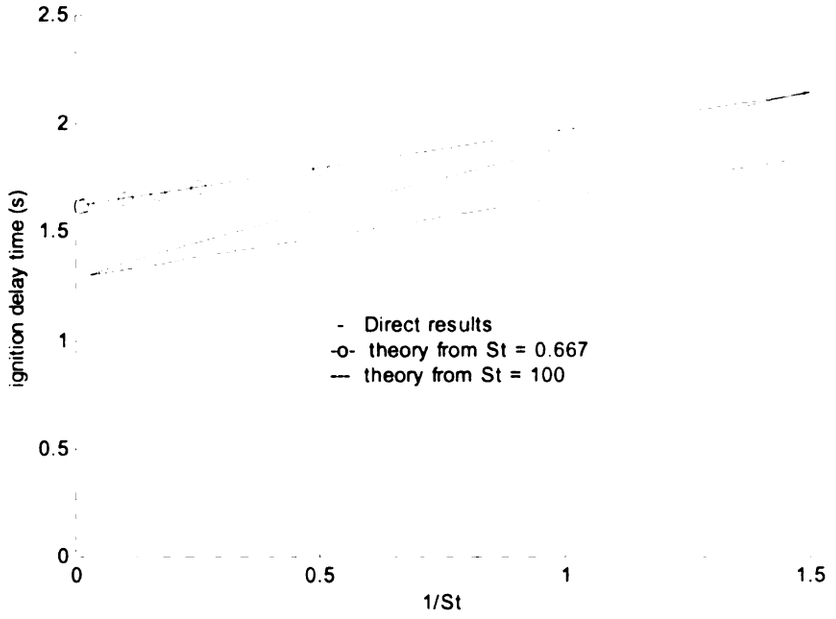

(18-c)

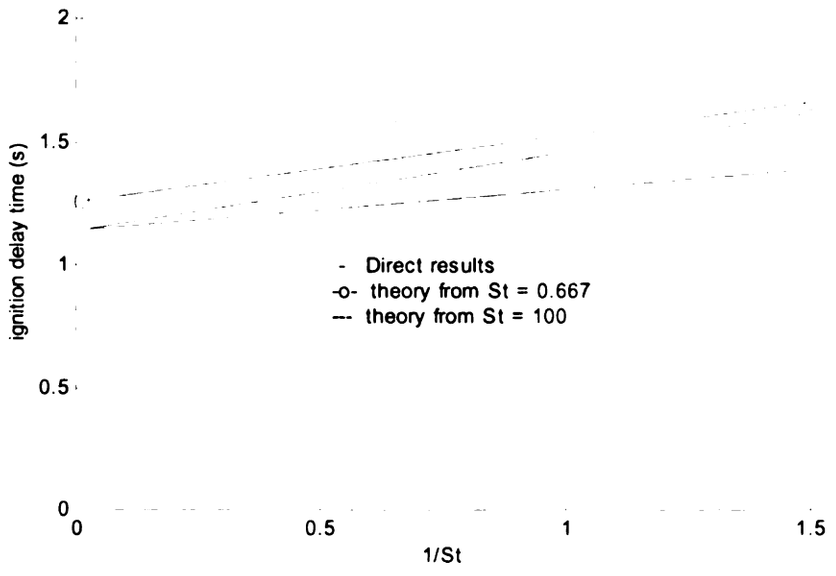

(18-d)

Figure 18 Ignition delay time: a simple theory and direct results (solid line) vs. *St* for (a) the Navier Stokes model with $\dot{q}_{ig} = 5W/m^2$ (b) the Oseen model $\dot{q}_{ig} = 5W/m^2$ (c) the Navier Stokes model with $\dot{q}_{ig} = 9W/m^2$ (d) the Oseen model with $\dot{q}_{ig} = 9W/m^2$.

NUMERICAL MODELING OF FLAME DEVELOPMENT OVER POLYMERIC MATERIALS

Volume II

By

Guanyu Zheng

A DISSERTATION

Submitted to
Michigan State University
in partial fulfillment of the requirements
for the degree of

DOCTOR OF PHYLOSOPHY

Department of Mechanical Engineering

2000

CHAPTER 7

MODELING OF BUBBLE TRANSPORT FOR OVERHEATED MELTING POLYMERS

1. Introduction

The influence of bubbles on flame spread can be summarized in three aspects: (1) formation of dynamic porous structure in condensed phase; (2) absorption of heat via evaporation mechanism; (3) surface mass injection to the gas phase. Models of bubble transport abound in the literature, and single bubble growth and movement receive extensive research efforts. Group-bubble transport is investigated in relatively primitive form, normally described by one-dimensional configurations. In the current work a two-scale transport model will be established to describe the two-dimensional heat and mass transport of an overheated polymer, which undergoes melting during initial phase and the following bubble generation. The mathematical model is composed of a macro-scale transport model and a micro-scale transport model. The former, by means of global heat transfer mechanism, determines the thermal behavior of the condensed phase including a solid and a porous liquid melt. The latter accounts for single-bubble behavior in terms of bubble nucleation, bubble growth and bubble movement by using simplified hydrodynamic relationships. The two scale models interface with each other by several global properties such as porosity, velocity, etc., which are volume-averaged quantities from bubbles' agglomerated behaviors. The methodology proposed in this chapter, to the author's knowledge, has not been used by previous researchers. Several relevant investigations are discussed here. Amon [69] solved bubble radius history for a system

of bubbles growing in expanding foams. Bubble growth is induced by diffusion of a dissolved gas into a thin cell. The single bubble is interfaced to the global parameters (Pressure) through a mass balance relation. Arefmanesh et al. [70] did similar studies on the foaming bubble growth by using two scale models. The micro scale model is for a bubble surrounded by a hypothetical polymer cell. The macro scale model includes a 1-D heat conduction equation and a simple Darcy-type pressure-velocity relation. The two scale models are coupled through velocity and density of the bulk materials. Wichman [71] derived a 1-D group-bubble transport model that treats the influence of bubbles as source terms into the mass, momentum and energy equations. Nucleation, evaporation, and regression of the surface were obtained from this model. There are other bubble transport models available, but they are either for single bubble, or only useful for specific conditions. In general, most of the models cannot account for 2-D configurations, requirement for flame spread studies. The purpose of the current modeling is to provide (1) a evaluation tool for the condensed phase bubble generation and its effects to global parameters; (2) a new methodology to combine both the macro-scale and micro-scale phenomena; (3) some results revealing the polymer's influence to flame development via some global parameters. It is worth noting that the modeling is by no means intended to exactly simulate the polymer materials due to lack of information in both experimental and analytical aspects. The highly viscoelastic nature of the overheated polymer liquid under flaming conditions is rarely investigated except some qualitative derivation from experiments such as viscosity's influence in Kashiwagi's work [13]. Analytical formulations are scarce and involve significant simplifications. Particularly, the dominant mechanism for bubble growth is unknown, which is possibly either diffusion or

evaporation, or a combination of both. With many unresolved complexities, the objective of the current modeling is to obtain the thermal response of a polymer subjected to external heating in qualitative manner. The emphasis is more on the methodology than detailed comparisons to experiments. The sub-models in the current modeling are in primitive form, the upgrade can be implemented by replacing them with more advanced ones in the future.

2. Physical Model

The physical model is composed of a macroscopic energy equation and single bubble transport model. The former provides results of temperature field, the liquid fraction and the moving phase boundary. The last one describes a large number of bubbles' behavior in terms of bubble's nucleation, location, velocity, etc. The two models are coupled through a group of global properties that will be defined in this section. One important assumption is that the global properties such as porosity, velocity, conductivity can be obtained by using volume averaging technique or ensemble averaging technique since these two averaging techniques are logically sound though not completely verified in practice. Other assumptions are introduced below.

1. The mass and momentum transport of the bubbles is assumed to be in direction parallel to that of gravity. In other words, we do not consider the longitudinal influence applied by surface tension driven flow or viscous flow.
2. Spherical bubble shape is preserved throughout the process of bubble development, and no bubble collapse occurs during the process.
3. Bubble bursting effect is negligible.
4. Group bubbles' interaction and its influence to single bubble's behavior are

negligible. Bubble merge is not considered in the modeling.

In the above assumptions, 2, 3, and 4 are used for the convenience of calculation. Others will be discussed further. Solution of the physical model yield global parameters such as temperature, liquid fraction, porosity, gas velocity, and micro-scale parameters such as single bubble's nucleation rate, bubble radius, and bubble velocity.

2.1 Single Bubble Model

2.1.1 Bubble Nucleation

Nucleation, like ordinary chemical kinetics, involves an activation process leading to forming of an unstable initial state. After this intermediate unstable state, further bubble growth proceeds. Experimental investigations indicate that there exist three types of bubble nucleation, homogeneous nucleation, heterogeneous nucleation, and mixed type. The homogeneous nucleation, by definition, occurs when bubble creation is completely in the liquid. The heterogeneous nucleation occurs when a third phase is formed at the interface of two existing phases. By comparison, the homogeneous nucleation generates more violent process and a higher temperature. In this model, it is assumed that bubble nucleation is homogeneous. The activation process of nucleation leads to the formation of unstable embryos. Thermodynamics indicates that there exists a critical radius called nucleus over which a bubble grows and below which bubble shrinks. In this study, the nucleus (with critical radius) is taken as 5×10^{-6} m. Nucleation of gas bubbles in a liquid has been studied for a long time, and numerous formulations appeared [72]. These formulations use thermodynamic properties such as surface tension, vapor pressure and kinetic properties. To predict the nucleation rate, the classical nucleation theory assumes that gas bubble embryos can be described in terms of the bulk thermodynamics

properties. In a single component system the rate of bubble nucleation (number of bubble/m^3 s) is given by,

$$J = M\sqrt{\frac{2\sigma}{\pi \mathrm{M}B}}\exp(-\frac{16\pi\sigma^3}{3k_BT(P_g - P_l)^2}) \quad (1)$$

where M is the number of molecules per unit volume , k_B is the Boltzman constant, σ is the surface tension, and M is the gas molecular weight, and B is constant. The classical nucleation theory, although useful in qualitative nature, is not satisfactory quantitatively [73]. Comparison between the classical nucleation theories with experiments indicates that the predicted nucleation rate from Equation (1) is almost zero [73]. One coarse though convenient approach is to express bubble nucleation by

$$J = N\exp(-\frac{C}{T}) \quad (2)$$

where N is the number density of the liquid, and C is constant. The magnitudes of N and C can be conveniently adjusted to experiments.

2.1.2 Single Bubble Translational Velocity

Bubble movement is due to various determining factors such as gravity, surface tension gradient, and viscosity gradient. Depending on different mechanisms of bubble movement, numerous formulas have been derived. Some formulas are simply derived by using force balance between two types of forces during steady state [73,74]; others are empirical due to interaction of a large population of bubbles [75]. It is worth noting that temperature gradient, as a major factor, produces surface tension gradient, viscosity gradient, and determines bubble density. It plays an important role for bubble transport in overheated polymers. In table 1, several simple velocity formulas are listed as candidates

for modeling considerations. In general, spherical bubble shape, low Re, and quasi-equilibrium assumptions are used in their derivations. Other specific assumptions are listed in Table 1.

Table 1. Translational velocity formulas of bubble movement.

Physical Background	Formula	
Mechanisms: Balance of forces between viscous drag and buoyancy. Assumptions: creeping flow. [74]	$v_b = \frac{2}{3}\frac{gR^2(\rho_l - \rho_g)}{\mu}\left(\frac{1+\kappa}{2+3\kappa}\right)$ $\kappa = \mu_g / \mu_l$	(3)
Mechanisms: balance of forces between viscous drag and thermally induced surface stress due to temperature gradients. Assumptions: linear temperature gradient, linear dependence of surface tension on temperature. [76]	$v_b = \frac{2}{3}\mu_l \frac{[\mu_l \gamma_g R T_c - (\rho_l - \rho_g) g R^2 (\mu_l + \mu_g)]}{(3\mu_l + 2\mu_g)}$ $T_c = 3T_1/(2 + k_g / k_l)$	(4)
Mechanism: velocity induced by viscosity gradient due to temperature gradient. Assumptions: the induced velocity by viscosity gradient could be linearly superimposed onto the overall velocity fields. [77]	$v_b = -\frac{2}{3} R\dot{R}\frac{\partial \ln \mu}{\partial T}\frac{\partial T}{\partial z}$	(5)

In table 1, Equation (3) is a well-known formula that was derived from Stokes' law, and it is incorporated into the modeling to predict bubble velocity. In addition, various other formulas of bubble terminal velocity, where either high Reynolds number or surface-active solute is participating the process etc., are reviewed in [78].

2.1.3 Bubble Growth Rate

Bubble growth is subjected to several influences such as mass diffusion, evaporation,

and surface tension effect. Three typical growth rate models are summarized in Table 2.

Table 2. Growth rate of a single bubble in liquid polymer.

Physical background	Formula or equation system	
Mechanism: diffusion between monomer and polymer. Assumptions: (1) the inertia is negligible; (2) the concentration of the dissolved gas at interface is proportional to the gas pressure inside the bubble. (Henry's law), (3) polynomial profile of gas concentration in the liquid cell surrounding the bubble [70].	$\frac{d}{dt}(\rho_g R^3) = A\frac{\rho^2 D(c_0 - c_w)^2 R^4}{\rho_g R^3 - \rho_{g0} R_0^3}$ $c_w = k_h p_g$ $4\eta\frac{\dot{R}}{R} + \frac{2\sigma}{R} + p_f - p_g = 0$ $p_g = \rho_g R_u T$	(6)
Mechanisms: balance of heat between the heat flow into the bubble and the vapor latent heat. Assumptions: neglect of surface tension and liquid inertia. [79]	$\dot{R} = \sqrt{\frac{\pi}{3}}\frac{k_l}{\rho_g L}\frac{\Delta T}{\sqrt{\alpha_l t}}$	(7)
Mechanisms: diffusion between two species. Assumptions: (1) convection from bubble expansion is neglected. (2) saturated solution is at the bubble interface. [80]	$\dot{R} = DS'(\frac{P_0}{P_c} - 1)[\frac{1}{R} + \frac{1}{\sqrt{\pi D t}}]$	(8)

In table 2, Equation (6) is used for foaming polymers where (1) diffusion mechanism is dominant, (2) externally applied pressure transition is involved; (3) large population of bubbles are involved. The assumption of a thin cell surrounding a bubble is used too because small spacing between bubbles is observed during foam injecting molding process. Note Equation (6) cannot yield analytical formula, instead it has to be solved by numerical techniques. Equation (7) is for saturated nucleate boiling phenomena where the liquid is superheated above the atmospheric boiling point and evaporation occurs at the liquid-vapor interface. The heat is supplied from the superheated liquid by conduction though a boundary layer. Equation (8) is derived where inter-species diffusion is considered as the dominant. Other bubble growth models are available for some specific situations, such as those considering rheological effects or the viscous-elastic effects [81],

etc.

For bubble movement in superheated polymer liquids, both evaporation and diffusion might contribute to bubble growth. If taking PMMA as an example, the boiling temperature of its pyrolysis product MMA is 373K, while the temperature of liquid layer ranges from 500-700 K in a normal flame spread situation. The nucleate-boiling type bubble growth might be important because of large overheats. At the same time, the pyrolysis product MMA and melted PMMA co-exist in a state of liquid, thus inter-species diffusion might also be important. It is not clear which mechanisms is the dominant one, either theoretically or experimentally [13]. For the current phase of bubble development, it is pointed out [75] that bubbles grow via evaporation with two phases of development: (1) *An initial phase* due to the effects of liquid inertia and surface tension; under low pressures, a Rayleigh solution gives, $R(t) \sim (\rho_g \Delta T)^{1/2} t \sim (p_g \Delta T)^{1/2} t$, and the vapor obeys the ideal gas law; (2) *An asymptotic phase* due to heat diffusion and evaporation, which gives $R(t) \sim (\Delta T / p) t^{1/2}$ (apparently the radial growth rate satisfies $\dot{R} \sim t^{-1/2}$). In the modeling, we assume that the asymptotic phase dominates the whole process of bubble growth.

2.2. Macro-scale Volume Averaged Equations

Before the macroscopic equations appeared in literature, micro-scale equations were commonly encountered in most engineering applications since most materials are conveniently treated as continuous media, for example, density is defined by $\rho = \lim_{\Delta V \to 0} \Delta M / \Delta V$. According to Reynolds' transport theorem, the general form of micro-scale transport equation of a certain quantity Φ can be rigorously derived from

conservation laws and is given by $\frac{\partial \Phi}{\partial t} + \nabla \cdot (\Phi V) = \nabla J + S$, where J represents diffusion term, and S represents source term. The well-known Navier-Stokes equation belongs to this category. The macro-scale model was introduced previously from research of porous media in order to capture the scale that is small enough to describe global fluid motion and structure change but large enough to smooth out the details of morphological complexities and inter-pore heat and mass transport. The direct application of micro-scale model to bubble transport phenomena is difficult mainly because of the morphological complexities and disparate scales. To account for these complexities, an extremely fine mesh grid system is needed to determine both the single bubbles and the surrounding liquid. Obviously this is not realistic by seeing the limited computational power. Instead we are going to use the macro-scale equations. The morphological characteristics will be accounted for by some global parameters through the macroscopic equations. From literature, direct application of the volume-averaging concept into bubbling polymers is rare; to the knowledge of the author, there is no publication available that is directly relevant to the current modeling efforts. Therefore, the volume-averaged macroscopic energy equations are introduced first, and then the macroscopic properties.

2.2.1 Volume Averaged Energy Conservation Equation

Appendix VI presented the detailed volume averaging techniques used to derive the macroscopic energy conservation equations. The energy equation in the condensed phase is written as:

$$\overline{\rho}\overline{C}_P \frac{\partial T}{\partial t} + \overline{\rho} C_{Pg} \overline{V} \nabla \cdot T = \nabla \cdot [\overline{k} \nabla T] - \Delta h_{vap} \overline{\dot{m}} - \sum_i h_i^0 \overline{w}_i . \qquad (9)$$

Two major assumptions are used: (1) The liquid monomer and liquid polymer have the

same heat capacity; (2) The liquid around bubbles is quiescent. The first assumption is introduced for convenience and the second is examined in section 3.2.2. The physical mechanisms considered, in turn, are transient explicit heat increase, convection resulting from bubble movement, conduction, evaporation due to bubble growth and nucleation, and pyrolysis. The definitions of $\overline{\rho}$, $\overline{C}_p$, $\overline{k}$, $\overline{\dot{m}}$, and other properties root from the derivation process of the volume averaged equations in Appendix VI. They do not necessarily follow the arithmetic mean formulations from intuition. For example, the definition of $\overline{C}_p$ is not a arithmetic mean of the two phases.

2.2.2 Volume Averaged Physical Prosperities

The phase function γ_g is defined as unity in gas phase and zero in solid phase. It is a function of both spatial location and time. This function is useful for definition of the forthcoming properties.

2.2.2.1 Porosity ε_g

For a given control volume V, porosity is the volume fraction of the bubbles in the liquid

$$\varepsilon_g = \frac{1}{V}\int_V \gamma_g(x,y,t)dV . \tag{10}$$

In the control volume V, if bubble number N and bubble radius R_i are given, where i denotes the index of each single bubble in a population, ε_g is obtained

$$\varepsilon_g = \sum_{i=1}^{N} 4\pi R_i^3 / 3V . \tag{11}$$

N is dependent on the dynamic process of bubble generation and movement in the

liquid. During a time period δt, the following balance always holds for a control volume,

$$\delta N = N_{\text{nucleated}} + N_{\text{in}} - N_{\text{out.}} \tag{12}$$

where δN denotes the change of bubble numbers during δt. As seen from this equation, the change of N is due to three types of bubbles that: (1) are newly nucleated; (2) move into the control volume; (3) move out of the control volume. If the bubble number density n is defined as the number of bubbles per volume (with a unit of #/m^3), we have $N = nV$.

2.2.2.2 Volume Averaged Density $\overline{\rho}$

Volume averaged density $\overline{\rho}$ can be directly obtained from porosity by using arithmetic mean formulation

$$\overline{\rho} = \frac{1}{V}\int_V \rho(x,y)dV = \rho_g \varepsilon_g + \rho_l(1-\varepsilon_g). \tag{13}$$

2.2.2.3 Volume averaged velocity $\overline{v}$

Concerning the convection in the liquid polymer, it is assumed that liquid polymer contains *moving* gas bubbles and *quiescent* liquid surroundings. This assumption is reasonable in that the viscosity of the polymer melt is normally very large, therefore diminishing either the friction-driven liquid flow from bubble movement or the surface tension-driven flow near the gas-condensed interlace. For the latter, although the temperature gradient would be very large near the flame front, the resulting flow is assumed to be hindered because of the large viscosity. In Appendix VI, the volume-averaged velocity is defined as

$$\overline{v} = \overline{\rho}_g^g \varepsilon_g \overline{v}_g^g / \overline{\rho} \tag{14}$$

, where $\overline{\rho}_g^g$ and $\overline{v}_g^g$ are the intrinsic volume averaged bubble quantities, $\overline{\rho}$ is the volume-averaged density. In the above equation, $\overline{\rho}_g^g \overline{v}_g^g$ is obtained as a single entity since velocity and volume of each bubble are coupled. Therefore, we have the averaged velocity in terms of group of bubbles,

$$\overline{v} = (\sum_{i=1}^{N} 4\pi R_i^3 v_{bi} \rho_{bi}) / 3V\overline{\rho} . \tag{15}$$

2.2.2.4 Heat Capacity $\overline{C}_p$

In Appendix VI, the heat capacity $\overline{C}_p$ is defined as

$$\overline{C}_P = [\varepsilon_g \rho_g C_{Pg} + \varepsilon_l \rho_l C_{Pl}] / \overline{\rho} \tag{16}$$

Note that $\overline{C}_p$ is not a simple arithmetic average. The arithmetic mean was used by some researchers but in less rigorous form, detailed discussions of volume averaging techniques are presented in [82].

2.2.2.5 Volume Averaged Conductivity $\overline{k}$

According to the definition in Appendix VI, $\overline{k}$ has the form of

$$\overline{k} = \varepsilon_\beta k_\beta^* + \varepsilon_\gamma k_\gamma^* \tag{17}$$

where k^* denotes the effective conductivity [82]. The bounds of $\overline{k}$ could be used as an initial estimate. The simplest formulation shows that the magnitude of $\overline{k}$ always lies between the arithmetic mean and harmonic mean of the k_g and k_l, that is,

$$\frac{1}{\varepsilon_b / k_g + (1 - \varepsilon_b) / k_l} < \overline{k} < \varepsilon_b k_g + (1 - \varepsilon_b) k_l . \tag{18}$$

There are more advanced formations available that provide smaller range between upper and lower bounds.

2.2.2.6 Volume Averaged Mass Rate of Evaporation

For a given control volume V and time duration δt, the evaporation rate $\overline{\dot{m}}$ is defined conceptually

$$\overline{\dot{m}} = -\rho_l \frac{\partial \varepsilon_l}{\partial t} \tag{19}$$

For a given control volume, $\dot{m}$ is calculated by summing up: (1) the mass rate of change for existing bubbles with time; (2) mass of bubbles that are nucleated. The former is obtained by

$$\overline{\dot{m}} = 4\pi \int_t^{t+\delta t} (\sum^N R_i^3 \rho_{bi}) dt / 3V\delta t. \tag{20}$$

The heat absorption term could be obtained by multiplying $\dot{m}$ with the evaporation enthalpy in the macroscopic energy equation.

2.2.2.7. Surface Mass Flow Rate

The surface mass flow rate is defined as a transient function of longitudinal position x along the interface. It works as an input to the flame model in the gas phase, directly affecting the fuel supply rate and further flame size. Physically it comes from: (1) the gasification rate at the polymer surface; (2) bubble transport rate from inside the polymer liquid. Experimentally, there is no quantitative information as to what proportion of each source contributes to this mass flow rate. It is assumed that the mass flow rate comes exclusively from bubble transport at surface. In Figure 2, if given a chunk of the condensed phase covering a distance dx parallel to the surface, and its volume is V_{dx},

we obtain mass flow rate from single bubbles by

$$\dot{m}_{interface} = 4\pi \sum_{interface} R_i^3 \rho_i / 3dx. \tag{21}$$

where "interface" denotes all those bubbles reaching the interface. $\dot{m}_{interface}$ is dependent on the specific location along the surface with a unit of kg/m^2/s.

3. Numerical Implementations

The goal of the numerical model is to predict the physical process of melting, nucleation, and bubble transport, with emphasis on the influence of material properties. Three responses of the condensed phase are available: (1) polymer from solid state to melting; (2) bubble nucleation; (3) bubble growth and movement. Solution of the overall model involves both the macro-scale model and micro-scale model as governed by Equations (2, 3, 7, 9-20); the coupling of the two-scale models is given in Figure 1. In general, if the temperature field is given, the bubble radius, velocity, and number density of each single bubble can be obtained by using the formulas presented in section 2.1. Then global parameters such as porosity ε_g, evaporation mass rate $\overline{\dot{m}}$, and velocity $\overline{v}$ etc. are obtained based on section 2.2.2. Other parameters such as averaged density $\overline{\rho}$, heat capacity $\overline{C_P}$, and thermal conductivity $\overline{k}$ are calculated based on ε_g. After all the global properties are obtained, the macroscopic energy equation is solved by using numerical techniques for melting phenomena, as well as numerical techniques that will be discussed. Again, the resulting temperature field is used as input to calculate the next level's bubble development. The computational procedure is iterative between the two-scale models. Several issues are addressed below. Figure 2 presents the computation procedure of the numerical model.

(1) For each single bubble, there exists a lifetime that starts from nucleation and ends when it reaches the surface. In numerical implementation a dynamic database is constructed that contains all the bubbles in the liquid polymer. It not only records parameters of each bubble (evolution time, position, velocity, density, temperature, etc.) when bubbles are nucleated, it also records during their evolutions. When a bubble bursts out of the surface, it is removed from the database. In addition, at each new time level, all the bubble parameters are updated. The numerical technique is integration over time, for example, update of bubble vertical location is carried out by $Y^{n+1} = Y^n + v^l dt$, where "n+1" represents the new time level, and "n" represents the old time level, the v^l might be a quantity taken from the average of n level and n+1 level. The integration duration is dependent on bubble nucleation frequency.

(2) Bubble nucleation essentially is a discrete phenomenon with time, which corresponds to a frequency. This matches with numerical implementation since all numerical methods in principle discretize time and space in similar manner. The nucleation frequency is chosen to be consistent with a time step of 5×10^{-4}. The influence of the oscillating behavior will be discussed for some representative computational cases.

(3) A typical bubble nucleation in boiling condition [75] generates $10^{13}-10^{23}$ bubbles per volume per second. For such a large number, it is not possible to calculate all bubbles' behavior due to the formidable task of computing. As a simplification, a rather small number of bubbles are used to represent all the bubbles. A transient bubble at the center of a control volume is assumed to represent all bubbles that *are nucleated* in this grid at this time level. The bubble group effect is reflected by bubble nucleation rate in that control volume. Note that the representative bubble is generated at nucleation, after

which its behavior is governed by the transport equations introduced before.

4. Results and Discussion

4.1 Properties

The geometrical configuration is the same as that used before, a 2-D thick polymer. In order to show the features of this numerical model, a constant heat flux of 50000W/m^2 is applied to the polymer surface from 9mm to 12 mm. The influence of the gas is not considered here. The physical process includes the preheating, melting, bubble nucleation, growth, and movement. The nucleation occurs after the temperature attains a critical temperature of 500 K. The reason is that once the temperature is over 500K, it is in overheated liquid state since the boiling temperature of MMA is 373 K, therefore the bubble nucleation should take place immediately. In addition, a constant nucleation rate of 5.0e+11 (#/m^3/s) is formulated. The other bubble properties are (1) the initial bubble radius is 5.0×10^{-6} m; (2) the evaporation heat is 1000000.0 (J/kg); (3) the conductivity of bubble is 0.020 W/(m·K); (4) the bubble heat capacity is 500.0 J/(kg·K). The solid and liquid properties are the same as [55]. In order to make comparisons, a reference state is selected where the liquid latent heat corresponds $St = 2$.

4.2 Time History of Bubble Development

The time history of the bubble development is observed during heating of a polymer. Only the global parameters are presented here since they are of direct interest to us. Figure 4, 5 and 6 show the heating of the polymers at 5s, 10s and 19s with respect to (a) temperature distribution, (b) porosity distribution, (c) velocity distribution, and (d) surface mass flux. In addition, the temperature is compared to a model without bubble generation. It is observed that the temperature fields resemble the model without bubble

generation as seen in Figures 4(a), 5(a) and 6(a). A comment is made about the discontinuities observed in the porosity field and the velocity field, as seen by Figures 5(b), 5(c), 6(b), and 6(c). Recall that the bubble generation is in essence a discrete phenomenon, characteristic of which is the bubble nucleation frequency. In this model, we use 5×10^{-4}s as the interval between two neighboring nucleation in time. The nucleation frequency is therefore 2000. After nucleation occurs, recall again that we use volume-averaging method to account for the behavior of a group bubbles. Numerically, we use each grid control volume as the control volume; thereby the porosity is obtained by adding all the volumes of single bubbles and then divides by the grid control volume. The discontinuity is observed during the boiling process [75], for example, the non-uniform bubble size and number density distributions. Another example is Figure 3 in Chapter 1 for a heated polymer. Note that although we do not consider the bubble merging or collapse, the discontinuity is still available. The discontinuity shows the transient clustering of bubbles in some scattered locations; see Figure 5(b) and 6(b). One question arises; will the randomly clustered bubbles results in a random behavior of the condensed phase. The answer is, in the short term, it does, however, in the long term, the overall behavior of the condensed phase is well defined and will not depend on the randomly localized bubbles with time. The representative parameter is the temperature field, as shown by Figures 4(a), 5(a), and 6(a). It is found that the temperature constant levels do not show any discontinuities. It is speculated that the *scale* of bubble parameters such as porosity or velocity influence the overall temperature distribution and energy transfer.

Between the model with bubbles and the model without bubbles, the temperature

field has negligible difference in Figure 4(a), noticeable difference in Figure 5(a), and higher difference in Figure 6(a). This is consistent with the development of bubbles in that the number of bubbles increases with time. In addition, the bubble generation impedes the heat transfer process, resulting in a smaller size of the constant temperature contours, as observed by Figure 5(a), and 6(a). To analyze this, the influence of the bubble on heat transfer can be categorized by: (1) the decrease of the heat capacity due to porosity; (2) the decrease of the density due to porosity; (3) the bubble flow toward the surface; (4) the decrease of heat conductivity due to porosity; (5) the heat absorption due to evaporation. Among the five factors, (1-3) enhance the heat transfer, and (4-5) impede the heat transfer. The thermal diffusivity is not important since it is actually larger in bubble model. This leads us to ascribe the major influence to the evaporation mechanism. It is found to be so since we uses a large evaporation heat of 1000000 (J/kg). In reality the effect of bubbles on the heat transfer is an outcome from the competition among several heat transfer factors. The material properties indeed have a deep impact on the thermal behavior of the bubbling polymers.

With time, the melt layer expands in space, as observed by observing the temperature fields in Figures 4(a), 5(a), and 6(a) and the porosity field in Figures 4(b), 5(b) and 6(b). Unlike temperature field, the porosity has a much higher gradient near the interface. Recall that the porosity of a control volume is contributed by all the bubbles that have transported from down below due to buoyancy. Since a higher vertical location has a thicker liquid layer below it, the number of bubbles that are generated within this liquid layer is larger. The number of bubbles that are transported to the control volume is certainly larger due to the accumulative effects. In an extremity, if we assume that the

moving velocity is constant and the bubble does not grow, the porosity is an integral function of the liquid thickness below it. Even with the variable bubble radius and velocity, the accumulative nature of the porosity does not change. Especially near the interface, the porosity gradient is so large that it well exceeds the gradient that farther lies below, as observed from Figure 5(b) and 6(b). The velocity profiles show a similar trend with the porosity, as shown in Figure 5(c) and 6(c). Again, the discontinuities appear in the liquid and were discussed already. The velocity, by definition from Equation (14), is dependent on the porosity. In addition, it is also dependent on the density and velocity of single bubble. Near surface, it has a large gradient. It is worth pointing out that in general it is a trivial influence on the temperature distribution, since it has scale of magnitude $10^{-7} m/s$, which is too small in terms of the convection heat transfer. It is further deduced that negligence of the bubble flow in the condensed phase is justifiable in this case. However, in some special situations such as the overheated boiling, the bubbles induce the liquid viscous flow due to drag forces and affect the energy distribution significantly. The mass flux distribution at the interface is plotted in Figure 4(d), 5(d), and 6(d). It is found that the mass flux peak at 10s and 19s are 5 times and 10 times as much as 5s, showing the strong transient behavior of the bubble generation. The mass flux is formulated from bubble evaporation. Numerically it is obtained from the bubbles that burst out of the surface. The mass flux is an integral parameter of all single bubbles that attains the surface. The mass flux has a peak at the center of the heated surface; and this peak corresponds to the maximal thickness of the heated layer, and obviously, the maximal bubble porosity along transverse direction. It is consistent with the distribution of bubble radius in the liquid layer. Note that the mass flux also reflects the random in-

depth bubble behavior by showing that the mass flux distributions at three times have some local irregularities, however, in general, the mass flux follows well with the physical trends. That is, the higher the heating time, the higher the mass flux.

4.3 Influence of Nucleation Rate

It is very interesting to know how the nucleation rate will influence the bubble behavior. Intuitively, we expect that a higher nucleation rate result in a larger bubble generation rate and larger mass flux rate. This is true by observing Figure 7, where four cases are selected with nucleation rate (a) 0.25 times; (b) 0.5 times; (c) 1.0 times; (4) 2 times of the reference state of 5.0e+11 ($\#/m^3/s$). The mass flux rate is observed to increase with the nucleation rate. The temperature field is plotted in Figure 8 and the temperature without the complication of bubble is also plotted. It is observed again that the model with bubbles result in a smaller heated region due to evaporation effect. In addition, the lower nucleation rate results in a larger heated region. In Figure 8, the order of the constant temperature contours with decreasing nucleation rate is "0.25", "0.5", "1", "2" and "no bubble". Figure 9 presents the porosity profiles for the four cases. It is clear that the larger nucleation rate results in a larger porosity field. The order of the size of the porous region is the same as the order of the nucleation rate. The velocity fields for the four cases are presented in Figure 10, where the order of the velocity still follows the order of the nucleation rate. The velocity region is found to be the same as the porous region in various cases. As a summary, the higher the nucleation rate, the higher the surface mass flux, the porous region, and the velocity region. The physical explanations as to the shapes and contours are already given before.

4.4 Influence of Initial Bubble Size

After nucleation, the critical radius (of nucleus) serves as the initial state of the bubble evolvement. It is of interest to know the influence of this radius on global bubble behavior. Figure 11 through Figure 13 present the mass flux distribution, the temperature field, the porosity field and the velocity field for four cases. They correspond to different radius of 0.25, 0.5, 1, and 2 times of the reference state. In addition the temperature field without the complication of bubbles are presented in Figure 12. Several observations are drawn from these figures. First, it is found that the porosity varies very little with the increase of the initial radius, although the size of porous region still increases with increasing radius, as seen from Figure 13. Second, the velocity field shows the similar pattern by comparison; it increases with increasing radius (though in a weaker manner). To seek an explanation, we go back to the bubble growth and movement formulation, as indicates by Equations (3) and Equation (7). The velocity of the bubble is a polynomial function of the radius; bubble growth rate, with some simplification, is a polynomial function of the resident time in the condensed phase. As a consequence, a higher initial bubble radius results in a higher velocity and a lower resident time. The bubble growth rate, on the contrary, results in a lower value due to the lower resident time. To estimate porosity, it is a volume-averaged quantity that receives contributions from single bubbles down below, as defined by Equation (11). Two competing mechanisms are available: a higher initial bubble radius helps to increase the porosity; however, the lower growth rate decreases the porosity. The two competing factors control the magnitude of the porosity. As observed from Figure 13, the two competing factors contribute in almost the same weights, thus resulting little difference of porosity contours among the three cases. The overall velocity of the bubble, as defined by Equation (15), is presented in Figure 14.

From Equation (15), because the velocity is a polynomial function of the bubble radius, $\overline{v}$ essentially is also polynomially dependent on the radius. This is why we observe the similar trend of $\overline{v}$ with the porosity. By observing the temperature profile, as is given in Figure 12, it is found that there is negligible difference between the four contours with bubble influence. The contour without the influence of bubble in this case again has a larger heated region due to the evaporation effect of bubble generation. The negligible difference due to the influence of initial bubble radius indicates that the bubble radius results in almost the same spatial distribution among 4 cases. A bubble radius is almost independent of the initial radius; however, the higher initial radius results in lower growth rate. The mass flux distribution is not plotted here, instead an integral quantity, the total mass flow rate (kg/s) at the surface is obtained and plotted in Figure 11. It is observed that the total mass flow rate decreases with the initial bubble radius. It indicates that the rate of bubble removal decreases with the bubble radius.

4.5 Influence of St

The influence of the latent heat to the bubble phenomena is investigated by varying St. Figures 15, 16, 17 and 18 report mass distribution, phase interface, porosity field and velocity field for three cases of St with values of 0.667, 2 and 6. Note that the use of lower latent heat results in a lower mass of the liquid, as reported by Figure 16, where the size of phase interface increases with increasing St. A higher latent heat requires a higher energy barrier, resulting in a smaller liquid region. The magnitude of the porosity is related to the size of the liquid region, as observed from Figure 17, where a larger liquid region has a larger porous region. This can be explained since a larger liquid region provides more nucleation sites, larger cumulative volume (since porosity is basically a

integral quantity that is dependent on the thickness of the liquid below), and longer bubble development space (longer time of evolvement). The overall effect of St is presented in Figure 18 in such a manner that the size of the liquid region is almost proportional to the number of the constant levels in that region. In addition, the pair of $St = 2$ and $St = 6$ is not so significantly different as compared to the pair of $St = 0.667$ and $St = 2$ because the former pair has a larger difference of the latent heat (recall that St is inversely proportional to the latent heat). The velocity field, as represented by Figure 18, indicates the similar phenomena with St, with a larger magnifying effect because the bubble velocity (Equation (3)) introduces an additional order of two for the bubble radius. Still, near the interface, the velocity and velocity have larger gradients due to the cumulative effect of the porosity. The total mass flow rate is plotted in Figure 15, showing an almost linear relation between the total mass flow rate and St. The mass flow rate is consistent with the size of liquid region in that a larger liquid region results a higher mass flux at the surface.

4.6 Influence of Evaporation Heat

In the reference state, we take the evaporation heat as 1000000 (J/kg). In order to investigate its influence, Figure 19 and Figure 20 present the total mass flow rate and the temperature field for three choices of the evaporation heat. They are 0.1 times, 1 times and 10 times of the reference state. Qualitatively, the increase of the evaporation heat removes more energy in the condensed phase, resembling the increase of the pyrolysis heat, and the temperature contours will have a smaller size, as seen by Figure 20. It is observed that the case with 10 times evaporation heat results in much smaller heated region compared to the reference state by observing that its temperature contour of 650 is

located along the surface. On the contrary, the case with 0.1 times of the evaporation heat results in a less significant difference from the reference state. The temperature contours indicate that there exists a range of evaporation heat where the temperature field might be very sensitive. The mass flux in Figure 19 shows that the total mass flow rate decreases with the increase of the evaporation heat. The lower mass flux comes from a smaller heated region as a consequence of the higher evaporation heat.

5. Conclusions

A transport model for condensed phase is constructed that encompasses the macro-scale transport of energy and micro-scale transport of bubbles in the condensed phase. In the micro-scale, each bubble is described in terms of its growth, movement by means of a set of analytical formula. In the macro-scale model, the energy equation that accounts for melting and heat conduction is volume-averaged by introducing bubble effects in the condensed phase. The resulting overall equation system is organized in such a way that (1) the micro-scale model, by using the temperature field from the macro-scale model, provides information on the radius, velocity, and locations of each representative bubble; (2) the macro-scale model, by using the information of the representative bubbles from the micro-scale model, calculates the volume averaged energy equation and obtain the temperature field. The macro-scale and micro-scale model are coupled together by a set of global parameters such as the velocity, the porosity, the mass rate of evaporation, which are directly derived from the volume averaging. The nucleation formulation is used to control the creation of the bubbles. A dynamic bubble database is constructed to maintain all the bubbles that are created in the liquid. The overall model is solved iteratively by numerical techniques. A representative 2-D case is calculated for the

transient heating of a polymer material subjected to a constant external heat flux at the surface. The time history of global parameters are presented and analyzed. It is found that there exist some discontinuities of porosity or velocity in the transient behavior of the condensed phase due to the discrete temporal formulation of bubble nucleation. However, the bubbles do not show the randomly or discontinuous behavior from the temperature contours. In order to evaluate the dependence of the model on the materials properties, sensitivity analysis is carried out for the bubble nucleation rate, the bubble initial radius, the latent heat, and the evaporation heat. It is found that these material properties have an impact on the transport process of the condensed phase. Generally, the increase of the nucleation rate, increase of the evaporation heat and decrease of the latent heat magnify the bubble transport; increase of the initial bubble radius does not change significantly the bubble behavior due to the complication of the bubble velocity and growth formulation. The bubble transport model shows the potential in predicting related problems such as the flame spread over the condensed phase with melting and bubble generation.

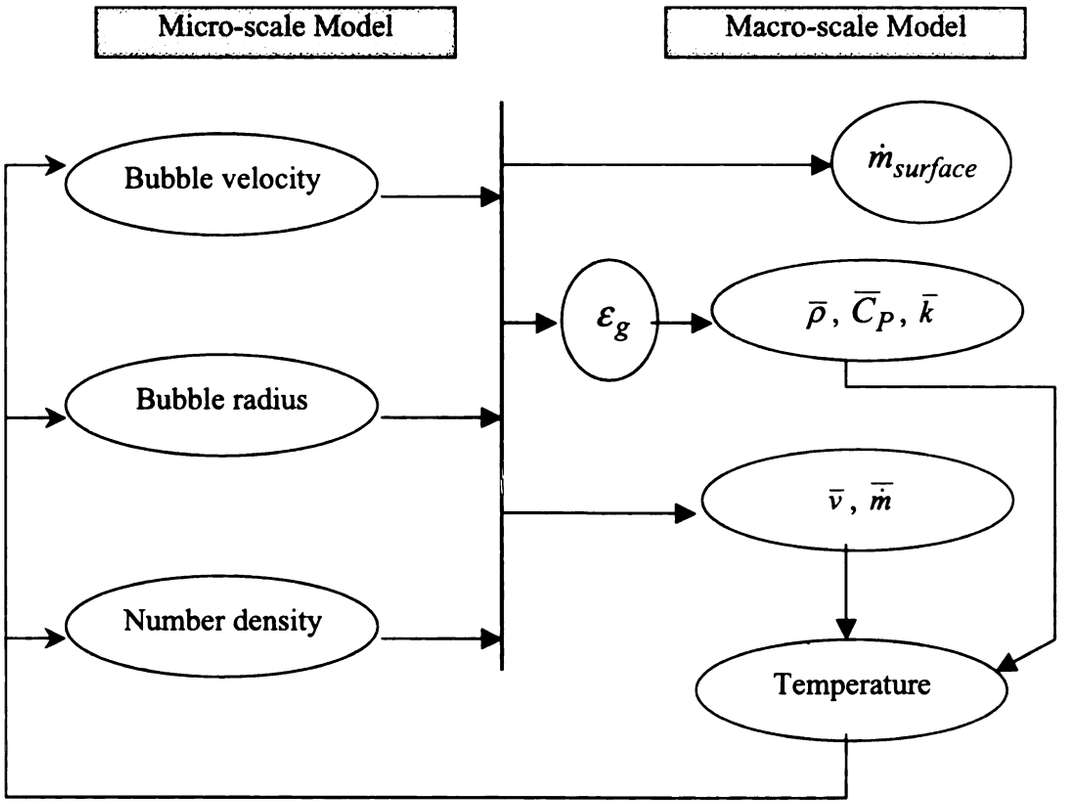

Figure 1 Relationship between macro-scale model and micro-scale model.

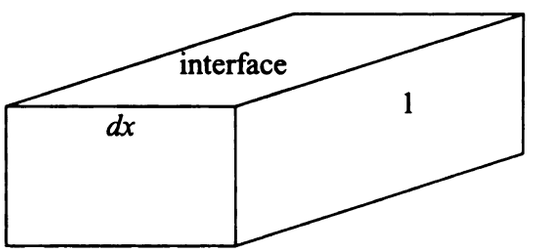

Figure 2 A control volume selected to obtain $\dot{m}_{interface}$.

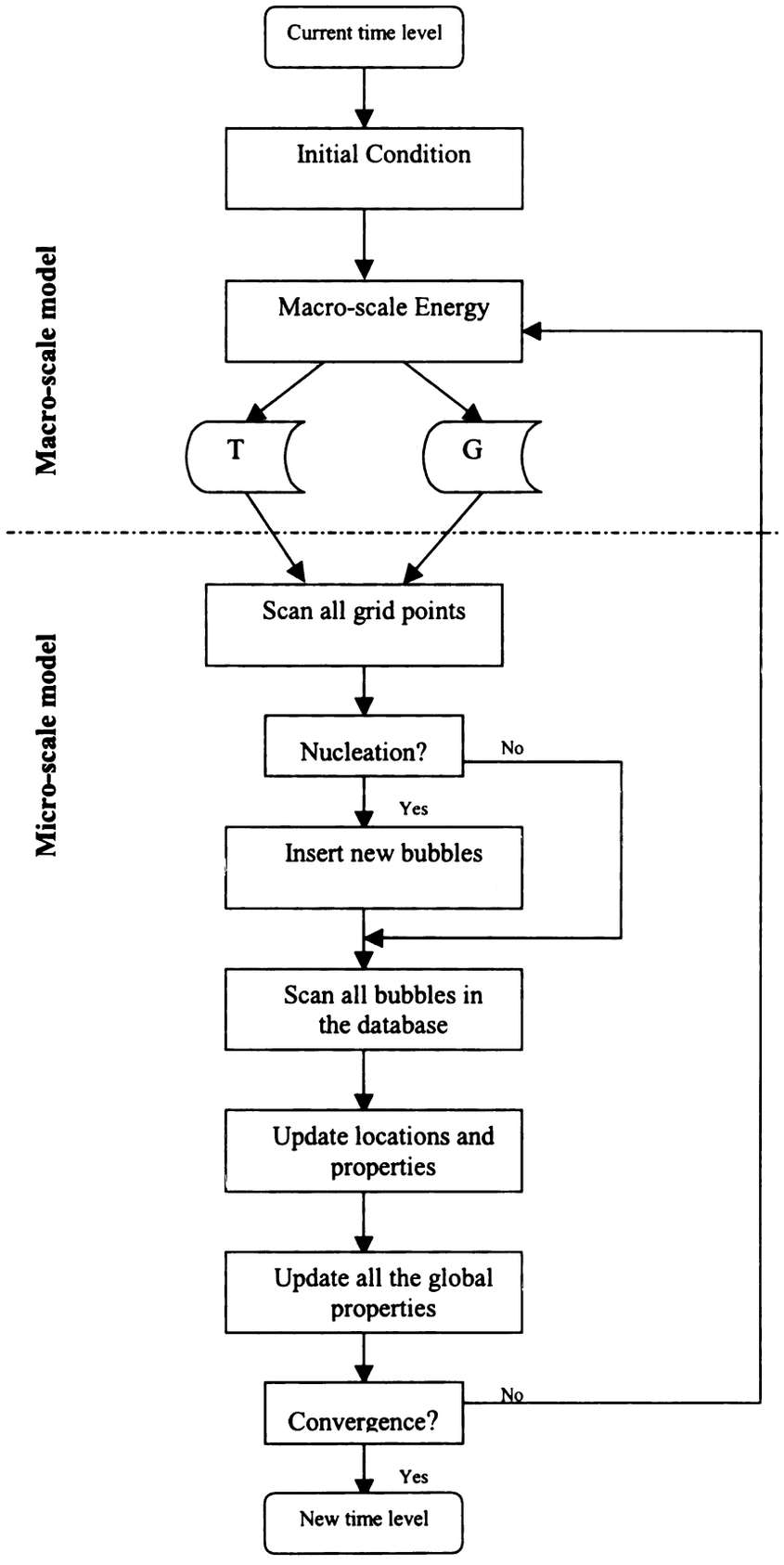

Figure 3 Flow chart of the iterative procedure for the solution of the two scale model

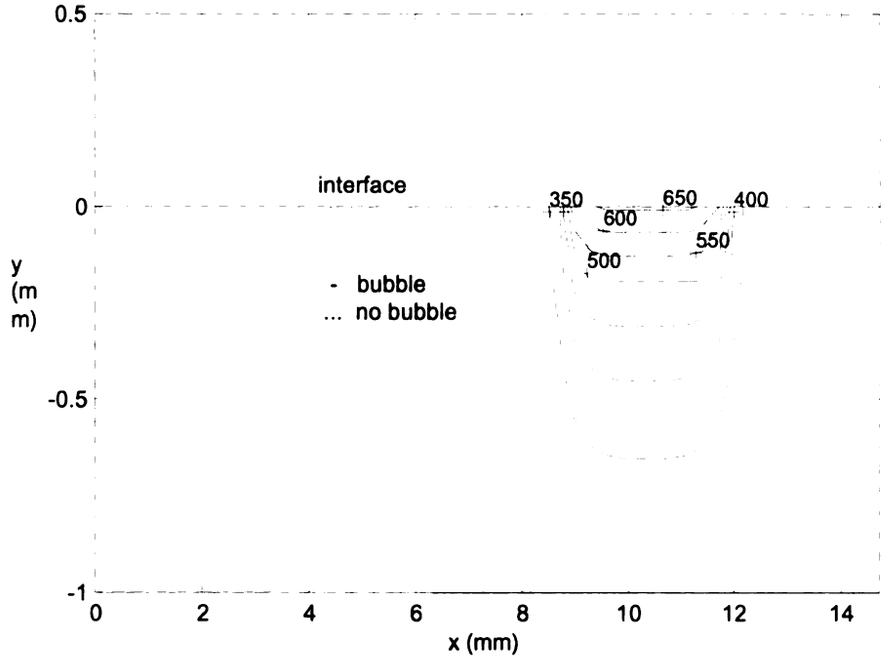

Figure 4 (a) Temperature constant levels at 5s.

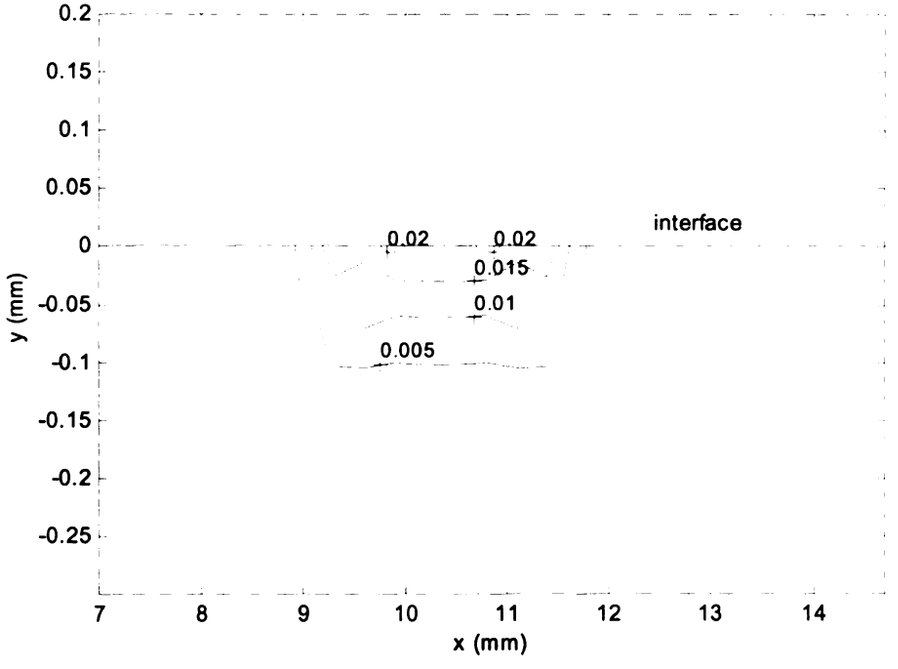

Figure 4 (b) The porosity constant levels at 5s.

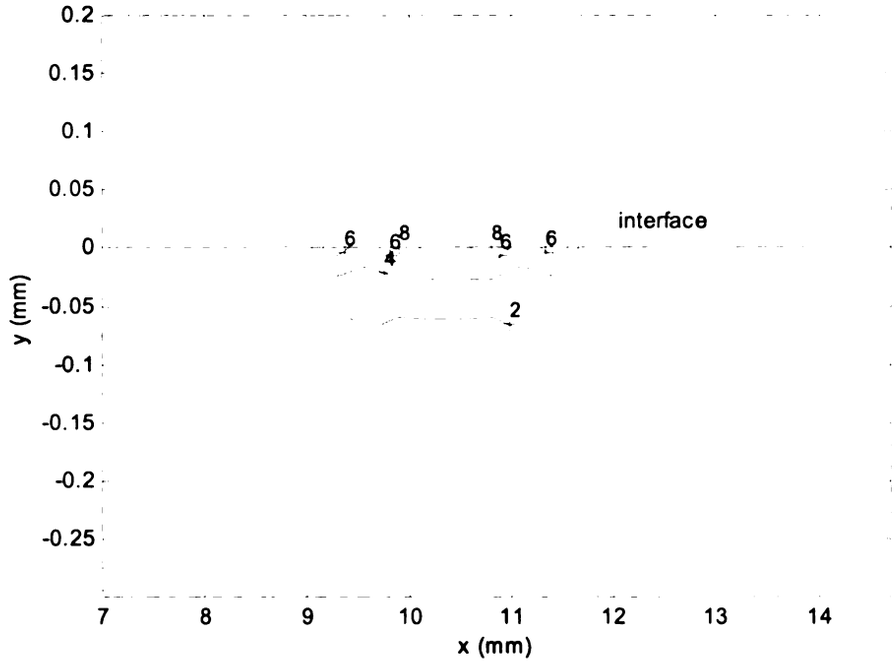

Figure 4 (c) The velocity constant contour at 5s with unit of $1\times10^{-7}\,m/s$ for each label.

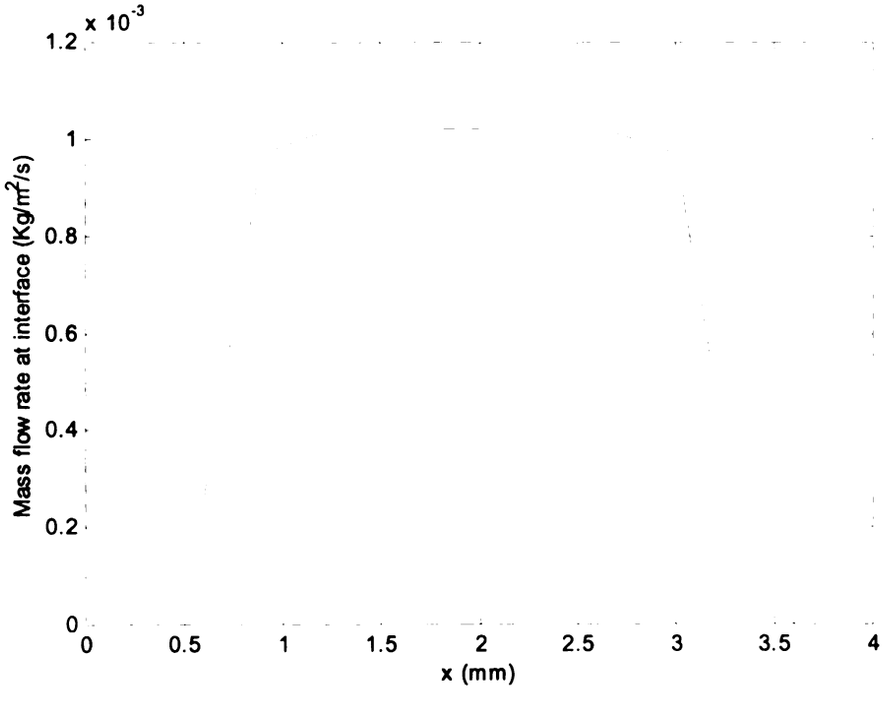

Figure 4 (d) The mass flow rate out of the interface at 5s.

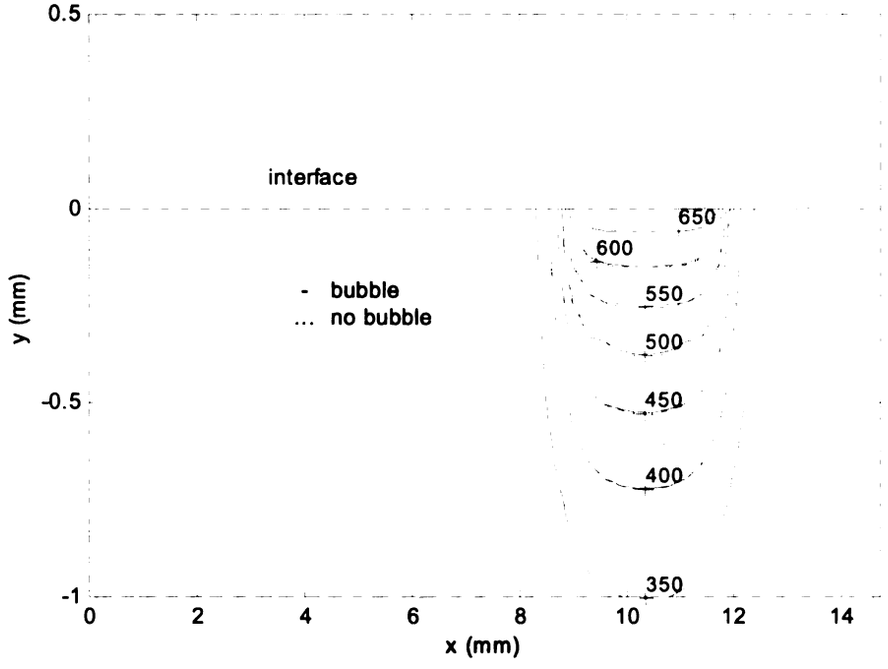

Figure 5 (a) Temperature field at 10s.

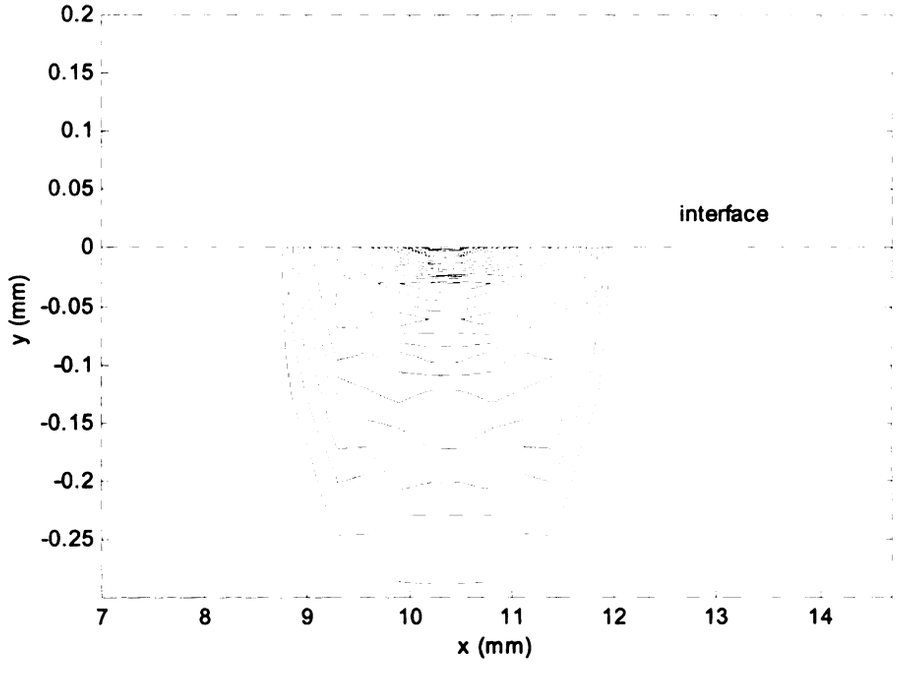

Figure 5 (b) Porosity Field at 10s. The constant levels start at the minimum of 0.005 with step of 0.005.

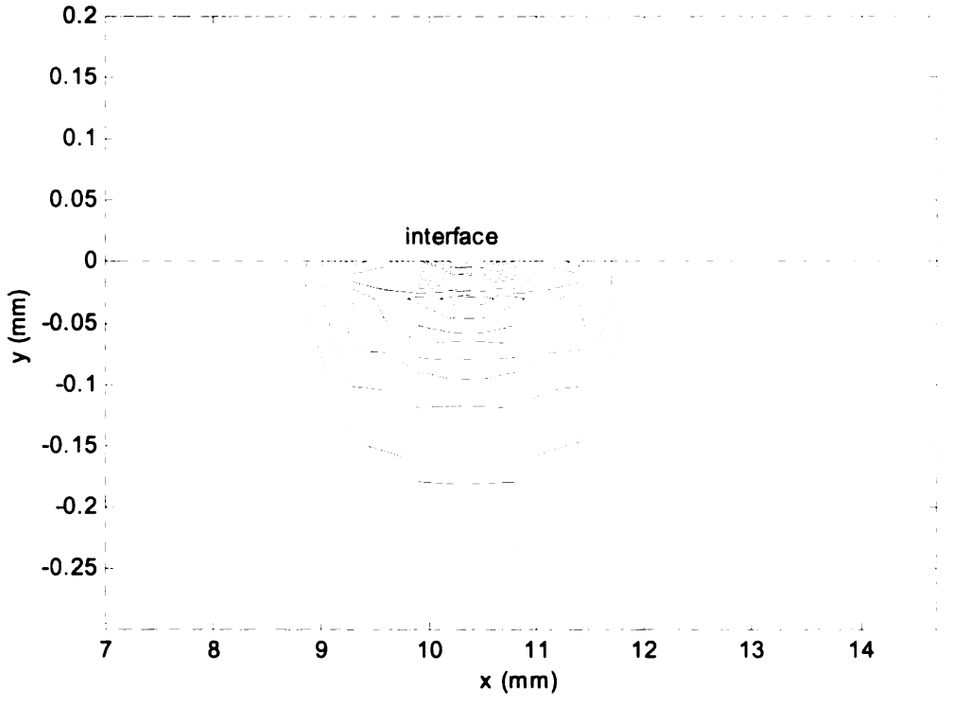

Figure 5 (c) Velocity constant levels at 10s. The minimum level is 5×10^{-7} with step of 5×10^{-7}.

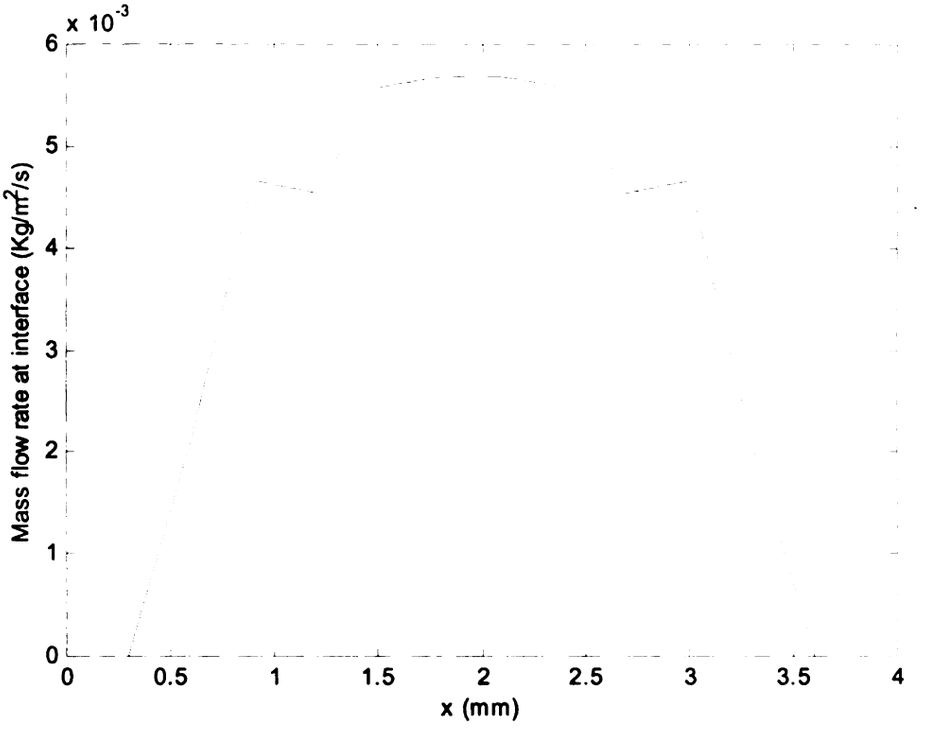

Figure 5 (d) The mass flow rate out of the interface at 10s.

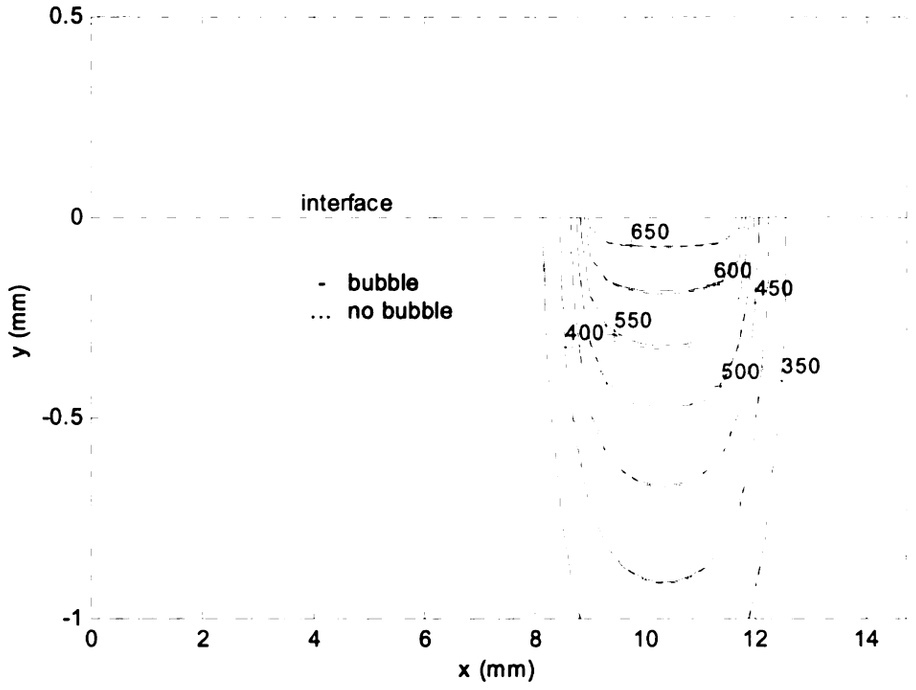

Figure 6 (a) Temperature field at 19s.

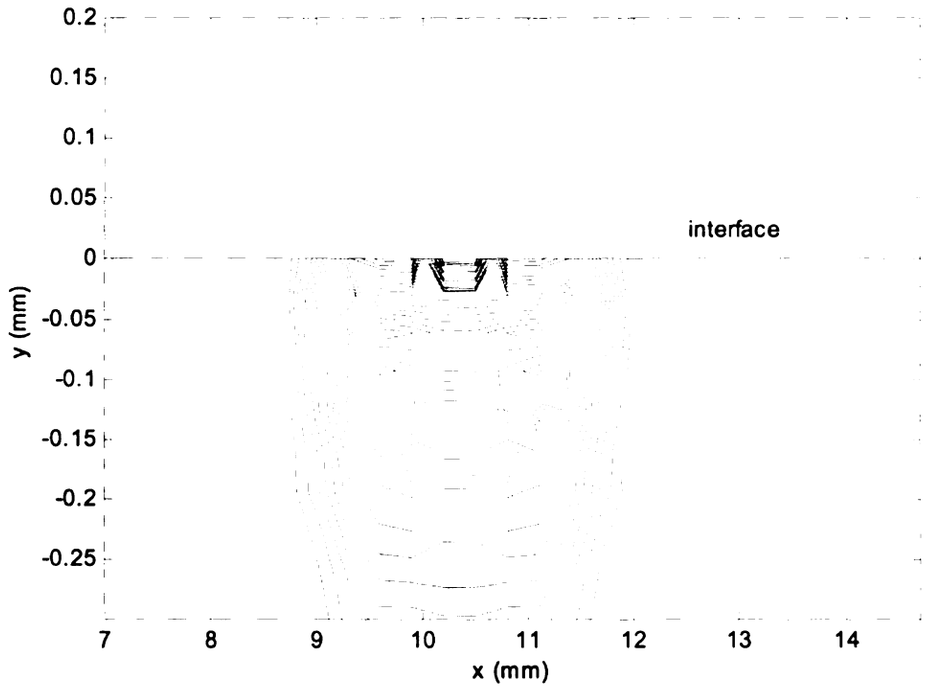

Figure 6 (b) Porosity Field at 19s. The constant levels start at the minimum of 0.005 with step of 0.005.

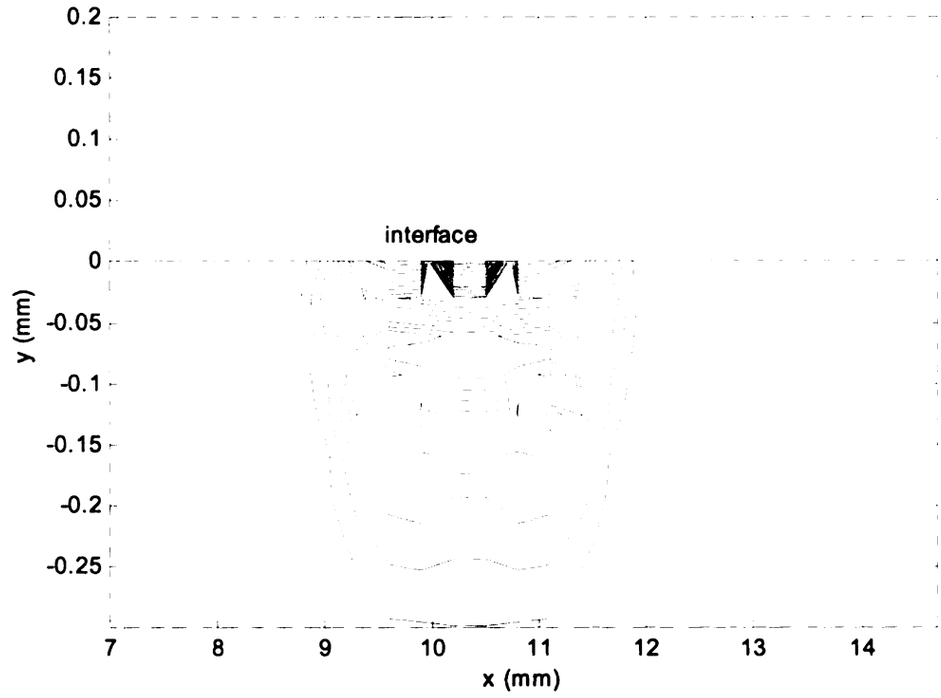

Figure 6 (c) Velocity constant levels at 19s. The minimum level is 5×10^{-7} with step of 5×10^{-7}.

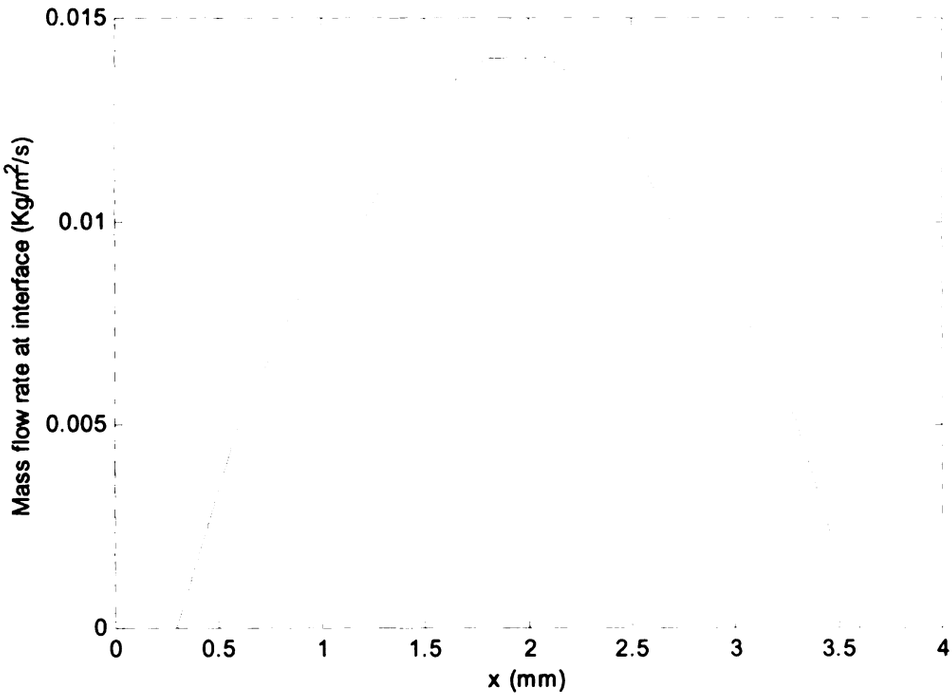

Figure 6 (d) The mass flow rate out of the interface at 19s.

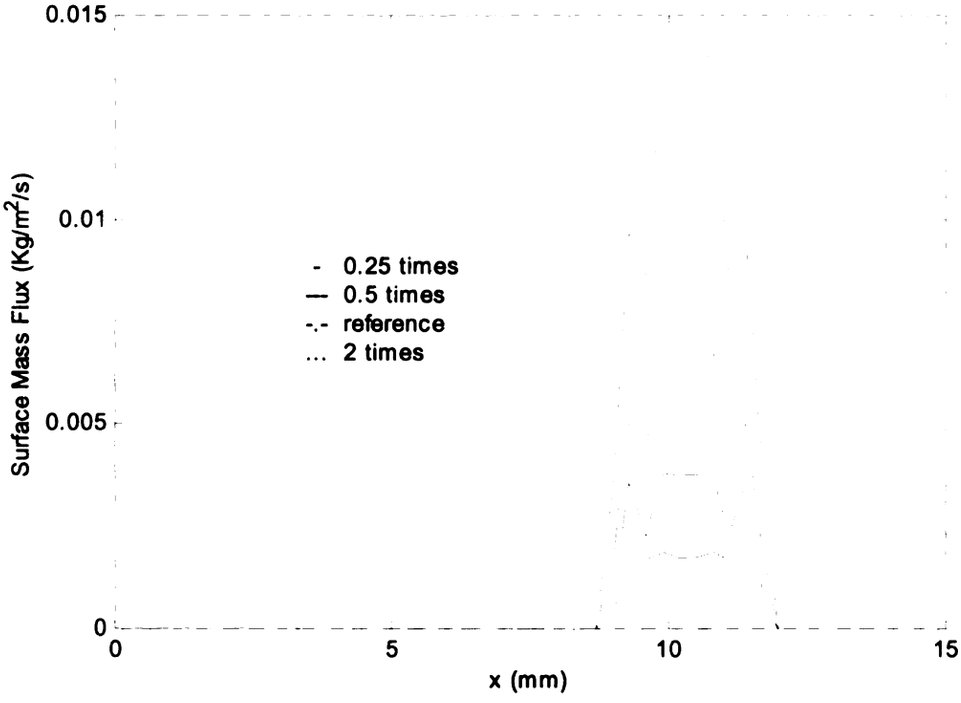

Figure 7 The surface mass flux for 4 cases with different nucleation rate at 10s. The reference nucleation rate is 5.0e+11 (#/m^3/s).

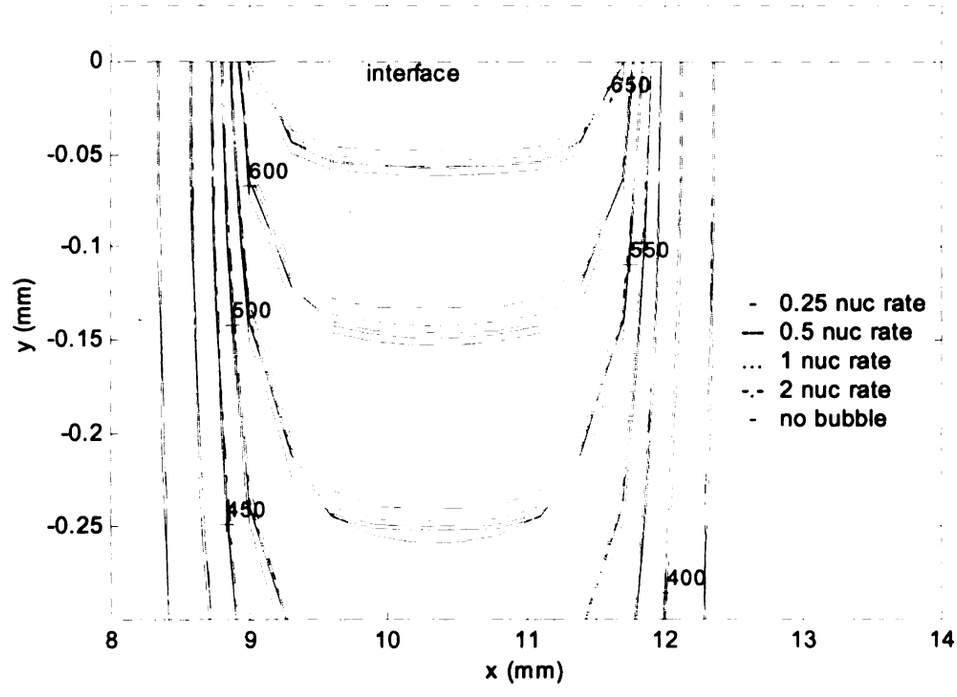

Figure 8 The temperature constant contours for 4 cases with different nucleation rate at 10s. The reference nucleation rate is 5.0e+11 (#/m^3/s).

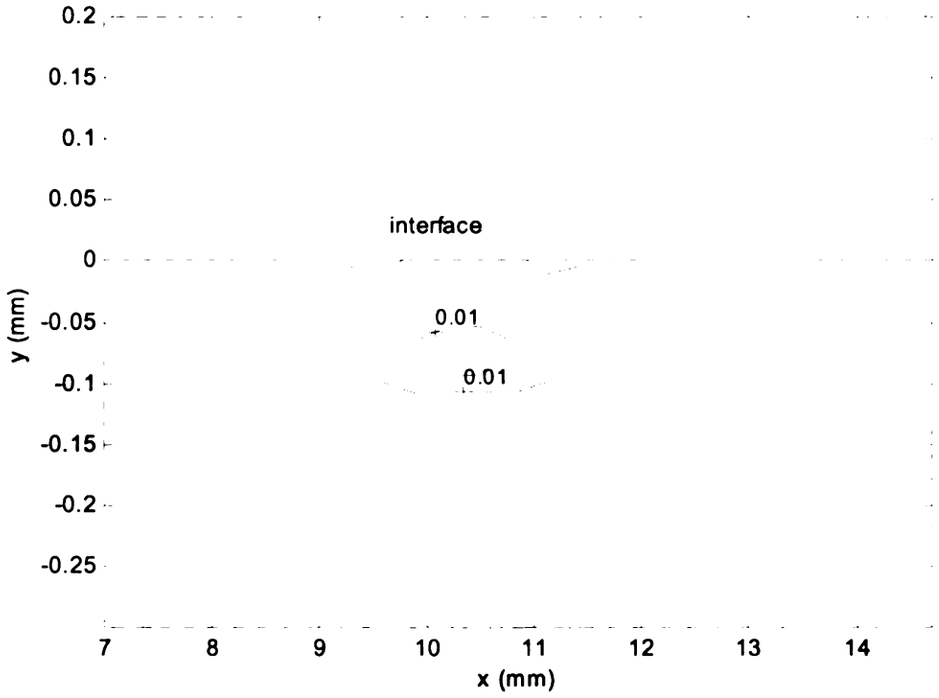
0.2
0.15
0.1
0.05
0
-0.05
-0.1
-0.15
-0.2
-0.25
y (mm)
interface
0.01
0.01
7
8
9
10
11
12
13
14
x (mm)

(9-a)

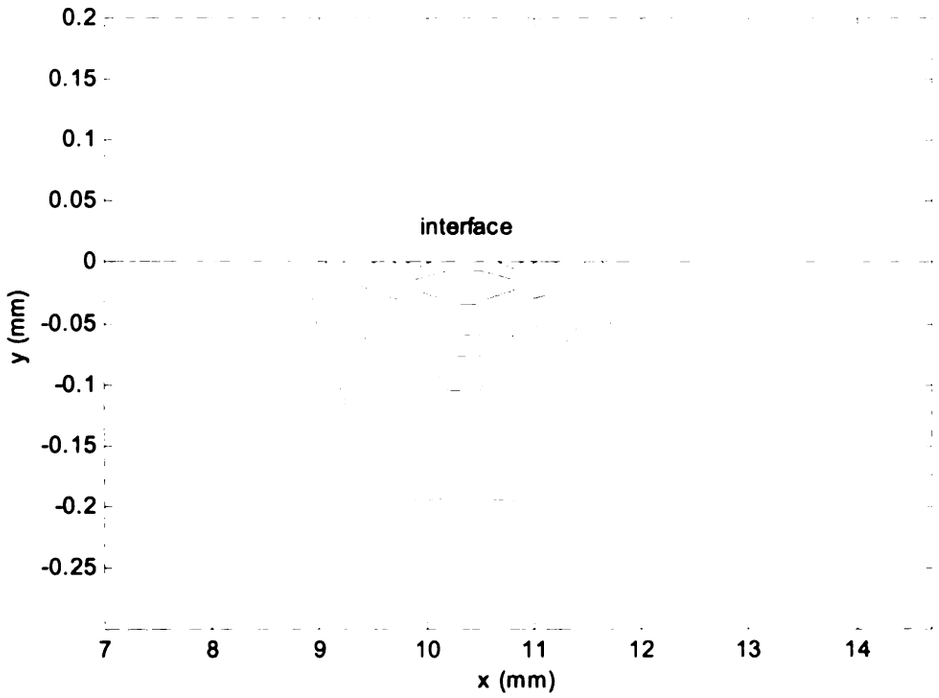
0.2
0.15
0.1
0.05
0
-0.05
-0.1
-0.15
-0.2
-0.25
y (mm)
interface
7
8
9
10
11
12
13
14
x (mm)

(9-b)

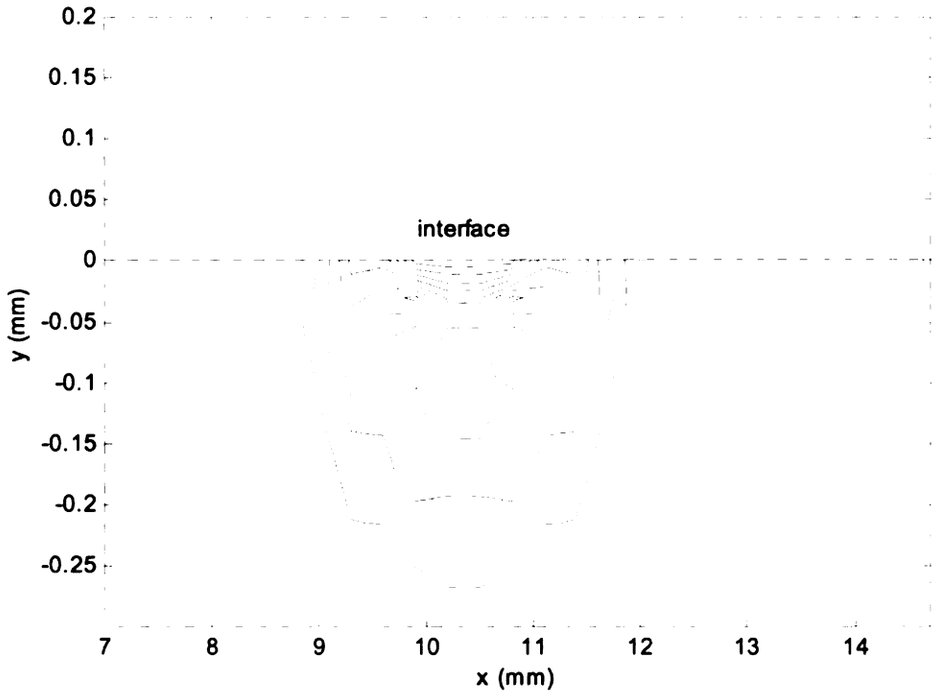

(9-c)

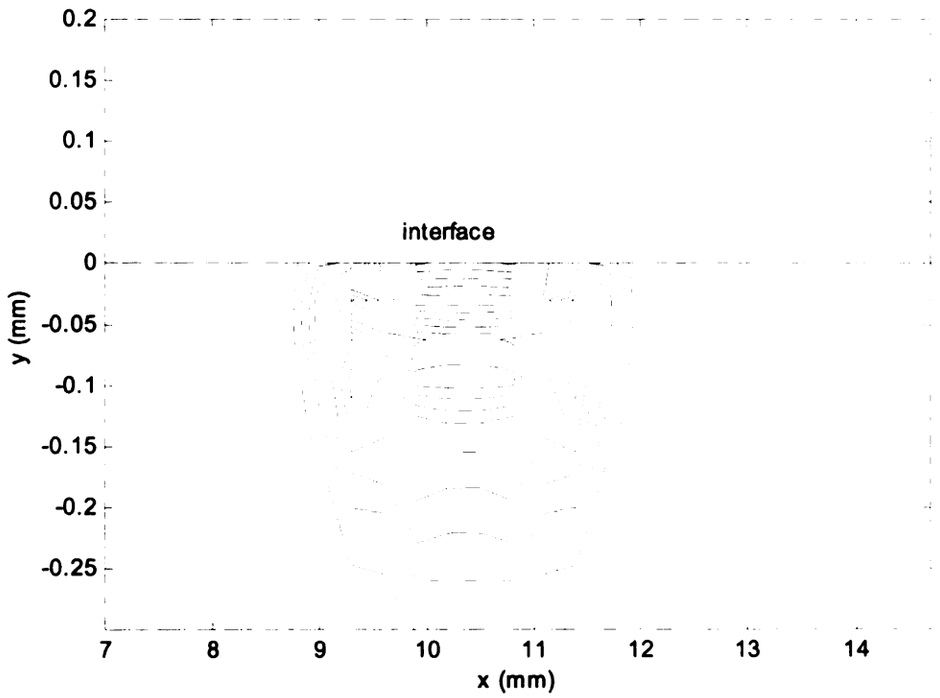

(9-d)

Figure 9 The porosity constant contours in the condensed phase at 10s for 4 cases with different nucleation rate: (a) 0.25 times (b) 0.5 times (c) 1 times (d) 2 times of the reference rate. The outmost constant level is 0.01 and step is 0.01.

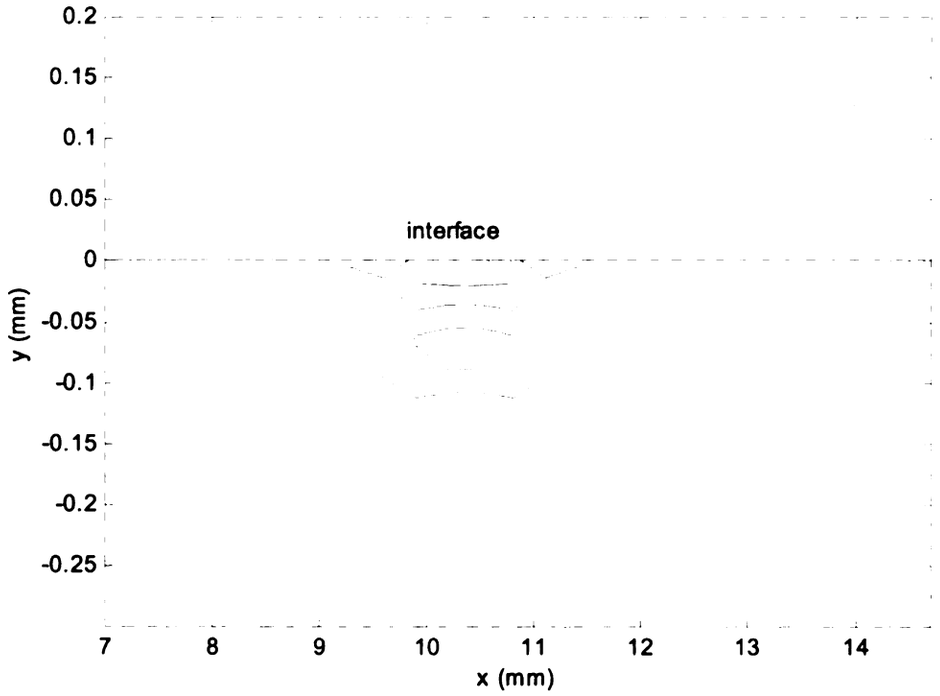
0.2
0.15
0.1
0.05
0
-0.05
-0.1
-0.15
-0.2
-0.25
interface
y (mm)
7
8
9
10
11
12
13
14
x (mm)

(10-a)

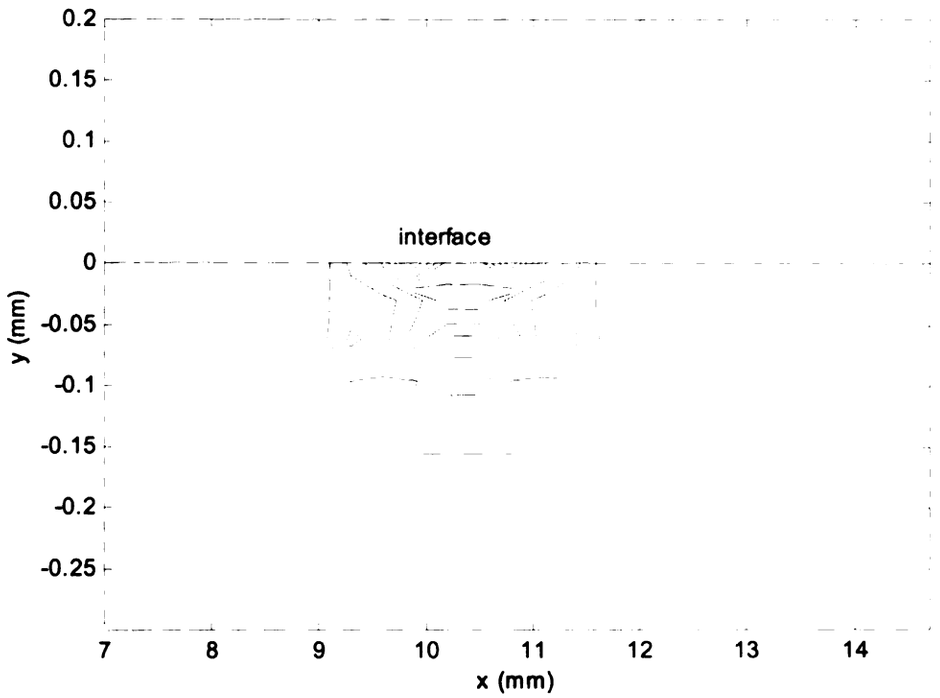
0.2
0.15
0.1
0.05
0
-0.05
-0.1
-0.15
-0.2
-0.25
interface
y (mm)
7
8
9
10
11
12
13
14
x (mm)

(10-b)

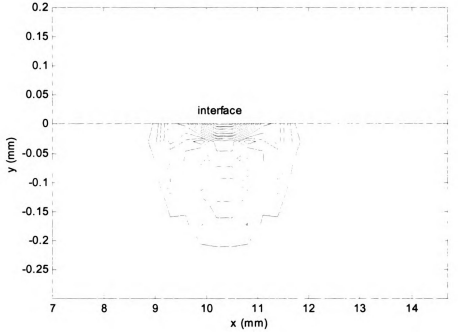

(10-c)

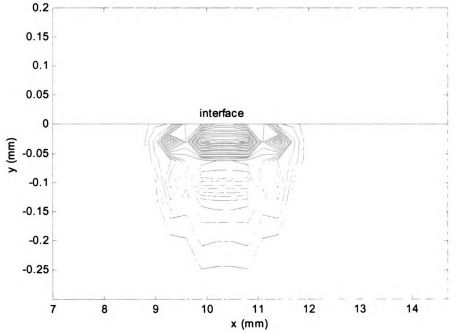

(10-d)

Figure 10 The velocity constant contours in the condensed phase at 10s for 4 cases with different nucleation rate: (a) 0.25 times (b) 0.5 times (c) 1 times (d) 2 times of the reference rate. The outmost constant level is 5×10^{-7} and step is 5×10^{-7}.

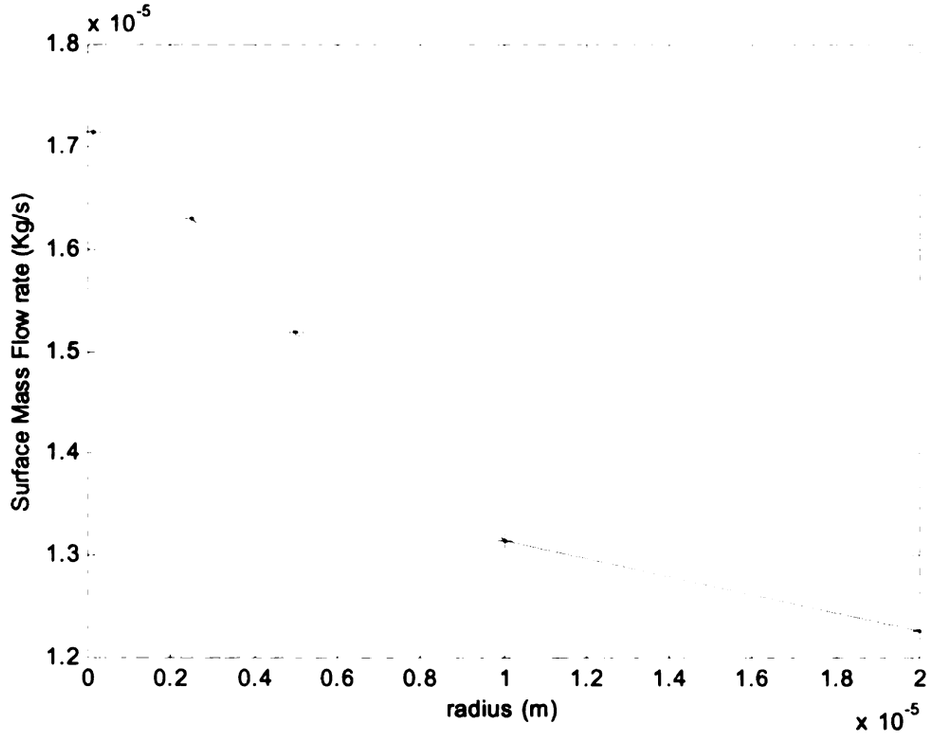

Figure 11 The surface mass flow rate vs. the bubble initial radius.

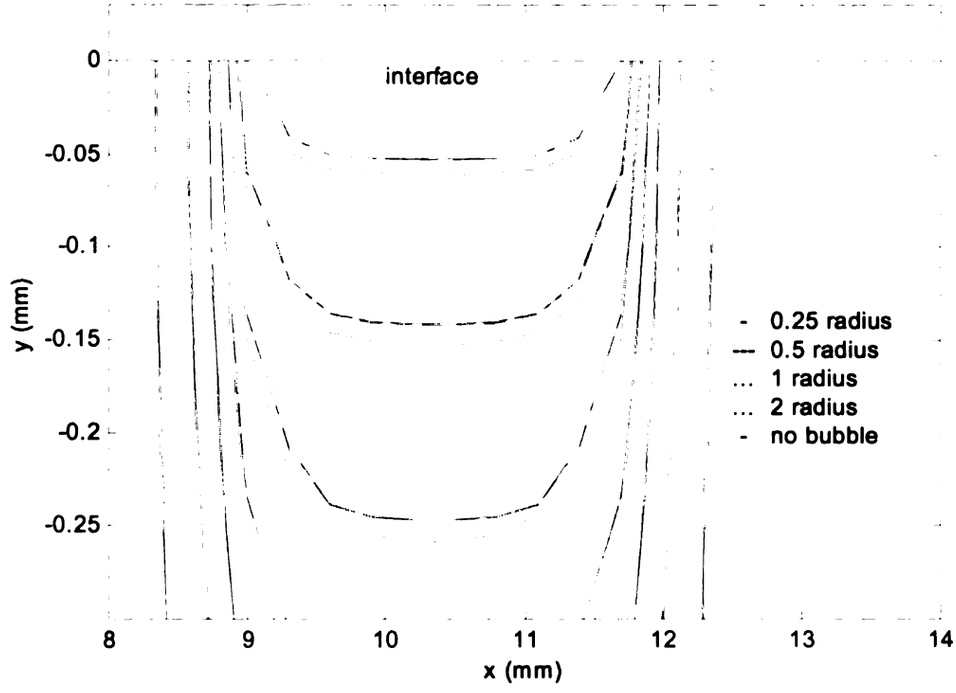

Figure 12 The temperature constant contours for 4 cases with different initial bubble radius at 10s. The reference bubble initial radius is 5×10^{-6} m.

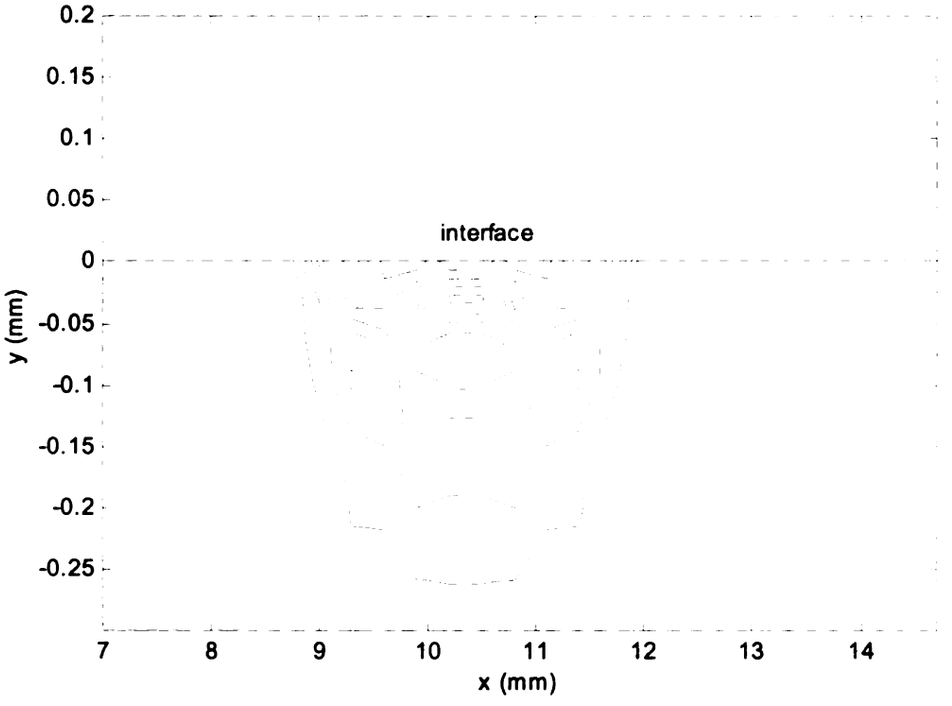
0.2
0.15
0.1
0.05
0
-0.05
-0.1
-0.15
-0.2
-0.25
interface
y (mm)
7
8
9
10
11
12
13
14
x (mm)

(13-a)

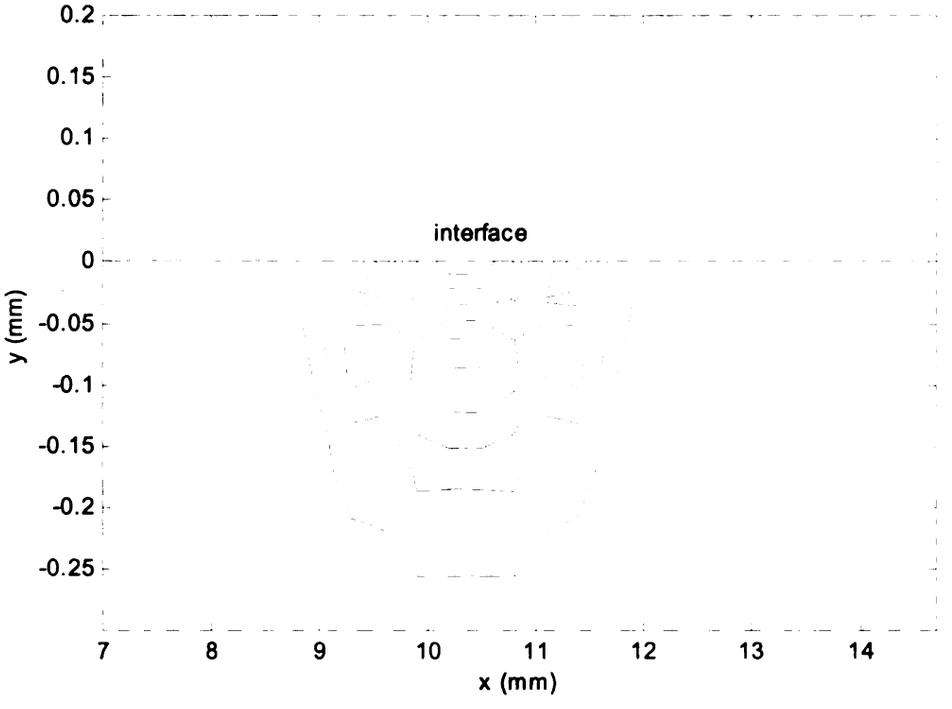
0.2
0.15
0.1
0.05
0
-0.05
-0.1
-0.15
-0.2
-0.25
interface
y (mm)
7
8
9
10
11
12
13
14
x (mm)

(13-b)

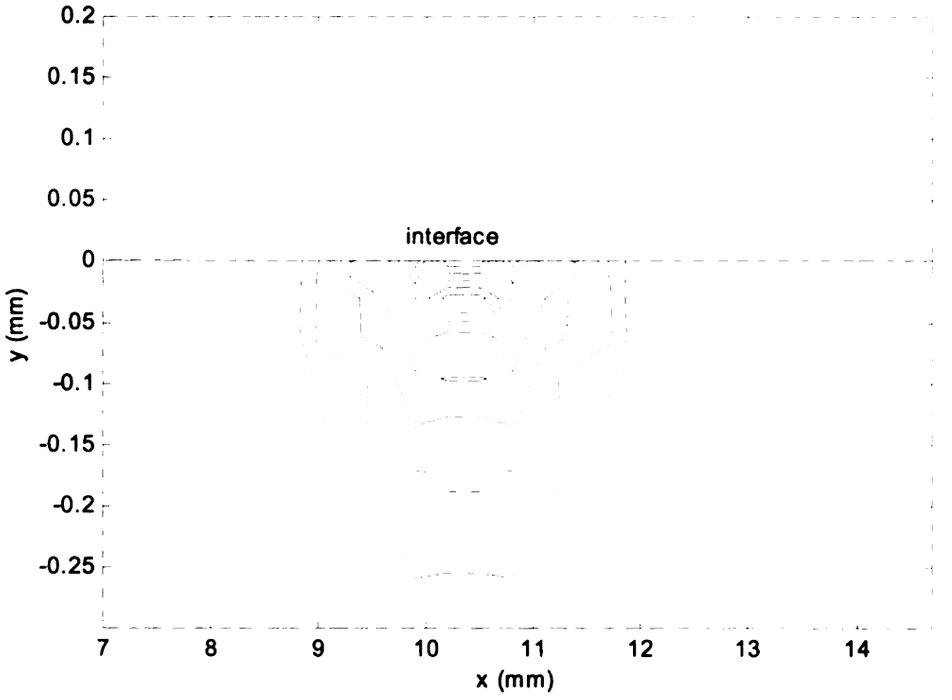

(13-c)

Figure 13 The porosity constant contours in the condensed phase at 10s for three cases with different initial bubble radius: (a) 0.25 times (b) 0.5 times (c) 2 times of the reference radius. The reference bubble initial radius is 5×10^{-6} m. The outmost constant level is 0.01 and step is 0.01.

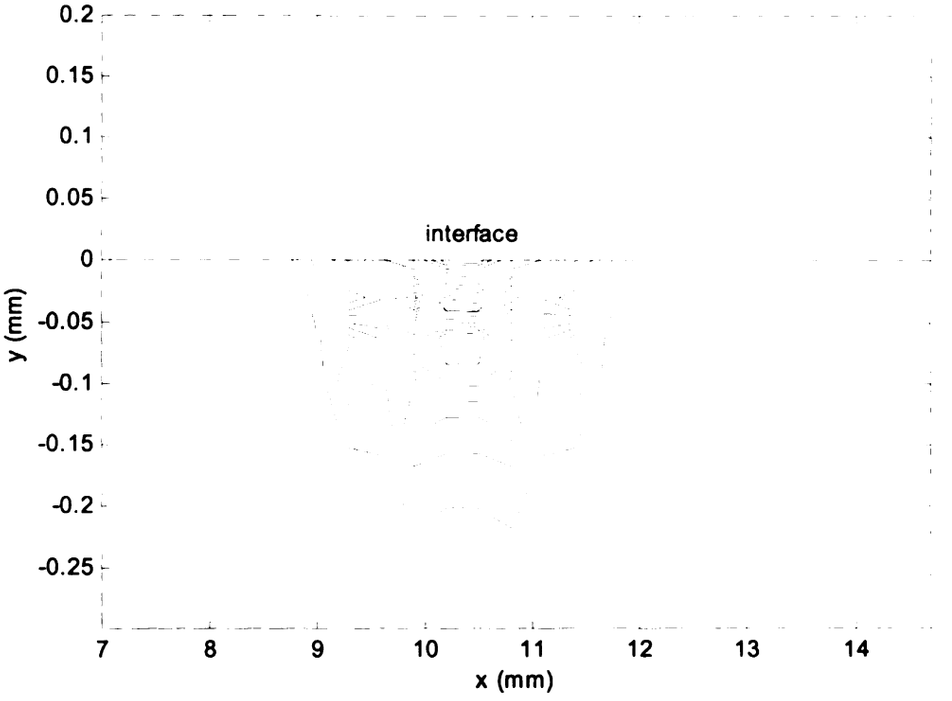

(14-a)

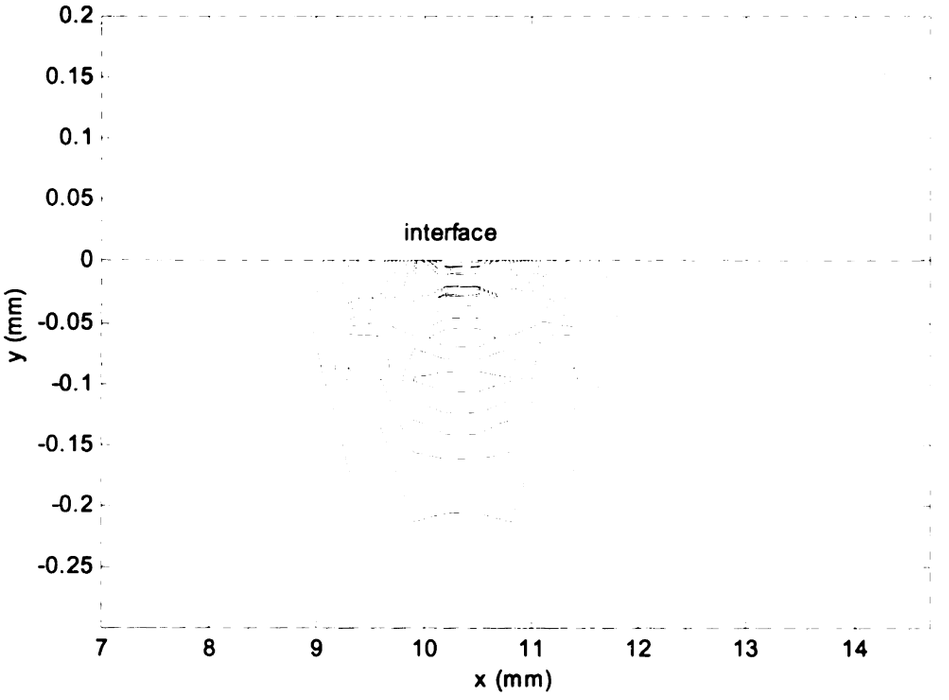

(14-b)

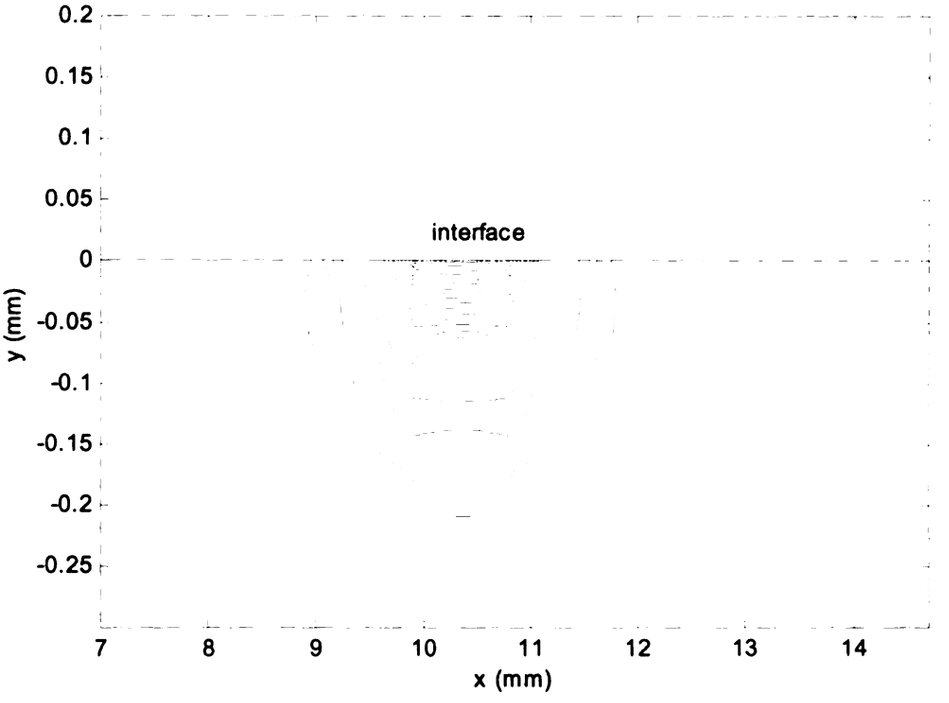

Figure (14-c)

Figure 14 The velocity constant contours in the condensed phase at 10s for three cases with different initial bubble radius: (a) 0.25 times (b) 0.5 times (c) 2 times of the reference radius. The reference bubble initial radius is 5×10^{-6} m. The outmost constant level is 5×10^{-7} and step is 5×10^{-7}.

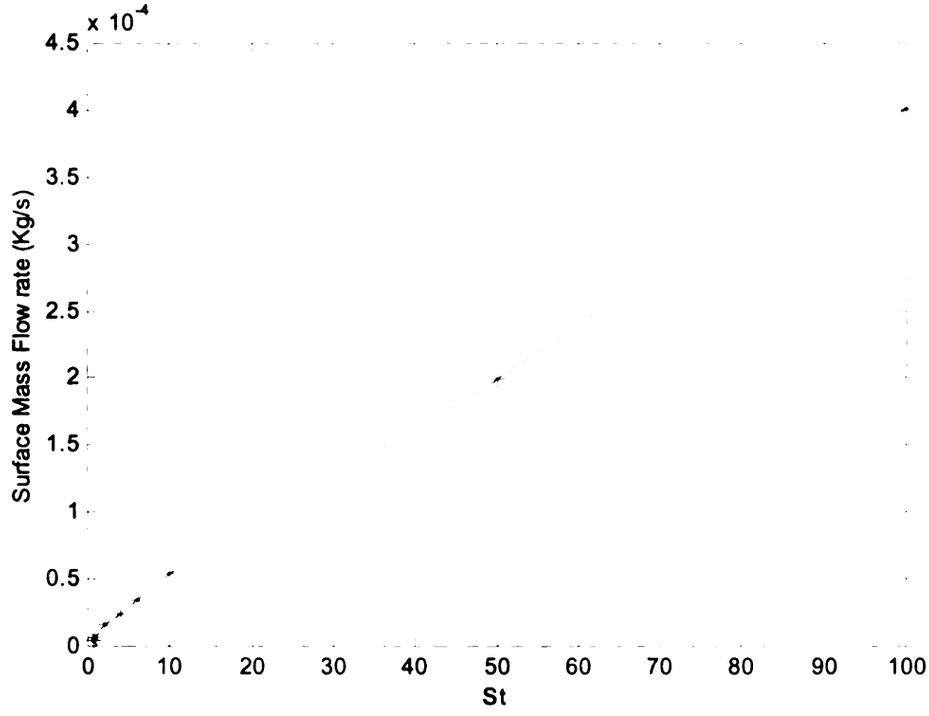

Figure 15 The surface mass flow rate vs. St.

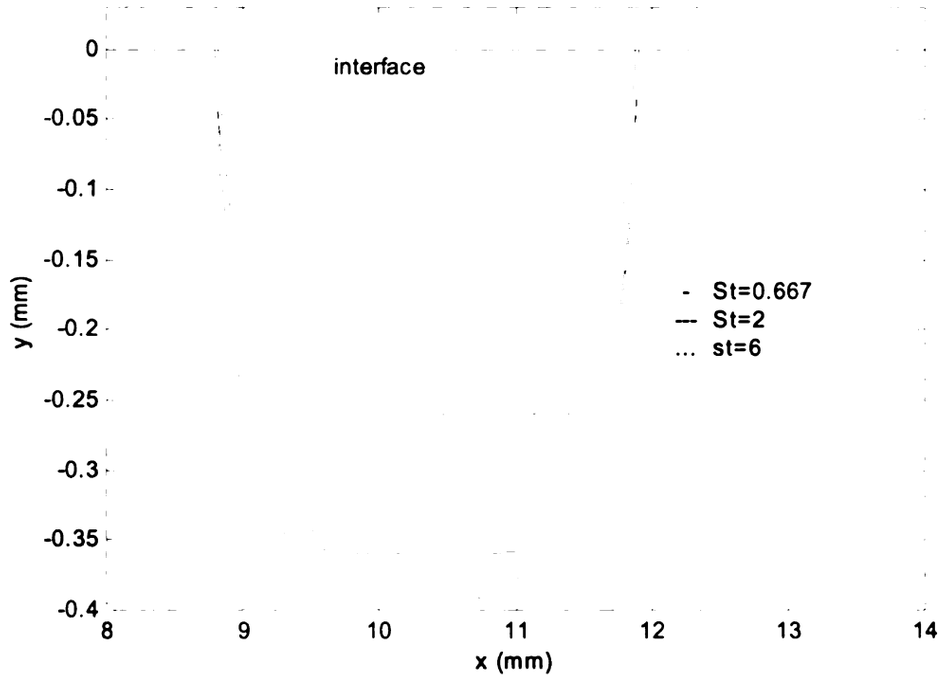

Figure 16 The phase interface for three cases of St.

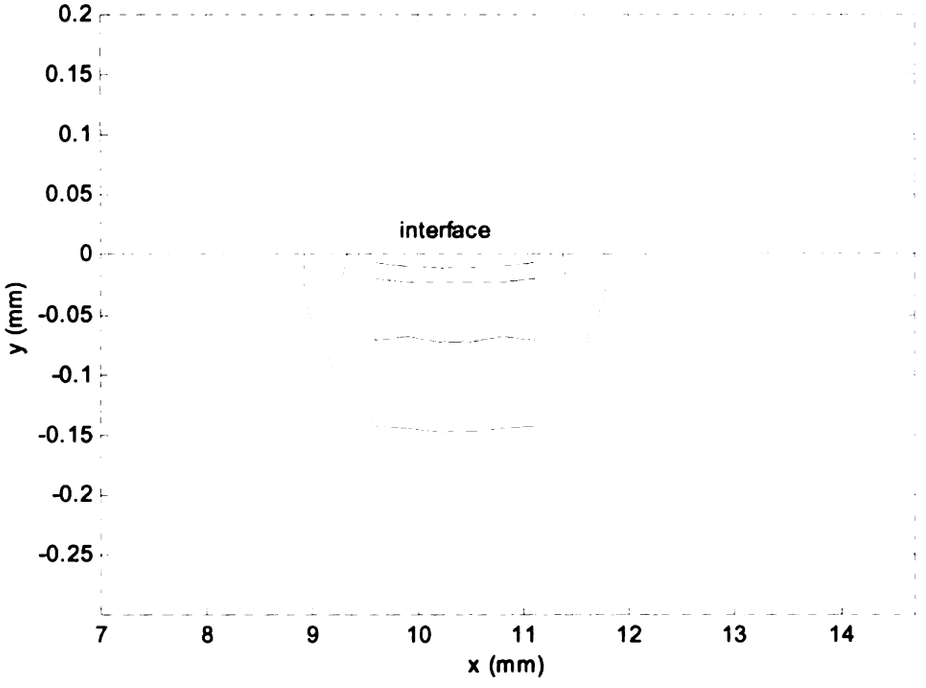
0.2
0.15
0.1
0.05
0
-0.05
-0.1
-0.15
-0.2
-0.25
interface
y (mm)
7
8
9
10
11
12
13
14
x (mm)

(17-a)

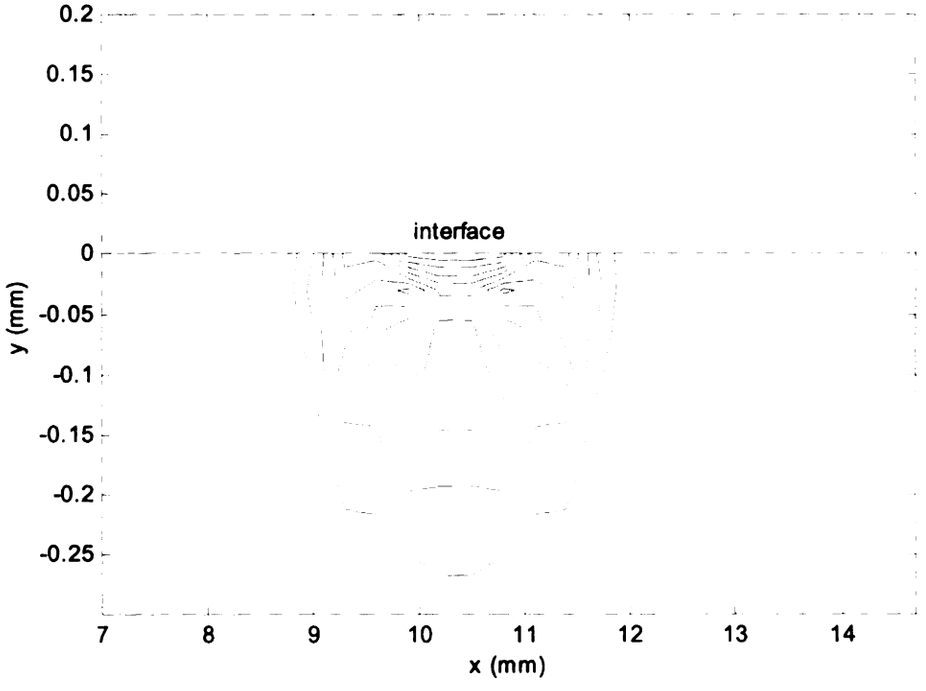
0.2
0.15
0.1
0.05
0
-0.05
-0.1
-0.15
-0.2
-0.25
interface
y (mm)
7
8
9
10
11
12
13
14
x (mm)

(17-b)

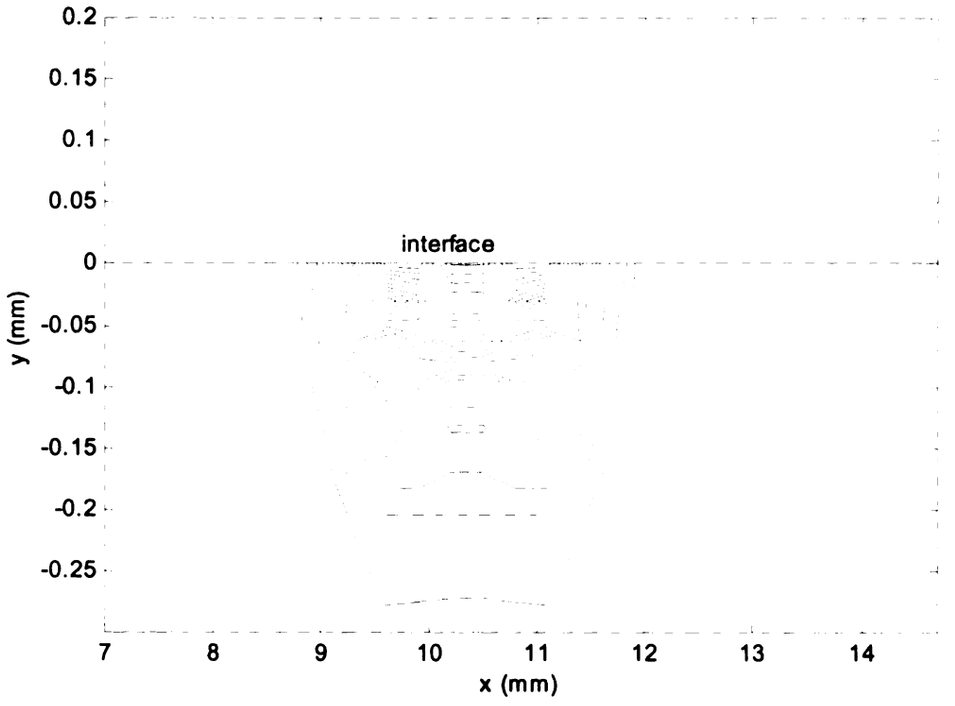

(17-c)

Figure 17 The porosity constant contours in the condensed phase at 10s for three cases with different St: (a) $St = 0.667$ (b) $St = 2$ (c) $St = 100$. The outmost constant level is 0.01 and the step is 0.01.

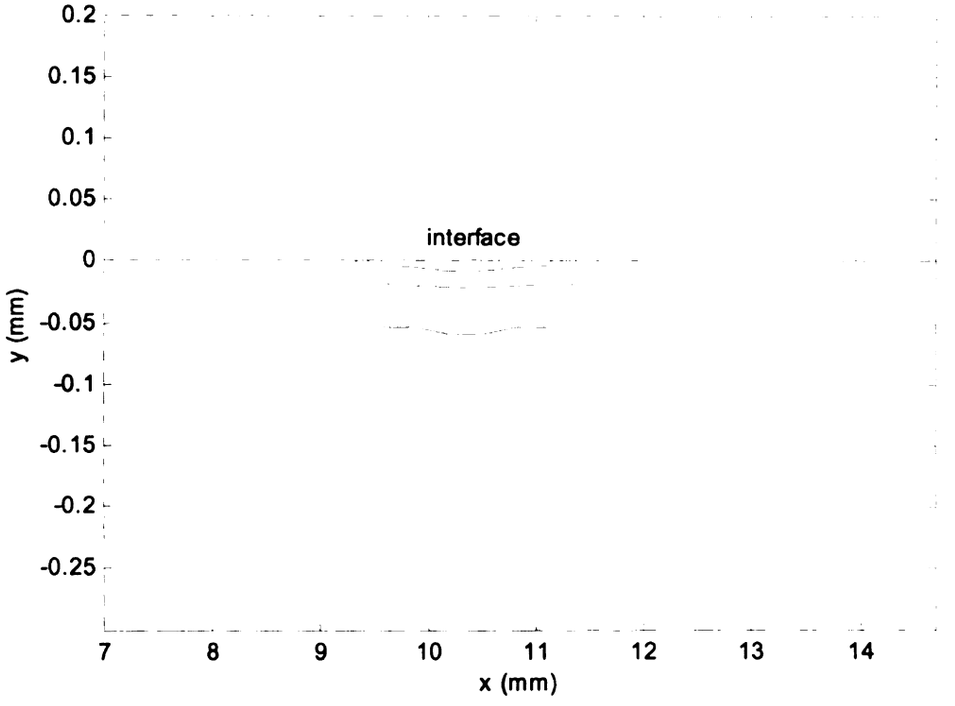

(18-a)

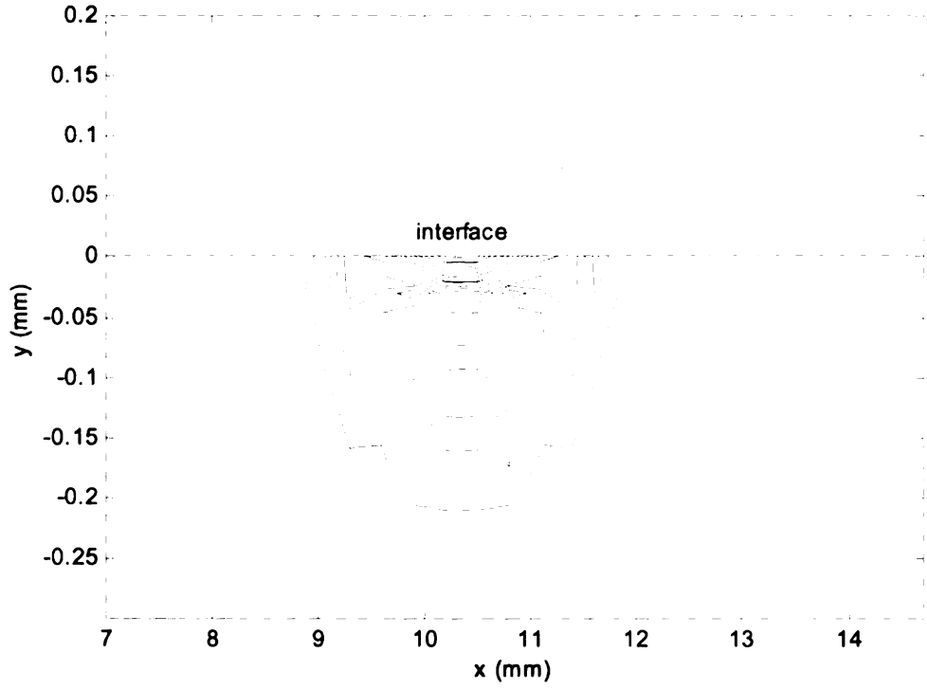

(18-b)

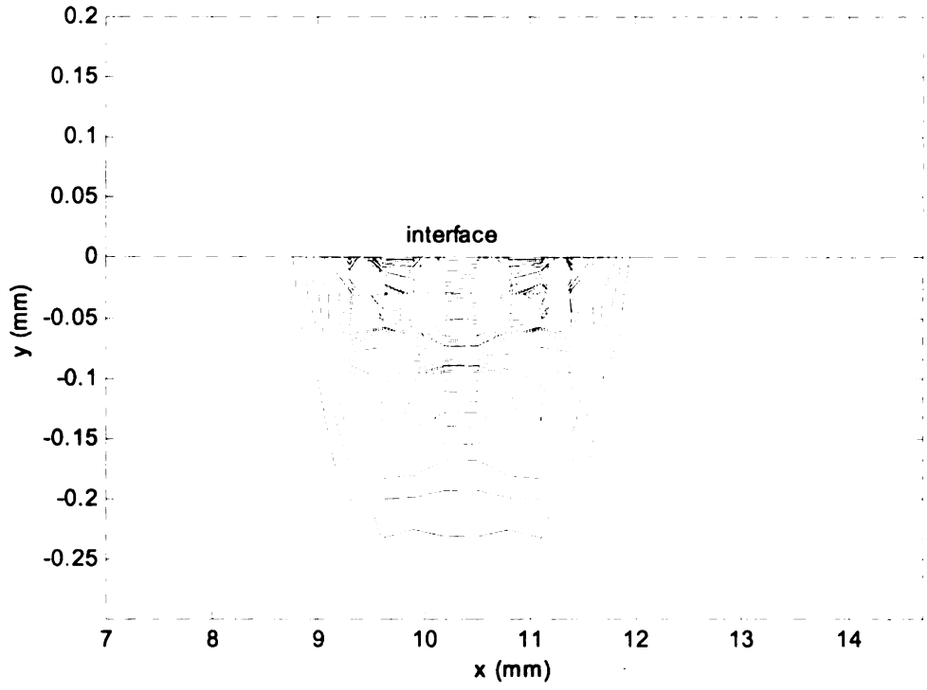

(18-c)

Figure 18 The velocity constant contours in the condensed phase at 10s for three cases with different St: (a) $St = 0.667$ (b) $St = 2$ (c) $St = 100$. The outmost constant level is 5×10^{-7} and the step is 5×10^{-7}.

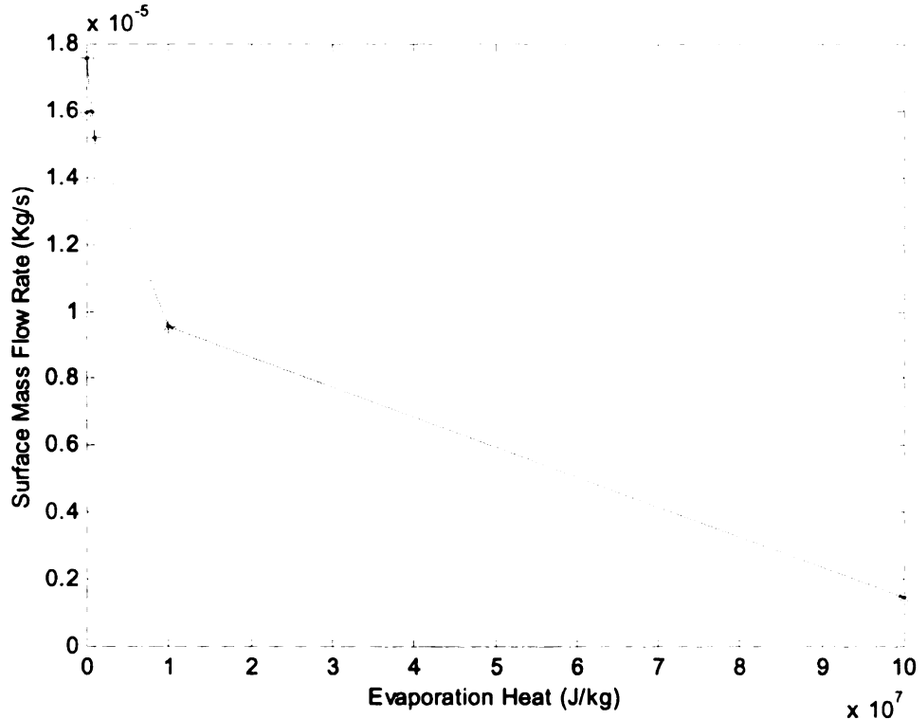

Figure 19 The surface mass flow rate vs. evaporation heat.

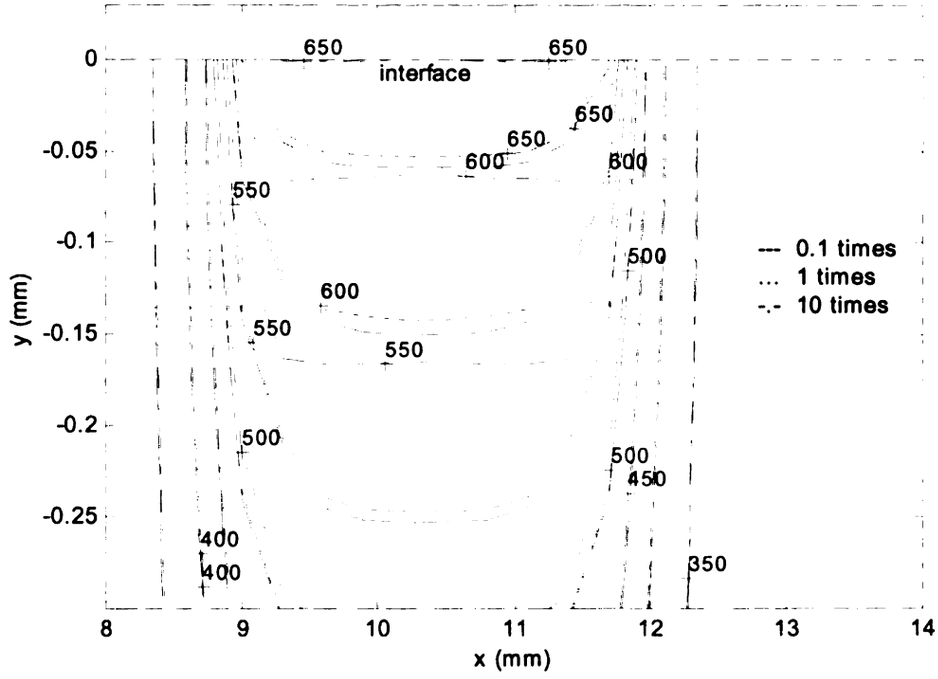

Figure 20 The phase interface for three cases of evaporation heat.

CHAPTER 8

CONCLUSIONS AND FUTURE WORK

Transient flame development over plastic polymeric materials is of both fundamental and practical importance to fire safety. The flame behavior is determined by various coupling physical and chemical mechanisms such as (1) in the gas phase, combustion reaction, channel cross flow, reaction-induced thermal expansion, and interface injection flow; (2) in the condensed phase, melting, pyrolysis reaction, bubble nucleation, growth, and movement; (3) at interface, radiation heat loss and fuel and oxidizer transport. A two dimensional numerical model is established to describe such transient flame spread process with emphasis on the influence of condensed phase.

In Chapter 2, the influence of the solid anisotropy is investigated. The Oseen approximation is applied in order to remove the complication of flow coupling. Transient behavior such as pre-heating, ignition, and steady spread is qualitatively identified. The dependence of ignition delay time and flame spread rate on thermal conductivities is obtained by introducing a ratio of k_{sx}/k_{sy} while keeping k_{sxy} and $(k_{sx}+k_{sy})$ constant. With the increase of this ratio, it is found that the flame spread rate increases while the ignition delay decreases.

In Chapter 3, flame spread over melting polymers is investigated by varying three material properties including liquid thermal conductivity ($\bar{k}_l$), latent heat of melting (St) and liquid heat capacity ($\overline{C}_{Pl}$). In addition, the Oseen approximation is still preserved. The numerical model provides very good agreement with an analytical formula [28]. DeRis 's flame spread formula, however, results in a constant spread rate value higher

than the numerical result. Physically, a lower latent heat or a lower thermal capacity generates a lower energy barrier for the flame, hence a larger spread rate. The increase of $\bar{k}_l$, on the other hand, denoting the diffusion away of the thermal energy for preheating, results in a lower spread rate. The dependence of flame structure on St, $\bar{k}_l$, and $\overline{C}_{Pl}$ were studied. With the increase of St or $\bar{k}_l$, or with the decrease of $\overline{C}_{Pl}$, the flame size increased. These results are consistent with the qualitative nature of the dependence of the flame spread rate on the three parameters. The mechanisms of flame spread are interpreted by applying energy balance analysis. A ratio between the total heat applied to the condensed material upstream of the flame leading edge and the spread rate reveals the physical mechanisms that control the preheating of the condensed material to the ignition temperature. Comparisons of this ratio in situations of varying St, $\bar{k}_l$, and $\overline{C}_{Pl}$ reveals the difference in physical mechanisms that control the preheating of the condensed phase to the ignition temperature.

In Chapter 4, the influence of channel flow is investigated by incorporating the Navier Stokes equations into the overall model. The flame spread formula [28] is examined in the new situation and good agreement is again obtained between the numerical model and the flame spread formula. The effect of the gas phase on the flame spread behavior is explored with specific attention given to the injection flow from the interface and gas expansion due to the high combustion temperature gradient. Parameters such as pressure, velocity, and streamlines are interpreted in terms of their coupling to the temperature, species field and interface conditions. In addition, an energy balance analysis of a spatially-varying control volume is applied to the four cases in order to

understand the flame spread mechanism. It is found that streamwise heat conduction in the condensed phase has a very small magnitude compared to the interface condensed-phase heat conduction. This result is in agreement with previous theory [55]. The comparison between the model with the Navier Stokes flow calculation and the model with the Oseen approximation is made. The quench layer thickness is smaller in the Oseen model than in the Flow model, mainly because a much stronger reaction rate formulation is used in the former. In addition, it is found that the flame front is located ahead of the phase front, and the heat flux front is located ahead of the mass flux front. These discrepancies can be explained in terms of gas phase thermal expansion and interface injection flow. Analysis was also carried out on the influences of gas flow and melting in order to understand the flame spread mechanisms associated with their influences.

In Chapter 5, flame spread over an anisotropic polymer solid is investigated again with a realistic flow field accompanied by melting of the anisotropic solid. The condensed phase therefore consists of an isotropic liquid near the heated interface and an anisotropic solid surrounding it. The flame spread rate is computed and compared to a numerical case without melting and an analytical formula for a pure solid. It is found that the flame spread rate resembles the former case by producing an almost inversely decreasing curve with respect to the transverse conductivity. The analytical formula has a sharper rate of decrease with increasing transverse conductivity. At the reference state where only the isotropic solid and the liquid are present, the flame spread rate is lower than the analytical formula, indicating that the energy barrier of the melting lowers the flame spread rate. In addition, the flame spread rate generally does not show

independence of the longitudinal conductivity in that it actually decreases with increasing k_{sx}. Energy balance analysis is also applied to the flame spread process. It is observed that the magnitude of each heat transfer mechanism depends inversely on k_{sx} and k_{sy}. In general, a higher magnitude of either k_{sx} or k_{sy} results in a smaller flame size. The lower conductivity in any given direction results in a lower rate of heat loss by condensed phase conduction. The interface phenomena are also investigated by means of the interface temperature, the mass flux, and the net heat flux to the condensed phase. It is found that a smaller size of the heated region or heat flux region results from a higher magnitude of k_{sx} or k_{sy}, which is consistent with the above analysis.

In Chapter 6, a two-dimensional ignition model is examined for two different flow patterns, the one with a realistic flow (Navier Stokes calculation) and the one with an assumed flow (Oseen approximation). From the numerical results, the flow pattern has an impact on the ignition process. It influences the magnitude of the ignition delay time, the interface heat balance, and the reaction rate. The use of the Oseen approximation enhances interface convection; thereby decreasing the interface temperature. The decreased radiation loss, in turn, helps to produce a shorter ignition delay time. In general, the Oseen model results in a weaker reactive region, smaller size of flame and lowered heat and mass flux at the interface. The influence of condensed phase material properties such as latent heat, conductivity, and heat capacity are investigated for each flow pattern. A theory to determine the ignition delay time is derived from the numerical observations by employing the energy balance principle. The predicted ignition delay times agree well with the direct numerical results. The theory is useful for interpreting and estimating the ignition delay over a range of values calculated from numerical cases.

The influence of the external radiation is investigated by changing its magnitude in a wide range. The numerical results indicate that the ignition time is approximately inverse to the *square* of the radiation heat flux. The square relationship indicates that the ignition under this study is for "thermally thick" polymer [59]. The melting does not change the square relationship though yields a less steep curve than the pure solid as a consequence of higher energy barrier. In addition, the surface temperature at ignition is found to be dependent on the external heat flux. The higher radiant heat flux generates a higher surface temperature. This indicates the limitation of using temperature as the measure of ignition in real multiphase coupled systems. In addition, the realistic cross flow influences ignition and subsequent flame spread. The qualitative dependence, however, is unchanged except for some isolated (but important) features of the problem.

In Chapter 7, a transport model for condensed phase is constructed that encompasses the macro-scale transport of energy and micro-scale transport of bubbles in the condensed phase. In the micro-scale, each bubble is described in terms of its growth, movement by means of a set of analytical formula. In the macro-scale model, the energy equation that accounts for melting and heat conduction is volume-averaged by introducing bubble effects in the condensed phase. The overall model is solved iteratively by numerical techniques. A representative 2-D case is calculated for the transient heating of a polymer material subjected to a constant external heat flux at the surface. The time history of global parameters are presented and analyzed. It is found that there exist some discontinuities of porosity or velocity in the transient behavior of the condensed phase due to the discrete temporal formulation of bubble nucleation. However, the bubbles do not show the randomly or discontinuous behavior from the temperature contours. In order

to evaluate the dependence of the model on the materials properties, sensitivity analysis is carried out for the bubble nucleation rate, the bubble initial radius, the latent heat, and the evaporation heat. It is found that these material properties have an impact on the transport process of the condensed phase. Generally, the increase of the nucleation rate, increase of the evaporation heat and decrease of the latent heat magnify the bubble transport; increase of the initial bubble radius does not change significantly the bubble behavior due to the complication of the bubble velocity and growth formulation.

By considering the controlling mechanisms for flame spread over polymeric materials, several possible extensions to the current model are derived. These extensions should not separate from the theoretical and experimental development; instead they must be heavily coupled to the latter two to provide better predictions.

(1) In terms of gas phase combustion, there is a practical need to incorporate the realistic combustion kinetics into the overall model. Especially for a specific material, if we know the fuel composition as a consequence of pyrolysis, it is a relatively easy matter to incorporate the realistic kinetics into the gas phase submodel because the gas phase combustion kinetic is well defined if the fuel type and concentration are given. In this way, the contribution from the condensed phase can be further evaluated in terms of its fuel composition. Obviously, the technique to reduce the total steps of a typical combustion should be used by seeing an overwhelmingly large number of reaction steps in real situation. In addition, the incorporation of more realistic chemical reaction is meaningful since no related paper has been published in the flame spread field.

(2) Radiation is a very important mechanism to influence the ignition and further the flame spread. Its contribution to ignition is very significant for some particular situations

such as the configuration with quiescent gas phase and a very high external heat flux. Its contribution to flame spread is important when the size of the flame grows over some limits. The spread of a large-scale fire is dominated by the radiation heat transfer. In terms of the radiation type for a typical flame spread, there are radiation absorption and emission of the gas phase, radiation absorption and emission of interface. Their coupled influences constitute complex phenomena for flame spread process, and are less understood relative to other heat transfer mechanisms. In order to gain understanding of the radiation mechanism, experimental tests are necessary to obtain the quantitative contribution of different types. Numerical modeling should be implemented by interfacing with experiments to provide quantitative evaluations as to how important the radiation will influence the flame spread.

(3) As suggested in section (1), in order to simulate the gas phase combustion, a more realistic description of the condensed phase pyrolysis is needed. In particular, the detailed information of the products of the pyrolysis is needed since the heat transfer aspect of the pyrolysis, as seen in chapter 3, 4 and 6, normally do not significantly influence the energy distribution of the condensed phase. In literature, there are few models that employ the realistic pyrolysis reaction; if any, they are limited to the thermal aspects [40], eliminating the influence of fuel species on gas phase combustion. Therefore, the possible model development could be toward some realistic pyrolysis reaction with emphasis on both chemical and energy aspect. Some step-reducing techniques are necessary, similar to the treatment of combustion.

(4) The melt flow in the condensed phase is not well understood. Generally it was induced by the temperature gradient near the flame front, that is, the surface tension

gradient. There are some fundamental questions unanswered till now. One would be, "how important is the melt flow in terms of its energy transport and mass transport to the flame spread". To answer this question, a numerical submodel is needed to describe the melt flow. One advantage of the melt flow modeling is that it is well defined in mathematical formulation, unlike the bubble transport phenomena.

(5) The bubble transport relies heavily on the material properties; different characteristics may appear for different materials. For example, the evaporation effect as an energy aspect may be more important to the structural changes in some specific situations, as examined in Chapter 7. The experimental tests are especially important in providing benchmark information for the numerical model. The model development for bubble transport, such as the movement of the bubble and the growth of the bubble, should be derived from experimental observations. Furthermore, the bubble transport is so relied on a specific material that it should be in some way coupled with the experimental data to accurately predict the transport phenomena.

APPENDIX I

COMPARISON OF NUMERICAL RESULTS WITH ANALYTICAL SOLUTION FOR 1-D MELTING PROCESS IN CONDENSED PHASE

1. Problem with Uniform Thermal Properties across Phase Interface

1.1 Problem Formulation

Initially a one-dimensional solid rod, as shown in Figure 1, has the melting temperature T_m. Then a fixed higher temperature of T_w is applied at the left end while keeping the right end insulated. It is obvious that the melt phase front will propagate from left to right. The transverse heat transfer will be neglected. Let the enthalpy be designated as *h*, density ρ, and thermal conductivity k, the mathematical formulation in enthalpy form is,

$$\rho \frac{\partial h_c}{\partial t} = k_c \frac{\partial^2 T_c}{\partial x^2} \tag{1-a}$$

where the subscript c represents the condensed phase. The enthalpy-temperature relationship is shown in Figure 2. It is also provided to ensure a unique solution. It is assumed that the phase change occurs at a fixed melting temperature, T_m, which is true for certain pure crystalline materials. It is also assumed that the solid and liquid coexist with uniform thermal properties, which leads partially to $C_{Ps} = C_{Pl}$ and is represented by the same slope dh_c / dT in both solid and liquid domains in Figure 2. In addition, during melting the solid phase must overcome an energy obstacle of latent heat *L* to attain further temperature increase, as shown in Figure 2 by the enthalpy discontinuity at T_m.

From a mathematical point of view, an alternative formulation in terms of temperature can be given as

$$\begin{cases} \dfrac{\partial T}{\partial t} = \alpha \dfrac{\partial^2 T}{\partial x^2}, & 0 < x < X(0,t) \\ T(X,t) = T_m, & x = X(t) \\ \rho L \dfrac{\partial X}{\partial t} = -k_l \dfrac{\partial T}{\partial x}, & x = X(t) \end{cases} \tag{1-b}$$

The boundary conditions are

$$\begin{cases} T(0,t) = T_w \\ \dfrac{\partial T(x,t)}{\partial x}\Big|_{x=L} = 0 \end{cases} \tag{2}$$

The above equations comprise 1-D, unsteady, closed-form equations that will be solved.

1.2 Analytical Solution

From equation (1-b), the use of a similarity variable $\xi = \dfrac{x}{\sqrt{t}}$ leads to the Neumann analytical solution [83], and only the solution itself is listed below. The moving phase front position is obtained as a function of time and eigenvalue λ,

$$X(t) = 2\lambda\sqrt{\alpha t} \tag{3}$$

where λ is obtained from the following equation

$$\lambda \exp(\lambda^2) erf(\lambda) = \frac{St}{\sqrt{\pi}} \tag{4}$$

where $St = \dfrac{C_P \Delta T}{L}$, and $\Delta T = (T_w - T_\infty)$.

The transient temperature is obtained as a function of time, position and eigenvalue λ,

$$T(x,t) = T_w - \Delta T \frac{erf(x/2\sqrt{\alpha t})}{erf(\lambda)} \tag{5}$$

The above exact solution will be used for further comparisons with numerical results.

1.3 Comparisons

The performance of the 2-D numerical solid model using the ADI Source Update Method is employed for solving the one-dimensional melting Stefan problem. The numerical experiments are similar to those in [48]. Material with a phase change temperature $T_m = 0$ and thermal properties $\rho = c = K = 1$ is contained in the half space $x \geq 0$. At $t < 0$ the material is at a temperature $T_i = 0$. At $t = 0$ the temperature of the surface at $x = 0$ is increased and fixed at a temperature of $T = 1$, so that, with time, the liquid phase attaches to $x = 0$ and grows. A grid of exponentially increasing space of 40 steps with ratio of 1.0007, minimal grid size 0.1 and variable initial time step of $\Delta t = 0.002$ are used, and four different cases corresponding to latent heat values of $L = 0.01\,(St = 100)$, $L = 0.1\,(St = 10)$, $L = 10(St = 0.1)$, and $L = 100(St = 0.01)$ are investigated. To ensure the accuracy of the iterative solution process, the difference between any two most recent temperatures or enthalpies should fall into the convergence limit, 0.0001.

$$\left|T_{i,j}^{l+1} - T_{i,j}^{l}\right| < 0.0001 \quad \left|h_{i,j}^{l+1} - h_{i,j}^{l}\right| < 0.0001 \tag{6}$$

To determine the moving phase front numerically, an observation [84] indicates that the liquid fraction of $g = 0.5$ always corresponds well with phase front position. Figures 3 gives the moving phase front position history.

At a low Stefan number, $St = 0.01$ and $St = 0.1$, the latent heat is much larger than

the sensible heat, and the phase front moves very slowly. The behavior of the larger St number, where the latent heat is small, is almost the reverse of the small St number case. The numerical results show very close agreement with the analytical solution. The oscillations, which result from the enthalpy method [48], are not clearly shown in the above four figures.

The numerical temperature profiles at a certain time are also compared with the analytical solutions in Figure 4. It is observed that the numerical results of temperature profiles provide very good agreement with the analytical solution in the above four cases.

2. Problem with Discontinuous Thermal Properties across Phase Interface

2.1 Problem Formulation

A liquid at a uniform temperature T_i that is higher than the melting temperature T_m of the solid phase is confined to $x > 0$. At time $t = 0$, the boundary surface at $x = 0$ is lowered to a temperature T_o below T_m and maintained at that temperature for $t > 0$. As a result the solidification starts at the surface $x = 0$ and the solid-liquid interface moves in the positive x direction. This problem is a two-region problem because the temperatures are unknown in both solid and liquid phases. In the following analysis we determine the temperature distributions in both phases and the location of the solid-liquid interface, this problem is more general than the one considered in the previous example. The mathematical formulation in temperature form is given as

$$\begin{cases} \dfrac{\partial T}{\partial t} = \alpha_s \dfrac{\partial^2 T}{\partial x^2}, & 0 < x < X(0,t) \\ \dfrac{\partial T}{\partial t} = \alpha_l \dfrac{\partial^2 T}{\partial x^2}, & X(0,t) < x < L \\ T(X,t) = T_m, & x = X(t) \\ \rho L \dfrac{\partial X}{\partial t} = k_s \dfrac{\partial T}{\partial x} - k_l \dfrac{\partial T}{\partial x}, & x = X(t) \end{cases} \tag{6}$$

The boundary conditions and the enthalpy-temperature relationship are the same as the previous example.

2.2 Analytical Solution

In the solid phase,

$$\frac{T - T_0}{T_m - T_o} = \frac{erf[x/2\sqrt{\alpha_s t}]}{erf(\lambda)} \tag{7}$$

In the liquid phase,

$$\frac{T - T_i}{T_m - T_i} = \frac{erfc[x/2\sqrt{\alpha_l t}]}{erfc[\lambda\sqrt{\alpha_s/\alpha_l}]} \tag{8}$$

where λ is obtained from

$$\frac{e^{-\lambda^2}}{erf(\lambda)} + \frac{k_l}{k_s}\left(\frac{\alpha_s}{\alpha_l}\right)^{1/2} \frac{T_m - T_i}{T_m - T_0} \frac{e^{-\lambda^2(\alpha_s/\alpha_l)}}{erfc[\lambda\sqrt{\alpha_s/\alpha_l}]} = \frac{\lambda L\sqrt{\pi}}{C_{Ps}(T_m - T_0)} \tag{9}$$

and $X(t) = 2\lambda\sqrt{\alpha_s t}$.

2.3 Comparisons

If $\rho_s = \rho_l = 1$, $C_{ps} = C_{pl} = 1$ and $k_s = 1.0$ $k_l = 0.5$, $T_m = 0; T_0 = -1; T_i = 1$,

then two cases with $St = \dfrac{C_{Ps}(T_m - T_0)}{L}$ of 0.1 and 10 are selected to make the

comparisons between the numerical results and analytical solutions.

It is observed that numerical method, which uses the harmonic mean to approximate the discontinuous thermal properties across the interface, underestimates the phase front position with a relative error of 2%. It is pointed out [85] that the Kirchoff transformation method provides closer results to the analytical solution. However, the harmonic mean treatment is used here for its simplicity. Later the Kirchoff formulation will be used into flame model, which does provide accurate prediction.

3. Conclusions

Numerical modeling of phase change in condensed phase is verified by a 1-D analytical solution that is derived from problems with both uniform and discontinuous thermal properties across phase interface. The numerical results of the solid model agree well with analytical solutions, and can be utilized directly into the overall model of flame spread over condensed phases.

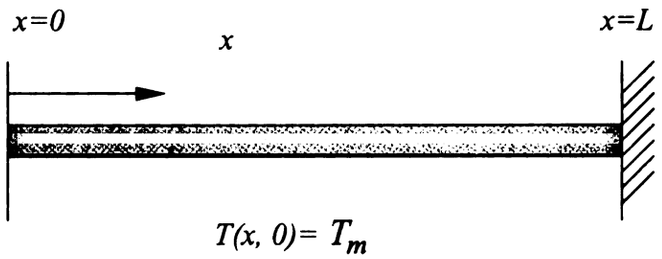

Figure 1 Schematic description of one-dimensional melting of a rod.

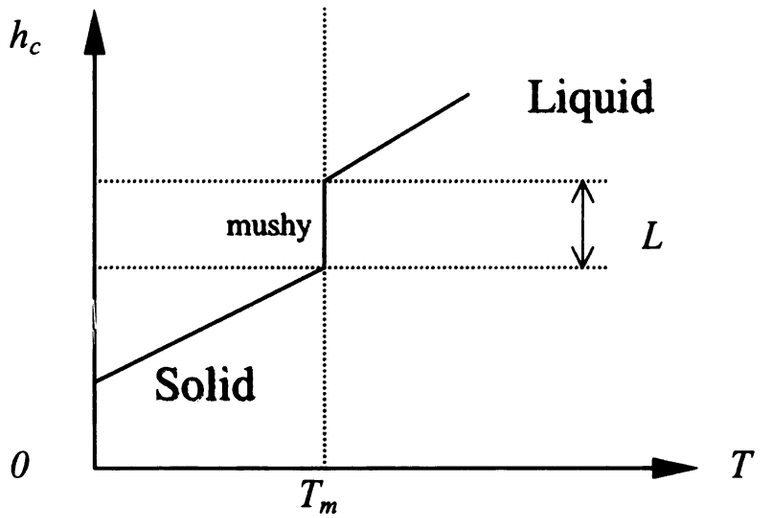

Figure 2 The schematic relationship between enthalpy and temperature.

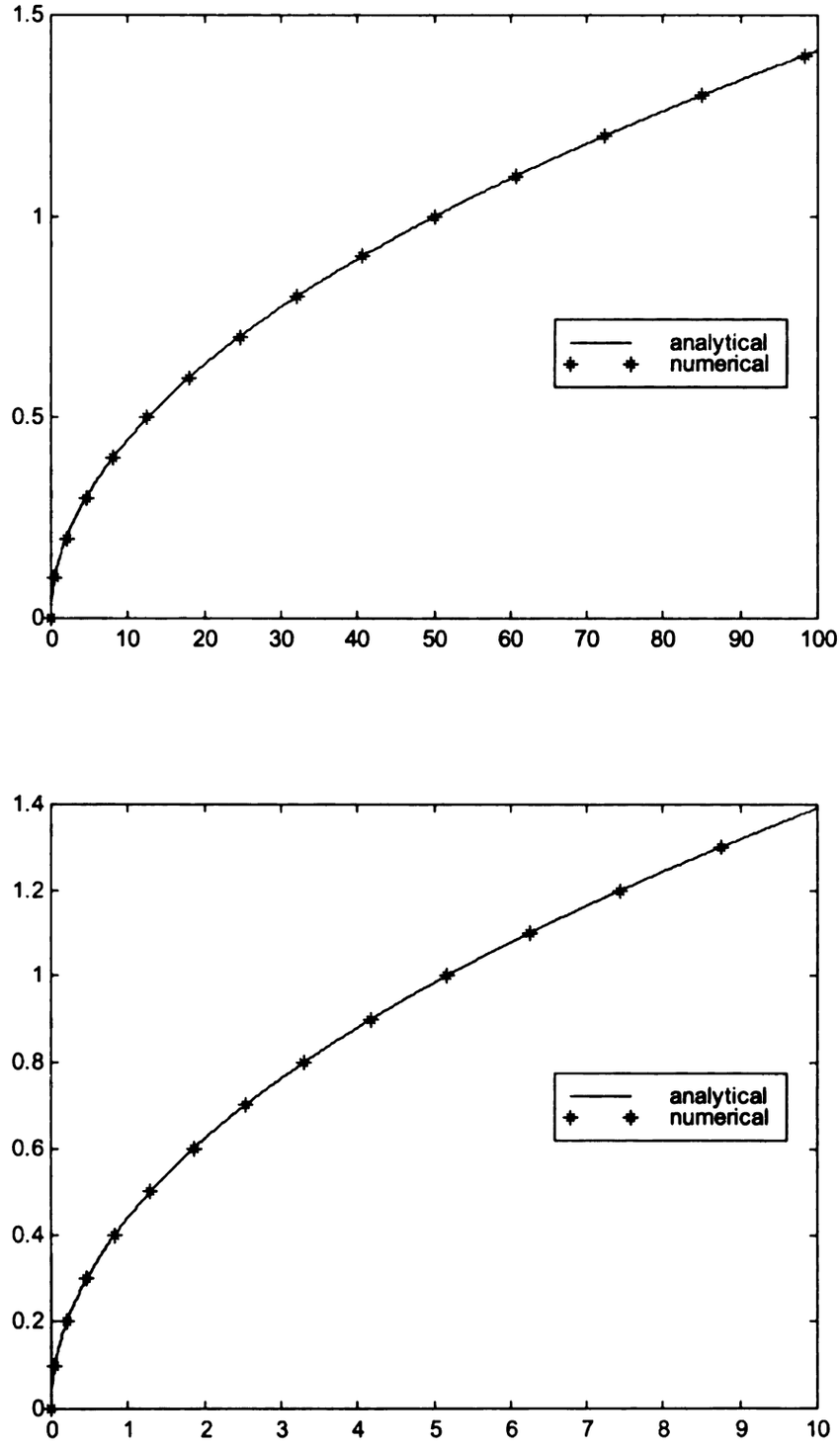

Figure 3(a) Phase front movement for $St = 0.01$ (upper) and $St = 0.1$ (lower).

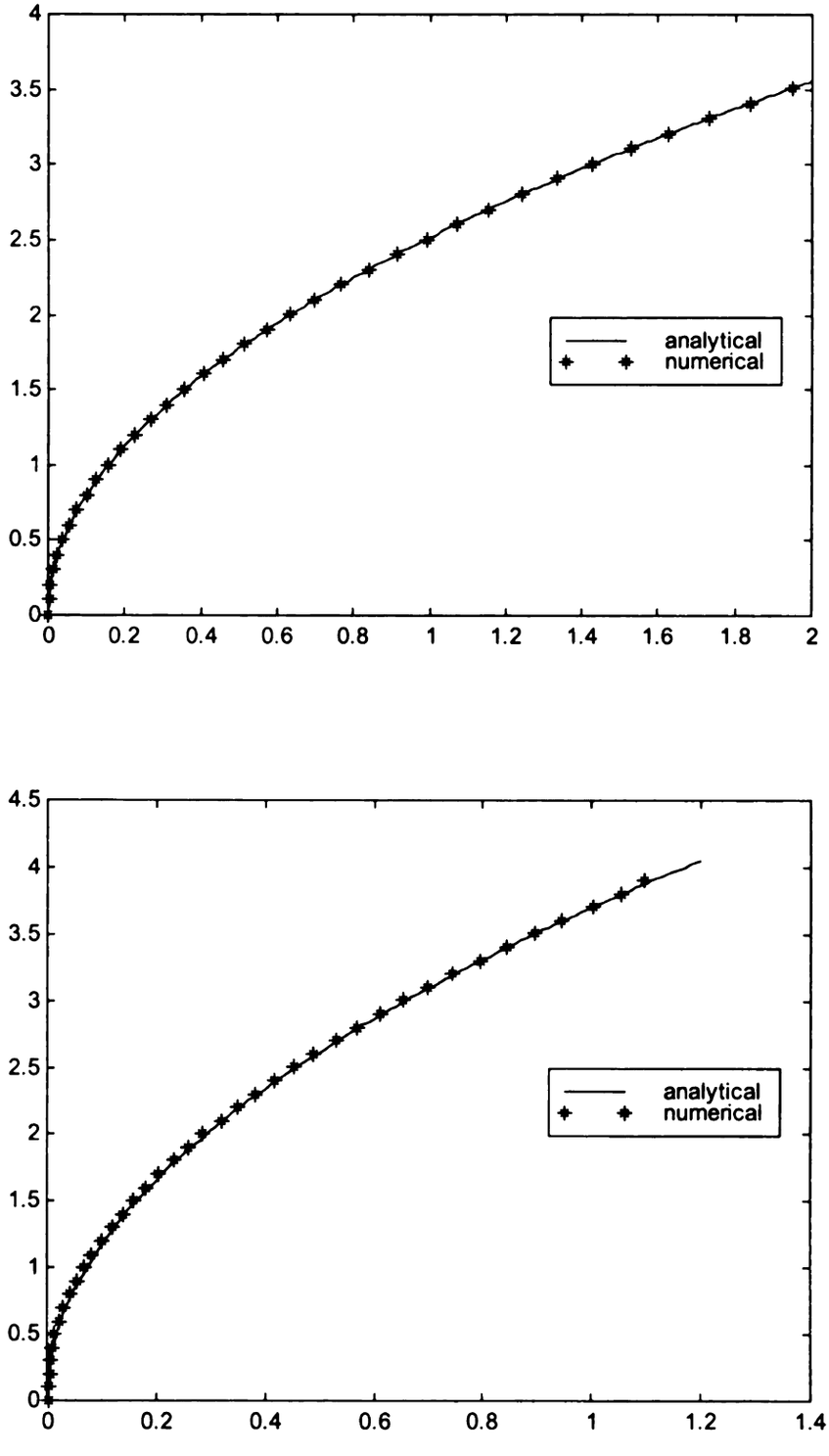

Figure 3(b) Phase front movement for $St = 10$ (upper) and $St = 100$ (lower).

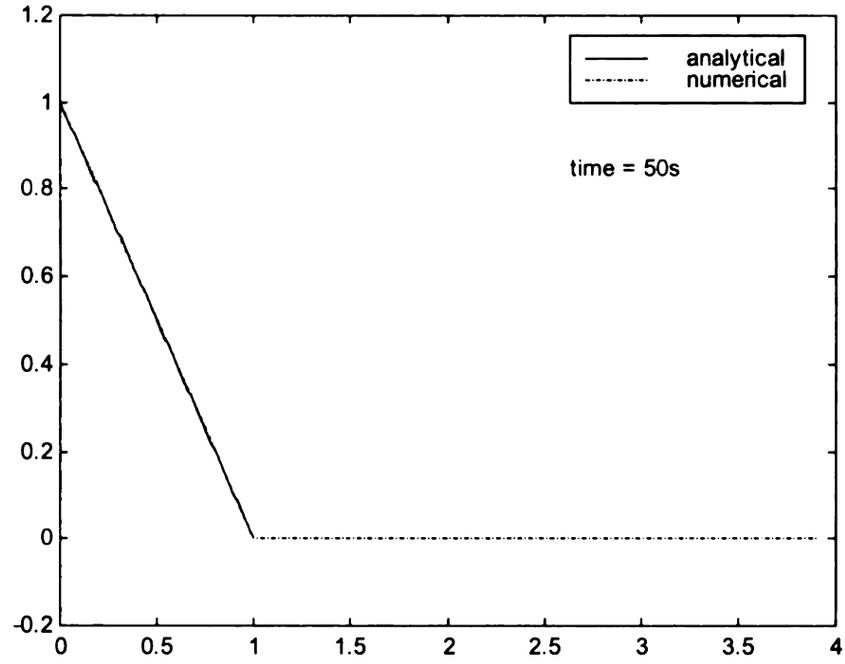

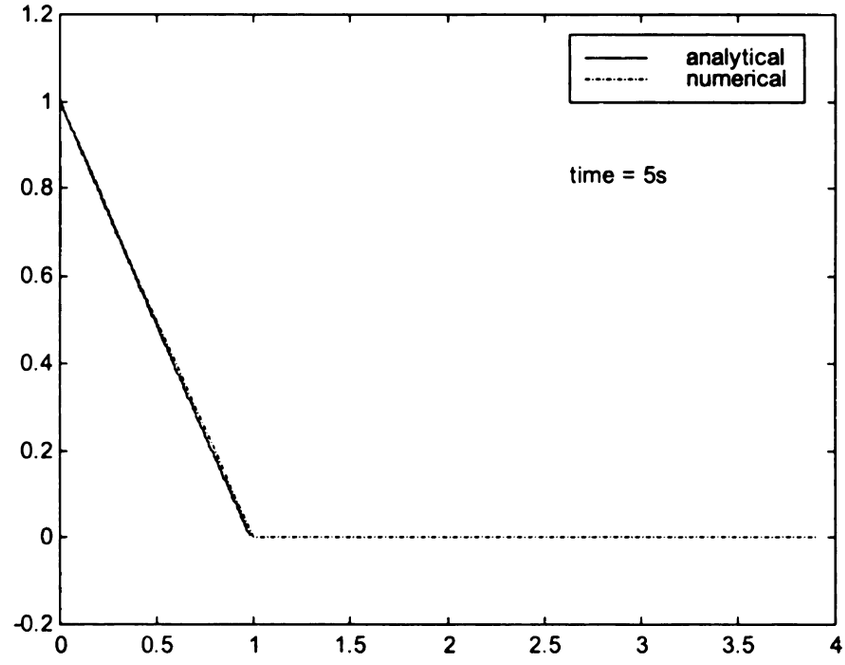

Figure 4(a) Temperature distributions for $St = 0.01$ at 50s (upper) and $St = 0.1$ at 5s (lower).

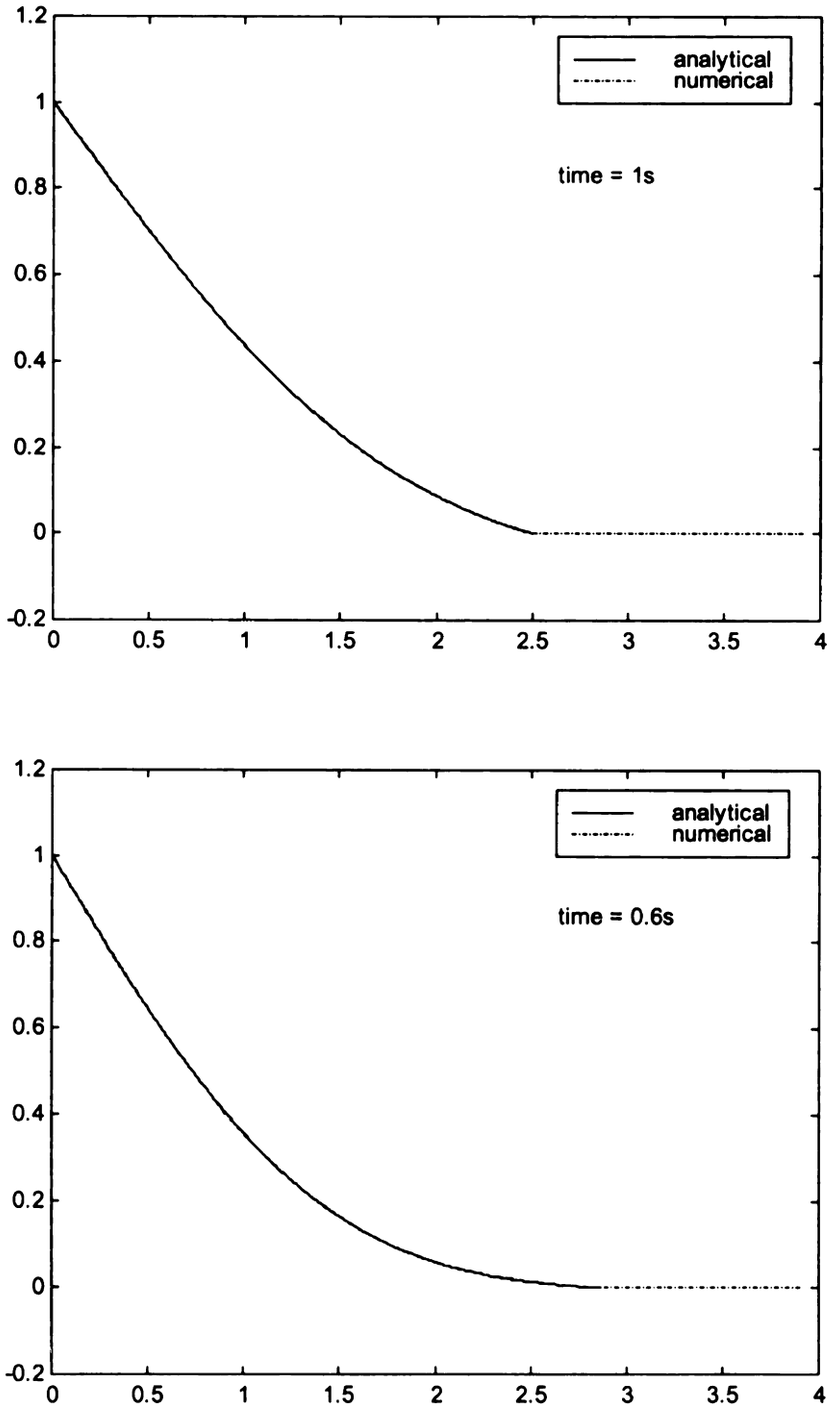

Figure 4(b) Temperature distributions for $St = 10$ at 1s (upper) and $St = 100$ at 0.6s (lower).

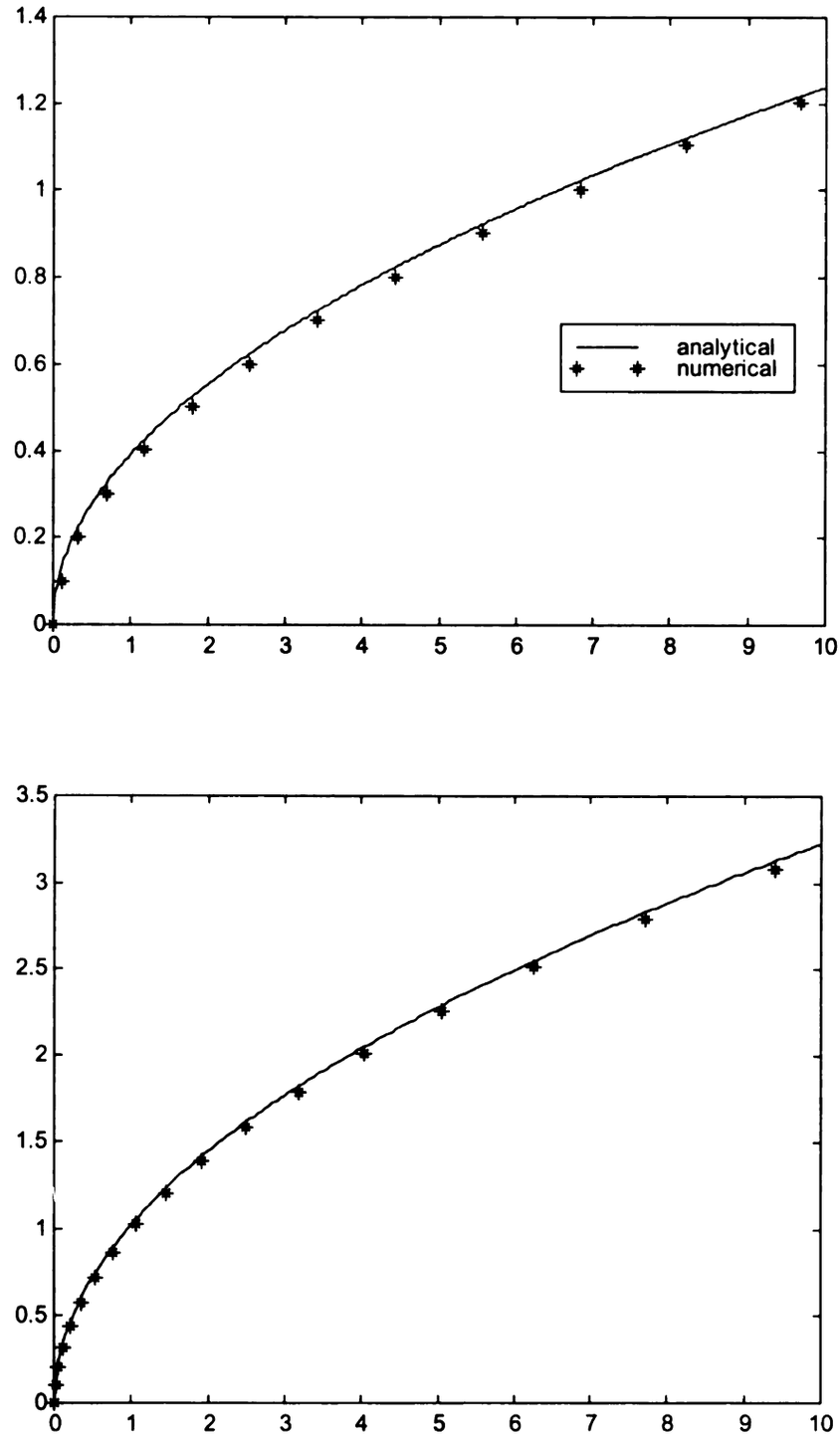

Figure 5 Phase front movement for $St = 0.1$ (upper) and $St = 10$ (lower).

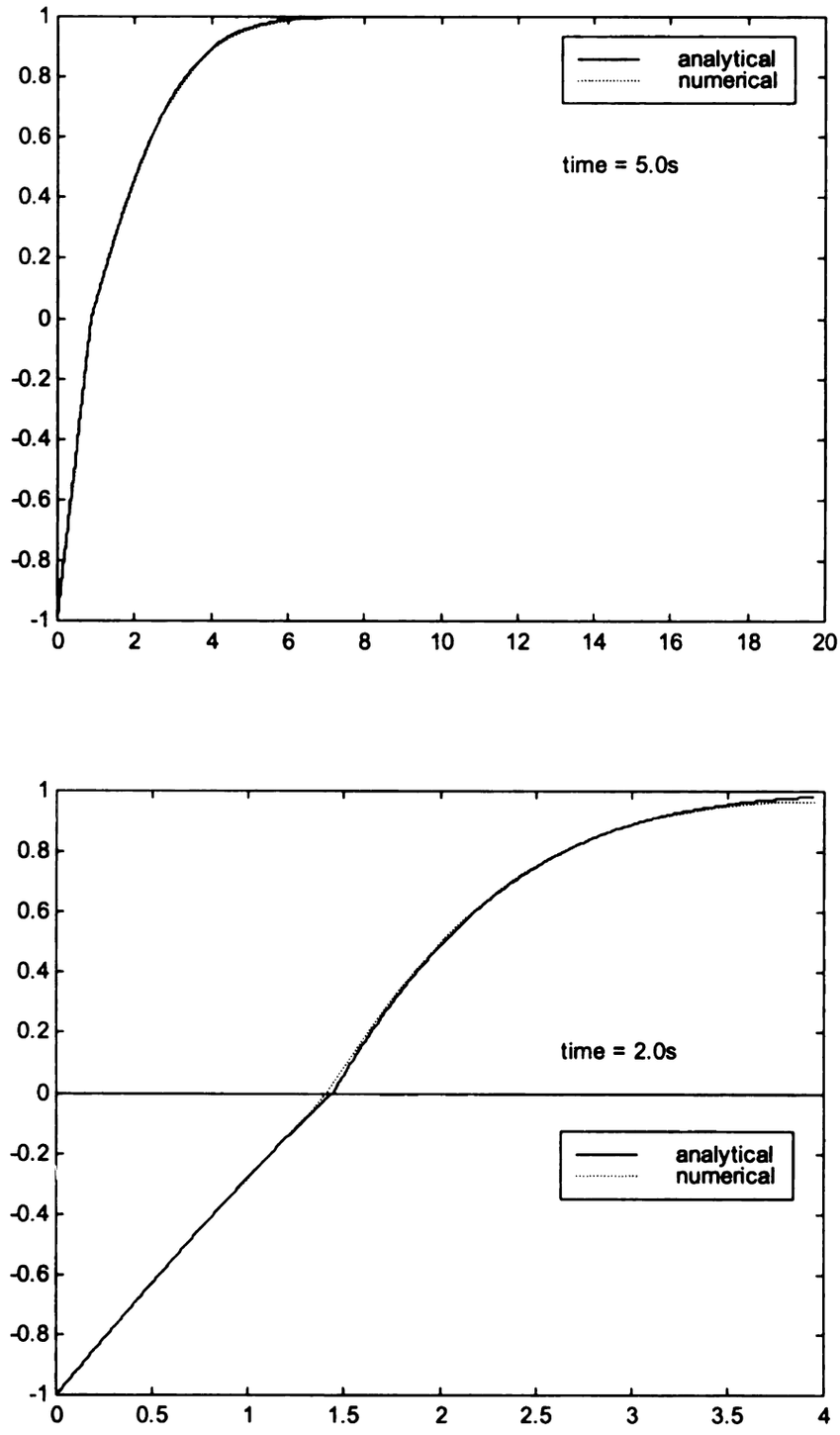

Figure 6 Temperature distributions for $St = 0.1$ at 5s (upper) and $St = 10$ at 2s (lower).

APPENDIX II

NUMERICAL METHOD FOR FLAME SPREAD OVER MELTING POLYMERS WITHOUT FLOW CALCULATION

1. Discretization

1.1 The Control Volume Formulation

The control-volume formulation is physically sound and lends itself to direct physical interpretation. Figure 1 shows a typical grid control volume. For melting problems, the enthalpy equation can be solved exactly by using this formulation [46].

For illustration purpose, we take the general conservation equation as an example,

$$\frac{\partial U}{\partial t} + u_{\infty}\frac{\partial U}{\partial x} = \beta\nabla^2 U \tag{1}$$

where U is an independent variable and β is the diffusion coefficient. The chemical term is neglected here and will be discussed later. By treating all transport terms implicitly, we have the following terms:

Y_+ direction diffusion: $q_{Y^+} = -\beta\dfrac{U_{i,j}^{n+1} - U_{i,j+1}^{n+1}}{\Delta y}\Delta x$

Y_- direction diffusion: $q_{Y^-} = -\beta\dfrac{U_{i,j}^{n+1} - U_{i,j-1}^{n+1}}{\Delta y}\Delta x$

X_+ direction diffusion: $q_{X^+} = -\beta\dfrac{U_{i,i}^{n+1} - U_{i+1,j}^{n+1}}{\Delta x}\Delta y$

X_- direction diffusion: $q_{X^-} = -\beta\dfrac{U_{i,j}^{n+1} - U_{i-1,j}^{n+1}}{\Delta x}\Delta y$

X direction convection: $q_{con} = u_\infty (U_{i-1,j}^{n+1} - U_{i,j}^{n+1})\Delta y$

Transient increment: $q_{trans} = \dfrac{(U_{i,j}^{n+1} - U_{i,j}^{n})}{\Delta t}\Delta x \Delta y$

According to the conservation law in integral form, the above terms are combined as

$$q_{trans} = q_{con} + q_{X^+} + q_{X^-} + q_{Y^+} + q_{Y^-} \tag{2}$$

The finite difference equation is derived as follows.

$$a_E U_{i-1,j} + a_S U_{i,j-1} + a_P U_{i,j} + a_N U_{i,j+1} + a_W U_{i+1,j} = b \tag{3}$$

in which

$$a_E = -\beta \frac{\Delta t}{\Delta x^2}$$

$$a_S = -\beta \frac{\Delta t}{\Delta y^2}$$

$$a_P = 1 + 2\beta \frac{\Delta t}{\Delta x^2} + 2\beta \frac{\Delta t}{\Delta y^2} + \frac{u_\infty \Delta t}{\Delta x}$$

$$a_N = -\beta \frac{\Delta t}{\Delta y^2}$$

$$a_W = -\beta \frac{\Delta t}{\Delta x^2} - \frac{u_\infty \Delta t}{\Delta x}$$

$$b = U_{i,j}^{n}$$

A more convenient form of representation is δ-form, which uses the $\delta U = (U^{n+1} - U^n)$ as the independent variable.

$$a_E \delta U_{i-1,j} + a_S \delta U_{i,j-1} + a_P \delta U_{i,j} + a_N \delta U_{i,j+1} + a_W \delta U_{i+1,j} = RHS \tag{4}$$

The coefficients on LHS are the same as equation (3), while the RHS becomes

$$RHS = U_{i,j}^{n} - a_E U_{i+1,j}^{n} - a_W U_{i-1,j}^{n} - a_P U_{i,j}^{n} - a_N U_{i,j+1}^{n} - a_S U_{i,j-1}^{n}$$

A more self-evident and compact form is the following,

$$\{I + \Delta t[u_\infty D_x - \beta(D_x^2 + D_y^2)]\}\delta U_{i,j} = U_{i,j}^{n} + \Delta t[u_\infty D_x - \beta(D_x^2 + D_y^2)]U_{i,j}^{n} \quad (5)$$

A general rule will be applied here and thereafter. In Equation (5), the convection term $u_\infty D_x$ is differentiated by using upwind scheme, and the diffusion term $(D_x^2 + D_y^2)$ is treated by central difference method.

1.2 Boundary Conditions

For interface or boundary conditions, the control volume is the half grid control volume. Figure 2 shows the grid control volume near the interface.

Y- direction diffusion: $q_{Y^-} = -k\dfrac{T_{i,j}^{n+1} - T_{i,j-1}^{n+1}}{\Delta y}\Delta x$

X+ direction diffusion: $q_{X^+} = -k\dfrac{T_{i,i}^{n+1} - T_{i+1,j}^{n+1}}{\Delta x}\dfrac{\Delta y}{2}$

X- direction diffusion: $q_{X^-} = -k\dfrac{T_{i,j}^{n+1} - T_{i-1,j}^{n+1}}{\Delta x}\dfrac{\Delta y}{2}$

X- Heat flux from gas phase: $q_{gas} = \dot{q}\Delta x$

Transient increment: $q_{trans} = \rho C_P\dfrac{(T_{i,j}^{n+1} - T_{i,j}^{n})}{\Delta t}\dfrac{\Delta x \Delta y}{2}$

According to the conservation law of $q_{trans} = q_{gas} + q_{X^+} + q_{X^-} + q_{Y^-}$, the finite difference equation is

$$a_E T_{i-1,j} + a_S T_{i,j-1} + a_P T_{i,j} + a_W T_{i+1,j} = b \tag{6}$$

where

$$a_E = -\frac{k}{\rho C_P}\frac{\Delta t}{\Delta x^2}$$

$$a_S = -2\frac{k}{\rho C_P}\frac{\Delta t}{\Delta y^2}$$

$$a_P = 1 + 2\frac{k}{\rho C_P}\left(\frac{\Delta t}{\Delta x^2} + \frac{\Delta t}{\Delta y^2}\right)$$

$$a_W = -\frac{k}{\rho C_P}\frac{\Delta t}{\Delta x^2}$$

$$b = T_{i,j}^n + \frac{\dot{q}}{\rho C_P}\frac{2\Delta t}{\Delta y}$$

1.3 Treatment of Convection-Diffusion Terms

In the above formulation, the convection term is treated by upstream scheme and the diffusion term is treated by central difference method. Some other schemes are available in [46] and will be discussed briefly here. A specific scheme should be selected according to a ratio of $Pe = \frac{\rho u \Delta x}{\beta}$, which represents relative importance of the convection or diffusion. One instance of this family is Hybrid Scheme, which uses one of three schemes according the value of Pe.

$$\begin{cases} P_e < -2 & \dfrac{a_E}{D_E} = -P_e \\ |P_e| < 2 & \dfrac{a_E}{D_E} = 1 - \dfrac{P_e}{2} \\ P_e > 2 & \dfrac{a_E}{D_E} = 0 \end{cases} \tag{7}$$

Among these schemes, the upwind and hybrid scheme are commonly used, while the power-law scheme was recommended as a better substitute [46]. In this modeling, since the flow velocity is low, implying a small Pe number, the upwind scheme is used for convenience. Other schemes were also attempted; it was found that different schemes result in small difference in accuracy and efficiency.

1.4 Treatment of Chemical Terms

The chemical term of polymer combustion is changing in a more rapid manner compared to droplet combustion. In another words, the characteristic time of polymer combustion is much smaller, which requires a very small time step in computation. In fact, the chemical term is the most costly in terms of computational time.

In rigorous mathematical sense, the chemical terms can be differentiated in three parts with respect to T, Y_f and Y_o. The chemical term has a form of $w_g = -A_g \rho_g \exp(-E_g / RT_g) Y_O Y_F$, the derivative of which is

$$\delta w_g = w'_T \, \delta T + w'_{Y_O} \delta Y_O + w'_{Y_F} \delta Y_F \tag{8}$$

where

$$w'_T = \frac{A_g \rho_g \exp(-E_g / RT_g) Y_O Y_F E_g}{RT_g^2}$$

$$w'_F = -A_g \rho_g \exp(-E_g / RT_g) Y_O$$

$$w'_O = -A_g \rho_g \exp(-E_g / RT_g) Y_F .$$

The straightforward way to treat this source term is expressing it in vector form, and put it into a coupled equation system that must be solved by direct solution. Such a solution procedure is termed the block implicit method, or fully implicit method. The advantage of this method is that it is faster and more efficient than semi-implicit iterative procedure. The disadvantage is that (1) it will need big storage and CPU time; (2) it needs extreme care in specifying boundary condition otherwise divergence occurs. Instead we use the semi-implicit method where all equations are solved sequentially. Only one partial derivative for each primary variable (T, Y_F or Y_O) is preserved in each (energy, fuel or oxygen) conservation equation. The important rule for treatment of chemical term is discussed in detail in [46], which requires that the derivatives of source term be negative, otherwise the unstable solution will arise. Examining the equation system in gas phase, it can be observed that the species equations all follow this rule quite well, while the energy equation has a positive derivative, which is against this rule. To overcome this difficulty, the source term in energy equation is solved by using a special technique [47]. The details are given next.

2. The Computational Procedure

2.1 Non-linearities

As is mention in Chapter 1, the combustion process over polymer materials, physically, can be split into two half cycles, the heat cycle and the fuel cycle. In the former, heat that is generated from combustion or from external flux is fed at the interface. In the latter, the pyrolyzed gas generated by the heat from interface is moved

into the gas phase and reacts with the inflow oxygen and consumed. Therefore the interface constitutes one non-linearity in computational procedure. The mass flow rate, temperature and heat flux etc. at the interface act as the communication factors through the two phases. Another non-linearity is from the chemical terms, which are combustion source term and pyrolysis source term. Obviously the iterative method is required for such process.

2.2 The Newton-Raphson Scheme

The discretization should be done in iterative sense; requiring all the terms be discretized with reference to *l* time level instead of n time level, where *l* time level is the most recent (iterative) level. The δ formulation is modified here with

$$\delta U_{i,j} = U_{i,j}^{n+1} - U_{i,j}^{l} \tag{9}$$

There is minor change in the δ definition and this convention will be used in the rest of the appendix. Next the chemical terms will be treated.

$$S_F = \mu_F w_g = -\mu_F A_g \rho_g EXP(-E_g / RT_g) Y_O Y_F$$

By differentiation,

$$S_F^{n+1} = S_F^l + \delta S_F = S_F^l + S_F' \delta Y_F ,$$

in which $S_F' = -\mu_F A_g \rho_g EXP(-E_g / RT_g^l) Y_O^l$.

If chemical term is added into the formulation, Equation (5) becomes

$$[I + \Delta t[u_\infty D_x + \beta(D_x^2 + D_y^2)] - S_F']\delta Y_{Fi,j} = RHS \tag{10}$$

where

$$RHS = (Y_{Fi,j}^n - Y_{Fi,j}^l) + \Delta t[u_\infty D_x + \beta(D_x^2 + D_y^2)]Y_F^l + S_F^l .$$

For the energy conservation equation, the source term is:

$$S_T = q_g w_g = -q_g \mu_F A_g \rho_g \exp(-E_g / RT_g) Y_O Y_F$$

By differentiation,

$$S_T^{n+1} \approx -q_g \mu_F A_g \rho_g \exp(-E_g / RT_g^l) Y_O^l Y_F^l$$

Its treatment will be discussed later. For boundary conditions, take fuel conservation equation as an example, the source term at RHS is expressed as $(1 - Y_{Fi,j}^{n+1})\dot{m}$, therefore, the time discretization is $(1 - Y_{Fi,j}^l - \delta Y_{Fi,j})\dot{m}$, then the LHS will become $LHS + \dot{m}\delta Y_{Fi,j}$ and RHS will become $RHS + (1 - Y_{Fi,j}^l)\dot{m}$. For oxygen conservation equation, the source term at RHS is $Y_{Oi,j}^{n+1}\dot{m}$, the time discretization is $(Y_{Oi,j}^l + \delta Y_{Oi,j})\dot{m}$, then the LHS becomes $LHS - \dot{m}\delta Y_{Oi,j}$ and the RHS becomes $RHS + \dot{m} Y_{Oi,j}^l$.

2.3 Alternate Direction Implicit (ADI) with Special Source Treatment

To enhance the efficiency of solving a 5-points linear algebra equations, the ADI method is applied. In principle, the ADI method split the 5 points formulation into a combination of a 3-point X equation and a 3-point Y equation, by sweeping each direction in turn. This only involves tri-diagonal system of equation, thereby significantly saving CPU time and storage. In source term treatment, a method based on approximate factorization was proposed. The original scheme [47] did not consider the diffusion term; therefore its scheme was extended to include the diffusion term. We have

$$[N + \Delta t(u_\infty D_x + \beta D_x^2)]N^{-1}[N + \Delta t\beta D_y^2]\delta T_{i,j} = RHS$$

$$N = I + \Delta t S'_F \tag{11}$$

The solution procedure is the following,

Step 1: $[N + \Delta t(u_\infty D_x + \beta D_x^2)]\delta u^*_{i,j} = RHS$

Step 2: $[N + \Delta t\beta D_y^2]\delta u_{i,j} = N\delta u^*_{i,j}$

where the $\delta u^*_{i,j}$ is the temporary variable.

2.4 Enthalpy Method

2.4.1 Source Update Method

For solid phase the PDE at phase change becomes

$$\rho C_P \frac{\partial T}{\partial t} = k\nabla^2 T - \rho L \frac{\partial g}{\partial t} \tag{12}$$

where g is the liquid volume fraction. Then

$$\frac{\partial T}{\partial t} = \beta\nabla^2 T - \frac{L}{C_P}\frac{\partial g}{\partial t} \tag{13}$$

here β is the thermal diffusivity. The finite difference equation has the following form,

$$\begin{aligned}[I + \Delta t\beta(D_x^2 + D_y^2)]\delta T_{i,j} \\ = (T^n_{i,j} - T^l_{i,j}) + \Delta t\beta(D_x^2 + D_y^2)T^l_{i,j} - \frac{L}{C_P}(g^{n+1}_{i,j} - g^n_{i,j})\end{aligned} \tag{14}$$

The Source Update Method given in [85] is the extended to ADI procedure as below

1. At the start of the time step, the initial iterative fields are set to the previous time step values.

2. **Prediction**: From the known nodal temperature and phase change enthalpy fields at **iteration** l, the equation (14) is reformatted as

$$a_E \delta T_{i-1,j} + a_S \delta T_{i,j-1} + a_P \delta T_{i,j} + a_N \delta T_{i,j+1} + a_W \delta T_{i+1,j} = (T_{i,j}^n - T_{i,j}^l) + \Delta t\beta(D_y^2 + D_x^2)T_{i,j}^l - \frac{L}{C_P}(g_{i,j}^l - g_{i,j}^n), \quad (15)$$

and solved in two steps

Step 1: $[I + \Delta t\beta D_x^2]\delta T_{i,j}^* = (T_{i,j}^n - T_{i,j}^l) + \Delta t\beta(D_y^2 + D_x^2)T_{i,j}^l - \frac{L}{C_P}(g_{i,j}^l - g_{i,j}^n)$

Step 2: $[I + \Delta t\beta D_y^2]\delta T_{i,j} = \delta T_{i,j}^*$

Note that in step 1, the $(g_{i,j}^{n+1} - g_{i,j}^n)$ in equation (14) is replaced by $(g_{i,j}^l - g_{i,j}^n)$ as an approximation.

3. Correction: The nodal phase change enthalpy, H_e, needs to be evaluated before the next iteration can proceed. To correct the above approximation, it is recognized that the nodal temperature during phase change will keep constant, which implies that

$$T_{i,j}^{n+1} = T_m \Rightarrow \delta T_{i,j} + T_{i,j}^l = T_m \quad (16)$$

Therefore the equation (14) is in fact

$$a_E \delta T_{i-1,j} + a_S \delta T_{i,j-1} + a_P(T_m - T_{i,j}^l) + a_N \delta T_{i,j+1} + a_W \delta T_{i+1,j} = (T_{i,j}^n - T_{i,j}^l) + \Delta t\beta(D_y^2 + D_x^2)T_{i,j}^l - \frac{L}{C_P}(g_{i,j}^{n+1} - g_{i,j}^n). \quad (17)$$

The difference between equation (17) and (19) need to be corrected, we subtract equation (19) from (17) and obtain

$$\delta g_{i,j} = \frac{C_P}{L}\lambda a_P(\delta T_{i,j} + T_{i,j}^l - T_m) \quad (18)$$

, where λ is a relaxation factor. After the evaluation of temperature field, the phase change enthalpy update is applied at every node point, followed by the correction:

$$g_{i,j}^{n+1} = \max[0, \min[g_{i,j}^{n+1}, 1]] \tag{19}$$

Steps 2 and 3 are repeated until convergence. In this way, the scheme will conserve energy.

2.4.2 Treatment of Discontinuous Thermal Properties

In condensed phase, the thermal properties are discontinuous across the phase change front. In fixed grid calculations, the treatment of discontinuous thermal properties requires some special procedures. If a nodal lumping approach is used, discontinuities in specific heat and density can be readily calculated in terms of nodal average values, e.g.

$$C_P = gC_{Pl} + (1-g)C_{Ps} \tag{20}$$

where g is the liquid fraction of the control volume around the node. The difficulty comes in dealing with discontinuities in the thermal conductivity, k. In constructing coefficients, the values of k need to be calculated at integration points of control volumes, which generally do not coincide with the node points. A recommended approach is to use Kirchhoff transformation [85].

$$\phi = \int_{T_{ref}}^{T} k(\alpha) d\alpha \tag{21}$$

With the Kirchhoff transformation,

$$\frac{\partial \phi}{\partial x} = k\frac{\partial T}{\partial x}, \quad \frac{\partial \phi}{\partial y} = k\frac{\partial \phi}{\partial y} \tag{22}$$

Therefore

$$k_x = \frac{\partial \phi}{\partial x} / \frac{\partial T}{\partial x},\ k_y = \frac{\partial \phi}{\partial y} / \frac{\partial T}{\partial y} \tag{23}$$

Then the diffusion terms can be written as

$$\nabla \cdot (k \nabla T) = \frac{\partial}{\partial x}(k_x \frac{\partial T}{\partial x}) + \frac{\partial}{\partial y}(k_y \frac{\partial T}{\partial y}) \tag{24}$$

A central difference approximation of equation (23) leads to the following expression for the interface conductivity:

$$k_e = \frac{\phi_E - \phi_P}{T_E - T_P},\ k_n = \frac{\phi_N - \phi_P}{T_N - T_P}$$

$$k_w = \frac{\phi_W - \phi_P}{T_W - T_P},\ k_s = \frac{\phi_S - \phi_P}{T_S - T_P} \tag{25}$$

It was pointed out that equation (25) is a convenient and accurate means of dealing with the discontinuities in thermal conductivity in a fixed grid, control volume solution of phase change problem. The numerical features are:

- The formulation results in a set of nonlinear equations, which are solved upon employing an iterative technique and the nodal values of ϕ and k are calculated using the temperature values from the previous iteration.
- In general, the calculation of ϕ field involves the evaluation of an integral, which requires slightly more work than the calculation of temperature dependence nodal conductivity.
- The discrete equations will be in terms of the nodal temperature; that is, the solution of Kirchhoff variable is not required.
- Upon convergence, the discrete equation will be equivalent to the direct Kirchhoff approach.

If the conductivity in separate phases is constant, a general relation can be obtained using Kirchhoff transformation, for the control volume around node (i, j) and $(i+1, j)$,

$$\phi_{i,j} = (T_{i,j} - T_m)k_{i,j}$$

$$\phi_{i+1,j} = (T_{i+1,j} - T_m)k_{i+1,j} \tag{26}$$

in which $k_{i,j} = (1 - g_{i,j})k_s + g_{i,j}k_l$.

The expression of k_w can be written as

$$k_w = \frac{\phi_{i+1,j} - \phi_{i,j}}{T_{i+1,j} - T_{i,j}} = k_{i,j} + \frac{(T_{i+1,j} - T_m)(k_{i+1,j} - k_{i,j})}{T_{i+1,j} - T_{i,j} + \varepsilon} \tag{27}$$

, where the first term in RHS is the conductivity in CV (i, j), the second term is correction of the conductivity, which should be at interface. ε is a very small number to prevent the zero denominator. In the same sense with the CV $(i+1, j)$,

$$k_w = \frac{\phi_{i+1,j} - \phi_{i,j}}{T_{i+1,j} - T_{i,j}} = k_{i+1,j} + \frac{(T_{i,j} - T_m)(k_{i+1,j} - k_{i,j})}{T_{i+1,j} - T_{i,j} + \varepsilon} \tag{28}$$

The k_w can be derived by averaging equation (27) and (28)

$$k_w = (\frac{k_{i+1,j} + k_{i,j}}{2}) + \frac{[(\frac{T_{i,j} + T_{i+1,j}}{2}) - T_m](k_{i+1,j} - k_{i,j})}{T_{i+1,j} - T_{i,j} + \varepsilon} \tag{29}$$

Equation (29) is derived mainly to overcome the possible zero denominators. Three cases are derived from equation (29)

$$\begin{cases} g_{i,j} = 0, g_{i+1,j} = 0 & k_w = k_s \\ g_{i,j} = 1, g_{i+1,j} = 1 & k_w = k_l \\ 0 < g_{i,j}, g_{i+1,j} < 1 & k_w = ? \end{cases} \tag{30}$$

3. Coordinate Transformation - Clustered Grids Near the Interface

An extremely small grid size is required near the interface for combustion computation because of the large gradient there. In droplet combustion, a normal grid size at droplet surface is 0.015 mm; in this model the minimal normal grid size taken as 0.025 mm. With such a small grid, the uniform grid system is obviously not good. Some researchers [4] used two uniform grid systems; a grid system nearby the interface with very small grid and a grid system far away from the interface with large grid size. This treatment is not robust physically, since the errors will arise in evaluating the flux term at the conjunction points between the two grid control volumes. Another drawback is that non-smooth results appear at the conjunction of the two grid systems. A smooth non-uniform grid system must be used. One example is the adaptive grid generation, but its implementation is too complex. For convenience, two exponential grid systems in y direction are used, as seen in Figure 3. The grid at the interface has the smallest size. Coordinate transformation is required. The grid size along y direction from interface will increase in exponential order: $\Delta_y, r\Delta_y, r^2\Delta_y, r^3\Delta_y \ldots$ while keeping Δx uniform along x direction. η and ξ are new coordinates with relationship of

$$\begin{cases} x = \xi \\ y = \dfrac{\Delta_y}{r-1}(r^{\frac{\eta}{\Delta_\eta}} - 1) \end{cases} \tag{31}$$

in which Δ_y is minimal normal grid size in $y-x$ grid system and Δ_η is the grid size in a transformed uniform $\eta-\xi$ coordinate system. For coordinate transformation, space derivative over x has the same form as that of ξ. However, space derivative over y has

different from comparing to η, and the relation of 1st and 2nd order derivatives are

$$\begin{cases} \dfrac{\partial T}{\partial y} = a\dfrac{\partial T}{\partial \eta} \\ \dfrac{\partial^2 T}{\partial y^2} = a^2\dfrac{\partial^2 T}{\partial \eta^2} - b\dfrac{\partial T}{\partial \eta} \end{cases} \tag{32}$$

where $a = \dfrac{(r-1)\Delta_\eta}{\log r \Delta_y} r^{-\frac{\eta}{\Delta_\eta}}$ and $b = a^2 \dfrac{\log r}{\Delta_\eta}$. Two major changes are introduced if the equation system is expressed in $\eta - \xi$ system.

- The interface condition becomes

$$\begin{cases} -\rho_g a_g D\dfrac{\partial Y_F}{\partial \eta} = \dot{m}(1-Y_F) \\ -\rho_g a_g D\dfrac{\partial Y_i}{\partial \eta} = -\dot{m}Y_i, \ i=O,P,I \\ T_s = T_g \\ -k_g a_g \dfrac{\partial T_g}{\partial \eta} = -k_s a_s \dfrac{\partial T_s}{\partial \eta} - \varepsilon\sigma(T_s^4 - T_0^4) + \dot{q}_{ext} \end{cases} \tag{33}$$

, which implies that the heat or mass flux were "decreased" to some extent in $\eta - \xi$ system.

- The energy conservation equation of gas phase becomes

$$C_{Pg}\rho_g\left[\frac{\partial T_g}{\partial t} + u_\infty \frac{\partial T_g}{\partial \xi}\right] + k_g b\frac{\partial T_g}{\partial \eta} = q_g w_g + k_g\left(\frac{\partial^2 T_g}{\partial \xi^2} + a^2\frac{\partial^2 T_g}{\partial \eta^2}\right), \tag{34}$$

where a new flow term with positive velocity $\dfrac{k_g b}{C_{Pg}\rho_g}$ is introduced.

- For discontinuity across the phase change front, the Kirchhoff transformation in y

direction is

$$k_y = \frac{\partial \phi}{\partial y} / \frac{\partial T}{\partial y} = \frac{\partial \phi}{\partial \eta} / \frac{\partial T}{\partial \eta} \tag{35}$$

Therefore there is no need to adjust this term for $\eta - \xi$ coordinate system.

4. The Solution Procedure

The flow chart for current model is given in Figure 4. First the solid phase temperature is solved, and the results are used to obtain the interface mass flow rate and interface temperature. The former is used as boundary condition for two species equations in gas phase, and the latter is used as boundary condition for energy equation in gas phase. The gas phase equations are solved; yielding temperature field. The heat conduction at interface is obtained, and its results are used as input for solid phase boundary condition. The computational process continues until the relative error of the two recent iterative values fall into a convergence range with a limit of 0.0001.

$$\frac{T_{i,j}^{l+1} - T_{i,j}^{l}}{T_{i,j}^{l}} < \varepsilon_T \tag{36}$$

In addition, the Line-By-Line Gauss-Sedel iteration is attempted, it was found that both the scanning in y direction and the scanning in x direction are not as efficient as the ADI method.

5. Data Structure and Others

General features of the data structure are (1) All of the solid data and gas data are defined from two basic classes: SolidNode and GasNode, which encompass all the necessary information about a node. (2) The memory use is dynamically administrated; (3) Data access is performed by pointers or references through some specialized function

interface.

The code development is carried out in MS Visual C++ environment in a Pentium III 600 MHz PC. A scheme with variable time step is employed in order to minimize the running time. A typical flame spread case has time steps ranging from 10^{-3} s to 10^{-5} s. It is found that the time step is very sensitive to the selection of pre-exponential factor and activation energy in the gas combustion. In addition, the minimal time step, which corresponds to the most rapid change of flame behavior, occurs during transition stage. The total running time is normally 10 seconds after ignition is established, which guarantees the establishment of steady flame spread. Normally shorter ignition time implies shorter time to attain steady flame spread. In addition, a graphical user interface is developed, which provide overall parameter control in a user-friendly manner. This GUI was developed by using MFC library.

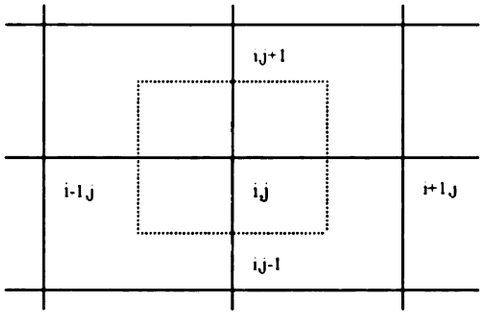

Figure 1 Control volume formulation of partial differential equations.

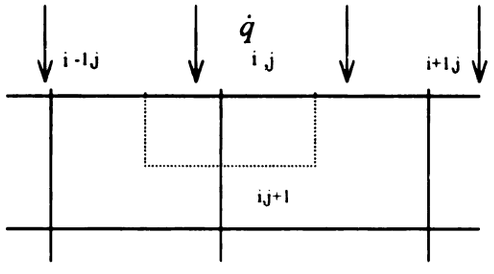

Figure 2 Control volume formulation of boundary condition.

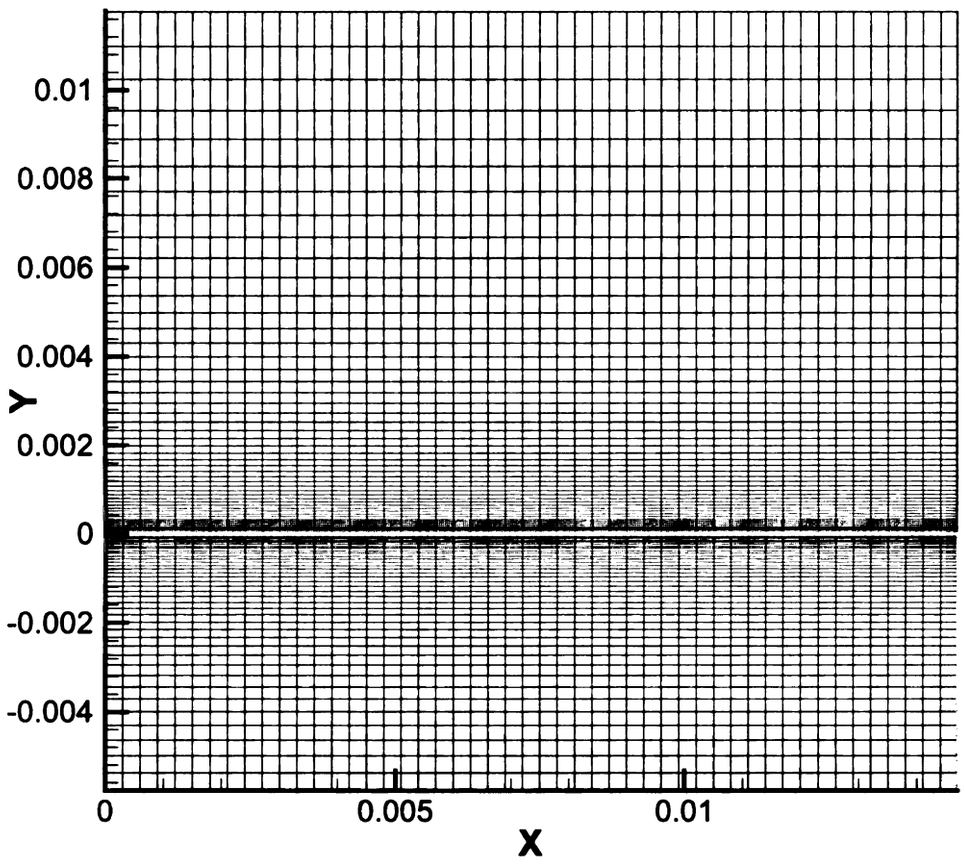

Figure 3 The mesh system with clustered grid near the interface. Only the temperature type grid system is present in the gas phase. (We recall that there are three types of grids in the gas phase for non-uniform staggered grid system).

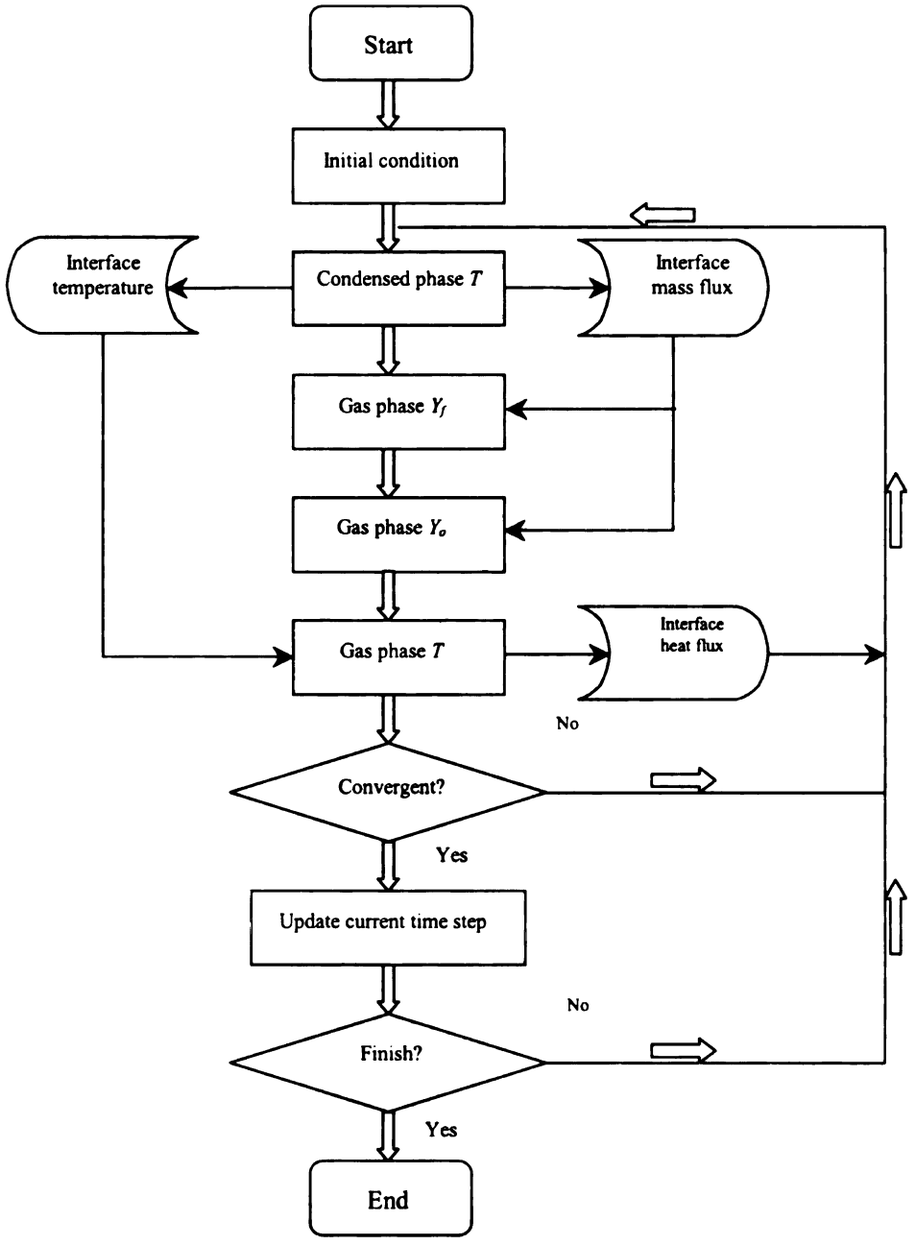

Figure 4. Flow-chart of the solution procedure of the numerical model.

APPENDIX III

DERIVATION OF A FLAME SPREAD FORMULA FOR MELTING POLYMERS

The flame-spread formula of Equation (13) in Chapter 3 is derived mathematically. This model examined here is built upon that of [28]. The spread mechanism is driven by a "surface flame" located along the gas-condensed phase interface. Following [28] we assume negligible upstream conduction in both gas and solid, thereby invoking the global energy balance principle described at length therein. The energy equation in the three phases are given by $\rho_j u_j C_{Pj} \partial T_j / \partial x = k_j \partial^2 T_j / \partial y^2$ where $j = g,l,s$ and $u_l = u_s$. For the gas we have $0 < x < \infty$, $y > 0$, for the liquid $0 < x < \infty$, $0 < y < f(x)$, for the solid $0 < x < \infty$, $y > f(x)$, where $y = f(x)$ describes the shape of solid/liquid interface. Along this contour, we are able to write the interfacial energy balance in the form

$$k_l[(\partial T_l / \partial x)^2 + (\partial T_l / \partial y)^2]^{1/2} = k_s[(\partial T_s / \partial x)^2 + (\partial T_s / \partial y)^2]^{1/2}$$
$$+ \rho_s u_s L_s \{(\partial f / \partial x)/[(\partial f / \partial x)^2 + (\partial f / \partial y)^2]^{1/2}\}$$

, where L_s is the enthalpy of liquefaction (positive) and the third term in the energy balance represents the liquefaction energy flux along the liquefaction front $y = f(x)$. We define dimensionless variables $\tau_j = (T_j - T_\infty)/(T_i - T_\infty)$, $j = g,l,s$, $\xi = x/L$, $\eta = y/L$ $(L = \lambda_s / \rho_s C_{Ps} u_s)$ where T_i is the downstream gas-liquid interface temperature (gasification or "vaporization" temperature). The equations, when transformed into parabolic cylinder coordinates $\xi = (s^2 - n^2)/2$, $\eta = sn$ (n=constant defines a family of parabolic arcs with $n = 0$ the downstream gas/liquid interface $y = 0$,

$x > 0$). The governing equations transform to $N_j n d\tau_j / dn = -d^2\tau_j / dn^2$, $j = g,l,s$ with $N_g = [u_g / u_s][\alpha_s / \alpha_g]$, $N_l = (\alpha_s / \alpha_l)$, $N_s = 1$. Along the liquid/solid interface we have $\tau_l = \tau_s = \tau_m$ and $\Lambda[\tau_{l,\xi}{}^2 + \tau_{l,\eta}{}^2]^{1/2} = [\tau_{s,\xi}{}^2 + \tau_{s,\eta}{}^2]^{1/2} + \tau_m St \hbar_\xi / [\hbar_\xi{}^2 + \hbar_\eta{}^2]^{1/2}$, where $\Lambda = \lambda_l / \lambda_s$, $St = L_s / C_{Ps}(T_m - T_\infty)$ and $\hbar$ is non-dimensional h. Along this interface we have $n = c$=constant. In terms of (s,n) the interface condition above simplifies to the form $\Lambda \tau_{l,n} = \tau_{s,n} + \tau_m Stc$. The remaining conditions are $\tau_g = \tau_l = 1$ at $n = 0$, $\tau_l = \tau_s = \tau_m$ at $n = c$, τ_g and τ_s vanish as $n \to \infty$ in each medium.

The energy equations are easily solved in terms of error functions. The liquid/solid interface condition yields the following parametric relationship:

$$\Lambda \frac{(1-\tau_m)}{\tau_m} \sqrt{N_l} \frac{\exp(-\frac{N_l c^2}{2})}{erf(c\sqrt{\frac{N_l}{2}})} + \frac{\exp(-\frac{c^2}{2})}{erfc(\frac{c}{\sqrt{2}})} = c\sqrt{\frac{\pi}{2}} St \qquad (1)$$

We note that as $T_m \to T_i$ and $c \to 0$ the preceding equation gives $erf(c\sqrt{N_l / 2})/(T_i - T_m) \to \Lambda\sqrt{N_l}\ /(T_i - T_m) = [\rho_l C_{Pl} \lambda_l / \rho_s C_{Ps} \lambda_{ls}]^{1/2} / (T_i - T_\infty)$, which further reduces to the flame spread formula of [21]. Equation (13) in Chapter 3 for the spread rate is derived using the method of [28]. We write the net heat flux from the surface flame (at $y = 0$, $x > 0$) as $q_f = -\lambda_g \partial T_g / \partial y - \lambda_l \partial T_l / \partial y = [\sqrt{u_g \rho_g C_{Pg} \lambda_g} + \sqrt{u_s \rho_l C_{Pl} \lambda_l}\sqrt{\Phi}][T_i - T_\infty] / \sqrt{\pi x}$,

where $\Phi = \Lambda^2 N_l$. When we also write $q_f = (T_f - T_\infty)\sqrt{\rho_g C_{Pg} \lambda_g} / \sqrt{\pi x}$ we obtain the flame-spread formula

$$\frac{u_s}{u_\infty} = \frac{\rho_g C_{Pg} k_g}{\rho_l C_{Pl} k_l} \cdot (\frac{T_f - T_i}{T_i - T_m})^2 \cdot erf(c\sqrt{\frac{1}{2} \cdot \frac{\alpha_s}{\alpha_l}})^2$$

which is equation (13). We note that $St > 0$ is for ordinary endothermic solid $\rightarrow$ liquid liquefaction. As noted in [28], the first term in equation (1) is the non-dimensional heat flux to the interface from the liquid and it becomes infinite as $c \rightarrow 0$, zero as $c \rightarrow \infty$. The second term is the nondimensional heat flux leaving the interface into the solid, and it approaches unity as $c \rightarrow 0$ and infinity linearly with c as $c \rightarrow \infty$ (since $\lim_{x \rightarrow \infty} erfc(x) = \sqrt{\pi} x \exp(x^2)$). The third term is the heat absorbed at the solid/liquid interface.

APPENDIX IV

NUMERICAL METHOD FOR FLOW FIELD CALCULATION

1. Control Volumes

To solve the numerical model, the discretized equations are derived by integrating the governing differential equation over a sub-domain surrounding each grid point. These sub-domains, which are also referred to as control volumes, are defined in Figure 1; the dashed lines denote the control volume boundaries. There are two types of control volumes, interior control volumes and boundary control volumes. For the former, a given grid point communicates with four neighboring grid points through the four faces of the control volume. For the latter, as shown shaded in Figure 1, one face of the control volume coincides with the boundary of the calculation domain, and a boundary grid point is placed at the center of the control volume face. It communicates with only three neighboring nodes.

2. Discretization

The partial differential equations can now be integrated over control volumes. The control volume is constructed around the grid point P; the other grid points E, W, N, S are the eastern, western, northern, and southern neighbors of P. The corresponding faces of the control volumes are denoted by e, w, n, s. The discretization of the diffusion terms was the central difference method. The convective terms were discretized by using the upstream method. The linearization of the chemical terms is standard. Substitution of the relations derived before into the governing equations, we can obtain the final discretization of the general form. If the dependent variable is denoted by ϕ, the general form of the discretized equations can be written as:

$$a_P\phi_P = a_E\phi_E + a_W\phi_W + a_N\phi_N + a_S\phi_S + b \tag{1}$$

It is useful to write equation (1) in a more generalized form

$$a_P\phi_P = \sum a_{nb}\phi_{nb} + b \tag{2}$$

3. Staggered Grid

The original goal of the staggered grid is to eliminate the unrealistic flow field that may arise in the collocated grid. Figure 2 shows a portion of a 2-D grid. The locations for which the velocity components are calculated are shown by short arrows. In the staggered grid, the velocity components are calculated at the surfaces of the control volume. All other variables such as pressure, temperature, and concentrations are calculated at the grid points shown by dots. The advantage of this arrangement is that the normal velocity components are directly available at the control volume surfaces, where they are useful for calculating the mass flow rates. In addition, the pressure difference between two grid points can be used to "produce" the velocity component located between them. The disadvantage of the staggered grid is that (1) The boundary conditions are difficult to implement; (2) The complexity of the programming increases; (3) Interpolation of the properties at the grid points is needed for the staggered grid system.

4. Discretization of Gas Phase Equations

Detailed discretization is given [46] with specific interest in gas phase equations. The two-dimensional form of the gas phase equations except continuity equation is,

$$\frac{\partial}{\partial t}(\rho\phi) + \frac{\partial J_x}{\partial x} + \frac{\partial J_y}{\partial y} = S \tag{3}$$

where J_x and J_y are total (convective and diffusion) fluxes defined by

$$J_x = \rho u \phi - \Gamma \frac{\partial \phi}{\partial x} \tag{4-a}$$

and

$$J_y = \rho u \phi - \Gamma \frac{\partial \phi}{\partial y} \tag{4-b}$$

The integration over the control volume leads to

$$\frac{(\rho_P \phi_P - \rho_P^0 \phi_P^0)\Delta x \Delta y}{\Delta t} + J_e - J_w + J_n - J_s = (S_C + S_P \phi_P)\Delta x \Delta y \tag{5}$$

where the source term has been linearized in the usual manner, and further treatment was introduced before. With the introduction of staggered grid, ρ_P and ϕ_P are assumed to prevail over the whole control volume. The old value is represented by ρ_P^0 and ϕ_P^0. The quantities J_w, J_e, J_s, and J_n are integrated over the control volume faces. In a similar manner, the continuity equation can be derived,

$$\frac{(\rho_P - \rho_P^0)\Delta x \Delta y}{\Delta t} + F_e - F_w + F_n - F_s = 0 \tag{6}$$

where

$$F_e = (\rho u)_e \Delta y$$

$$F_w = (\rho u)_w \Delta y$$

$$F_s = (\rho u)_s \Delta y$$

$$F_n = (\rho u)_n \Delta y$$

Now we multiply Equation (6) by ϕ_P and subtract it from Equation (3), we obtain

$$(\phi_P - \phi_P^0)\frac{\rho_P^0 \Delta x \Delta y}{\Delta t} + (J_e - F_e\phi_P) - (J_w - F_w\phi_P) + (J_n - F_n\phi_P) - (J_s - F_s\phi_P) = (S_C + S_P\phi_P)\Delta x \Delta y \tag{7}$$

This is the discretized equation for momentum, energy, and species conservation. Note that this method maintains the conservation of both the continuity and other identities.

5. Under-Relaxation

In the previous Oseen-flow model, there are three major nonlinearities in the numerical model. First, the chemical reaction terms in the gas phase and the condensed phase constitute the strong non-linearity in the equation system. Second, at the interface, the balance of mass, heat, and momentum links the gas phase equations with the condensed equations. Third, the phase change in the condensed phase introduced a nonlinear source term that accounts for the enthalpy jump between two phases. In the complete model, the flow field calculation introduced a new non-linearity, that is, the inter-linkage between the velocity field and pressure. Because of these inter-linkages and non-linearities, the final solution must be obtained by an iterative procedure. At any given stage, the discretization coefficients can be calculated from the most recent estimates of all independent variables. With the improved estimates, all the independent variables will cease to change after a certain number of iterations, thus the final converged solution is reached. However it is not guaranteed that we can always attain a converged solution if we only increase the number of iterations. At times, the values of independent variables oscillate or drift away from a reasonable solution. To avoid such divergence, one method called under-relaxation is proposed that will slow the update of the nonlinear coefficients from iteration to iteration. Equation (2) can be rewritten as

$$\phi_P = \phi_P^* + [\frac{\sum a_{nb}\phi_{nb} + b}{a_P} - \phi_P^*] \tag{8}$$

where ϕ_P^* stands for the value of ϕ_P from the previous iteration. The bracketed content denotes the change in ϕ_P in the current iteration. To reduce the change, an under-relaxation factor α can be introduced so that

$$\phi_P = \phi_P^* + \alpha[\frac{\sum a_{nb}\phi_{nb} + b}{a_P} - \phi_P^*] \tag{9}$$

The selection of this factor, which depends on the flow situations, is empirical. In our solution procedure, α is given 0.6 for x and y momentum equations. It is worth noting that the pressure needs not to be under-relaxed for the SIMPLEC method, though it is under-relaxed in the SIMPLE method.

6. The SIMPLEC Scheme for Flow Calculation

To solve the flow field, one difficulty arises since pressure does not appear in the continuity equation. Numerically it is desired that pressure should serves as the primary unknown for direct solution. This difficulty is resolved by the Semi Implicit Method with Pressure Linked Equation (SIMPLE) and its improved versions such as SIMPLER (SIMPLE Revised) and SIMPLEC (SIMPLE Consistent). In our solution procedure, SIMPLEC is selected because of its consistency and because it is a straightforward extension of SIMPLE.

6.1. Derivation of Momentum Equations

The appropriate control volumes for velocity u_e pass through the grid points P and E. The corresponding momentum equation can be written as

$$a_e u_e = \sum a_{nb} u_{nb} + b + A_e (P_P - P_E) \tag{10}$$

where A_e is the area over which the pressure force acts. If the pressure is taken from an estimated field such as from the previous iteration P^*, then u^* denotes the velocity field based on the estimated pressure field. This implies

$$a_e u_e^* = \sum a_{nb} u_{nb}^* + b + A_e (P_P^* - P_E^*) \tag{11}$$

Similarly we can obtain the v^* velocity equation based on the estimated pressure field.

6.2. Derivation of Pressure Correction Equation

In order that the velocity field satisfy the continuity equation, the u^* and v^* must be corrected as a consequence of the pressure correction P' applied to the pressure P^*. Thus we have

$$P = P^* + P' \tag{12}$$

$$u = u^* + u'$$

Subtraction of Equation (10) from Equation (11) results

$$a_e u_e' = \sum a_{nb} u_{nb}' + A_e (P_P' - P_E') \tag{13}$$

With re-arrangement, we obtain

$$(a_e - \sum a_{nb}) u_e' = \sum a_{nb} (u_{nb}' - u_e') + A_e (P_P' - P_E') \tag{14}$$

In order to derive the velocity correction equation, it is assumed that the term $\sum a_{nb} (u_{nb}' - u_e')$ is negligible, we further obtain

$$u_e' = d_e (P_P' - P_E') \tag{15}$$

where $d_e = A_e / (a_e - \sum a_{nb})$. Note that under-relaxation must be applied to the

momentum equations in order to use the SIMPLEC scheme otherwise d_e will become infinity since $a_e = \sum a_{nb}$. However the pressure correction need not be under-relaxed so that $\alpha_P = 1.0$.

The continuity equation can be written as

$$(\rho uA)_w - (\rho uA)_e + (\rho vA)_s - (\rho vA)_n = 0 \tag{16}$$

The u_e, u_w, u_s and u_n are expressed by a equation like (10), thereby a discretized form of the pressure equation can be obtained and cast into the form

$$a_P P'_P = a_E P'_E + a_W P'_W + a_N P'_N + a_S P'_S + b \tag{17}$$

where

$$a_E = (\rho dA)_e,$$

$$a_W = (\rho dA)_w,$$

$$a_N = (\rho dA)_n,$$

$$a_S = (\rho dA)_s$$

$$a_P = a_E + a_W + a_N + a_S$$

$$b = (\rho u^* A)_w - (\rho u^* A)_e + (\rho u^* A)_s - (\rho u^* A)_n.$$

7. Boundary Conditions

The momentum equations are special cases of the general ϕ equation, and therefore the treatment to momentum equation applies to other equations as well. One problem may arise since p' does not come naturally as a variable. Some treatments are discusses in [46]. There are two types of boundary conditions, either the pressure is given or the velocity normal to the boundary is given. (1) Given the pressure at the boundary. If the

guessed pressure p^* is given, then the value of p' should be zero, which is akin to the given temperature boundary condition in heat-conduction problem; (2) Given normal velocity at the boundary. In this situation, the derivation of p' equation should be based on the flow rate that is expressed from the given velocity, not the u^*. In the pressure correction equation, the p' will not appear at the boundary points.

8. Overall Solution Procedure

1) Solve the condensed phase energy equation; obtain the interface temperature and pyrolysis product mass flow rate.

2) Solve the gas phase flow field. This includes the following steps

a. Guess the pressure field from the most recent values.

b. Solve the momentum equation to get u^* and v^*.

c. Solve the pressure correction.

d. Correct the pressure field and velocity field by the use of equations.

e. Consider the corrected pressure as the new guessed value and return to step "a" until convergence is obtained.

3) Solve the gas phase fuel concentration, oxidizer concentration, and energy equations, and then return to step 1 until convergence is obtained.

8.1. Solution of Algebraic Equations

8.1.1. Delta Formulation of Time Discretization

In terms of the time differencing, we discretize the governing equations in terms of the delta formulation; namely, for a given physical quantity the unknown is represented by the time increment instead of its magnitude. The advantage of this treatment is to decrease the round-off error of the iterative computation since each time only a small

increment need to be obtained. In principle, the delta formulation does not alter the numerical scheme. To describe the Delta formulation, we define δU as the increment for a given physical quantity U, we have

$$U_{i,j}^{n+1} = \delta U_{i,j} + U_{i,j}^{l} \tag{18}$$

where i and j denote the coordinate positions, "$n+1$" denotes the new time step, and "l" denotes the iterative time level or the most recent value.

The transformation from normal form to delta form is straightforward. Take the continuity equation for example. The fully implicit form of FDE equation is

$$\frac{\rho_g^{n+1} - \rho_g^n}{\Delta t} + D_x(\rho_g u)^{n+1} + D_y(\rho_g v)^{n+1} = 0 \tag{19}$$

where D_x and D_y denote 1st order space difference operator. With space discretization, equation (19) becomes

$$\frac{\rho_{gi,j}^{n+1} - \rho_{gi,j}^{n}}{\Delta t} + \frac{\rho_{gi+1/2,j}^{n+1} u_{i+1/2,j}^{n+1} - \rho_{gi-1/2,j}^{n+1} u_{i-1/2,j}^{n+1}}{\Delta x} + \frac{\rho_{gi,j+1/2}^{n+1} v_{i,j+1/2}^{n+1} - \rho_{gi,j-1/2}^{n+1} v_{i,j-1/2}^{n+1}}{\Delta y} = 0 \tag{20}$$

Substitute Equation (18) into equation (20), let $\rho^{n+1} \approx \rho^{l}$, and ignore the higher order terms, we obtain

$$\frac{\rho_{gi,j}^{l} - \rho_{gi,j}^{n}}{\Delta t} + \frac{\rho_{gi+1/2,j}^{l}(u_{i+1/2,j}^{l} + \delta u_{i+1/2,j}) - \rho_{gi-1/2,j}^{l}(u_{i-1/2,j}^{l} + \delta u_{i-1/2,j})}{\Delta x} + \frac{\rho_{gi,j+1/2}^{l}(v_{i,j+1/2}^{l} + \delta v_{i,j+1/2}) - \rho_{gi,j-1/2}^{l}(v_{i,j-1/2}^{l} + \delta v_{i,j-1/2})}{\Delta y} = 0 \tag{21}$$

With re-arrangement, we can obtain an equation of the following form

$$0 = a_{i+1/2,j}\delta u'_{i+1/2,j} + a_{i-1/2,j}\delta u'_{i-1/2,j} + a_{i,j+1/2,j}\delta u'_{i,j+1/2} + a_{i,j-1/2}\delta u'_{i,j-1/2} + b \quad (22)$$

where

$$a_{i+1/2,j} = \rho^{l}_{gi+1/2,j}$$

$$a_{i-1/2,j} = \rho^{l}_{gi-1/2,j}$$

$$a_{i,j+1/2} = \rho^{l}_{gi,j+1/2}$$

$$a_{i,j-1/2} = \rho^{l}_{gi,j-1/2}$$

$$b = \frac{\rho^{l}_{gi,j} - \rho^{n}_{gi,j}}{\Delta t} + \frac{\rho^{l}_{gi+1/2,j}u^{l}_{i+1/2,j} - \rho^{l}_{gi-1/2,j}u^{l}_{i-1/2,j}}{\Delta x} + \frac{\rho^{l}_{gi,j+1/2}v^{l}_{i,j+1/2} - \rho^{l}_{gi,j-1/2}v^{l}_{i,j-1/2}}{\Delta y}$$

The discretized form of the other equations can be obtained similarly.

9. Solution of the Pressure Correction Equation

For the unsteady model, the momentum and energy equations can be conveniently solved by using a solution such as the ADI method with an accuracy of $O(\delta t^2)$. However, the direct solution of the pressure correction equation cannot be attained because it requires excessive storage and computer time. Therefore, an iterative method for solving the algebraic pressure equations is employed. The solution of the p' equation can represent as much as 80% of the total cost of solving the normal fluid flow problem. In combustion calculations, it would be expected that the solution of the p' equation

would also be time-consuming. Therefore it is a high priority to solve for the pressure in an efficient manner. Pantankar [86] recommends a combination of a block correction to lines, followed by line-to-line iterations based on the tridiagonal matrix algorithm (TDMA). Van Doormaal [87] recommended a convergence accelerating technique based on Pantankar's methods. These methods are used in the solution procedure of the numerical model and will be briefly presented here.

1) Line By Line Technique

The method uses TDMA as its basic unit. In a two-dimensional problem, the values along one-grid lines will be solved by using the TDMA. The solution sequence can be a first scan along all horizontal lines and another scan along all vertical lines. In addition, all neighboring-line values are substituted from the best available estimates. The process can be repeated by choosing the alternate lines.

2) Block-Correction Procedure

The convergence of the line-by-line technique can be improved by block correction. The basic idea is that a converged solution can be obtained by adding uniform corrections along lines of constant i. The corrections are chosen so that integral conservation over the control volume blocks by each constant-i line is satisfied. The complete procedure includes a combination of a block correction to lines, followed by line-by-line iteration.

3) Convergence Acceleration Technique

Further recommendation is provided by [87] to accelerate the convergence. Equations for pressure corrections can be restated for a solution along a line of constant j,

$$a_{ij} p'_{ij} = b_{ij} p'_{i+1,j} + c_{ij} p'_{i-1,j} + [d_{ij} p'_{i,j+1} + e_{ij} p'_{i,j-1}] + f_{ij} \tag{23}$$

where

$$a_{ij} = a_P,\ b_{ij} = a_E,\ c_{ij} = a_W,\ d_{ij} = a_N,\ e_{ij} = a_S, \text{ and } f_{ij} = b.$$

Here i and j denote the nodal locations in the x and y directions. In deriving the accelerating-convergence method, suppose that a partially converged p' field, denoted as $[p']^0$, has been obtained for one or more TDMA based iterations. In the current iteration, Equation (23) is to be solved along each j line, sweeping in the direction of increasing j. One the j line, the best estimate of p'_{ij-1} is that obtained from the just-completed solution along the j-1 line. This is the offline value used in Equation (23). The available estimate of the p'_{ij+1} is from the previous iteration, i.e., $[p'_{ij+1}]^0$. An approximation is introduced as $[P'_{ij+1}]_{BE}$, which is defined as

$$\begin{aligned}[p'_{ij+1}]_{BE} &= [p'_{ij+1}]^0 + (\theta - 1)(p'_{ij+1} - [p'_{ij+1}]^0) \\ &\approx [p'_{ij+1}]^0 + (\theta - 1)(p'_{ij} - [p'_{ij}]^0)\end{aligned} \tag{24-a}$$

Therefore we obtained

$$\begin{aligned}\{a_{ij} - d_{ij}(\theta - 1)\}p'_{ij} &= b_{ij}p'_{i+1,j} + c_{ij}p'_{i-1,j} + \\ &\quad d_{ij}\{[p'_{i,j+1}]^0 - (\theta - 1)[p'_{ij}]^0\} + e_{ij}p'_{i,j-1} + f_{ij}\end{aligned} \tag{24-b}$$

A similar estimate is made for the solution along the i lines. It is suggested [87] that the value of θ should be in the range of [1.85, 1.95], and a conservative value of 1.85 is recommended. Therefore in this model we let $\theta = 1.85$.

4) Convergence Criteria

There are two loops of iterations in terms of the solution procedure. First, the solution of p' equation is attained by an iterative procedure. One approach of controlling this convergence is simply giving the number of iterations, such as 25, and is used in this

model solution. Another approach of convergence control is proposed in [87]. That is, a ratio between the Euclidean norm of the pressure equation residual during iteration and the Euclidean norm at the initial stage is used to control the convergence. The recommended ratio is 0.25. This ratio, by observation, results in a too slow computational procedure in this combustion process. This method thus is not recommended in this model. Second, the overall solution procedure for both gas and condensed phase calculation is attained in an iterative manner. The iterative cycle as presented in Appendix II. Moreover, additional convergence criteria are needed for the mass and momentum equations. For the mass conservation equation, we use the mass equation residual as criteria. For the momentum equation, or the energy equation, fuel concentration, etc., the relative difference between two recent iterative values is used as criteria.

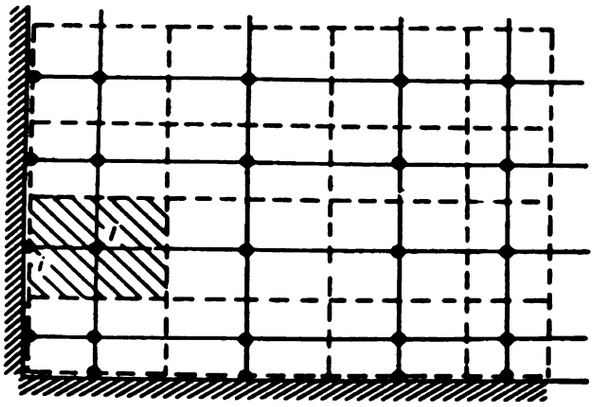

Figure 1 Grids and control volumes.

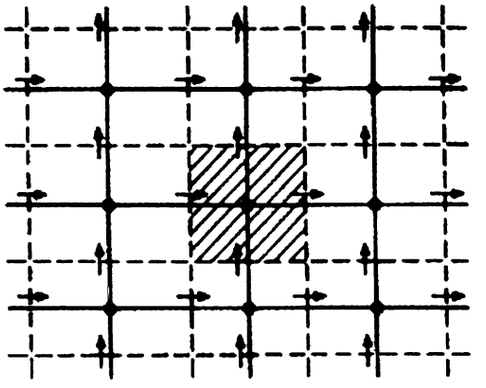

Figure 2 The staggered grid system.

APPENDIX V

DEFINITION OF THE HEAT TRANSFER MECHANISMS IN IGNITION ANALYSIS

The numerical derivation of the heat transfer mechanisms are the followings:

1. The total radiation heat is obtained by multiplication of the constant radiation heat flux with the ignition delay time.
2. The solid heat conduction is derived by

$$\int_0^{\tau_{ig}} \int_0^{l_x} k_c \frac{\partial T}{\partial y} dxdt$$

where k_c takes on the liquid or solid conductivity when appropriate; L_x is the longitudinal length of the interface.

3. The gas conduction is obtained in a similar manner by

$$\int_0^{\tau_{ig}} \int_0^{l_x} k_g \frac{\partial T}{\partial y} dxdt$$

4. The radiation heat loss is obtained by

$$\int_0^{\tau_{ig}} \int_0^{l_x} \varepsilon\sigma(T_{interface}^4 - T_0^4) dxdt$$

where T_0 is the initial temperature 300K.

APPENDIX VI

DERIVATION OF VOLUME AVERAGING EQUATIONS FOR BUBBLE FORMING PROCESS IN HEATED POLYMERS

1. The Basic Equations

1.1 Governing Point Equations

1.1.1 Assumptions

- The solid phase contains only polymer.
- The liquid phase contains both polymer and monomer.
- The gas phase contains only monomer; we do not consider the existence of dissolved gas.

1.1.2 Restrictions

- $h = h^0 + C_P(T - T^0)$ and $C_{Pi} = C_P = const$ for each species and separate phase.
- Conductivities are constant for the three separate phases.

1.1.3 Solid Phase

The *mass and species conservation equation* in the solid are trivial; the *energy equation* is given as

$$\frac{\partial}{\partial t}(\rho_\sigma h_\sigma) = \rho_\sigma C_{P\sigma}\frac{\partial T}{\partial t} = -\nabla \cdot q_\sigma \cdot \tag{1}$$

where $q_\sigma = -k_\sigma \nabla T$.

1.1.4 Liquid Phase

Mass Equation:

$$\frac{\partial \rho_\beta}{\partial t} + \nabla \cdot (\rho_\beta v_\beta) = 0 \tag{2}$$

where the averaged velocity v_β is obtained from $\rho_\beta v_\beta = \rho_m v_m + \rho_p v_p$.

Species Equation:

$$\frac{\partial \rho_i}{\partial t} + \nabla \cdot (\rho_i v_i) = w_i, \; i = m, p \tag{3}$$

In Equation (3), the decomposition of polymer into monomer takes place in the liquid and w is the reaction rate with the relationship of $w_p + w_m = 0$. We introduce $Y_i = \rho_i / \rho_\beta$ to denote the volume fraction of species i in the liquid phase. Writing the species velocity in terms of the mass averaged velocity, we obtain $v_i = v_\beta + u_i$, where u_i denotes the diffusing velocity. Therefore Equation (3) can be reorganized based on the above two definitions,

$$Y_i(\frac{\partial \rho_\beta}{\partial t} + \nabla \cdot (\rho_\beta v_\beta)) + \rho_\beta(\frac{\partial Y_i}{\partial t} + v_\beta \nabla \cdot Y_i) + \nabla \cdot (\rho_\beta Y_i u_i) = w_i$$

The first term on the left hand side is zero according to Equation (2), thereby,

$$\rho_\beta(\frac{\partial Y_i}{\partial t} + v_\beta \nabla \cdot Y_i) = -\nabla \cdot (\rho_\beta Y_i u_i) + w_i \tag{4}$$

The diffusive flux $\rho_\beta Y_i u_i$ can be formulated by,

$$\rho_\beta Y_i u_i = -\rho_\beta D \nabla Y_i \tag{5}$$

So that our final form of the species equation is

$$\rho_\beta(\frac{\partial Y_i}{\partial t} + v_\beta \nabla \cdot Y_i) = \nabla \cdot (\rho_\beta D \nabla Y_i) + w_i \tag{6}$$

If we define $\frac{D}{Dt}$ in terms of the volume averaged properties, i.e., $\frac{D()}{Dt} = \frac{\partial()}{\partial t} + v_\beta \cdot \nabla()$, we obtain

$$\rho_\beta \frac{DY_i}{Dt} = \nabla \cdot (\rho_\beta D \nabla Y_i) + w_i \tag{7-a}$$

Another form of the species equation is,

$$\frac{\partial \rho_i}{\partial t} + \nabla \cdot (\rho_i v_\beta) = \nabla \cdot (\rho_\beta D \nabla Y_i) + w_i \tag{7-b}$$

, and can be) directly obtained from Equation (3).

Energy Equation:

The appropriate form of energy equation for a multi-component system is:

$$\frac{\partial}{\partial t}(\sum_i \rho_i h_i) + \nabla \cdot (\sum \rho_i h_i v_i) = \nabla \cdot (k_\beta \nabla T) \tag{8-a}$$

But we will start from another form of energy equation,

$$\frac{\partial}{\partial t}(\rho_\beta h_\beta) + \nabla \cdot (\rho_\beta h_\beta v_\beta) = -\nabla \cdot q_\beta \tag{8-b}$$

where $q_\beta = -k_\beta \nabla T_\beta + \sum_i \rho_i u_i h_i$. The averaged enthalpy h_β is introduced by the definition of $\rho_\beta h_\beta = \rho_m h_m + \rho_p h_p$. This allows us to reduce the LHS of Equation (8) by using Equation (2).

$$h_\beta [\frac{\partial \rho_\beta}{\partial t} + \nabla \cdot (\rho_\beta v_\beta)] + [\rho_\beta \frac{\partial h_\beta}{\partial t} + \rho_\beta v_\beta \cdot \nabla h_\beta] = \rho_\beta \frac{Dh_\beta}{Dt} \tag{9}$$

Following from Equation (9),

$$\rho_\beta \frac{Dh_\beta}{Dt} = \rho_\beta \frac{D}{Dt}(\sum Y_i h_i) = \rho_\beta (\sum \frac{DY_i}{Dt} h_i + \sum Y_i \frac{Dh_i}{Dt}) = \rho_\beta \sum \frac{DY_i}{Dt} h_i + \rho_\beta C_{P\beta} \frac{DT}{Dt} \tag{10}$$

and using Equation (4), we obtain from the first term of Equation (10),

$$\rho_\beta \sum \frac{DY_i}{Dt} h_i = \sum(-\nabla\cdot(\rho_\beta Y_i u_i) + w_i)h_i$$
$$= \sum(-h_i\nabla\cdot(\rho_\beta Y_i u_i) + h_i w_i) \quad (11)$$
$$= \sum(-\nabla\cdot(h_i\rho_\beta Y_i u_i) + \rho_\beta Y_i u_i \nabla\cdot h_i + h_i w_i)$$
$$= \sum(-\nabla\cdot(h_i\rho_i u_i) + \rho_i u_i \nabla\cdot h_i + h_i w_i)$$

We substitute Equation (11) into Equation (10), and then substitute Equation (10) into Equation (8),

$$\sum(-\nabla\cdot(h_i\rho_i u_i) + \rho_i u_i\nabla\cdot h_i + h_i w_i) + \rho_\beta C_{P\beta}\frac{DT}{Dt} = k_\beta\nabla^2 T_\beta - (\sum\nabla\cdot(\rho_i u_i h_i)) \quad (12)$$

The first term on the left hand side cancel with the second term on the right hand side. In addition, we apply the restrictions of constant thermal capacity; the second term on the left hand reduces to

$$\sum\rho_i u_i\nabla\cdot h_i = (\sum\rho_i u_i C_{Pi})\nabla\cdot T = (\sum\rho_i u_i)C_{P\beta}\nabla\cdot T = 0 \quad (13)$$

The third term on the left hand side of Equation (12) is reduced to

$$\sum h_i w_i = \sum[h_i^0 + C_P(T-T^0)w_i] = \sum h_i^0 w_i + C_P(T-T^0)\sum w_i = \sum h_i^0 w_i \quad (14)$$

Finally we obtain the energy equation in temperature form,

$$\rho_\beta C_{P\beta}\frac{DT}{Dt} = k_\beta\nabla^2 T_\beta - \sum h_i^0 w_i \quad (15)$$

1.1.5 Gas Phase

Mass (species) Equation :

$$\frac{\partial\rho_\gamma}{\partial t} + \nabla\cdot(\rho_\gamma v_\gamma) = 0 \quad (16)$$

Energy Equation:

$$\frac{D(\rho_\gamma h_\gamma)}{Dt} = \rho_\gamma C_{P\gamma} \frac{DT}{Dt} = -\nabla \cdot q_\gamma \tag{17}$$

where $q_\gamma = -k_\gamma \nabla T$.

1.2 Boundary Conditions

The solid-gas boundary condition is trivial since the solid phase does not contact with the gas phase in this problem. We will present the solid-liquid and liquid-gas boundary conditions.

1.2.1 Solid-Liquid Interface

To derive the *energy boundary* condition, we will follow the approach given by [82]. The material control volume V_m is illustrated by Figure 1. It contains both the solid phase V_σ and the liquid phase V_β, and is separated by a singular surface $A_{\sigma\beta} = A_{\beta\sigma}$. The integral representation of the energy equation in V_m is given by:

$$\frac{D}{Dt} \int_{V_m} \rho h dV = - \int_{A_m} q \cdot n dA \tag{18}$$

We already know that

$$in\ phase\ \sigma \begin{cases} \rho h = \rho_\sigma h_\sigma \\ q = q_\sigma \end{cases} \qquad in\ phase\ \beta \begin{cases} \rho h = \rho_\beta h_\beta \\ q = q_\beta \end{cases} \tag{19}$$

First we integrate Equation (1) over volume V_σ to obtain

$$\int_{V_\sigma} \frac{\partial}{\partial t}(\rho_\sigma h_\sigma) dV = - \int_{V_\beta} \nabla \cdot q_\sigma dV \tag{20}$$

We can use the general transport theorem to express the first term in Equation (20) as

$$\int_{V_\sigma} \frac{\partial}{\partial t}(\rho_\sigma h_\sigma) = \frac{d}{dt} \int_{V_\sigma} (\rho_\sigma h_\sigma) dV - \int_{A_{\sigma\beta}} \rho_\sigma h_\sigma w \cdot n_{\sigma\beta} dA \tag{21}$$

Where $A_{\sigma\beta}$ is the interfacial area. As seen from Figure 1., the area integral over A_σ is zero because the velocity v_σ is zero there. Substituting Equation (21) into Equation (20) and applying the divergence theorem to the second term lead to

$$\frac{d}{dt}\int_{V_\sigma}(\rho_\sigma h_\sigma)dV - \int_{A_{\sigma\beta}}\rho_\sigma h_\sigma w\cdot n_{\sigma\beta}dA = -\int_{A_\sigma} q_\sigma\cdot n_\sigma dA - \int_{A_{\sigma\beta}} q_\sigma\cdot n_{\sigma\beta}dA \tag{22}$$

We can repeat these steps for Equation (8-b) to obtain the similar expression for the β phase.

$$\frac{d}{dt}\int_{V_\beta}(\rho_\beta h_\beta)dV + \int_{A_{\beta\sigma}}\rho_\beta h_\beta(v_\beta - w)\cdot n_{\beta\sigma}dA = -\int_{A_\beta} q_\beta\cdot n_\beta dA - \int_{A_{\beta\sigma}} q_\beta\cdot n_{\beta\sigma}dA \tag{23}$$

We now add Equation (23) and (22) together and observe the facts of

$$A_{\sigma\beta} = A_{\beta\sigma} \text{ and } \frac{D}{Dt}\int_{V_m}() = \frac{d}{dt}\int_{V_\sigma}() + \frac{d}{dt}\int_{V_\beta}()\cdot$$

$$\begin{aligned}\frac{D}{Dt}\int_{V_m}\rho h dV + \int_{A_{\sigma\beta}}&[\rho_\beta h_\beta(v_\beta - w)\cdot n_{\beta\sigma} - \rho_\sigma h_\sigma w\cdot n_{\sigma\beta}] \\ &= -\int_{A_m} q\cdot n dA - \int_{A_{\sigma\beta}}[q_\beta\cdot n_{\beta\sigma} + q_\sigma\cdot n_{\sigma\beta}]dA\end{aligned} \tag{24}$$

where V_m is the material volume and $V_m = V_\sigma + V_\beta$. Comparing Equation (24) and Equation (18) leads to the jump condition at the $\sigma-\beta$ interface.

$$\rho_\beta h_\beta(v_\beta - w)\cdot n_{\beta\sigma} - \rho_\sigma h_\sigma w\cdot n_{\sigma\beta} = -[q_\beta\cdot n_{\beta\sigma} + q_\sigma\cdot n_{\sigma\beta}] \tag{26}$$

The jump condition of *mass transfer* can be easily obtained:

$$\rho_\beta(v_\beta - w)\cdot n_{\beta\sigma} - \rho_\sigma w\cdot n_{\sigma\beta} = 0 \tag{27}$$

The derivation of *species* jump condition follows the same route

$$\rho_p(v_p - w)\cdot n_{\beta\sigma} - \rho_\sigma w\cdot n_{\sigma\beta} = 0 \tag{28}$$

$$\rho_m(v_m - w)\cdot n_{\beta\sigma} = 0 \tag{29}$$

Equation (26) can be further reduced. We substitute the definition of q_β and q_σ into Equation (26) and get.

$$\rho_\beta h_\beta(v_\beta - w)\cdot n_{\beta\sigma} - \rho_\sigma h_\sigma w\cdot n_{\sigma\beta} = [-\lambda_\sigma \frac{\partial T_\sigma}{\partial n_{\beta\sigma}} + \lambda_\beta \frac{\partial T_\beta}{\partial n_{\beta\sigma}} + \sum \rho_i u_i h_i \cdot n_{\beta\sigma}] \tag{30}$$

In addition, recalling the definition of

$$\rho_\beta v_\beta = \rho_m v_m + \rho_p v_p = \rho_m(v_\beta + u_m) + \rho_p(v_\beta + u_p) = \rho_\beta v_\beta + \rho_m u_m + \rho_p u_p$$

,

we obtain

$$Y_m u_m + Y_p u_p = 0 \tag{31}$$

According to Fick's Law, the diffusive heat flux $Y_i u_i$ can be expressed as $Y_i u_i = -D\nabla Y_i$, thus Equation (26) is reduced to the following form,

$$\rho_\sigma(h_\beta - h_\sigma)w\cdot n_{\sigma\beta} = [-\lambda_\sigma \frac{\partial T_\sigma}{\partial n_{\beta\sigma}} + \lambda_\beta \frac{\partial T_\beta}{\partial n_{\beta\sigma}} - \rho_\beta D(h_m - h_p)\frac{\partial Y_m}{\partial n_{\beta\sigma}}]. \tag{32}$$

1.2.2 Liquid-Gas Interface

By following the similar approach in section 1.2.1, we have the energy, mass, and species boundary condition,

Energy boundary condition,

$$\rho_\beta h_\beta(v_\beta - w)\cdot n_{\beta\gamma} + \rho_\gamma h_\gamma(v_\gamma - w)\cdot n_{\gamma\beta} = -[q_\beta \cdot n_{\beta\gamma} + q_\gamma \cdot n_{\gamma\beta}] \tag{33}$$

Mass boundary condition,

$$\rho_\beta(v_\beta - w)\cdot n_{\beta\gamma} + \rho_\gamma(v_\gamma - w)\cdot n_{\gamma\beta} = 0 \tag{34}$$

Species boundary condition,

$$\rho_m(v_m - w)\cdot n_{\beta\gamma} + \rho_\gamma(v_\gamma - w)\cdot n_{\gamma\beta} = 0 \tag{35-a}$$

$$\rho_p(v_p - w)\cdot n_{\beta\gamma} = 0 \tag{35-b}$$

The boundary conditions for the three phase interfaces are now complete, and we will derive the volume-averaged form of the transport equations. These equations will apply to every point in space, not just in each separate phase.

2. The Volume Averaging Method

Since the solid phase is independent of the transport process in the fluid including both the gas and the liquid, we restrict our attention to the fluid part.

2.1 Definitions and Theorems

2.1.1 Volume Fraction

$$\varepsilon_\beta = V_\beta / V\,,\ \varepsilon_\gamma = V_\gamma / V \tag{36}$$

2.1.2 Phase Averaged Quantity

$$\overline{\psi}_k = \frac{1}{V}\int_{V_k} \psi_k dV \tag{37}$$

The phase-averaged quantity is the averaged value of quantity ψ_k over the entire averaging volume V.

2.1.3 Intrinsic Phase Averaged Quantity

$$\overline{\psi}_k^k = \frac{1}{V_k}\int_{V_k} \psi_k dV \tag{38}$$

Here the averaging volume is the phase volume V_k. If ψ_k is uniformly distributed in V_k, then $\overline{\psi}_k^k = \psi_k$. By comparing Equation (38) and Equation (37), we can obtain,

$$\varepsilon_k \overline{\psi}_k^k = \overline{\psi}_k \tag{39}$$

2.1.4 Fluctuation Term

We formulate the quantity ψ_k by

$$\psi_k = \overline{\psi}_k^k + \tilde{\psi}_k \tag{40}$$

Where the fluctuation $\tilde{\psi}_k$ represent the deviation from the intrinsic phase average quantity $\overline{\psi}_k^k$. In addition we have the following relation [88],

$$\overline{\psi_k \Phi_k} = \varepsilon_k \overline{\psi}_k^k \overline{\Phi}_k^k + \overline{\tilde{\psi}_k \tilde{\Phi}_k} \tag{41}$$

2.1.5 Theorem 1: About Averaging of The Time Derivative

$$\overline{(\frac{\partial \psi_k}{\partial t})} = \frac{\partial \overline{\psi}_k}{\partial t} - \frac{1}{V} \int_{A_k} \psi_k w \cdot n_k dA \tag{42}$$

where A_k is the interfacial area of phase k with other phases, n_k is the outward unit normal vector of the area dA, and w is the interface moving velocity.

2.1.6 Theorem 2: About Averaging of The Spatial Derivative

$$\overline{\nabla \psi_k} = \nabla \overline{\psi}_k + \frac{1}{V} \int_{A_k} \psi_k n_k dA \tag{43}$$

2.2 The Derivation Procedure

The derivations summarized in [88] will be presented here. A general transport equation over phase k has the form,

$$\frac{\partial \psi_k}{\partial t} + \nabla \cdot (\psi_k v_k) = \nabla \cdot J_k + S_k, \tag{44}$$

Averaging the above equation over volume V_k leads to

$$\frac{1}{V} \int_{V_k} \frac{\partial \psi_k}{\partial t} dV + \frac{1}{V} \int_{V_k} \nabla \cdot (\psi_k v_k) dV = \frac{1}{V} \int_{V_k} \nabla \cdot J_k dV + \frac{1}{V} \int_{V_k} S_k dV \tag{45}$$

By applying the theorems 1 and 2, we obtain the following expression [88],

$$\frac{\partial \overline{\psi}_k}{\partial t} + \nabla \cdot (\overline{\psi}_k^k \overline{v}_k) = \nabla \cdot \bar{J}_k + \bar{S}_k + I_k^D + I_k^J + I_k^Q \tag{46}$$

where $I_k^D = \nabla \cdot \frac{1}{V} \int_V (-\tilde{\psi}_k \tilde{v}_k) dV$, $I_k^J = \frac{1}{V} \int_{A_k} J_k \cdot n_k dA$, and $I_k^Q = \frac{1}{V} \int_{A_k} \psi_k (w_k - v_k) \cdot n_k dA$.

I_k^D are the macroscopic deviation term, I_k^J and I_k^Q are the interfacial terms.

3. Macroscopic Equations

3.1 Assumptions

1. Only two phases are considered, the liquid phase β and the gas phase γ.

2. Variations of the material properties in V are neglected, i.e., $\tilde{\psi}_k \approx 0$, although globally they may vary [88].

3. All phases in the averaging volume are in thermal equilibrium, that is, $< T_\beta >^\beta = < T_\gamma >^\gamma = T$.

3.2 Macroscopic Equation of Mass Conservation

In this case, according to Equation (46), $\psi = \rho$, $J = 0$, and $S = 0$, therefore $I_k^D = 0$ from assumption 1 and $I_k^J = 0$. The liquid mass Equation (2) and gas mass equations (16) yield,

$$\frac{\partial \overline{\rho}_\beta}{\partial t} + \nabla \cdot (\overline{\rho}_\beta^\beta \overline{v}_\beta) = I_\beta^Q \tag{47-a}$$

$$\frac{\partial \overline{\rho}_\gamma}{\partial t} + \nabla \cdot (\overline{\rho}_\beta^\beta \overline{v}_\gamma) = I_\gamma^Q \tag{47-b}$$

Where $I_\beta^Q = \frac{1}{V} \int_{A_{\beta\gamma}} \rho_\beta (w_\beta - v_\beta) \cdot n_{\beta\gamma} dA$ and $I_\gamma^Q = \frac{1}{V} \int_{A_{\gamma\beta}} \rho_\gamma (w_\gamma - v_\gamma) \cdot n_{\gamma\beta} dA$. According to the interfacial boundary condition (34), we get,

$$I_\beta^Q + I_\gamma^Q = 0$$

If we define $\overline{\dot{m}} = I_\gamma^Q$, we obtain from Equation (47-a) and (47-b),

$$\frac{\partial \overline{\rho}_\beta}{\partial t} + \nabla \cdot (\overline{\rho}_\beta^\beta \overline{v}_\beta) = -\overline{\dot{m}} \tag{47-c}$$

$$\frac{\partial \overline{\rho}_\gamma}{\partial t} + \nabla \cdot (\overline{\rho}_\beta^\beta \overline{v}_\gamma) = \overline{\dot{m}} \tag{47-d}$$

We add Equation (47-c) and (47-d) together, and obtain

$$\frac{\partial}{\partial t}(\overline{\rho}_\beta + \overline{\rho}_\gamma) + \nabla \cdot (\overline{\rho}_\beta^\beta \overline{v}_\beta + \overline{\rho}_\beta^\beta v_\gamma) = 0 \tag{48-a}$$

Another form of the equation can be obtained if we use the definitions of $\overline{\rho}_k = \varepsilon_k \overline{\rho}_k^k$, $k = \beta, \gamma$, i.e.,

$$\frac{\partial}{\partial t}(\varepsilon_\beta \overline{\rho}_\beta^\beta + \varepsilon_\gamma \overline{\rho}_\gamma^\gamma) + \nabla \cdot (\varepsilon_\beta \overline{\rho}_\beta^\beta \overline{v}_\beta^\beta + \varepsilon_\gamma \overline{\rho}_\gamma^\gamma \overline{v}_\gamma^\gamma) = 0 \tag{48-b}$$

3.3 Macroscopic Equation of Energy Conservation

Averaging Equation (8) and (17) by using $\psi_k = \rho_k h_k$, $S_k = 0$, $J_k = q_k$ leads to

$$\frac{\partial}{\partial t}\overline{(\sum_i \rho_i h_i)} + \nabla \cdot \overline{(\sum_i \rho_i h_i v_i)} = \nabla \cdot \overline{(k_\beta \nabla T)} + I_\beta^Q + I_\beta^J \tag{49-a}$$

$$\frac{\partial}{\partial t}\overline{(\rho_\gamma h_\gamma)} + \nabla \cdot \overline{(\rho_\gamma h_\gamma v_\gamma)} = \nabla \cdot \overline{q_\gamma} + I_\gamma^Q + I_\gamma^J \tag{49-b}$$

where

$$I_\gamma^Q = \frac{1}{V}\int_{A_\gamma} \rho_\gamma h_\gamma (w_\gamma - v_\gamma) \cdot n_\gamma dA, \; I_\gamma^J = -\frac{1}{V}\int_{A_\gamma} q_\gamma \cdot n_\gamma dA,$$

$I_\beta^Q = \frac{1}{V}\int_{A_\beta} (\sum_i \rho_i h_i)(w_\beta - v_\beta) \cdot n_\beta dA$, , and $I_\beta^J = -\frac{1}{V}\int_{A_\beta} (k_\beta \nabla T) \cdot n_\beta dA$. We add

equations (49-a) and (49-b) together, and use the rearranged interfacial boundary condition from Equation (33), as obtained from [82],

$$\sum_i \rho_i h_i (v_i - w)\cdot n_{\beta\gamma} + \rho_\gamma h_\gamma (v_\gamma - w)\cdot n_{\gamma\beta} = (k_\beta \nabla T)\cdot n_{\beta\gamma} + q_\gamma \cdot n_{\gamma\beta}$$

Thereby we obtain,

$$\frac{\partial}{\partial t}[\overline{(\sum_i \rho_i h_i)} + \overline{(\rho_\gamma h_\gamma)}] + \nabla\cdot[\overline{(\sum_i \rho_i h_i v_i)} + \overline{(\rho_\gamma h_\gamma v_\gamma)}] = \nabla\cdot[\overline{(k_\beta \nabla T)} + \bar{q}_\gamma] \qquad (50)$$

The terms in Equation (50) need further discussions, as are presented in the following 3 sections.

3.3.1 Derivation of $\frac{\partial}{\partial t}\overline{(\rho_\gamma h_\gamma)} + \nabla\cdot\overline{(\rho_\gamma h_\gamma v_\gamma)}$

Since the gas phase has the single component monomer, the detailed derivation is similar to the procedure from (IIC-43) to (IIC-51) in [82]. Here only the final expression is given,

$$\frac{\partial}{\partial t}\overline{(\rho_\gamma h_\gamma)} + \nabla\cdot\overline{(\rho_\gamma h_\gamma v_\gamma)} = \varepsilon_\gamma \rho_\gamma C_{P\gamma}\frac{\partial \overline{T}_\gamma^{\chi}}{\partial t} + \rho_\gamma C_{P\gamma}\bar{v}_\gamma\cdot\nabla\overline{T}_\gamma^{\gamma} + I_{\gamma 1}^{D} + I_{\gamma 1}^{Q} \qquad (51\text{-a})$$

where $I_{\gamma 1}^{D} = C_{P\gamma}\nabla\cdot\overline{\tilde{\rho}_\gamma \tilde{v}_\gamma \tilde{T}_\gamma}$, and $I_{\gamma 1}^{Q} = [h_\gamma^0 + C_{P\gamma}(\overline{T}_\gamma^{\gamma} - T_\gamma^0)]\{\frac{1}{V}\int_{A_{\gamma\beta}} \rho_\gamma (w - v_\gamma)\cdot n_{\gamma\beta} dA\}\cdot$

3.3.2 Derivation of $\frac{\partial}{\partial t}\overline{(\sum_i \rho_i h_i)} + \nabla\cdot\overline{(\sum_i \rho_i h_i v_i)}$

Following the similar procedure used in the above section, we obtain,

$$\frac{\partial}{\partial t}\overline{(\sum_i \rho_i h_i)} + \nabla\cdot\overline{(\sum_i \rho_i h_i v_i)} = \sum_i \bar{\rho}_i C_{Pi}\frac{\partial \overline{T}_\beta^{\beta}}{\partial t} + \sum_i C_{Pi}\overline{\rho_i v_i}\cdot\nabla\overline{T}_\gamma^{\gamma} + I_{\beta 1}^{D} + I_{\beta 1}^{Q} \qquad (51\text{-b})$$

Where $I_{\beta 1}^{D} = \frac{\partial}{\partial t}(\sum_i C_{Pi}\overline{\tilde{\rho}_i \tilde{T}_\beta}) + \nabla\cdot\sum_i C_{Pi}\overline{\tilde{\rho}_i \tilde{v}_i \tilde{T}_\beta}$, and

$$I^{Q}_{\beta 1} = \sum_i [h_i^0 + C_{Pi}(\overline{T}_\beta^\beta - T_\beta^0)][\frac{\partial \overline{\rho}_i}{\partial t} + \nabla \cdot (\overline{\rho_i v_i})] \cdot$$

Here we substitute species conservation Equation (53-a) to simplify $I^{Q}_{\beta 1}$, thereby

$$I^{Q}_{\beta 1} = \sum_i [h_i^0 + C_{Pi}(\overline{T}_\beta^\beta - T_\beta^0)][\overline{w}_i + I^{Q}_{\beta i}] = \sum_i h_i^0 \overline{w}_i + \sum_i [h_i^0 + C_{Pi}(\overline{T}_\beta^\beta - T_\beta^0)] I^{Q}_{\beta i}$$

3.3.3 Derivation of $\nabla \cdot [\overline{(k_\beta \nabla T)} + \overline{q}_\gamma]$

$$\nabla \cdot [\overline{(k_\beta \nabla T)} + \overline{q}_\gamma] = \nabla \cdot [\overline{(k_\beta \nabla T)} + \overline{(k_\gamma \nabla T)}] = \nabla \cdot (\varepsilon_\beta k_\beta^* \nabla \overline{T}_\beta^\beta + \varepsilon_\gamma k_\gamma^* \nabla \overline{T}_\gamma^\gamma) \qquad (51\text{-c})$$

Here the formulation of an effective conductivity k_k^* is introduced, and the detailed derivation method is presented in [82].

After we derived all terms for Equation (50), we add them together and get the following expression,

$$\begin{aligned} &[\varepsilon_\beta \sum_i (\overline{\rho}_i^\beta C_{Pi}) + \varepsilon_\gamma \overline{\rho}_\gamma^\gamma C_{P\gamma}] \frac{\partial \overline{T}}{\partial t} + [\sum_i (\overline{\rho_i v_i} C_{Pi}) + \overline{\rho_\gamma v_\gamma} C_{P\gamma}] \nabla \cdot \overline{T} \\ &\qquad = \nabla \cdot [(\varepsilon_\beta k_\beta^* + \varepsilon_\gamma k_\gamma^*) \nabla \overline{T}] - \Delta h_{vap} \overline{\dot{m}} - \sum_i h_i^0 \overline{w}_i + I^{D}_{\beta 1} + I^{D}_{\gamma 1} \end{aligned} \qquad (52)$$

In Equation (52), $-\sum_i h_i^0 \overline{w}_i$ denotes the pyrolysis reaction effect, and $\Delta h_{vap} \overline{\dot{m}}$ denotes the evaporation effect. In the latter term, $\overline{\dot{m}}$ is already defined in Equation (47); and Δh_{vap} is defined as

$$\Delta h_{vap} = [h_\gamma^0 - h_{\beta p}^0 + (C_{P\gamma} - C_{P\beta p})(\overline{T} - T^0)] \cdot$$

3.4 Macroscopic Equation of Species Conservation

In this case, we average species equation (3) and obtain

$$\frac{\partial \overline{\rho}_i}{\partial t} + \nabla \cdot (\overline{\rho_i v_i}) = \overline{w}_i + I^{Q}_{\beta i}, \quad i = m, p \qquad (53\text{-a})$$

where $I^{Q}_{\beta i} = \frac{1}{V}\int_{A_{\beta\gamma}} \rho_i (w_\beta - v_\beta)\cdot n_{\beta\gamma} dA$. Another form of equation is obtained by averaging Equation (7-b), and we use $\psi_i = \rho_\beta Y_i$, $J_i = -\rho_\beta D \nabla Y_i$, and $S_i = w_i$ to obtain

$$\frac{\partial(\bar{\rho}^{\beta}_{\beta}\bar{Y}_i)}{\partial t} + \nabla\cdot(\rho_\beta \bar{Y}_i^{\beta}\bar{v}_\beta) = \nabla\cdot(\varepsilon_\beta \rho_\beta D^{*}_{\beta}\nabla \bar{Y}_i^{\beta}) + \bar{w}_i + I^{Q}_{\beta i}, \quad i = m, p \tag{53-b}$$

Note that the first term on the RHS of Equation (53) is written in terms of the effective diffusion coefficient by following the same argument in derivation of the energy equation. We will describe monomer and polymer equations one by one.

For polymer conservation equation, $I^{Q}_{\beta p}$ is zero according to interfacial boundary condition Equation (35-b),

$$\frac{\partial(\bar{\rho}^{\beta}_{\beta}\bar{Y}_p)}{\partial t} + \nabla\cdot(\bar{\rho}^{\beta}_{\beta}\bar{Y}_p^{\beta}\bar{v}_\beta) = \nabla\cdot(\varepsilon_\beta \rho_\beta D^{*}_{\beta}\nabla \bar{Y}_p^{\beta}) + < w_p > \tag{54-a}$$

For monomer species conservation equation, we add monomer conservation equation in the liquid (53) and monomer conservation equation in the gas (47-d), and use the interfacial boundary condition (35-a), and get

$$\frac{\partial}{\partial t}(\bar{\rho}^{\beta}_{\beta}\bar{Y}_m + \bar{\rho}_\gamma) + \nabla\cdot(\bar{\rho}^{\beta}_{\beta}\bar{Y}_m^{\beta}\bar{v}_\beta + \bar{\rho}^{\gamma}_{\gamma}\bar{v}_\gamma) = \nabla\cdot(\varepsilon_\beta \rho_\beta D^{*}_{\beta}\nabla \bar{Y}_m^{\gamma}) + < w_m > \tag{54-b}$$

3.5 Macroscopic Equation of Momentum Conservation

In traditional porous media flow, the porous media is assumed to be a fixed structure. However, in two-phase bubbly flow, there does not exist a fixed solid structure. That is, the Darcy's Law is no longer applicable to this situation. Therefore one has to use the general momentum equation to solve the flow field. In this case, we assume the Newtonian fluid and $\psi = \rho v$. For the liquid and the gas we obtain the momentum

equations respectively according to Equation (46),

$$\frac{\partial \overline{\rho}_\beta^\beta \overline{v}_\beta}{\partial t} + \nabla \cdot (\overline{\rho}_\beta^\beta \overline{v}_\beta^\beta \overline{v}_\beta) = -\nabla \overline{P}_\beta + \overline{\rho}_\beta g + \nabla \cdot [\overline{\mu_\beta \nabla v_\beta} + \overline{\mu_\beta (\nabla v_\beta)^t}] + I_\beta^Q + I_\beta^J \quad (55\text{-a})$$

$$\frac{\partial \overline{\rho}_\gamma^\gamma \overline{v}_\gamma}{\partial t} + \nabla \cdot (\overline{\rho}_\gamma^\gamma \overline{v}_\gamma^\gamma \overline{v}_\gamma) = -\nabla \overline{P}_\gamma + \overline{\rho}_\gamma g + \nabla \cdot [\overline{\mu_\lambda \nabla v_\gamma} + \overline{\mu_\gamma (\nabla v_\gamma)^t}] + I_\gamma^Q + I_\gamma^J \quad (55\text{-b})$$

where the body force is the gravitational force. The definition of I_k^Q and I_k^J can be readily obtained from Equation. (46). The viscous term on the RHS of the Equation (55-a) can be written in terms of the effective viscosity by following the same route in deriving the effective conductivity,

$$\overline{\mu_\beta \nabla v_\beta} + \overline{\mu_\beta (\nabla v_\beta)^t} = \varepsilon_\beta \mu_\beta^* [\nabla \overline{v}_\beta^\beta + (\nabla v_\beta^\beta)^t]$$

We add the two equations (55-a) and (55-b) together, and use the following interfacial boundary conditions,

$$I_\beta^Q + I_\gamma^Q = 0, \text{ and } I_\beta^J + I_\gamma^J = 0.$$

, then obtain the macroscopic form of the momentum equation,

$$\frac{\partial (\overline{\rho}_\beta^\beta \overline{v}_\beta + \overline{\rho}_\gamma^\gamma \overline{v}_\gamma)}{\partial t} + \nabla \cdot (\overline{\rho}_\beta^\beta \overline{v}_\beta^\beta \overline{v}_\beta + \overline{\rho}_\gamma^\gamma \overline{v}_\gamma^\gamma \overline{v}_\gamma) = -\nabla (\overline{P}_\beta + \overline{P}_\gamma) + (\overline{\rho}_\beta + \overline{\rho}_\gamma) g + \nabla \cdot [\varepsilon_\beta \mu_\beta^* [\nabla \overline{v}_\beta^\beta + (\nabla v_\beta^\beta)^t + \varepsilon_\gamma \mu_\gamma^* [\nabla \overline{v}_\gamma^\gamma + (\nabla v_\gamma^\gamma)^t] \quad (56)$$

4. Simplification of Macroscopic Equations

Several additional assumptions have been made to simplify the governing equations for the bubble forming process of polymers. They are listed here:

1. $\overline{v}_\beta = \overline{v}_\beta = v_\beta = 0$.

2. $\overline{T}_\beta^\beta = \overline{T}_\gamma^\gamma = T$

3. $C_{Pm} = C_{Pp} = C_{P\beta}$.

Assumption 1 is based on the fact that (1) the external heat flux is applied at the surface of the polymer, which tends to decrease the liquid natural convection due to buoyancies that further results from density changes; (2) the thickness of the liquid is normally very small, which confines the convection in a enclosed boundary. Assumption 2 is justifiable if the conduction dominates the convection. With these two assumptions, the macroscopic transport equations of mass, heat and species can then be simplified from equations (48), (52), (54) and (56), respectively, and yield

$$\frac{\partial}{\partial t}(\varepsilon_\beta \rho_\beta + \varepsilon_\gamma \overline{\rho}_\gamma^\gamma) + \nabla \cdot (\varepsilon_\gamma \overline{\rho}_\gamma^\gamma \overline{v}_\gamma^\gamma) = 0 \tag{57}$$

$$\begin{aligned}[\varepsilon_\beta \sum_i (\overline{\rho}_i^\beta C_{Pi}) + \varepsilon_\gamma \overline{\rho}_\gamma^\gamma C_{P\gamma}]\frac{\partial \overline{T}}{\partial t} + (\varepsilon_\gamma \overline{\rho}_\gamma^\gamma C_{P\gamma} \overline{v}_\gamma^\gamma)\nabla \cdot \overline{T} \\ = \nabla \cdot [(\varepsilon_\beta k_\beta^* + \varepsilon_\gamma k_\gamma^*)\nabla \overline{T}] - \Delta h_{vap} \overline{\dot{m}} - \sum_i h_i^0 \overline{w}_i\end{aligned} \tag{58}$$

$$\frac{\partial}{\partial t}(\varepsilon_\beta \rho_\beta \overline{Y}_p^\beta) = \nabla \cdot (\varepsilon_\beta \rho_\beta D_\beta^* \nabla \overline{Y}_p^\beta) + < w_p > \tag{59-a}$$

$$\frac{\partial}{\partial t}(\varepsilon_\beta \rho_\beta \overline{Y}_m^\beta + \varepsilon_\gamma \overline{\rho}_\gamma^\gamma) + \nabla \cdot (\varepsilon_\gamma \overline{\rho}_\gamma^\gamma \overline{v}_\gamma^\gamma) = \nabla \cdot (\varepsilon_\beta \rho_\beta D_\beta^* \nabla \overline{Y}_m^\gamma) + < w_m > \tag{59-b}$$

$$\begin{aligned}\frac{\partial(\varepsilon_\gamma \overline{\rho}_\gamma^\gamma \overline{v}_\gamma^\gamma)}{\partial t} + \nabla \cdot (\varepsilon_\gamma \overline{\rho}_\gamma^\gamma \overline{v}_\gamma^\gamma \overline{v}_\gamma^\gamma) \\ = -\nabla(\varepsilon_\beta \overline{P}_\beta^\beta + \varepsilon_\gamma \overline{P}_\gamma^\gamma) + (\varepsilon_\beta \rho_\beta + \varepsilon_\gamma \overline{\rho}_\gamma^\gamma) g + \nabla \cdot \{\varepsilon_\gamma \mu_\gamma^* [\nabla \overline{v}_\gamma^\gamma + (\nabla v_\gamma^\gamma)^t]\}\end{aligned} \tag{60}$$

Furthermore, we define the following parameters $\overline{\rho} = \rho_\beta \varepsilon_\beta + \varepsilon_\gamma \overline{\rho}_\gamma^\gamma$, $f_\beta = \rho_\beta \varepsilon_\beta / \overline{\rho}$, $f_\gamma = \overline{\rho}_\gamma^\gamma \varepsilon_\gamma / \overline{\rho}$, $\overline{V} = f_\gamma \overline{v}_\gamma^\gamma$, $\overline{C}_P = [\varepsilon_\beta \rho_\beta C_{P\beta} + \varepsilon_\gamma \overline{\rho}_\gamma^\gamma C_{P\gamma}] / \overline{\rho}$, $\overline{C}_{P\gamma} = C_{P\gamma}$, $\overline{k} = \varepsilon_\beta k_\beta^* + \varepsilon_\gamma k_\gamma^*$, $\overline{Y}_p = f_\beta \overline{Y}_p^\beta$ $\overline{Y}_m = f_\beta \overline{Y}_m^\beta + f_\gamma$, and $\overline{P} = \varepsilon_\beta \overline{P}_\beta^\beta + \varepsilon_\gamma \overline{P}_\gamma^\gamma$, where f_γ and

f_β are mass fractions of liquid and gas respectively. In addition, the viscous term in Equation (60) can be further simplified by the following formulation

$$\nabla \cdot \{\varepsilon_\gamma \mu_\gamma^* [\nabla \bar{v}_\gamma^\gamma + (\nabla v_\gamma^\gamma)^t]\} = \nabla \cdot \{\mu [\nabla \varepsilon_\gamma \bar{v}_\gamma^\gamma + (\nabla \varepsilon_\gamma v_\gamma^\gamma)^t]\}.$$

and viscosity μ in the above expression should be defined appropriately in terms of the liquid and gas properties. The advantage of this formulation is the ease with which this form complies with the traditional form of momentum conservation equation. Based on the above newly defined parameters, we obtain

the mass conservation equation,

$$\frac{\partial \bar{\rho}}{\partial t} + \nabla \cdot (\bar{\rho} \bar{V}) = 0 \tag{61}$$

the energy conservation equation,

$$\bar{\rho} \bar{C}_P \frac{\partial T}{\partial t} + \bar{\rho} \bar{C}_{P\gamma} \bar{V} \nabla \cdot T = \nabla \cdot [\bar{k} \nabla T] - \Delta h_{vap} \bar{\dot{m}} - \sum_i h_i^0 \bar{w}_i \tag{62}$$

the species conservation equations for polymer,

$$\frac{\partial (\bar{\rho} \bar{Y}_p)}{\partial t} = \nabla \cdot (\bar{\rho} f_\beta D_\beta^* \nabla \bar{Y}_p^\beta) + \bar{w}_p \tag{63-a}$$

$$\frac{\partial}{\partial t}(\bar{\rho} \bar{Y}_m) + \nabla \cdot (\bar{\rho} \bar{V}) = \nabla \cdot (\bar{\rho} f_\beta D_\beta^* \nabla \bar{Y}_m^\beta) + \bar{w}_m \tag{63-b}$$

and *the momentum conservation equation*,

$$\frac{\partial (\bar{\rho} \bar{V})}{\partial t} + \nabla \cdot (\frac{1}{f_\gamma} \bar{\rho} \bar{V} \bar{V}) = -\nabla \bar{P} + \bar{\rho} g + \nabla \cdot \{\mu \nabla \bar{V} + \mu (\nabla \bar{V})^t]\}. \tag{64}$$

In addition, if we rewrite the β *phase mass conservation* equation (47-c), we obtain,

$$\bar{\dot{m}} = -\rho_\beta \frac{\partial \varepsilon_\beta}{\partial t} \tag{65}$$

Equations (61-65) are the final forms of simplified macroscopic governing equations for the modeling of bubble forming process. The *constitutive equations* are needed to close the system, i.e.,

$$\varepsilon_\beta + \varepsilon_\gamma = 1 \tag{66}$$

$$Y_p + Y_m = 1 \tag{67}$$

$$\overline{w}_m = -\overline{w}_p = \rho_p A e^{-E/RT} \tag{68}$$

Seven unknowns are expected to be solved from the above equation system, that is, $\overline{\rho}$, T, $\overline{Y}_p$, $\overline{Y}_m$, $\overline{V}$, $\dot{m}$, ε_β, and ε_γ.

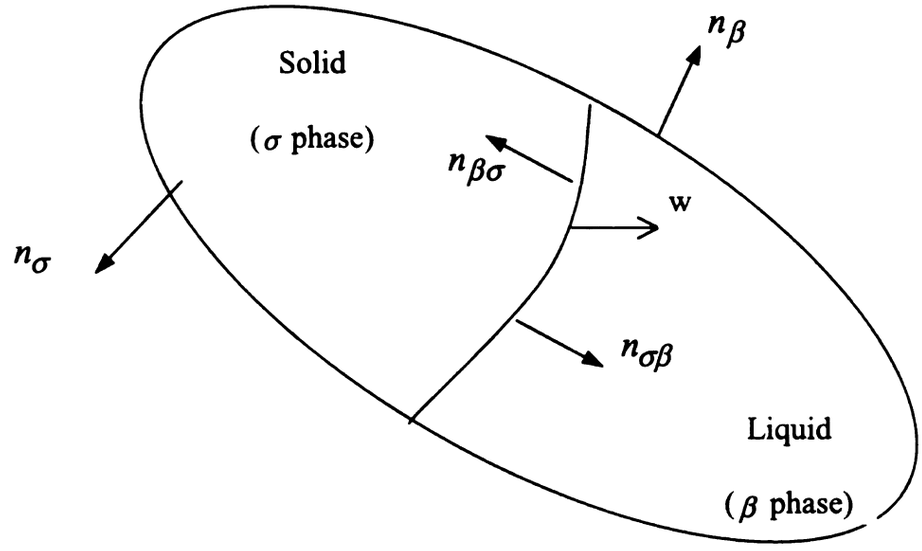

Figure 1 Material volume containing a solid-liquid interface.

REFERENCES:

1. Wichman, I. S., Progress of Energy and Combustion Science, 18: 553, 1992.
2. Ross, H. D., Progress in Energy and Combustion Science, 20: 17, 1994.
3. Law, C. K., Progress of Energy and Combustion Science, 10: 295, 1984.
4. Di. Blasi, C., Progress of Energy and Combustion Science, 19: 71, 1993.
5. Fernandez-Pello, A. C., Hirano, T., Combustion Science and Technology, 32: 1, 1983.
6. Cullis, C. F. and Hirschler, M. M, The Combustion of Organic Polymers (International Series of Monographs on Chemistry), Clarendon Press, Oxford, 1981.
7. Elomaa, M., Sarvaranta, L., Mikkola, E., Kallonen, R., Zitting, A., Zevenhoven, C. A. P., and Hupa, M., Critical Review in Biochemistry and Molecular Biology, 27(3): 137, 1997.
8. http://www.polysort.com, Cleveland, Ohio, Nov. 16, 1995.
9. Tewarson, A., and Ogden, S. D., Combustion and Flame, 89: 237, 1992.
10. Aminabhavi, T. M. and Cassidy, P. E., Polymer Plastic Technology Engineering, 28(7&8): 717, 1989.
11. Kashiwagi, T., Fire Safety Journal, 3: 185, 1981.
12. Ray, S. R., Fernandez-Pello, A. C., and Glassman, I., Journal of Heat Transfer, 102: 357, 1980.
13. Kashiwagi, T, Twenty-fifth Symposium on Combustion, The Combustion Institute, 1423, 1994.
14. Madorsky, S. L., Thermal Degradation of Organic Polymers, 1963.
15. Brauman, S. K., Journal of Polymer Science, Part B: Polymer Physics, 26: 1159,

1998.

16. Severs, E. T., Rheology of Polymer, Reinhold Publishing Corporation, 1962.
17. Fredinand R., Principles of Polymer Systems, McGraw-Hill, Inc, 1970.
18. Kashiwaki, T., Omori, A. and E. B. James, Fire Safety Science-Proceeding of the Second International Symposium, 107,1988.
19. Clift, R., Grace, J. R., and Weber, M. E., Bubbles, Drops, and Particles, Academic Press, New York, 1978.
20. Kashiwagi, T. and Ohlemiller, T. J., Nineteenth Symposium (International) on Combustion, The Combustion Institute, 815, 1982.
21. de Ris, J. N., Ph.D. thesis, Harvard University, 1968.
22. Fernandez-Pello, A. C., Ray S. R., and Glassman, I., Eighteenth Symposium (International) on Combustion, the Combustion Institute, 579, 1981.
23. Sirignano, W. A., Combustion Science and Technology, 6: 95, 1972.
24. Sirignano, W. A., Acta Astronautics 1: 1285, 1974.
25. Fernandez-Pello, A. and Willams, F. A., Combustion and Flame, 28: 251, 1977.
26. Frey, A. E. and Tien, J. S., Combustion and Flame, 36: 263, 1979.
27. Wichman, I. S., and Williams, F. A., Combustion Science and Technology, 33: 207, 1983.
28. Atreya, A., Eighth International Heat Transfer Conference, San Francisco, 1986.
29. Mao, C-P., Kodama, H., and Fernandez-Pello, A. C., Combustion and Flame, 57: 209, 1984.
30. Ray, S. R., and Glassman, I., Combustion Science and Technology, 32: 33, 1983.
31. Chen- C. H., Combustion Science and Technology, 69: 63, 1990.

32. West, J., Bhattacharjee, S., and Altenkirch, R. A., Combustion Science and Technology, 83: 233, 1992.

33. Di. Blasi C., AIAA Progress in Aeronautics and Astronautics N. 135, Numerical Approaches to Combustion, 643, 1991.

34. Williams, F. A., Sixteenth Symposium (International) on Combustion, the Combustion Institute, 1281, 1976.

35. Fernandez-Pello, A. C., Combustion Science and Technology, 39:119, 1984.

36. Aseeva, R. M., and Zaikov, G. E., Combustion of Polymer Materials, Hanser Publishers, Munich, 1985.

37. Wichman, I. S., Combustion and Flame, 63: 217, 1986.

38. Di. Blasi, C., and Continllo, G., The Use of Computers in Chemical Engineering, Proceeding of Chemical Engineering Fundamentals XVII Congress, Giardini-Nixos, 261, 1987.

39. Di. Blasi, C., Crescitell, S., Russo, G. and Fernandez-Pello, A.C., Combustion Science and Technology, 64: 289, 1989.

40. MacGrattan K. B., Kashiwagi, T., Baum H. R., and Olson, S. L., Combustion and Flame, 106: 377, 1996.

41. Di. Blasi, C., Twenty-Fifth Symposium (International) on Combustion, The Combustion Institute, 332, 1994.

42. Nakabe, K., McGrattan, K. B., Kashiwagi, T., Baum, H. R., Yamashita, H., and Kushida, G., Combustion and Flame, 98: 361, 1994.

43. Wichman, I. S., and Williams, F. A., Combustion Science and Technology, 32: 91, 1983.

44. Nayagam, V. and Williams, F. A., Physical Review Letters, 84(3): 479, 2000.

45. Hostler S. R., Nayagam, V., Proceedings of Central States Sections of the Combustion Institute, 218, 2000.

46. Patankar S. V., Numerical Heat Transfer and Fluid Flow, McGraw-Hill NY, 1980.

47. Shih, T. I-P. and Chyu, W. J., AIAA Journal, 29: 1759, 1991.

48. Voller, V. R., An Overview of Numerical Methods for Solving Phase Change Problems, Advances in Numerical Heat Transfer, 1995.

49. Wichman, I. S., Combustion and Flame, 50: 287, 1983.

50. Higuera, F. J., Linan, A., and Iglesias I., Combustion Theory and Modeling, 1: 65, 1997.

51. Sirignano, W. A., Acta Astronautica, 1: 1285, 1974.

52. Sirignano, W. A. and Glassman, I., Combustion Science and Technology, 1: 307, 1970.

53. Wichman, I. S. and Lakkaiaju, N., and Ramadan, B., Combustion Science and Technology, 127: 141, 1997.

54. Wichman, I. S., and Ramadan, B., Physics of Fluids, 10(12): 3145, 1998.

55. Zheng, G., Wichman, I. S., and Benard, A., Combustion and Flame, accepted for publication, 2000.

56. Chu, L., Chen, C. H., Tien, J. S., Combustion Science and Technology, 50: 283, 1986.

57. Di. Blasi C., and Wichman, I. S., Combustion and Flame, 102: 229, 1995.

58. Fernandez-Pello, A. C., and Williams, F. A., Fifteenth Symposium (international) on Combustion, the Combustion Institute, 217, 1975.

59. Mikkola, E. and Wichman, I. S., Fire and materials, 14: 87, 1989.

60. Abu Eaid, M., and Atreya, A., International Association for Fire Safety Science, Vol: 2, 1987.

61. Atreya, A. and Wichman I. S., Journal of Heat Transfer, 111: 719, 1989.

62. Banford, C. H., Crank, J., and Malan, D. H., Proceedings of the Cambridge Philosophical Society, 42: 166, 1945.

63. Martin, S., Tenth Symposium (International) on Combustion, The Combustion Institute, 877-896, 1965.

64. Saver, F.M., Interim T.R. AFSWP-868, USDA Forest Service, 1956.

65. Staggs, J. E. J. and Nelson, M. I., Combustion Theory and Modeling, submitted for publication, 2000.

66. Linan, A., and Williams, F., A., Combustion Science and Technology, 3: 91, 1971.

67. Kashiwagi, T., Combustion Science and Technology, 8: 225, 1974.

68. Kashiwagi, T., Combustion Science and Technology, 20: 225, 1979.

69. Amon, M., Ph.D. thesis, University of Delaware, 1982.

70. Arefmanesh, A., Ph.D. thesis, University of Delaware, 1991.

71. Wichman, I. S., A Model Describing The Steady-State Pyrolysis of Bubble Forming Polymers in Response to an Incident Heat Flux, NBSIR 85-3130, 1984.

72. Blander, M. and Katz, J. L., AICHE J., 21: 833, 1975.

73. Han, J. H. and Han, D. H., Journal of Polymer Science: Part B: Polymer Physics, 28: 711, 1990.

74. Clift, R., Grace, J. R. and Weber, M. E., Bubbles, Drops and Particles, Academic Press, 1978.

75. Sjoerd, V. S., and Robert C., Boiling Phenomena, Physicochemical and Engineering Fundamentals and Applications, Hemisphere Publishing Company, 1979.

76. Young, N. O., Goldstein, J. S., and Block, M. J., Journal of Fluid Mechanics, 6: 350, 1959.

77. Butler, K. M., Baum, H. R., and Kashiwagi, T., Fire Safety Science: Proceedings of the Fifth International Symposium, 523, 1997.

78. Harper, J. F., Advances in Applied Mechanics, 12:.59, 1972.

79. Prosperetti, A., and Plesset, M., S., Journal of Fluid Mechanics, 85: 349, 1978.

80. Epstein, M. L., and Plesset, M. S., Journal of Chemical Physics, 18: 1505, 1950.

81. Torquato, S., Applied Mechanics Review, 44(2): 37, 1991.

82. Whitaker, S., Simultaneous Heat, Mass, and Momentum Transfer in Porous Media: A Theory of Drying, Advanced Heat Transfer, 9: 119, 1977.

83. Necati Ozisik, M., Heat Conduction, John Wiley & Sons, 1980.

84. Price, P. H., and Slack, M. R., British Journal of Applied Physics, 5: 285, 1954.

85. Voller, V. R., Swaminathan, C. R., Journal of Numerical Heat Transfer, Part B., 24: 161, 1993.

86. Patankar, S. V., Journal of Numerical Heat Transfer, 4: 409, 1981.

87. Van Doormaal, J. P. and Raithby, G. D., Journal of Numerical Heat Transfer, 7: 147, 1984.

88. Shyy, W., Thakur, S. S., Ouyang, H., Liu, J., and Blosch, E., Computational Techniques for Complex Transport Phenomena, Cambridge University Press, 1997.